RÉPUBLIQUE FRANÇAISE
Liberté Égalité Fraternité

Université de Toulouse

Doctorat de l'Université de Toulouse

préparé à l'INSA Toulouse

Intégration localisée de matériaux magnétiques doux à partir de nanoparticules pour des applications RF

Thèse présentée et soutenue, le 15 décembre 2025 par

Mélik MAKSEM

École doctorale
SDM - SCIENCES DE LA MATIERE - Toulouse

Spécialité
Chimie Organométallique et de Coordination

Unité de recherche
LPCNO - Laboratoire de Physique et Chimie des Nano-Objets

Thèse dirigée par
Lise-Marie LACROIX et Thomas BLON

Composition du jury
Mme Catherine AMIENS, Présidente, Université de Toulouse
M. Jerome FRESNAIS, Rapporteur, CNRS Paris-Centre
M. Christophe LEFEVRE, Rapporteur, CNRS Alsace
Mme Lise-Marie LACROIX, Directrice de thèse, Université de Toulouse

Membres invités
M. Thierry PARRA, Co-encadrant, Université de Toulouse
M. Thomas BLON, Université de Toulouse

Localized Integration of Soft Magnetic Materials Derived from Nanoparticles for RF Device Applications

General introduction

These days, digital **issues** are becoming increasingly important, and radio communications are becoming indispensable in both everyday life and critical sectors such as mobile telephony, medicine, security, aeronautics, and environmental monitoring. The rapid and continuous development of wireless communication systems has led to a substantial increase in energy consumption, which must be carefully controlled. Moreover, the growing expansion of the Internet of Things (IoT) further accentuates this challenge, as it requires highly compact, low-maintenance systems with extremely low power consumption to ensure long battery lifetimes [1]. In addition, the range of frequency bands in use is constantly expanding to prevent bandwidth saturation in the face of increasing data exchange [2]. The electronic microcomponents are essentially made up of inductors, which occupy more than 50% of the chip surface, and are responsible for most of the losses. This is mainly due to resistive losses in coils at high frequencies, and above the self-resonant frequency, parasitic capacitance becomes dominant [3]. Increasing the quality factor of inductors (the ratio of the energy stored to the dissipated one) is the key for reducing losses. Various strategies are considered, such as optimizing the geometry of the inductor, or by using low loss dielectric substrate. However, these methods are no longer sufficient for increasing performance while miniaturizing the electronic components. The integration of magnetic materials optimized for RF devices is one way to achieve both energy efficiency and miniaturization requirements. Integrating a soft material concentrates the local magnetic flux, enabling the inductor to be made smaller while significantly reducing resistive losses and radiation, all without compromising efficiency. The soft material must ideally exhibit a high magnetic permeability, which is maintained at least up to the desired operating frequency. Eddy current losses being faced in conductive material, magnetic insulators are mandatory. Since 1945, industrial-scale production of soft ferrites has been mastered [4,5]. Ferrites are magnetic oxides with the formula $X_xFe_{3-x}O_4$, where X designates transition metals such as manganese (Mn), zinc (Zn), nickel (Ni), cobalt (Co) etc... These materials are already used in many RF applications because they are cheap and are very good electrical insulators [6]. However, these materials do not have sufficiently high permeabilities to ensure continued technological progress. For this reason, research into exploiting the properties of soft metallic iron and cobalt alloys has begun [6,7]. These materials have the best magnetic properties, magnetizations, permeabilities,

etc... but metals are also good electrical conductors and cannot be used on their own since they are short-circuiting the two conductors involved in an RF waveguide. It is therefore necessary to develop strategies that enable their use by the implementation of dielectric properties, and reduced conductivity on the materials. In that aim, composite materials are produced by combining these metals with insulators. The most common form of integration currently in use is relatively complex and involves creating laminated structures with alternating layers of magnetic and insulating materials [8–10]. By adding insulating properties to the material and limiting the thickness of the magnetic layers to around a hundred nanometers (less than the skin depth), eddy currents are limited, losses are greatly reduced, and the material is competitive [11,12]. In this context, the aim of this thesis is to develop new composite materials for high-frequency applications, by further simplifying the methods of manufacturing and integrating composite materials for a microelectronics approach.

As a consequence, this thesis builds on several disciplines, notably the chemical synthesis of nanoparticles and electromagnetism, two disciplines in which Michael Faraday played a major role. An understanding of the historical development of these fields may be valuable, as their progress provides the foundation for our current work.

The “magic” of **magnetism** has been known since ancient times. Two permanent magnets, or a permanent magnet and an object that can be magnetized, can attract each other. This attraction is strong enough to be perceived by the naked eye. It was in China, during the Song dynasty, that the first descriptions of magnetic instruments for orientation are found [13]. In 1086, Shen Kuo described the manufacture, principle and use of the first compass [14]. It consisted of magnetized steel needles suspended in a liquid. They were aligned according to the Earth's magnetic field, and it was already possible to observe declines in the Earth's magnetic field. The 19th century marked the beginning of the understanding of electromagnetics. The impetus was given by Hans-Christian Oersted in 1820 [15], who demonstrated the connection between electricity and magnetism by deflecting the orientation of a compass using an electric current. Various studies of magnetic and electric fields, notably those by Michael Faraday and André-Marie Ampère [16], enabled James Clerk Maxwell to formulate a precise mathematical description of electromagnetic fields and interactions in 1864 [17]. The 20th century saw major advances in the study of the structure of matter at the atomic scale, the development of quantum mechanics and the description of

spin. This led to a fundamental understanding of magnetism at the atomic scale, and in particular to the development of molecular magnetism and spintronics.

The special properties of **nanoparticles** have been used and synthesized unintentionally since ancient times [18]. Glassmakers used plasmonic nanoparticles, in particular gold, silver and copper, to give specific colors and dichroic properties depending on the lighting. The most famous example is the Lycurgus cup. In 1857, Faraday gave the first precise description of the synthesis of gold nanoparticles and their specific optical properties [19]. The development of nanoscience was greatly facilitated by improvements in microscopy methods, in particular the invention of the transmission electron microscope (TEM) by Max Knoll and Ernst Ruska in 1931 [20,21], followed by the development of near-field microscope methods such as the scanning tunnelling microscope (STM) in 1981 [22,23]. The second half of the 20th century, and the 21st, saw the rise of nanoscience, with numerous methods and strategies being developed to control the composition, shape and surface of nanoparticles. The first synthesis of magnetic nanoparticles was reported by René Massart in 1981 [24]. This was a co-precipitation synthesis that produced 12 nm magnetite nanoparticles without a stabilizing agent. This type of nanoparticle was quickly applied as contrast agents for magnetic resonance imaging (MRI) in the 1980s [18].

Radio frequencies (RF) refer to electromagnetic wave frequencies between 3 kHz and 3 GHz. The main applications of this frequency range are radio communications and radars. Radiocommunications began with the invention of the wireless telegraph by Guglielmo Marconi in 1895 [25]. Information was sent using antenna signals in Morse code. In 1898, Oliver Lodge developed the tuner, which enabled parasitic signals to be eliminated by selecting the desired frequencies from LC circuits resonating at these frequencies [26]. The first radio broadcasts began in the 1920s [27]. Since the beginning of telecommunications, electronic engineers have been interested in soft magnetic materials, which retain their properties at very high frequencies. These materials were quickly adopted as cores to enhance the performance and reduce the size of inductive components, including inductors, transformers, filters, antennas, motors, and electrical generators [16,28].

The figure 0.1 shows the various discoveries mentioned above on the same timeline.

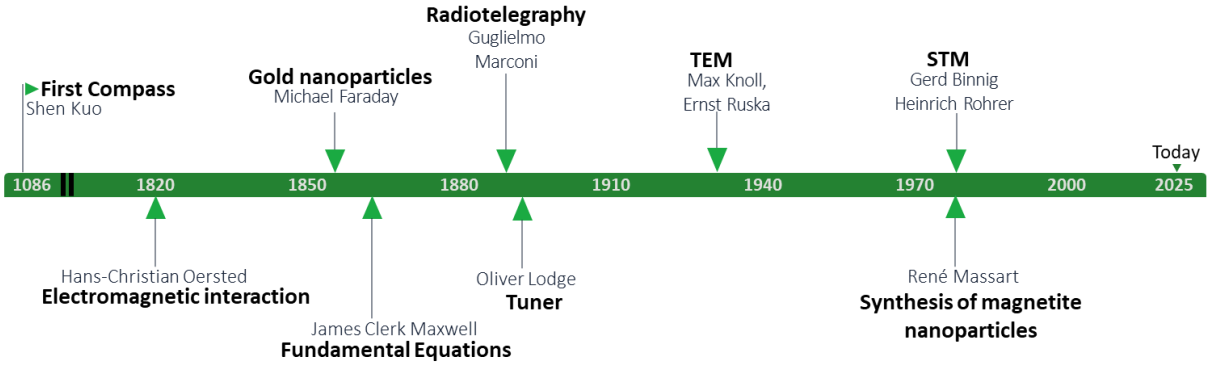

Figure 0.1. Timeline of major milestones in the history of magnetism and nanomaterials leading to this research project (1086–2025).

In recent years, progress has been made in the synthesis of magnetic nanoparticles and in deposition methods worldwide. Here, at the LPCNO (Laboratoire de Physique et Chimie des Nano-objets), Cyril Garnero has developed in 2016 an organometallic approach for synthesizing chemically ordered FeCo nanoparticles with promising radio frequency properties [29], and Pierre Moritz has developed in 2019 a new deposition approach, compatible with cleanroom processes, benefiting from the magnetophoresis force to yield integrated permanent magnets [30,31]. Combining such a driven assembly with optimized soft magnetic nanoparticles is at the heart of this work.

The **objective** of this study is indeed to fabricate soft magnets with high permeability using a bottom-up approach in order to increase the performance of microcomponents in the radiofrequency domain. In this process, magnetic nanoparticles are first synthesized and subsequently assembled into micromagnets on the microcomponents, in particular on inductors, using magnetophoresis.

The first step is the chemical synthesis of Fe, Co and Ni-based nanoparticles that will serve as building blocks. The fine tuning of the particles is crucial, since their intrinsic properties play a major role in the final properties of the assembled magnet. For this reason, the static magnetic properties of these particles are characterized by systematically using conventional magnetometry. To limit eddy current losses, these particles must be smaller than the thickness of the skin depth and coated with organic ligands that can act as electrical insulators between densely packed particles. Typically for iron at 1 GHz, the skin depth is about 200 nm. The surface passivation of the nanoparticles to preserve the properties over time is

an important issue, the oxidation due to air exposure can indeed deteriorate the magnetic properties of the materials over time.

Once the optimized building blocks are obtained, the second step is their directed assembly using magnetophoresis. This fast method allows producing fairly dense 3D magnets of sub-millimetric size under mild conditions (room temperature, atmospheric pressure), localized on a chip in a material-efficient manner. The deposition being controlled by different parameters (nanoparticles concentration, solvent nature, magnetic field…) their effects on the organization of the deposit have been studied using Small Angle X-Ray Scattering (SAXS) techniques.

The third step is to characterize the magnetic properties at radio frequencies and evaluate their impact on the performance of inductors. To do so, a vector network analyzer is used to measure the transmission and reflection parameters (*S* parameters). The objective is to determine the resonance frequencies and to characterize the real and imaginary parts of the permittivity (ε) and permeability (μ) of a coplanar waveguide coated with a micromagnet. These values characterize the electromagnetic properties of the material and therefore its interactions with the electromagnetic waves. Planar inductors, which are the simplest micro-components, have been used as demonstrators in order to directly illustrate the effect of the material. Indeed, the inductance value is directly related to the effective magnetic permeability of the medium, any increase of this inductance value illustrates the effect of the submillimeter magnet covering the inductor.

To address this research plan, the manuscript is organized as follows.
The first chapter provides a bibliographic study introducing the theoretical background necessary to understand and interpret the experiments and results presented in the subsequent chapters. Particular emphasis is made on nanomagnetism and magnetic core–inductor interactions, in order to establish criteria for selecting the most suitable materials and inductor geometries. A non-exhaustive overview of liquid-phase synthesis methods for monodisperse magnetic nanoparticles with controlled size, shape, and composition is then presented. Finally, the forces and mechanisms governing the assembly of magnetic nanoparticles under an applied field are discussed.

The second chapter focuses on nanoparticle synthesis, presenting a practical guide for the preparation of Fe, FeCo, and CoNi nanoparticles with controlled size, shape, and composition. The objective is to enable fine-tuning of their static magnetic properties through both compositional and dimensional control. A post-synthesis treatment strategy involving carburization is also introduced to prevent surface oxidation.

The third chapter addresses the assembly of nanoparticles under an external magnetic field. Assemblies are prepared using different types of particles and conditions, including dispersion in solution, deposition on microscopy glass slides, and magnetophoretic processes. The aim is to understand and rationalize the micromagnet formation, and to identify the key factors determining whether isotropic or anisotropic structures are obtained.

Finally, the fourth chapter is devoted to dynamic properties and radiofrequency (RF) applications. The influence of nanoparticle size and composition on the magnetic properties of micromagnets is analyzed, with particular attention to their impact on inductance enhancement. Based on these findings, optimal nanoparticle size and composition for RF applications are proposed.

References

[1] Rancy R. IMT for 2020 and Beyond. 5G Outlook – Innov. Appl. 1st ed., New York: River Publishers; 2022, p. 69–83.

[2] Dangi R, Lalwani P, Choudhary G, You I, Pau G. Study and Investigation on 5G Technology: A Systematic Review. Sensors 2021;22:26. https://doi.org/10.3390/s22010026.

[3] Sai R, Shivashankar SA, Yamaguchi M, Bhat N. Magnetic Nanoferrites for RF CMOS: Enabling 5G and Beyond. Electrochem Soc Interface 2017;26:71–6. https://doi.org/10.1149/2.F08174if.

[4] Sugimoto M. The Past, Present, and Future of Ferrites. J Am Ceram Soc 1999;82:269–80. https://doi.org/10.1111/j.1551-2916.1999.tb20058.x.

[5] Owens C. A Survey of the Properties and Applications of Ferrites below Microwave Frequencies. Proc IRE 1956;44:1234–48. https://doi.org/10.1109/jrproc.1956.274947.

[6] Soft Magnetic Materials. Wiley Encycl. Electr. Electron. Eng. 1st ed., Wiley; 2016, p. 1–42. https://doi.org/10.1002/047134608x.w4504.pub2.

[7] Silveyra JM, Ferrara E, Huber DL, Monson TC. Soft magnetic materials for a sustainable and electrified world. Science 2018;362:eaao0195. https://doi.org/10.1126/science.aao0195.

[8] Shokrollahi H, Janghorban K. Soft magnetic composite materials (SMCs). J Mater Process Technol 2007;189:1–12. https://doi.org/10.1016/j.jmatprotec.2007.02.034.

[9] Wan K-H, Hsiang H-I. Next-generation laminated nanocrystalline magnetic cores for high-frequency power electronics: enhancing magnetic properties and thermal stability. J Magn Magn Mater 2025;629:173299. https://doi.org/10.1016/j.jmmm.2025.173299.

[10] Hamler A, Goričan V, Šuštaršič B, Sirc A. The use of soft magnetic composite materials in synchronous electric motor. J Magn Magn Mater 2006;304:e816–9. https://doi.org/10.1016/j.jmmm.2006.03.003.

[11] Liu Y, Eimer S, Zhao J, Chen Y. Magnetic and Dielectric Properties of CoFeB Multilayer Thin Films With Oxide Capping Layer. IEEE Magn Lett 2024;15:1–5. https://doi.org/10.1109/lmag.2024.3459813.

[12] Guo Y, Wang D, Wang Z, Zhao R, Lv Z, Li Y, et al. Magnetic properties and dielectric properties of CoFeB/NdFeB composite films at Terahertz. Compos Commun 2025;53:102242. https://doi.org/10.1016/j.coco.2024.102242.

[13] Ebrey PB. The Cambridge illustrated history of China. Cambridge New York Melbourne: Cambridge university press; 1996.

[14] McElroy G. Dream pool essays. Vancouver, B.C: Talonbooks; 2001.

[15] Ørsted HC, Jackson AD, Knudsen O, Ørsted HC. Selected scientific works of Hans Christian Orsted. Princeton, NJ: Princeton Univ. Press; 1998.

[16] Coey JMD. Magnetism and magnetic materials. Paperback edition. Cambridge New York Port Melbourne: Cambridge University Press; 2018.

[17] Maxwell JC. VIII. A dynamical theory of the electromagnetic field. Philos Trans R Soc Lond 1865;155:459–512. https://doi.org/10.1098/rstl.1865.0008.

[18] Bayda S, Adeel M, Tuccinardi T, Cordani M, Rizzolio F. The History of Nanoscience and Nanotechnology: From Chemical–Physical Applications to Nanomedicine. Molecules 2019;25:112. https://doi.org/10.3390/molecules25010112.

[19] X. The Bakerian Lecture. —Experimental relations of gold (and other metals) to light. Philos Trans R Soc Lond 1857;147:145–81. https://doi.org/10.1098/rstl.1857.0011.

[20] Ruska E. The Development of the Electron Microscope and of Electron Microscopy (Nobel Lecture). Angew Chem Int Ed Engl 1987;26:595–605. https://doi.org/10.1002/anie.198705953.
[21] Freundlich MM. Origin of the Electron Microscope: The history of a great invention, and of a misconception concerning the inventors, is reviewed. Science 1963;142:185–8. https://doi.org/10.1126/science.142.3589.185.
[22] Binnig G, Rohrer H. Scanning tunneling microscopy. Surf Sci 1983;126:236–44. https://doi.org/10.1016/0039-6028(83)90716-1.
[23] Binnig G, Rohrer H. Scanning tunneling microscopy—from birth to adolescence. Rev Mod Phys 1987;59:615–25. https://doi.org/10.1103/revmodphys.59.615.
[24] Massart R, Cabuil V. Synthèse en milieu alcalin de magnétite colloïdale : contrôle du rendement et de la taille des particules. J Chim Phys 1987;84:967–73. https://doi.org/10.1051/jcp/1987840967.
[25] Bondyopadhyay PK. Guglielmo Marconi - The father of long distance radio communication - An engineer's tribute. 25th Eur. Microw. Conf. 1995, Bologna, Italy: IEEE; 1995, p. 879–85. https://doi.org/10.1109/euma.1995.337090.
[26] Syntonic wireless telegraphy; with specimens of large-scale measurements. Proc R Soc Lond Ser Contain Pap Math Phys Character 1909;82:227–56. https://doi.org/10.1098/rspa.1909.0030.
[27] Harte B. When Radio Was the Cats Whiskers. Sydney: Rosenberg Pub.; 2002.
[28] Kazimierczuk MK. High-frequency magnetic components. 2nd edition. Chichester, Sussex, UK: John Wiley & Sons; 2014.
[29] Garnero C, Lepesant M, Garcia-Marcelot C, Shin Y, Meny C, Farger P, et al. Chemical Ordering in Bimetallic FeCo Nanoparticles: From a Direct Chemical Synthesis to Application As Efficient High-Frequency Magnetic Material. Nano Lett 2019;19:1379–86. https://doi.org/10.1021/acs.nanolett.8b05083.
[30] Moritz P, Gonon A, Blon T, Ratel-Ramond N, Mathieu F, Farger P, et al. Magnetophoresis-Assisted Capillary Assembly: A Versatile Approach for Fabricating Tailored 3D Magnetic Supercrystals. ACS Nano 2021;15:5096–108. https://doi.org/10.1021/acsnano.0c10215.
[31] Moritz P, Lecerf I, Gonon A, Maties G, Blon T, Cayez S, et al. Hybrid Ni–Co–Ni Structures Prepared by Magnetophoresis as Efficient Permanent Magnets for Integration into Microelectromechanical Systems. Adv Eng Mater 2022;24:2200733. https://doi.org/10.1002/adem.202200733.

Table of Contents

Chapter I

1 Electromagnetism and radio frequency application..... 15

1.1 Basics of nanomagnetism 15

1.2 Magnetization dynamics..... 18

1.3 Choice of magnetic materials for inductors 25

1.4 Magnetic effect on inductors 31

2 Synthesis of magnetic nanoparticles in liquid phase 39

2.1 Synthesis of magnetic metal oxide nanoparticles 39

2.2 Synthesis of magnetic metallic nanoparticles 43

3 Assembly of magnetic nanoparticles under a magnetic field 49

3.1 Magnetic dipolar interactions 49

3.2 Formation of chains 51

4 Conclusion 62

5 References..... 64

Chapter II

1 Organometallic synthesis 75

1.1 Synthesis of iron (Fe) nanoparticles 76

1.2 Synthesis of iron-cobalt (FeCo) nanoparticles..... 88

1.3 Synthesis of iron carbide (FeC) nanoparticles 95

1.4 Conclusion on the NPs prepared by the organometallic approach..... 98

2 Toward the synthesis of larger FeCo particles 99

3 Cobalt-Nickel (CoNi) polyol synthesis..... 102

3.1 Size control – Heterogeneous nucleation and growth model..... 103

3.2 Magnetic properties of the CoNi particles 115

3.3 Conclusion on the CoNi particles prepared by the polyol synthesis 117

4 Conclusion 119

5 References 120

Chapter III

1 Methods for preparing and analyzing samples 126

1.1 Sample preparation 126

1.2 Structural analyses 129

1.3 Random close pack assemblies of particles 135

2 Assemblies of FeCo NPs 138

3 Ordered assemblies of nanoparticles: the case of nanocubes 140

3.1 Characterization of the different nanocubes used 140

3.2 Characterization of the micromagnet obtained by magnetophoresis 140

3.3 Characterization of the assemblies in solution 143

3.4 Organization of thin films 147

4 Mechanism investigation 151

4.1 Effect of the NP shape on the thin film assembly 151

4.2 Effect of the magnetic field on the thin film assembly 153

4.3 Effect of the polydispersity 155

4.4 Other parameters (concentration, solvent) 156

4.5 Proposed mechanism 159

5 Conclusion 162

6 References 163

Chapter IV

1 Sample designs, measurements, and characteristic extraction methods 169

1.1 Electrical measurements 169

1.2 RF electrical characterization chips 176

2 FeCo particles obtained from reduction approach 187

2.1 Reproducibility and measurement uncertainty 187

2.2 Characterization of dynamics properties 189

2.3 Demonstrations on inductors 190
3 Nanoparticles from organometallic approach 192
3.1 Oxidation issue interactions 192
3.2 Overcoming the issue of oxidation (epoxy protection, FeC) 194
3.3 Discussion 201
4 CoNi particles from polyol synthesis 204
4.1 Control of dynamical magnetic and dielectric properties 204
4.2 Application of the implementation of inductor core 209
5 Conclusion 215
6 References 217

General conclusion and perspectives 220

Appendix 224

Chapter I. Review of preparation of soft magnetic materials for radio frequency inductors applications

Summary of Chapter I

1 Electromagnetism and radio frequency application 15

1.1 Basics of nanomagnetism 15

1.2 Magnetization dynamics 18

1.2.a Governing spin equations 18

1.2.b Ferromagnetic resonance (FMR) 19

1.3 Choice of magnetic materials for inductors 25

1.3.a Permeability, Ferromagnetic Resonance, and Snoek's Law 25

1.3.b Minimizing Magnetic Losses 27

1.4 Magnetic effect on inductors 31

1.4.a Inductors 31

1.4.b Other examples of integration 38

2 Synthesis of magnetic nanoparticles in liquid phase 39

2.1 Synthesis of magnetic metal oxide nanoparticles 39

2.1.a Coprecipitation method 39

2.1.b Solvothermal method 41

2.2 Synthesis of magnetic metallic nanoparticles 43

2.2.a Thermal decomposition 43

2.2.b Organometallic synthesis 44

2.2.c Polyol synthesis 46

3 Assembly of magnetic nanoparticles under a magnetic field 49

3.1 Magnetic dipolar interactions 49

3.2 Formation of chains 51

3.2.a 1D chains 51

3.2.b Interchain interaction 56

4 Conclusion 62

5 References 64

Magnetic nanoparticles (MNPs) have attracted considerable attention in recent decades due to their magnetic properties and their potential integration in diverse technological domains, in particular in advanced electronic devices. A key advantage of MNPs lies in the tunability of their properties, which can be tailored through controlled chemical modifications. Their implementation in microelectronics and radiofrequency (RF) components, such as inductors, requires a comprehensive understanding at multiple scales, from nanoscale synthesis to device-level design. Achieving efficient magnetic cores with increased inductance values demands not only precise control over nanoparticle synthesis but also a deep knowledge of their collective organization under external magnetic field and their fundamental electromagnetic interaction within the inductor.

The present review follows this multiscale trajectory. We begin with fundamental electromagnetic properties of magnetic materials, inductors and their interactions in order to determine specific criteria for material selection and for the design and optimization of magnetic cores within inductors. Subsequently, an overview of the synthesis routes for MNPs in liquid phase is presented, including both metal oxide and metallic systems, with a focus on representative methods rather than exhaustive coverage. Finally, we examine how MNPs assemble under the influence of magnetic fields, emphasizing the role of dipolar interactions, chain formation, and interchain coupling phenomena. This section bridges the gap between single-particle properties and the emergence of collective magnetic behaviors.

By structuring the review along with this progression from nanoparticle synthesis to their assembly, and their potential application on inductor, we aim to provide an integrated framework that highlights the interdependence of chemical, physical, and engineering considerations. This holistic approach emphasizes the necessity of combining expertise in chemistry (nanoparticle synthesis), physics (magnetic properties and interactions), and electrical engineering (device design and properties, characterization) to develop efficient nanoparticle-based magnetic materials for performant inductive components.

1. Electromagnetism and radio-frequency applications

1.1 Basics of nanomagnetism

To understand the integration of magnetic materials into inductors operating at radio frequencies, it is essential to first establish the fundamental concepts of ferromagnetism and ferrimagnetism, and then to discuss their dynamic magnetic properties.

Ferromagnetism arises from the collective ordering of atomic magnetic moments, which results from the competition and balance of several energy contributions. In transition metals such as Fe, Co, and Ni, the magnetic moments of atoms are mainly originating from spins and are aligned collinearly and in the same direction, giving rise to a ferromagnetic configuration. In contrast, ferrimagnetism occurs in materials where magnetic moments are aligned antiparallel but with unequal magnitudes, leading to net magnetization.

The total magnetic energy E_t of a system can be expressed as [1]:

$$E_t = E_{exch} + E_{an} + E_{dip} + E_{Zeeman} \qquad (\mathrm{I}.1)$$

where each term represents a distinct contribution:

Exchange energy (E_{exch}): This short-range interaction tends to align neighboring atomic magnetic moments. It is characterized by the exchange constant *J*, which reflects the strength of the interaction.

Magnetocrystalline anisotropy energy (E_{an}): In crystalline ferromagnets, the symmetry of the crystal lattice defines preferential directions for magnetization, known as easy axes, while other directions correspond to hard axes. For instance, body-centered cubic (bcc) Fe has easy axes along the {100} directions due to a positive first anisotropy constant (K_1), whereas face-centered cubic (fcc) Ni has easy axes along {111}, corresponding to a negative K_1. Hexagonal close-packed (hcp) Co exhibits an important uniaxial anisotropy along the ⟨0001⟩ direction. Materials with low anisotropy (e.g., cubic crystals) are typically considered soft magnetic materials, while those with high anisotropy (e.g., hexagonal crystals) are regarded as hard or semi-hard magnetic materials.

Dipolar energy (E_{dip}): The distribution of magnetization within a material gives rise to demagnetizing fields, which oppose the magnetization and depend strongly on the geometry of the material. This contribution is long ranged, in contrast with exchange interactions, and is responsible for shape anisotropy.

Zeeman energy (E_{Zeeman}): This term accounts for the interactions of the magnetic moments with an external magnetic field. It favors alignment of the magnetization moment with the external field direction and can be expressed as:

$$E_{zeeman} = -\mu_0 \vec{M} \cdot \vec{H} \qquad (\mathrm{I}.2)$$

Where μ_0 is the vacuum permeability, M the magnetization (the sum of all the magnetic moments per unit volume of a given matter), and H the applied magnetic field.

The interplay between these energies determines the equilibrium magnetic configuration.

The magnetization behavior of ferromagnetic materials under an applied magnetic field can be described by a hysteresis loop illustrated on figure I.1. Key parameters extracted from this curve include

- **Saturation magnetization (M_s):** the maximum magnetization when all moments are aligned with the applied field.
- **Remanent magnetization (M_r):** the residual magnetization at zero applied field.
- **Coercive field (H_c):** the magnitude of the reverse field required to bring the magnetization back to zero.

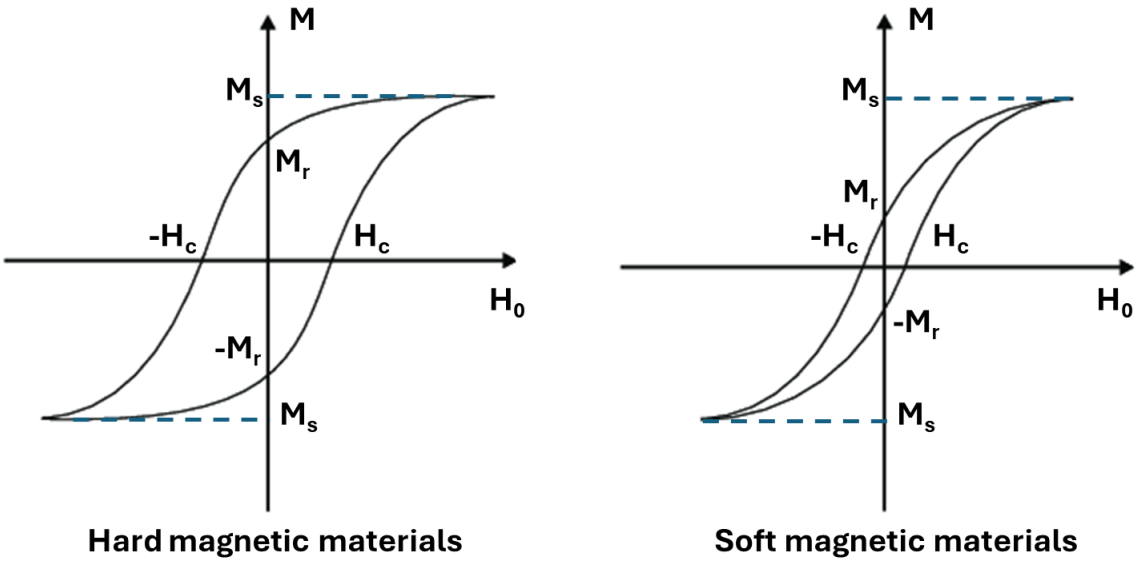

Figure I.1. Magnetization curve M(H): magnetization M depending on the intensity of an applied magnetic field H. Typically hard magnetic materials have higher coercive field and remanent magnetization than soft magnetic material [2].

In bulk ferromagnets, to minimize the dipolar energy there is the formation of magnetic domains (Weiss domains), separated by domain walls. However, when the particle size decreases below a critical diameter (D_{sd}), the formation of multiple domains becomes energetically unfavorable, and a single-domain configuration is stabilized. This critical size depends on intrinsic material parameters such as the exchange constant (J), the magnetocrystalline anisotropy constant (K_1), and the saturation magnetization (M_s). For intermediate particle size, intermediate vortex-like spin arrangements may occur, as experimentally observed in nanoscale Fe cubes [3,4].

Single-domain nanoparticles exhibit large coercivity due to coherent magnetization reversal. However, as the particle size decreases and falls below the superparamagnetic limit D_{sp}, the coercive field decreases and disappears, as the anisotropy energy (K_1V) becomes comparable to or smaller than the thermal energy (kT). In this regime, the particle moments fluctuate freely under thermal agitation, resulting in the disappearance of both coercivity and remanence typical of the superparamagnetic state. The size dependance of the magnetic properties and the critical size limit D_{sd} and D_{sp} for most common magnetic materials are given in figure I.2.

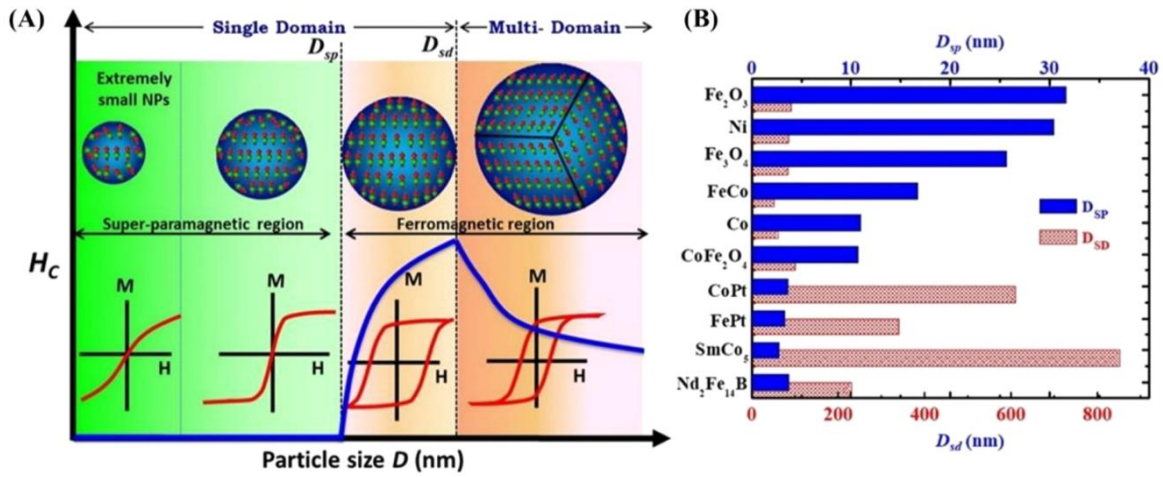

Figure I.2. (A) Size-dependent magnetization and magnetic coercivity (Hc) of nanoparticles: (top) schematic representation of multidomain and single-domain nanoparticles, and (bottom) variation in magnetic hysteresis behavior with decreasing nanoparticle size. The coercivity of ferromagnetic materials initially increases as particle size decreases, reaches a maximum at the critical single-domain size (D_{sd}), and then decreases with further size reduction, eventually entering the superparamagnetic regime due to thermal fluctuations (blue curve). (B) Critical single-domain sizes and superparamagnetic limits for various ferromagnetic and ferrimagnetic materials in quasi-static conditions [5–7].

1.2 Magnetization dynamics

1.2.a Governing Equation

The magnetization vector $\vec{M}$, which represents the collective sum of all atomic magnetic moments $\vec{m}$ aligned in the same direction, can deviate by an angle θ with respect to an applied magnetic field $\vec{H}$. In such a situation, the field exerts a torque on the magnetization, leading to a precession motion of $\vec{M}$ around the field direction.

By applying the angular momentum theorem, this motion is described as the Larmor precession: $\frac{d\vec{M}}{dt} = -\gamma \vec{M} \times \mu_0 \vec{H}$ (I. 3)

where γ is the gyromagnetic ratio.

The Landau–Lifshitz-Gilbert formalism refines this description by introducing a phenomenological damping term that accounts for energy dissipation during precession. This leads to the Landau–Lifshitz-Gilbert equation [8]:

$$\frac{d\vec{M}}{dt} = -\gamma(\vec{M} \times \mu_0 \overrightarrow{H_{eff}} - \alpha\vec{M} \times \frac{d\vec{M}}{dt}) \qquad (\text{I}.4)$$

Here, $\overrightarrow{H_{eff}}$ is the effective magnetic field that drives the precession, and α is the damping parameter. This equation is illustrated by figure I.3.

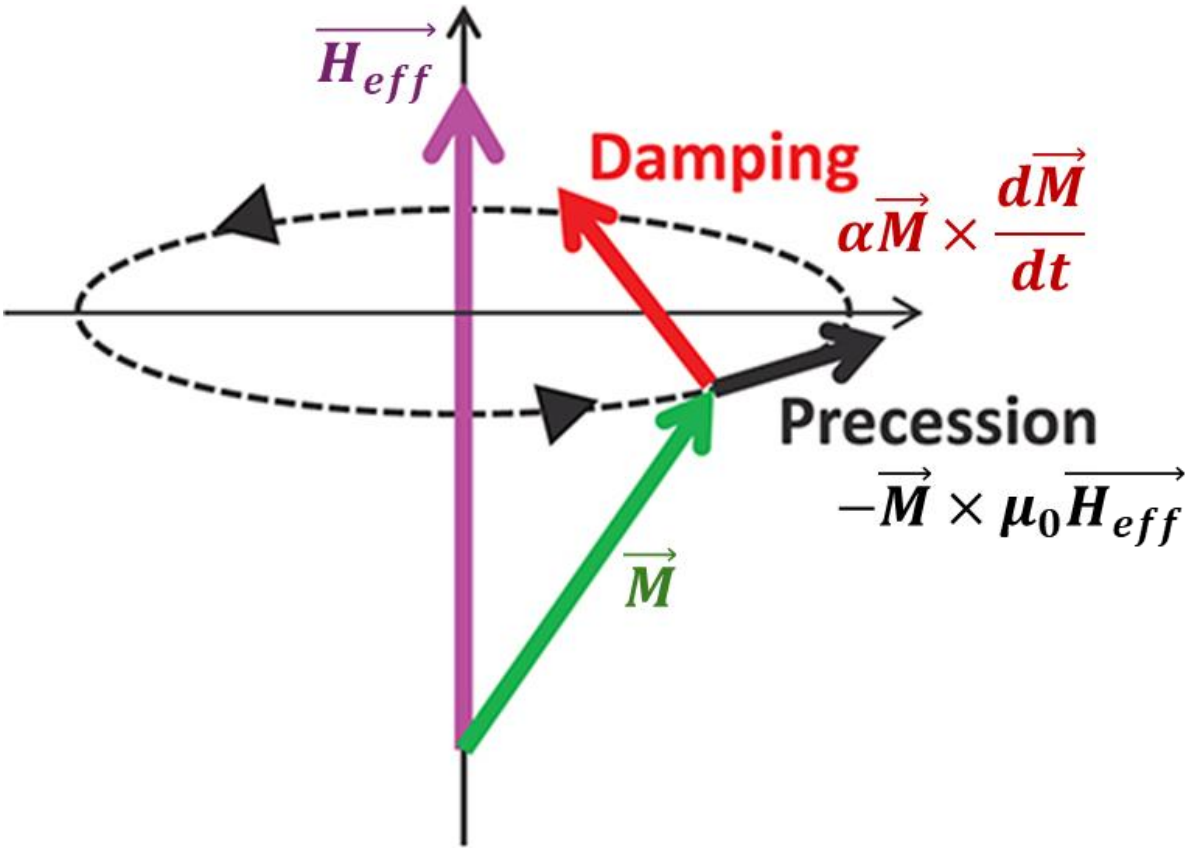

Figure I.3. Illustration of the Landau-Lifshitz Equation, the magnetic moment undergoes a damped precession movement around H_{eff} [9].

1.2.b Ferromagnetic resonance (FMR)

Ferromagnetic resonance (FMR) corresponds to the resonant excitation of magnetization precession. It occurs when a weak alternating magnetic field h applied perpendicular to the effective field H_{eff}, the alternating field compensates for damping loss. Under resonance, the applied field oscillates at the same frequency as the natural precession of M, and the magnetic system absorbs energy maximally.

The resonance condition depends on the effective field, which can be expressed as:

$$\overrightarrow{H_{eff}} = \overrightarrow{H_0} + \overrightarrow{H_{ex}} + \overrightarrow{H_a} + \overrightarrow{H_d} \qquad (\text{I. } 5)$$

where:

- H_0 is the externally applied magnetic field,
- H_{ex} represents exchange contributions,
- H_a arises from magnetocrystalline anisotropy,
- H_d is the demagnetizing field determined by the sample's geometry.

Thus, the resonance frequency depends not only on the applied field but also on the material's microstructure, shape, intrinsic magnetic anisotropy et magnetic inhomogeneity (influencing on H_{ex}).

Uniform Resonance Mode: Kittel's Model

The uniform mode, first described by Kittel [10–12], assumes coherent precession of all magnetic moments in the sample without spatial phase differences, it is the uniform resonance mode. In practice, this is achieved with a sufficiently large static applied magnetic field which saturates the sample magnetization, typically along z, while a transverse microwave small magnetic field h is applied in the xOy plane. Under these conditions, the resonance frequency can be obtained by solving the magnetization dynamics equation (Eq. (I.3)), neglecting damping effects. Notably, Kittel showed that the shape of the material influences the resonance frequency. For an ellipsoid magnetized along its symmetrical axis (z-axis) corresponding to easy uniaxial magnetocrystalline anisotropy of field H_a, under an external field $H_0$the resonance condition is:

$$\frac{\omega}{\gamma} = \sqrt{\left[H_0 + H_a - \left(N_y - N_z\right)\mu_0 M_S\right]\left[H_0 + H_a - (N_x - N_z)\mu_0 M_S\right]} \qquad (\text{I. } 6)$$

Here, N_x, N_y, N_z are the demagnetizing factors along the principal axes.

For spherical particles, where demagnetizing factors are isotropic, this expression is reduced simply to:

$$\frac{\omega}{\gamma} = H_a \qquad (\mathrm{I}.7)$$

This highlights the role of anisotropy, geometry, and composition in determining the resonance frequency.

Non-Uniform Resonance Modes: Walker and Aharoni Models

While Kittel's model assumes uniform precession across the sample, experiments have shown that non-uniform resonance modes may also occur leading to several magnetic resonance modes for the same material.

Walker's Model [13,14]**.** In 1957, Walker explained the multiresonance peaks observed in ferrite disks by White [15] and Dillon [16,17] where the RF magnetic exciting filed was inhomogeneous (large gradients). These resonances called magnetostatic modes concern relatively large particles where magnetostatic energies dominate over exchange interactions leading to non-uniform precession (spin waves). Note that the resulting magnetostatic or Walker modes may be higher or lower in frequency than the uniform mode, which may be considered to be a magnetostatic mode, and their frequencies are independent of the size of the particle. On figure I.4 some Walker modes of an YIG sphere are represented [18].

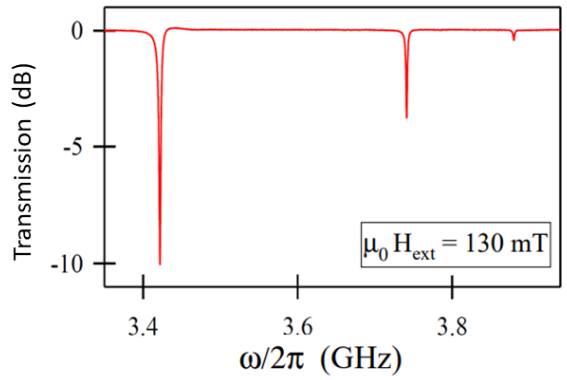

Figure I.4. Transmission spectrum of 1 mm YIG sphere measured at $\mu_0 H$ = 130 mT. Three resonant dips represent Walker modes [18].

Aharoni's Model [19,20]. For smaller particles (< 0.1 µm), exchange energy becomes dominant compared to magnetostatic contributions leading to exchange resonance modes. By considering the dynamic variation of magnetization under $\overrightarrow{H_{eff}}$, neglecting damping, for a spherical particle of radius R and by neglecting surface anisotropy, the resonance frequency ω_{kn} is given by:

$$\frac{\omega_{kn}}{\gamma} = \frac{C}{R^2 M_s}\mu_{kn}^2 + H_0 - \frac{4\pi}{3}M_s + H_a \qquad (\text{I}.8)$$

where C is the exchange constant, M_s the saturation magnetization, and μ_{kn}^2 are eigenvalues obtained from spherical Bessel functions:

$$\left(\frac{dj_n\left(\mu_{kn}\frac{r}{R}\right)}{dr}\right)_{r=R} = 0 \qquad (\text{I}.9)$$

This formulation predicts a linear dependence of the different resonance frequencies μ_{kn}^2, with the slope determined by exchange interactions and particle size as illustrated by figure I.5.

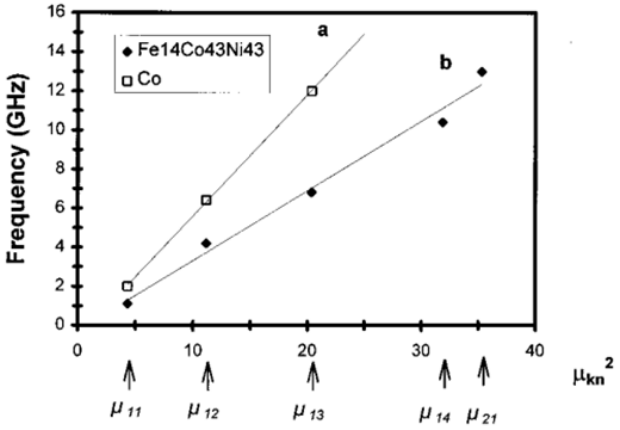

Figure I.5. The resonance frequencies are plotted as a function of the squared eigenvalues (μ_{kn}^2) obtained from the effective permeability of materials containing: ~20% $Fe_{14}Co_{43}Ni_{43}$ particles (60 nm) and ~35% Co particles (45 nm) [21].

It should be noted that when surface anisotropy is considered, the size dependance is less clear, because the eigenvalue condition is size dependent.

To summarize, the Kittel, Walker, and Aharoni models provide complementary frameworks for understanding FMR. While Kittel describes in-phase uniform precession of moments and

predicts a single resonance frequency, Walker and Aharoni account for non-uniform dynamics and multiresonance phenomena. Walker's theory applies to large particles dominated by magnetostatic effects, whereas Aharoni's approach addresses small systems where exchange interactions and particle size are critical. All models rely on simplifying assumptions such as spherical or ellipsoidal geometries, perfect homogeneity, and negligible interparticle interactions. Consequently, they are quite imprecise in real condition, however they serve as valuable guidelines for interpreting resonance behavior in real nanomagnetic systems.

Domain wall resonance [22–25]. Multiresonance phenomena can also arise from domain wall resonance. In this mechanism, domain walls behave as damped, forced harmonic oscillators, exhibiting a characteristic resonance frequency governed by the spin–lattice relaxation rate. This resonance typically occurs at much lower frequencies than those associated with spin rotational relaxation, generally in the tens of megahertz (MHz) range, compared to the gigahertz (GHz) frequencies characteristic of spin dynamics. Experimental evidence of this transition was first suggested in the early work of Rado et al. [25] as illustrated in Figure I.6, where the contrasting behaviors of multi-domain and single-domain regimes are highlighted. It is important to note that the magnetic permeability attainable in the domain-wall resonance regime is typically several orders of magnitude higher than that observed in the spin-resonance region, reflecting the significant contribution of domain wall motion to the overall magnetic response.

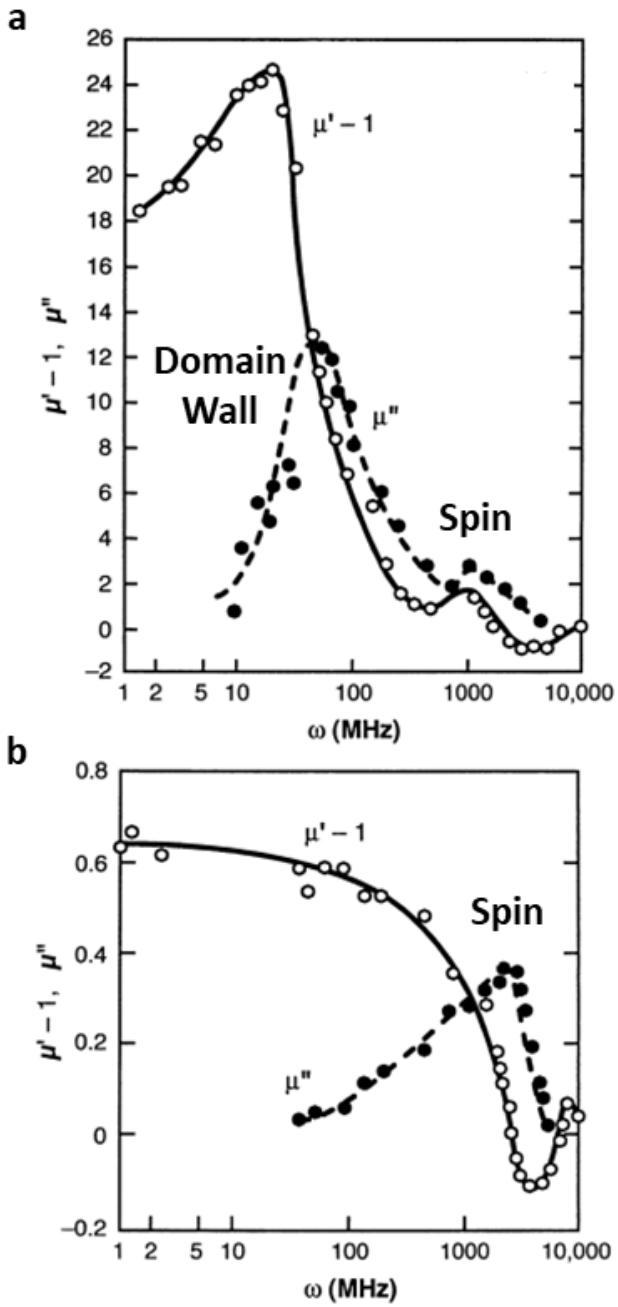

Figure I.6. Comparison of the permeability spectra for (a) a multi-domain magnesium ferrite ceramic and (b) a composite containing 70 wt.% of single-domain magnesium ferrite particles dispersed in wax [24,25].

1.3 Choice of magnetic materials for inductors

1.3.a Permeability, Ferromagnetic Resonance, and Snoek's Law

Dynamic magnetic permeability.

Under the influence of an alternating magnetic field, the magnetic flux density within the material undergoes precession. The magnetic induction can thus be expressed as

$$B = B_0 e^{i(\omega t - \delta)} \qquad (\mathrm{I}.10)$$

Where δ represents the phase lag between the magnetic induction B and the external applied magnetic field H.

The complex magnetic permeability is then defined as:

$$\mu(\omega) = \mu'(\omega) - j\mu''(\omega) \qquad (\mathrm{I}.11)$$

where $\mu'(\omega)$ and $\mu''(\omega)$ correspond respectively to the real part (the in-phase component of the magnetic response, or relative permeability) and the imaginary part (the out-of-phase component, associated with dynamic magnetic losses).

Magnetic permeability is a key parameter governing the inductive properties of a material, as it describes its ability to channel magnetic flux. For a ferromagnetic material placed under an external magnetic field H, the magnetic flux density B inside the material is given by:

$$\vec{B} = \mu_0(\vec{H} + \vec{M}) \qquad (\mathrm{I}.12)$$

Relative permeability is defined as:

$$\mu_r = \frac{\mu}{\mu_0} \qquad (\mathrm{I}.13)$$

and is linked to magnetic susceptibility χ, which characterizes how magnetization varies with the applied field according to a linear response:

$$\mu_r = 1 + \chi \quad (\mathrm{I}.14)$$

$$\chi = \frac{dM}{dH} \qquad (\mathrm{I}.15)$$

Thus, the flux density can also be written as:

$$B = \mu_0 \mu_r H = \mu H \qquad (\mathrm{I}.16)$$

A rough approximate expression for the static relative permeability of a ferromagnetic material is:

$$\mu_r = \frac{M_s}{H_a} + 1 \qquad (\mathrm{I}.17)$$

where M_s is the saturation magnetization and H_a is the anisotropy field, predominantly determined by magnetocrystalline anisotropy. To maximize permeability and thus improve inductance, the material should combine a high M_s with a small magnetocrystalline anisotropy constant K_1, i.e., it should be a soft magnetic material.

Magnetic permeability in frequency - Ferromagnetic resonance (FMR).

The resonance frequency f_{FMR} defined previously manifests as a maximum in the imaginary part of permeability $\mu''$and a sharp decrease in the real part μ'.

This frequency effectively acts as a cut-off: above it, real permeability rapidly diminishes. For RF and GHz-range inductor applications, it is therefore desirable to maximize f_{FMR}. This typical behavior can be seen in figure I.7.

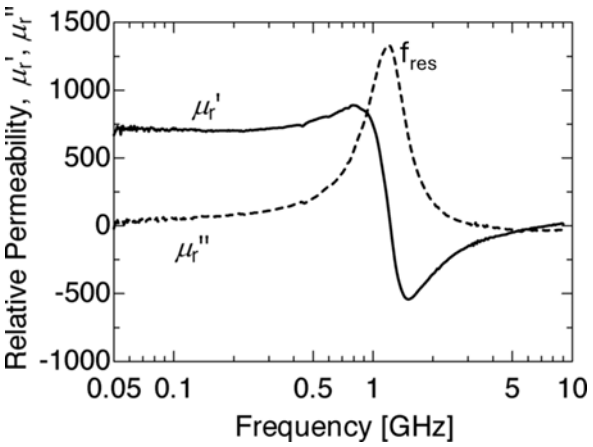

Figure I.7. Illustration of a typical frequency dependence of relative permeability for a magnetic material. This example is given by a CoZrNb film [26].

However, permeability and resonance frequency are intrinsically linked. According to the relation Eq. (I.18) defining static permeability, it appears that it varies oppositely with anisotropy compared with and the FMR frequency given by the equation (6): the greater the FMR frequency, the lower the static permeability. A trade-off is formalized by the Snoek's law [27]:

$$(\mu_r - 1) f_{RFM} = \frac{\gamma \mu_0 M_s}{2\pi} \qquad (\text{I. } 18)$$

Thus, extending the frequency response of soft magnetic material leads to a decline in permeability and a loss of performance. Since permeability and resonance frequency increase with M_s, materials with high saturation magnetization are highly preferable.

1.3.b Minimizing Magnetic Losses

Magnetic losses in RF fields originate from several mechanisms.

Eddy current losses. According to Faraday's law, a time-varying magnetic field induces electric currents inside conductive materials. These eddy currents circulate over a characteristic depth known as the skin depth e [28,29]:

$$e = \sqrt{\frac{2\rho}{\omega \mu_0 \mu_R}} \qquad (\text{I. } 19)$$

where ρ is the electrical resistivity of the material (Ω.m) and ω the angular frequency of the applied field. The induced currents generate a magnetic field opposed to the alternating magnetic field applied. Minimizing these losses requires reducing the particle dimensions below the skin depth or using materials with high resistivity, ideally insulating. Typically for iron at 1 GHz, the skin depth is about 200 nm.

Domain wall resonance. In multidomain systems, alternating fields can induce oscillations of the domain walls, which contribute to energy dissipation. Monodomain particles are therefore preferable for RF applications [30]. Typically Fe, FeCo, and Co particle respectively smaller than 25, 20, and 24 nm [1,31].

Hysteresis losses. Non-reversible magnetization processes also induce losses. However, at high frequencies, hysteresis contributions are relatively minor compared to eddy current and domain wall losses [1].

As a partial conclusion, magnetic material should consist of single-domain particles smaller than the skin depth to suppress the losses described hereabove. Magnetic oxides are naturally insulating and thus mitigate the eddy currents, but they often suffer from a low saturation magnetization and a limited permeability. Metallic nanoparticles can provide a higher M_s and higher permeability, but their high conductivity leads to eddy current loss. This challenge can be addressed by coating metallic nanoparticles with insulating shells [32,33]. Chemically synthesized nanoparticles are often capped with organic ligands, which can provide electrical insulation under mild operating conditions.

Effective medium considerations. When nanoparticles are dispersed in a matrix, the overall permeability of the composite (μ_{eff}) can be described by effective medium theories such as the Bruggeman model [34,35]:

$$C_{NPS}\frac{\mu_r - \mu_{eff}}{\mu_r + 2\mu_{eff}} + C_{matrix}\frac{\mu_{matrix} - \mu_{eff}}{\mu_{matrix} + 2\mu_{eff}} = 0 \qquad (\text{I. } 20)$$

where C_{NPS} and C_{matrix} are the volume fractions of the nanoparticles and the matrix, respectively. The resulting effective permeability is always lower than the one of the nanoparticles (μ_r), making the nanoparticle volume fraction a critical parameter. However, reaching a dense assembly may induce other losses. This effective medium is represented by Figure I.8.

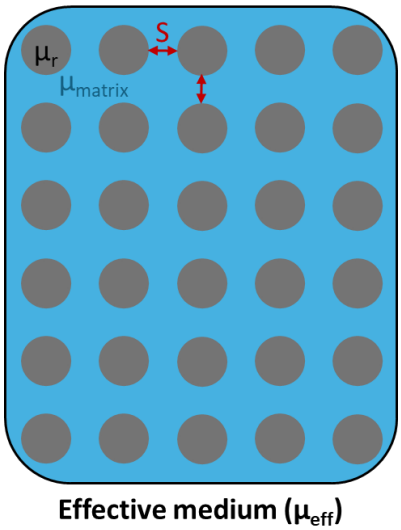

Figure I.8. Representation of an effective medium with an effective magnetic permeability (μ_{eff}). This composite medium consists of a matrix with intrinsic permeability μ_{matrix}, in which magnetic nanoparticles (μ_r) are dispersed and separated by an average interparticle distance S.

Exchange interactions in dense assemblies.

At high volume fractions, nanoparticles may interact via exchange coupling [36], provided that the particle diameter (D) and the interparticle distance separation (S) are smaller than the length of interaction length L_{int}:

$$L_{int} = \sqrt{\frac{A}{K_1}} \qquad (\mathrm{I}.21)$$

with A the exchange constant. As example, for FeCo, L_{int} is about 33 nm [31].

In this case, the effective anisotropy constant K_a is reduced as:

$$K_a \approx \frac{K_1}{\sqrt{n}} \qquad (\mathrm{I}.22)$$

where *n* is the number of particles within a volume of L_{int}^3. This reduction enhances permeability but shifts the resonance frequency downward, reflecting the unavoidable permeability–frequency compromise.

Conclusion on the dynamic properties of magnetic materials

Finally, to achieve optimized dynamic properties for RF inductors, nanoparticles should ideally combine:

- high saturation magnetization (M_s) for strong permeability, note that Fe, FeCo, Co, and Ni have respectively a M_s of 212, 230, 160 and 55 A.m².kg^{-1} [1],
- low anisotropy constants (K_1) to retain soft magnetic behavior,
- monodomain configurations to minimize magnetic losses.

Among candidate materials, FeCo alloys stand out. They exhibit the highest known saturation magnetization, together with a relatively low anisotropy constant, which enables both high permeability and reasonably high ferromagnetic resonance frequency. It is difficult to provide general quantitative values of permeability and ferromagnetic resonance (FMR) for a given magnetic material, and even more so for composite systems. As discussed earlier, these properties depend on a wide range of factors, including the shape and size of the nanoparticles, the metallic fraction and nature of the matrix, the ligand thickness, and the geometry of the nanoparticle assembly, among others. Nevertheless, the literature consistently reports that FeCo based assemblies exhibit promising properties in the RF range. For example, a thin assembly of ultrafine FeCo nanoparticles (2.69 ± 0.45 nm) isolated by ultrathin Al_2O_3 dielectric shells (0.63 ± 0.12 nm) demonstrates an excellent high-frequency response, with a permeability of approximately 100 up to a resonance frequency of 1.7 GHz (Figure I.9) [37].

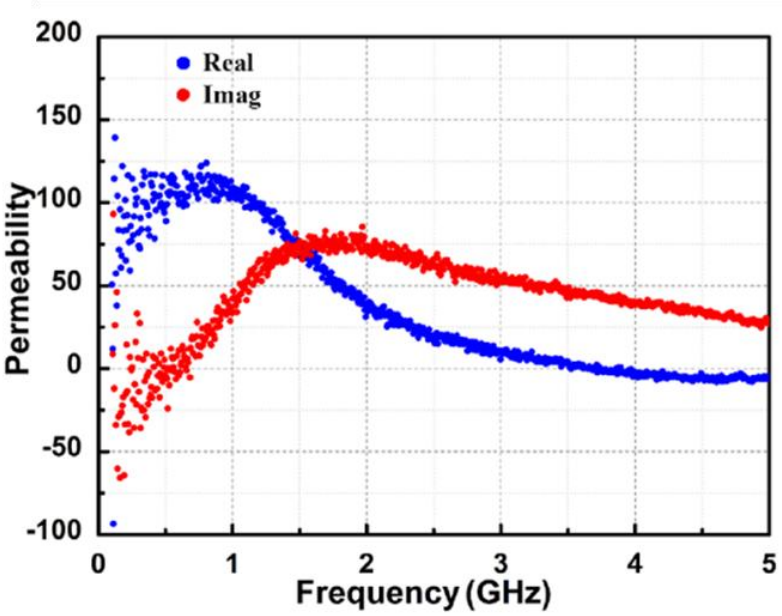

Figure I.9. Permeability spectra of FeCo nanoparticle film [37].

1.4 Magnetic effect on inductors

1.4.a Inductors

1.4.a.i General characteristics

An inductor is a passive electronic component which is commonly realized as a conductive wire wound into a coil. Its role is to store magnetic energy when a current flows through the wire. In the simplest configuration illustrated in Figure I.10, which consists of an air-core coil without magnetic material, the self-inductance can be approximated by:

$$L_0 = \frac{(\mu_0 N^2 A)}{l} \qquad (\mathrm{I}.23)$$

where N the number of turns, A the cross-sectional area of the coil and l its length.

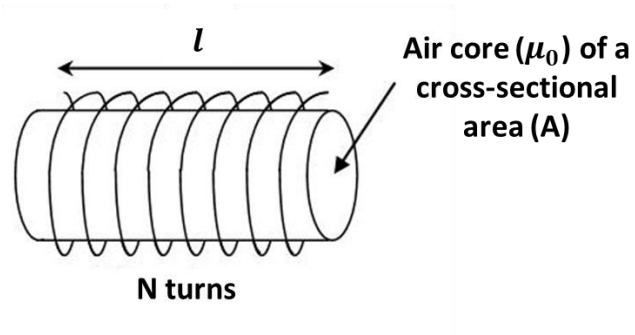

Figure I.10. Representation of a simple inductor, a conductive wire wound into a coil around a non-magnetic core.

The second key parameter of an inductor is the quality factor (Q) that quantifies its efficiency in storing magnetic energy relative to the energy lost per cycle. It is defined as the ratio between the inductive reactance and the equivalent series resistance at a given frequency:

$$Q = \frac{L\omega}{R} \qquad (\mathrm{I}.24)$$

Where ω is the angular frequency, L the inductance, and R the resistance. A high Q factor indicates low energy dissipation and therefore better performance, which is essential in radiofrequency (RF) applications where signal integrity and minimal losses are required. The quality factor is thus a critical metric for evaluating and optimizing inductor design.

Note that at radiofrequency the resistance in the wire is not only due to static resistance (R_{DC}) but also to dynamic resistance (R_{AC}). While R_{DC} is easily determined with the dimensions of the wire by the following equations:

$$R_{DC}\ (\Omega) = \frac{\rho l_w}{S} \qquad (\mathrm{I}.25)$$

Where ρ is the resistivity, l_w is the length of the wire, and S is the cross-sectional area of the wire.

R_{AC} is influenced by more complex phenomena. The skin effect introduced before happens also in the wire of the coil. As for the magnetic material, the eddy currents flow in the opposite direction to the main current near the center of the conductor and in the same direction near its surface. As a result, the amplitude of the total current decreases at the center and becomes concentrated near the periphery. As a consequence, the skin depth (e) represents the effective

thickness (and thus the corrected cross-sectional area) within which most of the current is confined. This causes dynamic resistance increases with frequency $R_{AC} = \alpha \times R_{DC}$, with α a frequency-dependent coefficient characteristic of the conductor.

R_{AC} is also influenced by the proximity effect which arises from the interaction between adjacent conductors carrying alternating currents. In multi-turn inductors, such as spiral inductors, this effect cannot be neglected. Because the magnetic field is strongest near the center of the inductor, its temporal variation induces parasitic electric fields within the nearby turns. These fields give rise to eddy currents, within the inner portions of the central turns, the eddy currents add to the main current, whereas they oppose it on the outer portions. As a result, the current density becomes concentrated toward the inner side of the turns, leading to a significant increase in the effective (dynamic) resistance of the inductor. This effect is increased more the turns are close to the center of the inductor and when the spacing between adjacent turns decreases, and the number of turns increases.

In microelectronics, planar spiral inductors are frequently employed due to fabrication constraints. For such geometries, the inductance is more accurately estimated using Wheeler's modified expression [38]:

$$L_0 = C_1 \mu_0 \frac{N^2 d_{avg}}{1 + C_2 \rho} \qquad \text{(I. 26)}$$

with N the number of turns, $d_{avg} = \frac{d_{in} + d_{out}}{2}$ the average diameter, $\rho = \frac{d_{out} - d_{in}}{d_{in} + d_{out}}$ the fill ratio, and C_1, C_2 are shape-dependent constants. These parameters are represented on Figure I.11.

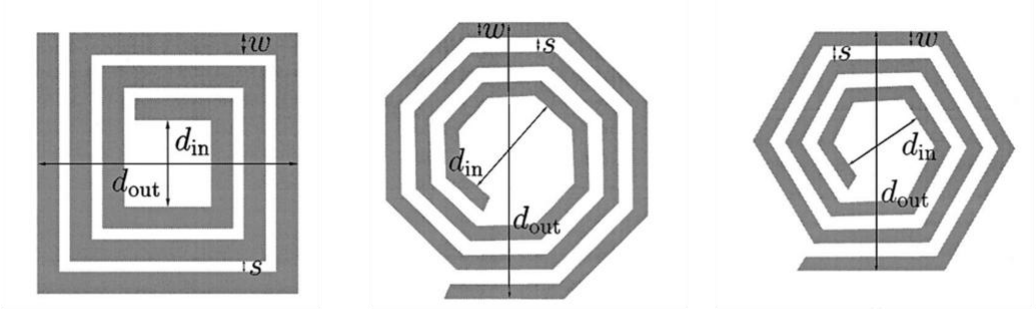

Figure I.11. Different types of planar inductor architectures, where d_{in} and d_{out} represent the inner and outer diameters, w is the width of the spiral trace, and s is the spacing between adjacent turns. C_1 and C_2 are coefficients that depend on the spiral geometry [38].

For a given conductor length, the inductance value scales quadratically with the number of turns N, contradicting the requirements for high quality-factor inductor (proximity effect). One alternative is to increase the average diameter and d_{in} to increase both inductance and quality factor. However, the consequence is to increase the size of the inductor. In microelectronics miniaturization is a key challenge because space is costly. This limitation can be alleviated by using high-permeability magnetic materials close to the inductor, thereby enhancing the inductance value without increasing the size of the inductor or increasing losses.

1.4.a.ii Inductor with a magnetic core

For a general coil which is inside an equivalent homogeneous medium whose magnetic permeability differs from that of air, the inductance is increased from L_0 to:

$$L_{mag} = L_0 \times \mu_{eff} \qquad (\mathrm{I}.27)$$

where μ_{eff} is the effective permeability of the equivalent homogeneous medium surrounding the inductor. This value depends on both the relative permeability of the magnetic material (μ_r) and the coverage ratio of the inductor by the magnetic layer:

$$L_{mag} = L_0 \times f(\mu_r, coverage) \qquad (\mathrm{I}.28)$$

For instance, in the idealized case of a planar inductor fully covered on one side by a magnetic material of relative permeability μ_r and infinite thickness while the opposite side is non-magnetic, the inductance increase is given by [39]:

$$L_{mag} = L_0 \times \frac{2\mu_r}{\mu_r + 1} \qquad (\mathrm{I}.29)$$

which theoretically allows a doubling of inductance when μ_r is high. In practice, the finite thickness of the deposited magnetic film limits the achievable gain. Roshen analyzed this effect using the method of images: a film with $\mu_r = 100$ and 100 µm thickness enhances inductance by ~60%, while a 1000 µm film can yield up to ~90% [40]. Partial coverage of the inductor surface by the magnetic material further reduces the effective permeability and therefore the improvement.

To overcome these limitations, it is interesting to use different inductance and/or deposition geometries to increase the coverage ratio, thereby increasing inductance. Alternative geometries and 3D deposition schemes have been proposed. For planar inductors, sandwich configurations, where both sides of the spiral are coated with magnetic films can provide higher enhancement. Wang *et al.*, for example, demonstrated an on-chip inductor incorporating a thin film of CoFeB/ZnO/CoFeB on both sides of the inductor [41]. This device exhibited a 41–71% inductance increase over 0.1–8 GHz with minimal degradation of the quality factor up to 4 GHz. Although effective, such approaches rely on sophisticated fabrication processes, combining deep silicon etching with sputtering deposition. Yang, Koh *et al*. has achieved an inductance increase between 85 and 130% without degrading the quality factor until 4 GHz. This was accomplished by drop casting a solution of nanoparticles dispersed in a photoresist on a cavity beneath a suspended inductor, resulting in a planar inductor covered on both sides with a micromagnet composed of ≈100nm nickel-iron permalloy nanoparticles ($Ni_{80}Fe_{17}Mo_3$) [42]. The process and the inductor before and after magnetic material deposition are shown on Figure I.12.

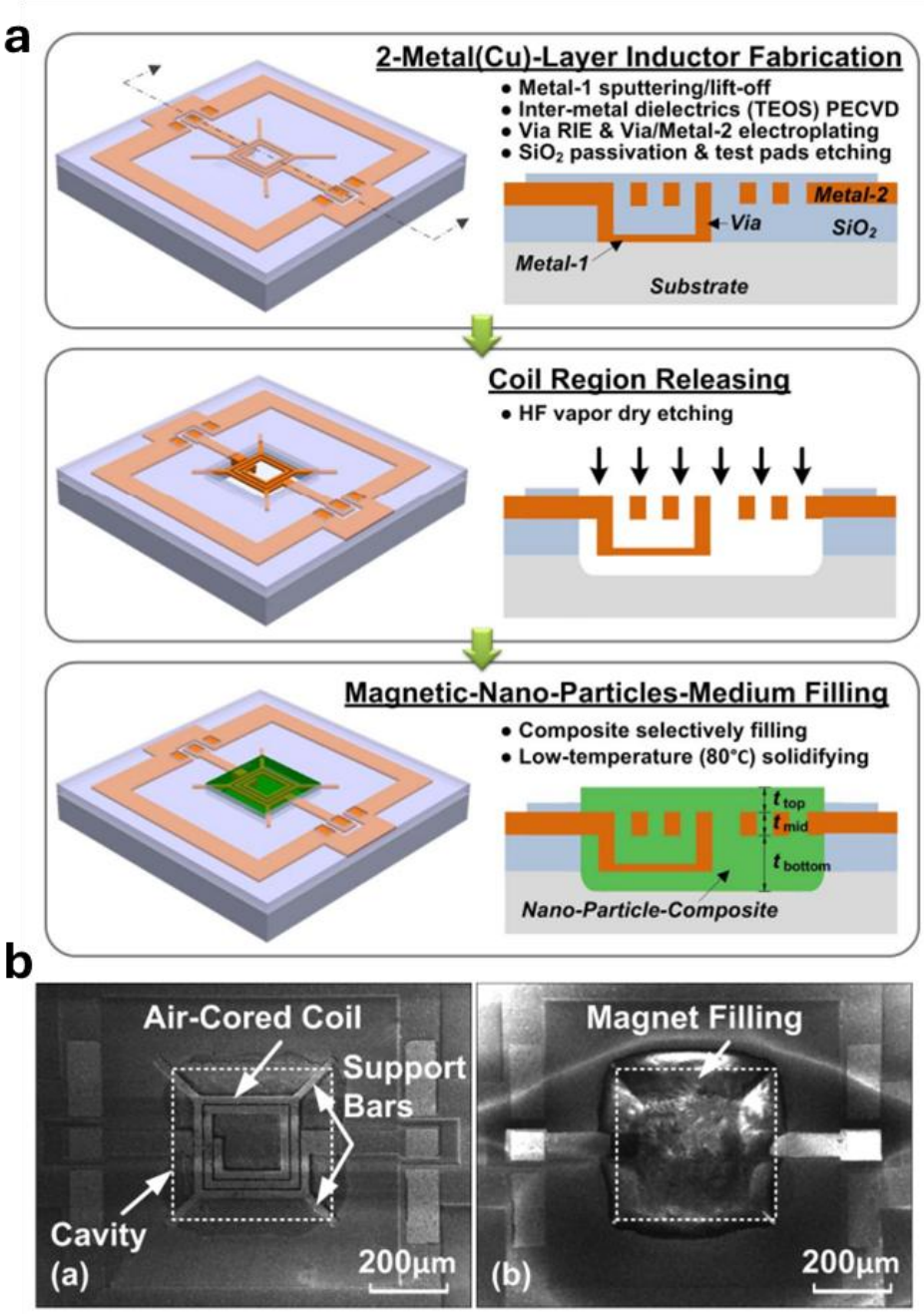

Figure I.12. (a) Description of the multi-step process for the fabrication of the inductance and the deposition of the magnetic composite. (b) SEM photos of (a) air-medium inductor coil and (b) magnetic nanoparticles medium filled inductor coil [42].

Another approach involves exploring alternative inductor geometries, such as stacked inductors, also described as multi-turn vertical inductors. For instance, Zhan *et al.* demonstrated that, using the same magnetic material (Co_2Z) on different planar inductor configurations, increasing the number of turns enhances the inductance gain from

approximately 16% to 40% at 1 GHz as the number of turns N increases from 2 to 4. Beyond this point, the gain tends to saturate with additional turns. In contrast, a six-layer stacked spiral inductor can achieve a slightly higher inductance gain, around 50% at 1 GHz, while reducing the device area by about 80% compared to a single-layer spiral inductor, with comparable performance [43–45]. The fabrication of this stacked inductor is described in Figure I.13.

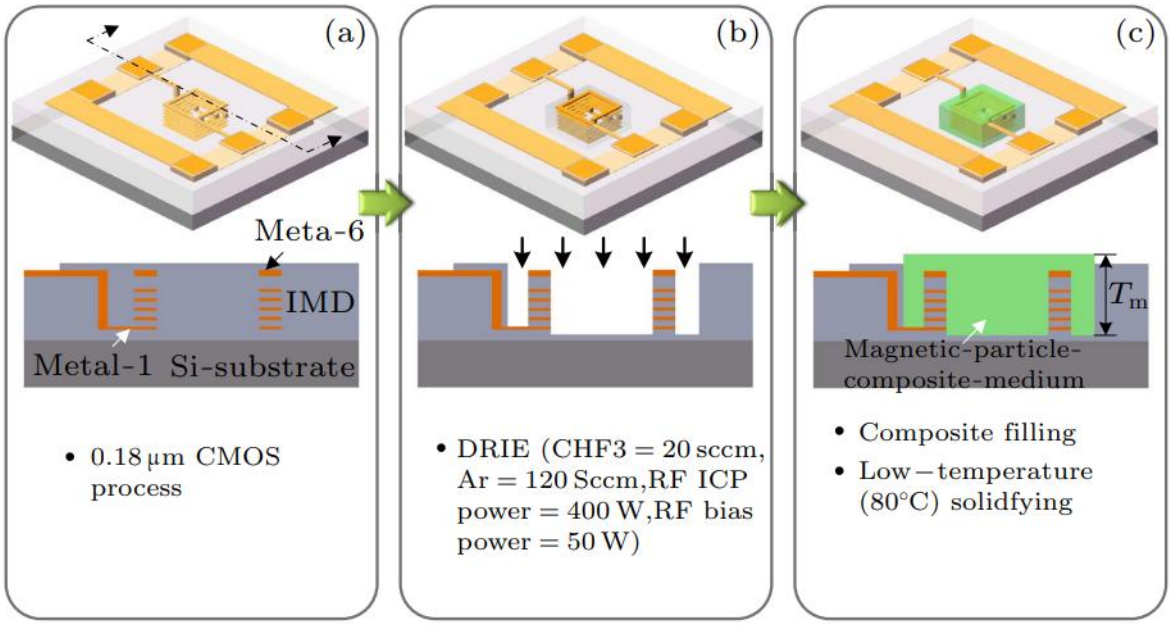

Figure I.13. Process flow of stacked inductor fabrication with integration of magnetic material [45].

In summary, integrating magnetic materials with planar or stacked spiral inductors enables two complementary advantages. For a given inductance, the use of magnetic materials allows the same inductance value to be achieved with a shorter conductor length, leading to both a reduction in device size and a decrease in resistive losses. Conversely, for a fixed inductor size, higher inductance values can be obtained. Since inductors are key components in microelectronic circuits operating at RF frequencies, the integration of high-permeability magnetic materials into inductors remains a major challenge.

1.4.b Other examples of integration of nanoparticle-based magnets on inductors

To supplement the few examples of magnetic core inductors for RF applications, here are some other important examples, though this list is not exhaustive.

Koh *et al.* reported that embedding $FeNi_3$ nanoparticles (50–150 nm) coated with 15–20 nm SiO_2 shells into a 90 µm thick composite layer led to inductance increases between 20% and 50%. The silica shell, while diluting the effective permeability, also ensured high ferromagnetic resonance frequencies, and higher quality factors as losses are reduced [46].

In our group, Desvaux, Venturin *et al*., have realized planar inductors which have been immersed in colloidal solutions of amorphous FeCo nanoparticles with carbon inclusions. A 20 µm thick deposited layer exhibited a permeability of 4 while an FMR at 1.5 GHz is obtained on inductors. This resulted in an inductance enhancement of 80% sustained up to 3 GHz [47,48].

Overall, the FeCo based micromagnets emerge as promising candidates for inductor core applications due to their high saturation magnetization and soft magnetic behavior. Inductance increase close to the theoretical maximum have already been reported for a suspended spiral inductor, but integration challenges remain [42]. Indeed, the integration of magnetic material onto inductors is mostly handmade, based on a pick and place method, or through a drop-casting method in a cavity without precise thickness control, thus lacking reproducibility. Moreover, no systematic study on the effect of the metallic nanoparticles used, in terms of mean NP diameter, size distribution and chemical composition was reported so far to the best of our knowledge. Also, the most effective configurations require the complete encapsulation of the inductor by the magnetic medium, which cannot be achieved in planar geometries.

2. Synthesis of magnetic nanoparticles in liquid phase

Since the bottom-up approach is at the heart of our approach, this review will be focused on liquid-phase chemical syntheses, which remain the most versatile and widely adopted approaches for preparing magnetic nanoparticles (MNPs) at large scale. The magnetic properties of MNPs are strongly dictated by their size, shape, and chemical composition. Achieving reproducible and tunable control over these parameters requires carefully designed synthetic routes with high reliability.

2.1 Synthesis of magnetic metal oxide nanoparticles

2.1.a Coprecipitation method

One of the earliest and most widely used methods to obtain iron oxide nanoparticles is the co-precipitation approach, first formalized by Massart and Cabuil in 1981 [49]. Known as the "Massart process," this route involves the simultaneous coprecipitation of Fe(II) and Fe(III) salts under alkaline conditions, following the reaction:

$$Fe^{2+} + 2Fe^{3+} + 8OH^- \rightarrow Fe_3O_4 + 4H_2O$$

The reaction conditions, such as the base type (e.g., NaOH, NH_4OH), the Fe^{3+}/Fe^{2+} ratio, the ionic strength and the pH, strongly influence the nucleation and growth processes, thereby determining the nanoparticle size and homogeneity [50]. Jolivet *et al.*, extensively analyzed these parameters in the 1990s, demonstrating that Fe^{3+}/Fe^{2+} ratios below 0.3 favor the formation of goethite (FeO(OH)), while values close to 0.5 yield stoichiometric magnetite (Fe_3O_4) with uniform particle size and composition [51]. Later studies revealed that higher Fe^{2+}/Fe^{3+} ratios also lead to larger crystallites generally, whereas higher pH and ionic strength inhibit the growth during the aging step, thus producing smaller nanoparticles with narrower distributions [52,53]. Babes *et al.* further underlined that only intermediate ratios (0.4–0.6) yield monodisperse particles suitable for diverse application such as biomedical uses as MRI

contrast agents [54–56]. Figure I.14 is a microscopy image of typical nanoparticles obtained from that method.

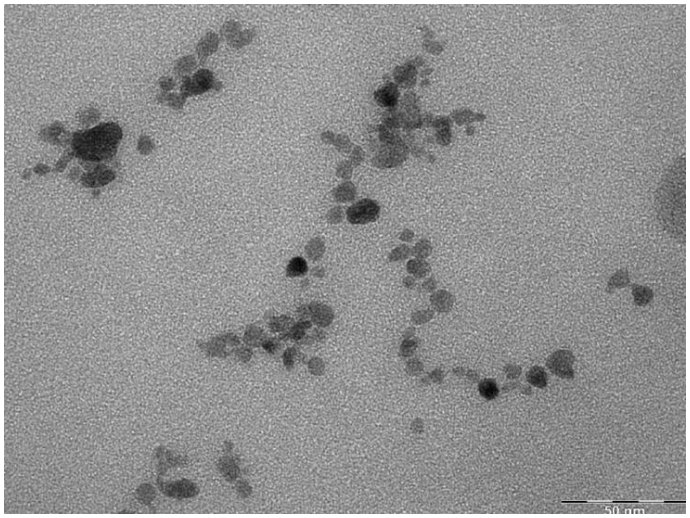

Figure I.14. TEM images of iron oxide nanoparticles synthesized by Massart process [56].

Other ferrites. The co-precipitation route is not restricted to magnetite but can be readily adapted to the synthesis of doped ferrites such as manganese, cobalt, or zinc ferrites, according to the general reaction [57]:

$$M^{2+} + 2Fe^{3+} + 8OH^{-} \rightarrow MFe_2O_4 + 4H_2O$$

Figure I.15 represents different ferrites synthesized using isopropanolamine (MIPA) as a coprecipitating agent instead of classical NaOH base. MIPA is acting both as alkaline agents and as complexing agents that allow give an easier control of the particle size during the synthesis process [57]. The nanoparticles obtained are highly dependent on the precursor type, the addition rate of the base, and the reaction medium (mixture of solvent, polymer, coprecipitation agents etc..), all of which control the balance between nucleation and growth. Variations in pH, ionic strength, and temperature allow fine-tuning of both particle size and crystallinity. Moreover, oxidative hydrolysis represents a useful variant, where Fe(II) salts are precipitated in alkaline media in the presence of a mild oxidant such as KNO_3. Adjusting oxidation kinetics through salt concentration or solvent composition makes it possible to access a wider range of morphologies. This method is also compatible with in situ polymer coatings, which stabilize the nanoparticles and improve their dispersibility [58–61].

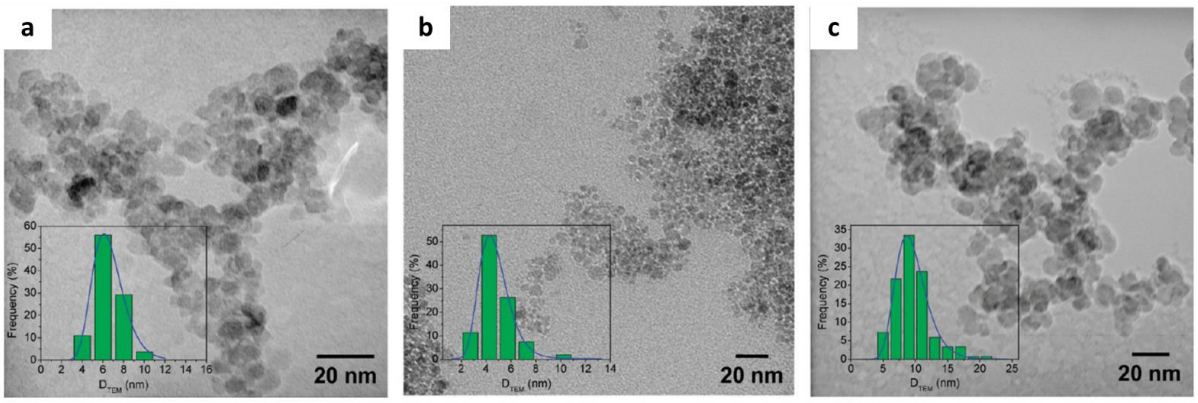

Figure I.15. TEM micrographs and corresponding particle size distribution histograms of MFe_2O_4 nanomaterials, where M = Fe, Co, or Mn, synthesized using isopropanolamine (MIPA) as an alkanolamine complexing and coprecipitating agent. The solid lines represent log-normal fits to the experimental particle size distributions [57].

2.1.b Solvothermal method

Beyond aqueous chemistry, solvothermal approaches offer greater control over crystallinity, dispersity, and morphology. A notable example was proposed by Pinna and co-workers, who employed benzyl alcohol simultaneously as solvent and coordinating agent for the thermal decomposition of $Fe(acac)_3$. This simple one-pot method yields monocrystalline magnetite nanoparticles of around 10 nm with limited surfactant content, facilitating the subsequent surface functionalization and dispersion in either polar or apolar solvents [62]. TEM, HRTEM, and electron diffraction illustrate the high crystallinity and homogeneity of the nanoparticles obtained from that process (Figure I.16).

Later, this synthesis was further refined through microwave-assisted heating, as demonstrated by Richard *et al*. The introduction of microwave irradiation drastically reduced the reaction time from several tens of hours to less than one, while enabling the reproducible preparation of ultra-small iron oxide nanoparticles (3–9 nm) in large batches [63]. The method is versatile and offers an efficient pathway to highly crystalline nanostructures with tunable surface chemistry.

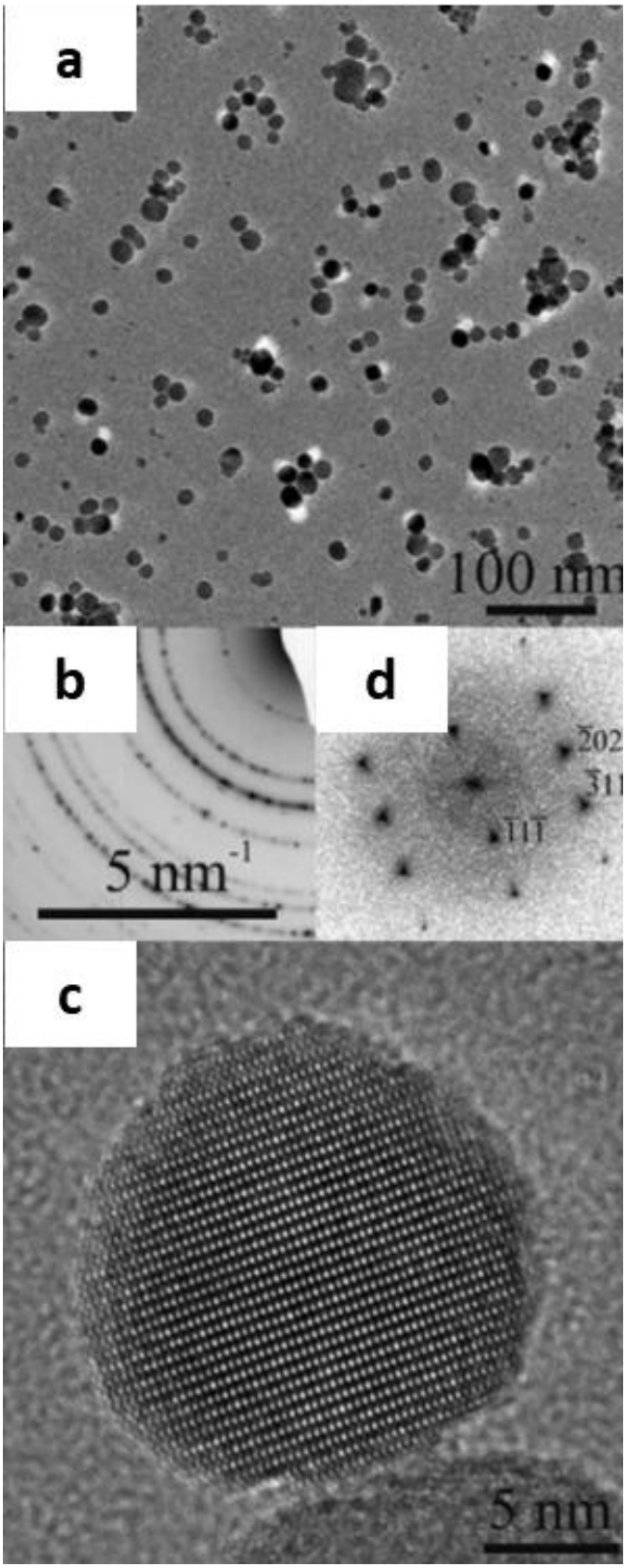

Figure I.16. (a) TEM overview of the particles synthesized with a solvothermal method at 200 °C with "Pinna process". (b) Electron diffraction patterns from a large region. (c) High-resolution TEM (HRTEM) image of an individual single-crystal particle, (d) and the corresponding fast Fourier transform (FFT) power spectrum [62].

2.2 Synthesis of magnetic metallic nanoparticles

The preparation of metallic magnetic nanoparticles represents an even greater challenge compared to their oxide counterparts. Metallic systems such as Fe, Co, and Ni exhibit outstanding magnetic properties; however, their high reactivity toward oxidation often leads to a rapid degradation of the surface and therefore a performance loss. To address this issue, dedicated synthetic strategies have been developed to ensure controlled growth, stabilization, and protection of the nanoparticles. Among the different routes, the thermal decomposition, the organometallic synthesis, and the polyol process are the most commonly used [64,65]. Being further used in our study, a brief overview of these approaches is given hereafter.

2.2.a Thermal decomposition

Thermal decomposition is one of the most established methods to produce zero-valent iron nanoparticles. This process involves heating thermally labile precursors at elevated temperatures typically ranging from 180 to 320 °C. Upon decomposition, nucleation occurs, followed by their growth into crystalline nanoparticles. The simplicity and reproducibility of this route have made it a widely used approach, although careful control of the reaction atmosphere is required to limit oxidation during and after synthesis. For iron nanoparticles synthesis, iron pentacarbonyl ($Fe(CO)_5$) is the most often used precursor, despite its toxicity and unstability. Studies of Lacroix *et al.* and Zhang *et al*. have shown that using halide ion (through CTAB or HDAHCl as example) during growth of iron nanoparticles facilitate their growth, crystalline structure and chemical stability thanks to the strong interactions between halide ions and Fe [66,67]. Nanoparticles obtained with or without halide ion are represented on TEM, and HRTEM images (Figure I.17). Because of the high volatility and toxicity of $Fe(CO)_5$, Watt *et al*. have proposed diiron nonacarbonyl ($Fe_2(CO)_9$) and triiron dodecacarbonyl ($Fe_3(CO)_{12}$) fewer volatile precursors as an alternative. These iron precursors were associated with an amine surfactant (dodecylamine, DDA) in 1-octadecene (ODE) to successfully synthesize Fe NPs. Extending this reaction to FePt, and FeCo NPs was possible [68] suggesting that the replacement of $Fe(CO)_5$ can be generalized.

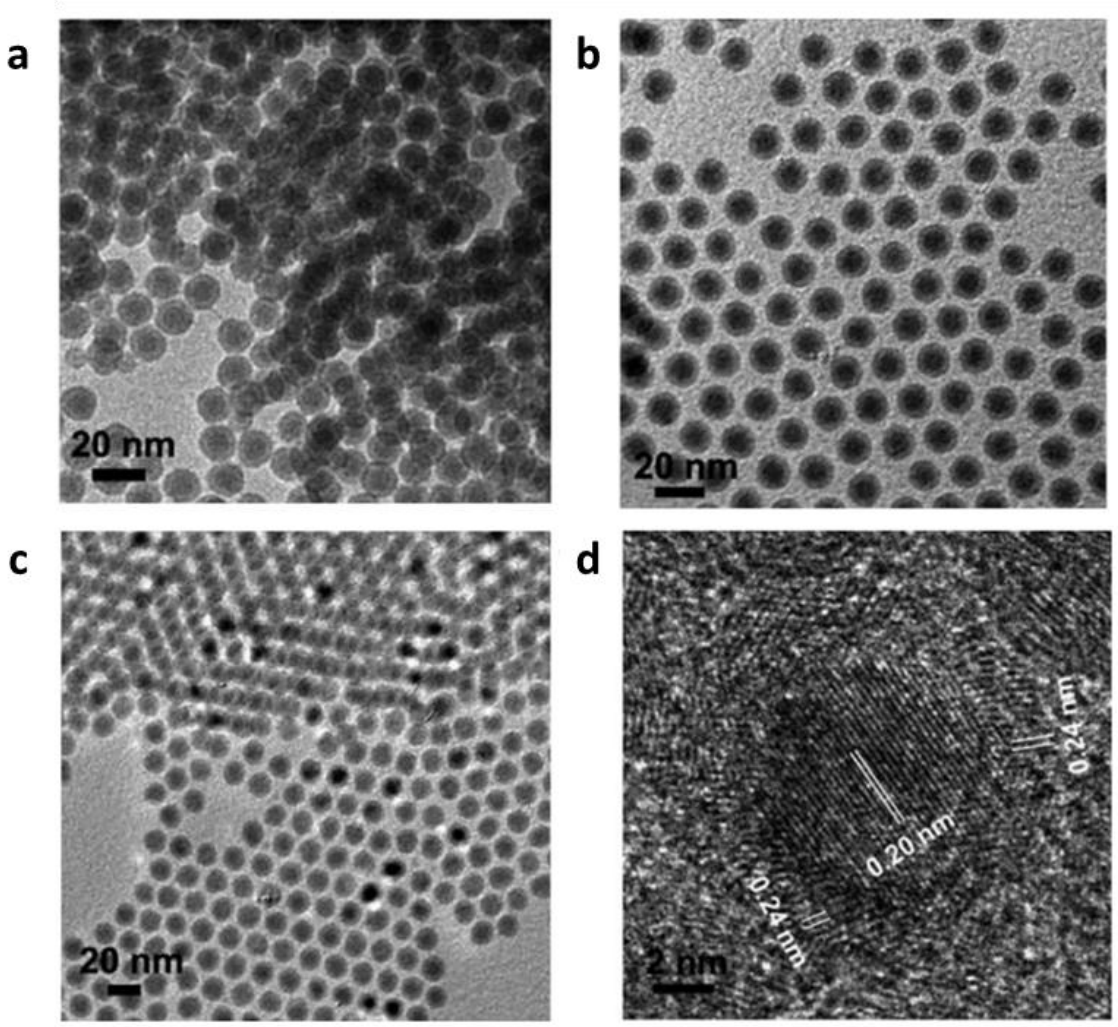

Figure I.17. TEM images of the synthesized nanoparticles by thermal decomposition: (a) 13 nm amorphous Fe NPs, (b) 12.5 nm bcc-Fe NPs obtained in the presence of HDAHCl, and (c) 12.5 nm bcc-Fe NPs obtained in the presence of NH_4Cl. (d) HRTEM image of a representative single-crystal bcc-Fe NP. The single-crystalline bcc-Fe NPs in (c,d) were synthesized using NH_4Cl [66].

2.2.b Organometallic synthesis

An alternative pathway relies on other organometallic precursors, which allow greater flexibility in tuning size, morphology, and crystallinity. Since the early 2000s, the groups at LCC and LPCNO have pioneered the synthesis of Fe(0) nanoparticles through the decomposition of tailored organometallic complexes. For instance, Dumestre *et al*. demonstrated that the hydrogen-assisted decomposition of $[\mathrm{Fe}(\mathrm{N}(\mathrm{Si}(\mathrm{CH_3})_3)_2)_2]_2$ in the presence of oleic acid and hexadecylamine produced highly monodisperse cubic nanoparticles with diameters around

7 nm [69]. Building on this, Lacroix *et al*. expanded the method by using palmitic acid (PA), enabling precise control over size (from 1.5 to 27 nm) and morphology (spheres, cubes, stars), while also elucidating the nucleation and growth pathways [67,70,71]. The effect of the PA concentration is illustrated on Figure I.18.

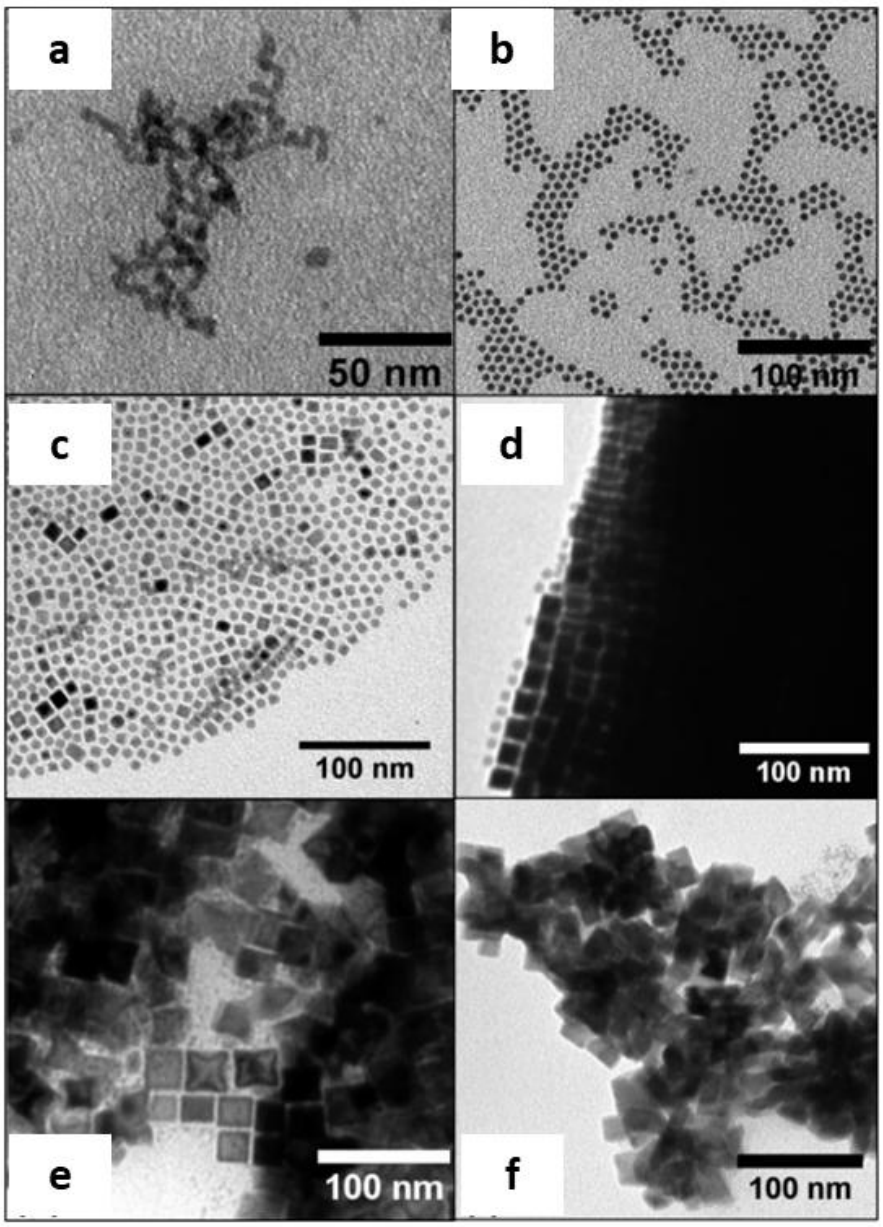

Figure I.18. TEM images of nanoparticles obtained by organometallic synthesis at 150 °C for 48 h in the presence of 2 equivalents of HDA and varying palmitic acid concentrations: (a) 0, (b) 1, (c) 1.2, (d) 1.4, (e) 1.6, and (f) 1.8 equivalents [70].

Later developments by Meffre *et al*. showed that hydrogen gas could be omitted altogether when long-chain amines (HDA with HDAHCl) were employed, as they served simultaneously as stabilizing ligands and reducing agents [72].

This method has also been adapted to produce alloy nanoparticles, such as FeCo, by combining iron and cobalt precursors, as reported by Desvaux *et al*. and Garnero *et al*. [48,73]. Nevertheless, metallic Fe and FeCo nanoparticles remain highly sensitive to oxidation, which can severely degrade their magnetic response. To circumvent this limitation, iron carbides (FeC) have been investigated as more stable alternatives. These materials incorporate carbon into the iron lattice, providing enhanced oxidation resistance while retaining strong magnetic properties ($M_s = 135\ A.m^2.kg^{-1}\ at\ 300\ K$). Meffre *et al*. reported the synthesis of uniform iron carbide nanoparticles and core–shell architectures with Fe cores surrounded by carbide shells, revealing phases such as $Fe_{2.2}C$ and Fe_5C_2. Although their saturation magnetization is lower than that of pure Fe ($M_s = 211\ A.m^2.kg^{-1}\ at\ 300\ K$), their superior chemical stability makes them promising candidates [74]. More recently, Bordet and co-workers demonstrated that preformed Fe nanoparticles could be carburized under CO/H_2 atmospheres while maintaining monodispersity. Optimization of the process, including water removal, reduced the carburization time from 140 h to 40 h, with the resulting FeC nanoparticles retaining both structural integrity and desirable magnetic performance much higher than previously reported $M_s = 170\ A.m^2.kg^{-1}\ at\ 300\ K$) [75,76].

2.2.c Polyol synthesis

The polyol method is another versatile route for producing metallic magnetic nanoparticles [77,78]. In this approach, a metal precursor reacts in a polyalcohol medium that acts as a solvent, reducing agent, and stabilizer simultaneously. The choice of polyol, together with the reaction temperature and time, enables control over particle size and morphology. While the method is particularly effective for cobalt, nickel, and their alloys, it is less suitable for pure iron nanoparticles due to the difficulty of preventing surface oxidation during the synthesis. For oxides, however, the polyol process can yield highly crystalline and monodisperse nanoparticles, making it a powerful tool for tailored nanomaterial preparation.

As an example, the shape of cobalt nanoparticles can be easily controlled from isotropic spheres to highly anisotropic rods by mainly playing on the nature of the cobalt carboxylate, the temperature ramp, and the basicity of the medium [79,80]. Jouini *et al*. demonstrated that the size and morphology of these cobalt nanorods can also be controlled by applying an external magnetic field during the growth step, anisotropic metallic particles with tunable lengths and aspect ratios being obtained as a function of the applied field [81]. This strategy also prevented the formation of enlarged tips at the nanorod ends as illustrated in Figure I.19, resulting in assemblies with significantly enhanced magnetic performance.

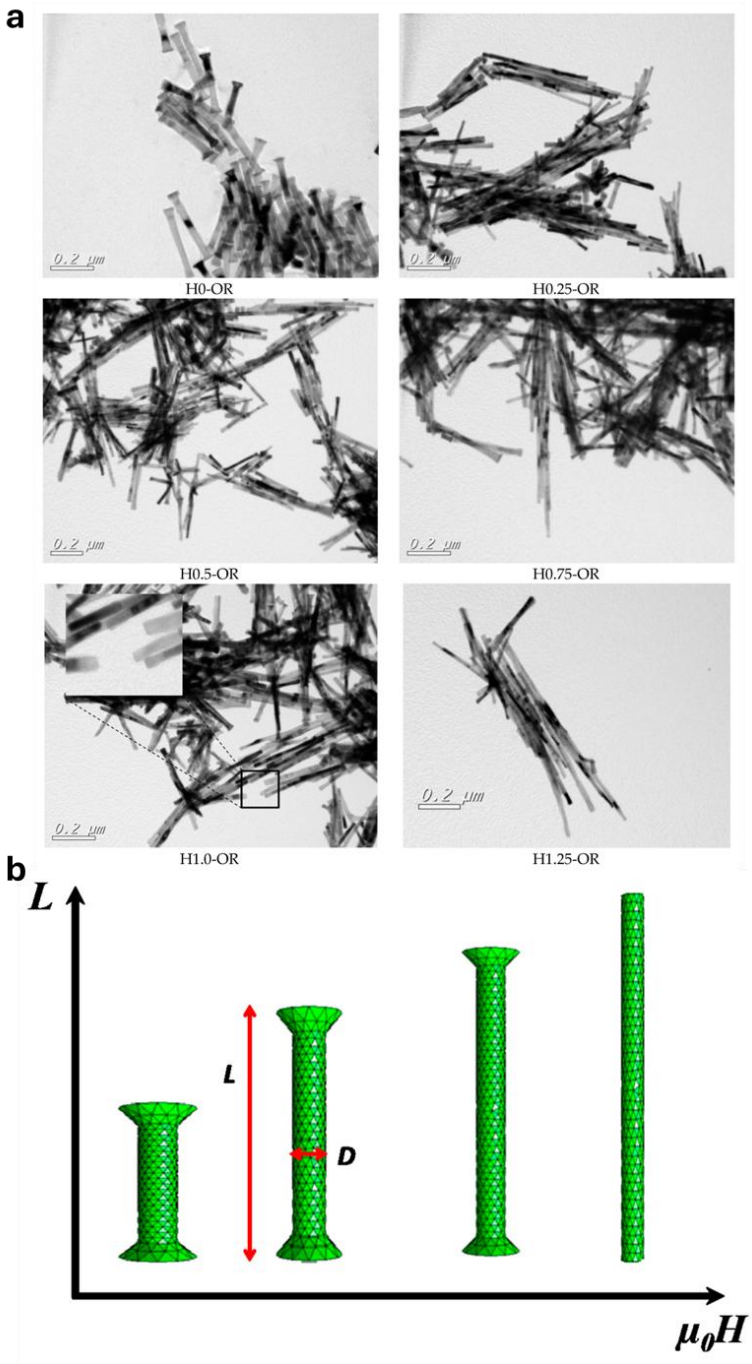

Figure I.19. (a) TEM images of cobalt nanorod samples synthesized under external magnetic fields ranging from 0 to 1.25 T in an open reactor. The insert provides a magnified view highlighting the presence or absence of conical tips. (b) Schematic illustration of the morphological evolution of Co nanowires as a function of the external applied magnetic field [81].

3. Assembly of magnetic nanoparticles under a magnetic field

For inductor core applications, it is mandatory to have micrometric assemblies of nanoobjects to match the dimensions of the inductors. Among the different strategies reported in the literature to obtain large-scale assemblies, the magnetic field directed one is chosen for its versatility. We will first present the forces called into play in this type of assembly and then report on some examples.

3.1 Magnetic dipolar interactions

To rationalize the self-organization of magnetic nanoparticles under an applied field, it is first necessary to describe the dominant interactions that govern their behavior. When particles can be approximated as uniform magnetizable spheres, they acquire an induced dipole moment m, which is proportional to the external magnetic field H_0. The dipolar model applied to a spherical particle of radius a and magnetic susceptibility χ is expressed as [82]:

$$m = \frac{4}{3}\pi a^3 \chi H_0 \quad (\mathrm{I}.30)$$

This model assumes a linear response of magnetization as a function of the applied field, *i.e.* the system remains far from saturation. If one considers each nanoparticle to be a point dipole located at its center, then the dipolar field generated at a distance r is given by:

$$\overrightarrow{B_{dip}}(r) = \frac{\mu_0}{4\pi}\left[\frac{3(\vec{m}.\vec{r})\vec{r}}{r^5} - \frac{\vec{m}}{r^3}\right] \qquad (\mathrm{I}.31)$$

Considering only dipole–dipole interactions, the effective field becomes $H_{eff} = H_0 + H_{dip}$. Considering two identical parallel moments $\overrightarrow{m_1} = \overrightarrow{m_2} = \vec{m}$ separated by $\vec{r}$, the interaction energy ε_p between the two moments may be considered as the energy of m_1 in the field $\overrightarrow{B_{21}}$ (from Eq. (I.31)) created by m_2 at $\vec{r}$ (or vice versa):

$$\varepsilon_p = -\vec{m}.\overrightarrow{B_{21}} = \frac{m^2}{4\pi\mu_0}\frac{1-3cos^2\theta}{r^3} \qquad (\mathrm{I}.32)$$

where θ is the angle between $\vec{m}$ and $\vec{r}$. The interaction of this pair is anisotropic: it is attractive in the head-to-tail configuration (lower in energy) and repulsive when dipoles are aligned side-by-side (unstable). The force and interactions described by this model are illustrated on Figure I.20.

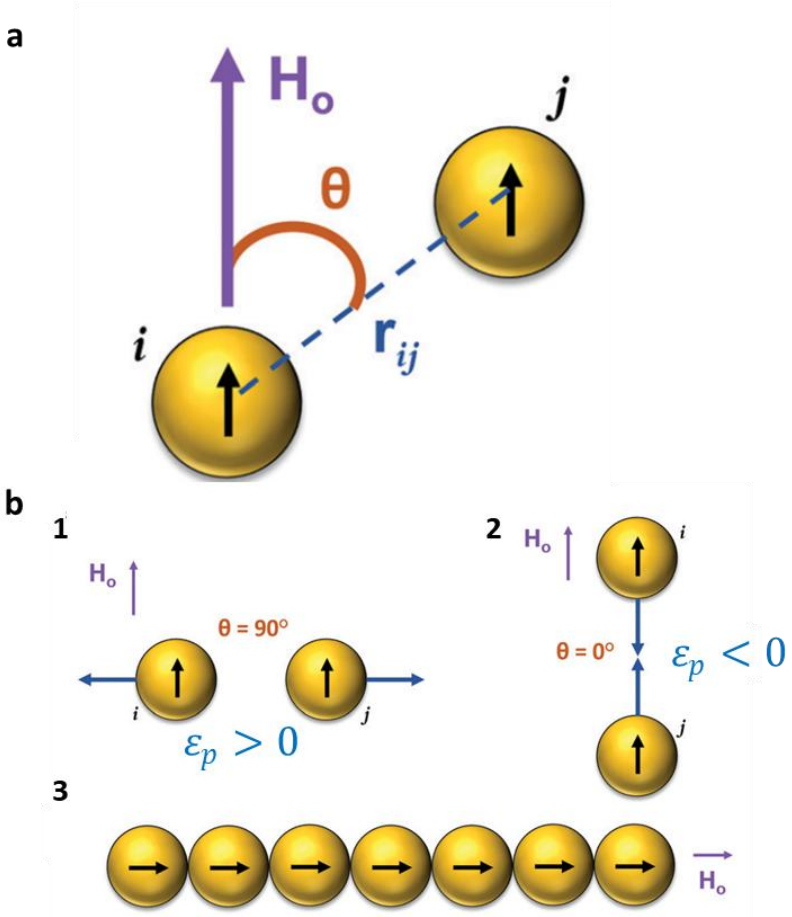

Figure I.20. (a) According to the dipolar model, the magnetic dipole–dipole interaction between two spherical magnetic particles (i and j) under a uniform external magnetic field H_0 separated by a distance r_{ij}, and an angle θ between the field direction and the line connecting the two particle centers. The black arrows inside the particles represent their magnetic moments (m_i and m_j), which have equal magnitude and are aligned parallel to the direction of the external field. (b) The dipolar interactions are anisotropic, depending on the angle θ. (1) Two dipoles aligned side-by-side ($\theta = 90°$) experience the strongest repulsive interaction ($\varepsilon_p > 0$). (2) Two dipoles aligned head-to-tail ($\theta = 0°$) experience the strongest attractive interaction ($\varepsilon_p < 0$). (3) As a result, the particles tend to self-assemble into chains, since the head-to-tail configuration minimizes the dipolar interaction energy [83].

Thus, dipoles that are free to move tend to aggregate into chains. The maximum of attraction is conveniently quantified by the dimensionless dipolar force constant λ for particles of radius a:

$$\lambda = -\frac{\varepsilon_p(r = 2a, \theta = 0)}{kT} = \frac{\pi a^3 \chi^2 H^2}{9kT\mu_0} \qquad (\text{I. } 33)$$

with kT representing the thermal energy. For $\lambda < 1$, Brownian motion dominates and suppresses aggregation, whereas $\lambda > 1$ favors the chain formation. This simplified framework disregards other types of interactions, such as van der Waals interactions, which are usually countered by surfactant layers. We are also assuming that the surface charges are weak, and therefore that electrostatic repulsion can also be neglected.

3.2 Formation of chains

3.2.a 1D chains

3.2.a.i Role of the magnetic field

Both numerical simulations and experimental studies have shown that applying an external magnetic field promotes the assembly of chains in dipolar colloids. Initially, the particles are randomly dispersed. Upon exposure to the field, short chains nucleate and subsequently merge to form elongated, one-dimensional arrays aligned along the field direction [84–86]. One typical simulation of the alignment process is illustrated in Figure I.21. For this process to occur, the dipolar interaction must overcome the competing factors such as thermal agitation and surface charges. For a given material, a critical field strength (H_0) value is therefore often required in experiments [87]. As predicted by the dipolar model, alignment is only feasible for $\lambda > 1$. However, this alignment cannot be guaranteed when considering other interactions.

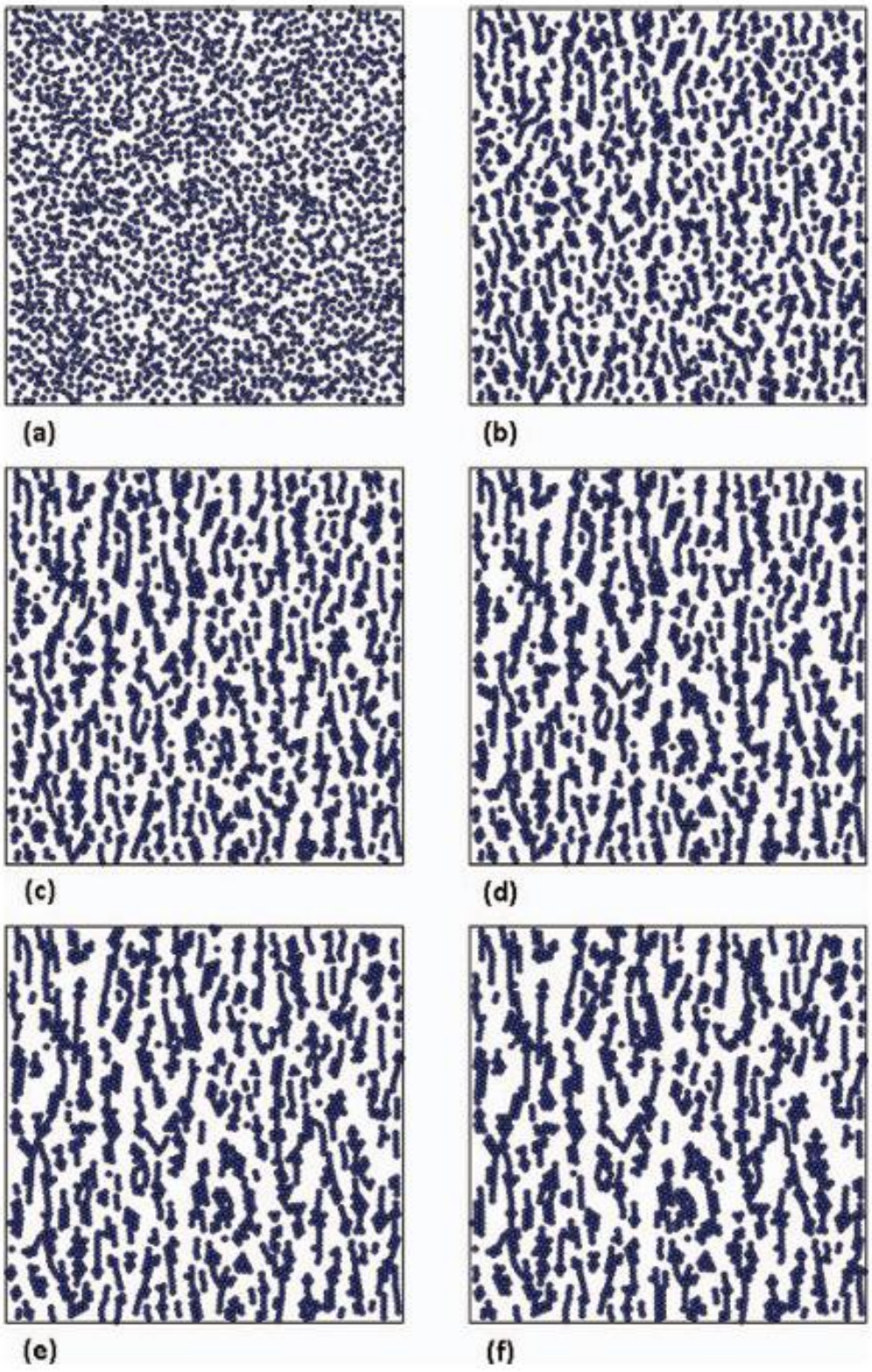

Figure I.21. Agglomeration of magnetic nanoparticles at a solid volume fraction of 0.20 under an external magnetic field. Snapshots correspond to a) 0, (b) 2, (c) 4, (d) 6, (e) 8, and (f) 10 .10^{-4} s [85].

3.2.a.ii Influence of the nanoparticles size, polydispersity, and coating

The particle size strongly affects the chains formation. Larger nanoparticles exhibit stronger dipolar interactions (large moment m) and therefore assemble more readily into chains. Smaller particles, on the other hand, often remain unassociated unless guided by cluster–cluster interactions. This has been reported experimentally by Myrovali *et al*., iron oxide nanoparticles of different diameters (10 to 80nm) have been subjected to an external magnetic field (40−400 mT) [88]. Eventually, this field dictates that the smaller particles (10 and 20 nm) form chain structures in two steps: first, they form clusters and then they undergo "cluster−cluster" interactions to form chains. Larger particles (50 and 80nm) readily form chains via "particle−particle" interactions.

In numerical simulation, bi-disperse systems reveal interesting cooperative effects: even though small particles alone experience weak interactions, they can modulate the chain morphology by attaching to chain extremities, effectively shortening or destabilizing aggregates. It is described as a poisoning effect (Figure I.22) [89,90].

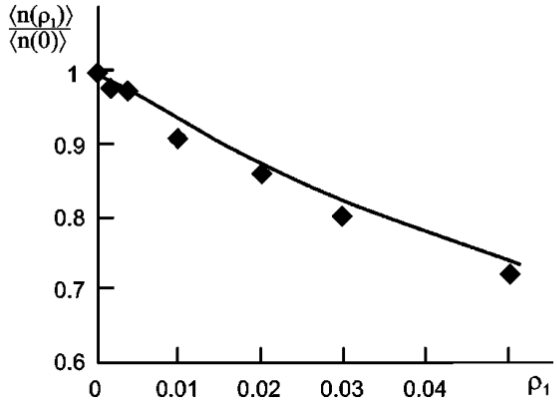

Figure I.22. Simulation of the poisoning effect on bidisperse ferrofluid. The relative decrease of <n> (the mean number of large particles per chains) plotted as a function of the small-particle volume concentration ρ_1 [89,90].

Surface chemistry also plays a crucial role. Increasing the interparticle spacing by using thicker organic coatings has been shown to suppress elongated aggregation in both simulations and

experiments. For example, 10 nm maghemite nanoparticles coated with longer alkyl chains (C12) fail to form extended structures compared with those functionalized with shorter ligands (C8). Experimentally, increasing the ligand chain length from C8 to C12 corresponds to an approximate 0.3 nm increase in interparticle spacing, which is sufficient to weaken dipolar coupling and inhibit chain formation [91]. In simulations without evaporation, no elongated structures are formed. This behavior can be interpreted as resulting from an increase in particle concentration (or volume fraction) due to the reduction of the accessible volume available to the particles. This study is resumed on Figure I.23.

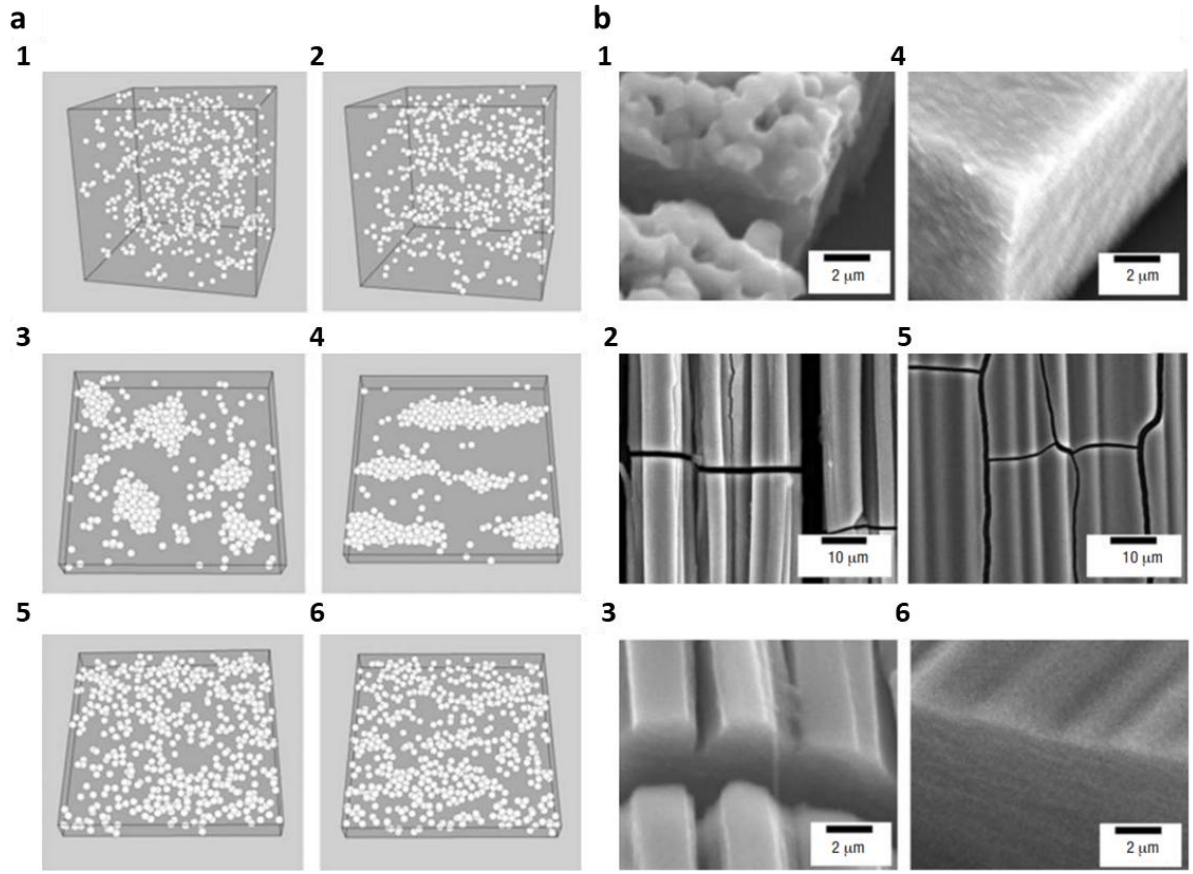

Figure I.23. (a). Snapshots of configurations obtained from Brownian dynamics simulations. (1,2) For a coating layer thickness of $d = 1.2$ nm, before solvent evaporation, no significant particle aggregation is observed, either without (1) or with (2) an applied magnetic field. (3,4) After evaporation, without an applied field (3), the particles form spherical clusters, whereas with an applied field (4), they assemble into elongated chains. (5,6) For a thicker coating ($d = 1.6$ nm), no aggregation occurs during evaporation, regardless of whether a magnetic field is absent (5) or present (6). (b) SEM images of γ-Fe_2O_3 nanocrystals with different surface coatings. (1–3) Nanocrystals coated with C8 ligands: (1) Deposited without a magnetic field, they form spherical aggregates; (2) when deposited under a magnetic field, elongated structures appear; (3) upon tilting the sample, superimposed tubular assemblies can be observed. (4–6) Nanocrystals coated with C12 ligands: (4) Deposited without a magnetic field, they form a dense, continuous film; (5) when a magnetic field is applied during evaporation, partially elongated structures emerge; (6) upon tilting the sample, only slight surface undulations of the thick film are visible. The magnetic field applied is 0.59 T [91].

3.2.b Interchain interaction

3.2.b.i Dipolar force and volume fraction

At higher particle concentrations, chain–chain interactions emerge, leading to the formation of dense superstructures. Thermodynamic analysis reveals that aggregation results from a competition between the decrease in energy caused by the formation of magnetically favorable structure, and the entropic penalties associated with forming structures of different sizes. The balance is captured by the aggregation parameter N^*, which incorporates both magnetic and thermodynamic contributions [92] :

$$N^* = \sqrt{\theta_0 e^{\lambda - 1}} \text{ with } \theta_0 = \frac{4\pi a^3 n}{3} \qquad (\text{I}.34)$$

where a is the particles radius, n is the particle number density, and λ defined in Eq. (I.33). For $N^* < 1$, entropy prevents assembly. For $N^* > 1$, elongated structures such as chains and bundles emerge. Small values of N^* correspond to chains of different sizes, whereas large values ($N^* > 10$) yield thicker aggregates formed by lateral association of long chains. N^* can be interpreted as the average number of nanoparticles in one structure, chains or bundle of chains. This is represented in Figure I.24.

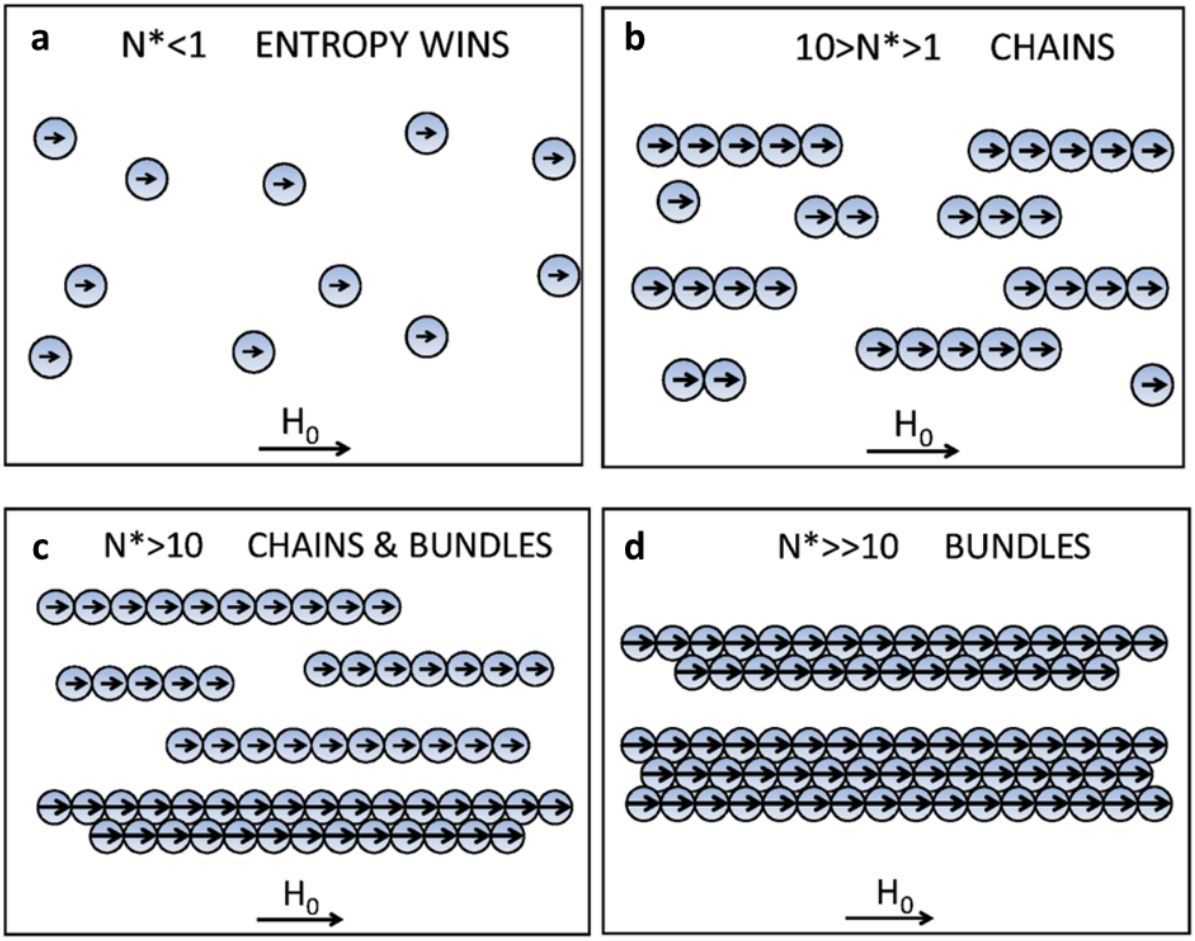

Figure I.24. Schematic illustration summarizing the self-assembly behavior of magnetic particles under an external magnetic field, as a function of the aggregation parameter N^*. (a) No self-assembly occurs. (b) Equilibrium state consisting of chains of various lengths, with an average length N^*. (c) Equilibrium state consisting of long chains and bundles formed by lateral aggregation of chains in a zipped, out-of-registry configuration. (d) Equilibrium state consisting of bundles of laterally aggregated chains.

3.2.b.ii Competitive aggregation: Head-to-tail aggregation and lateral aggregation

Depending on their length, chains can either grow via head-to-tail addition or undergo lateral "zippering" into bundled fibers [86,93,94]. Theoretical studies show that chains shorter than the critical length (~14 particles) preferentially extend linearly, whereas longer chains aggregate laterally in an out-of-registry fashion (Figure I.25) [92]. This offset arrangement minimizes repulsion and reduces the total magnetic energy, making it the dominant pathway at high field strengths or concentrations, as illustrated in Figure I.26. where several cases of

chain–chain interactions are illustrated. For aligned chains, the nature of the interaction evolves from the far-field to the near-field regime. When the lateral separation $\rho > 4a$, the interaction is repulsive, as it is dominated by the magnetic fields at the chain ends. At shorter distances ($\rho < 4a$), the interaction becomes stronger and can be either attractive or repulsive, depending on whether the particles in adjacent chains are in registry (dashed lines) or out of registry (solid lines). Figure 26 also illustrates that the interaction between chain ends can be minimized by axially offsetting the chains by half the chain length ($N/2$). This offset effectively eliminates the far-field interaction, leaving only the near-field attraction or repulsion, determined by the relative registry of the particles.

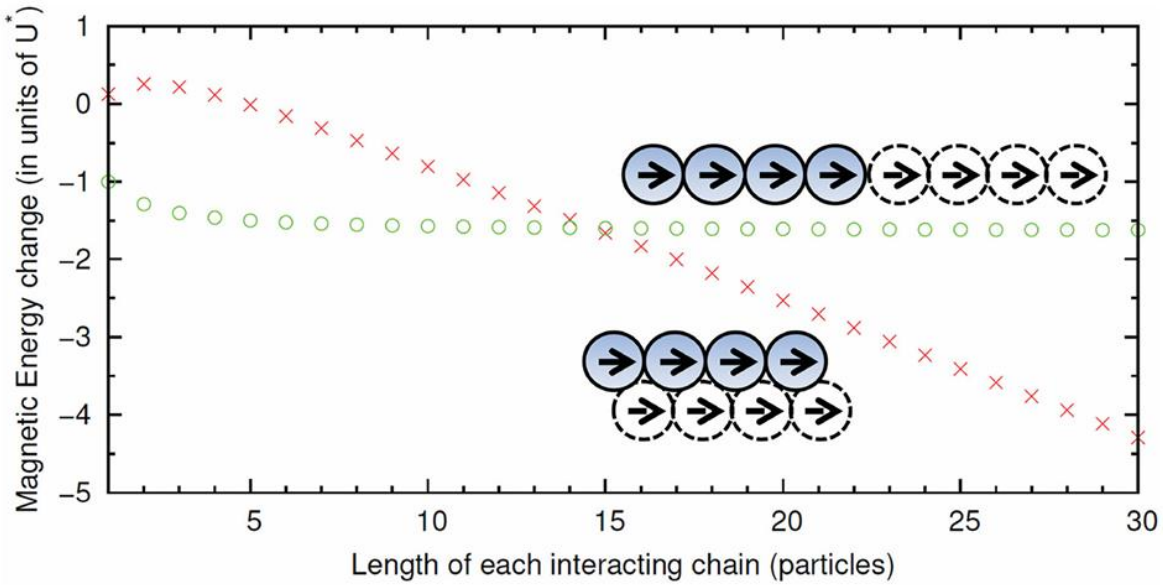

Figure I.25. Calculated variation of magnetic energy during the aggregation of two chains containing the same number of particles. Two configurations are compared: head-to-tail aggregation forming a longer chain (green circles), and lateral aggregation in a zippering arrangement producing a thicker chain (red crosses) [92].

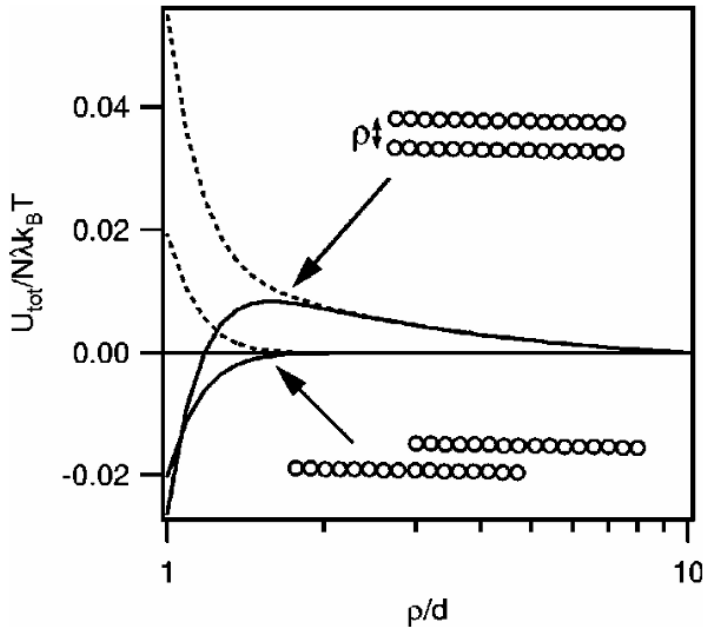

Figure I.26. Calculated interaction between rigid dipolar chains. Dashed and solid lines represent neighboring chains that are in registry or offset by a (particle radius), respectively. Registry configuration exhibit repulsive interaction while offset configuration exhibit attractive interaction at short range. Moreover chains with aligned ends show far-field repulsion, while chains offset by N/2 exhibit only short-range attraction without repulsion at far range [93].

3.2.b.iii Unambiguous experimental observations

The structures predicted by dipolar models have been observed experimentally through techniques such as cryogenic TEM and small-angle neutron scattering (SANS). For example, Klokkenburg *et al.* demonstrated that, even in the absence of an applied field, magnetite nanoparticles of sufficient size (≥ 21 nm for magnetite particle at 0.2 T) can self-assembled into chains as illustrated in figure I.27-a.: this chains are not oriented without external magnetic field [95]. Under applied fields, the same particle progressive ordering into chains and bundled fibers with hexagonal symmetry has been confirmed at 1 T. The larger particles exhibit a well-organized structure with greater anisotropy [96,97]. The in situ cryo-TEM and SANS of the magnetic structures are shown in figure I.27a.

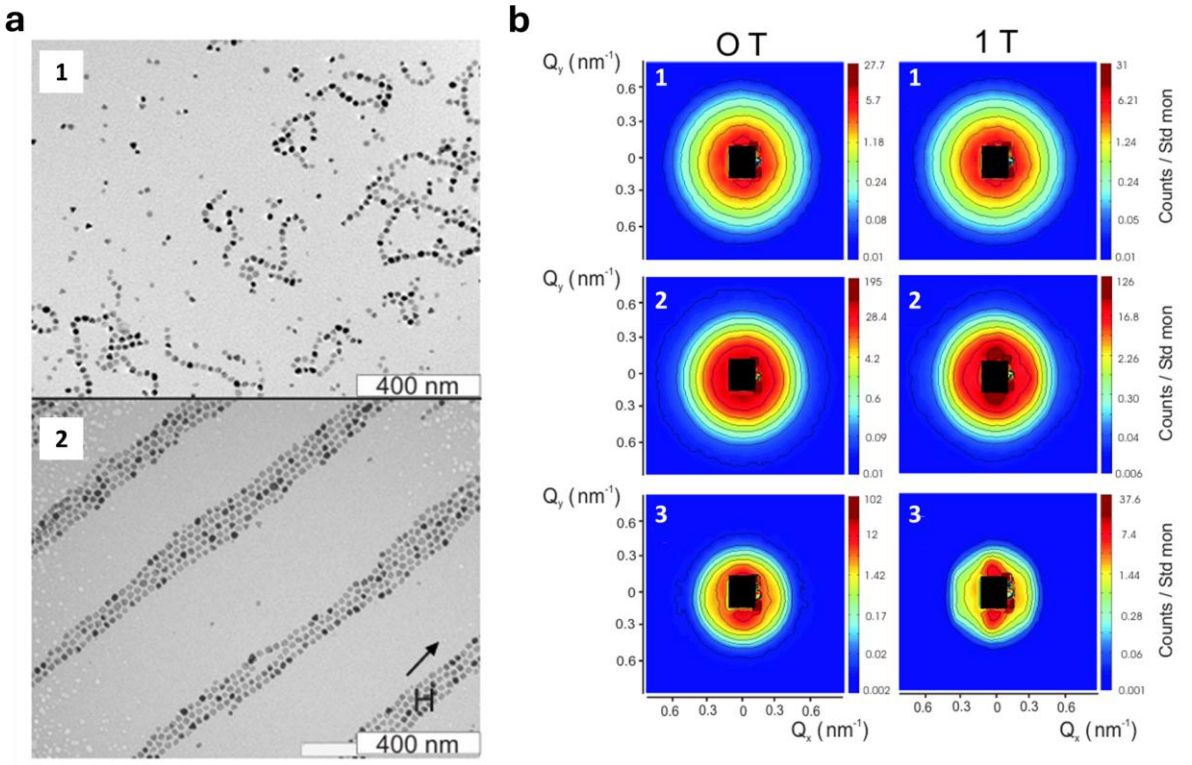

Figure I.27. (a) Representative in situ cryo-TEM images of vitrified 21 nm magnetite NPs. (1) in absence of any applied field, (2) under a homogeneous field of 0.2 T. The system transitions to an arrangement of equally spaced columns displaying a hexagonal symmetry. (b) 2D SANS scattering patterns recorded at 300K of 10 (1), 16 (2) and 21 nm magnetite NPs (3) in zero field (left panels) and under 1 T (right panels). The anisotropy of the arrangement is progressively revealed by transitioning from system 1 to system 3 [97].

During his phD thesis at LPCNO and LAAS, Pierre Moritz developed a magnetophoresis-assisted capillary assembly method for aligning Co nanoparticles into dense micromagnets [98,99]. Figure I.28 illustrates this approach, which enables the fabrication of sub-millimetric and millimetric magnetic structures with tunable architectures. Indeed, pre-patterned nickel templates serve as magnetic flux concentrators when an external field is applied. The resulting magnetophoresis force attracts the nanoparticles at their vicinity. Using an ultrafast camera and particle tracking, Antoine Gonon demonstrated during his PhD at IMFT and LPCNO that the magnetophoresis-driven assembly of hard magnetic nanoparticles proceeds in three stages [99,100]:

- the pre-alignment of Co nanorods in solution yielding micrometric fibers (Figure I.28-a),
- the attraction towards the area of large magnetic field gradients (Figure I.28-b),

- the compaction of the assembly during the solvent evaporation (Figure I.28-c).

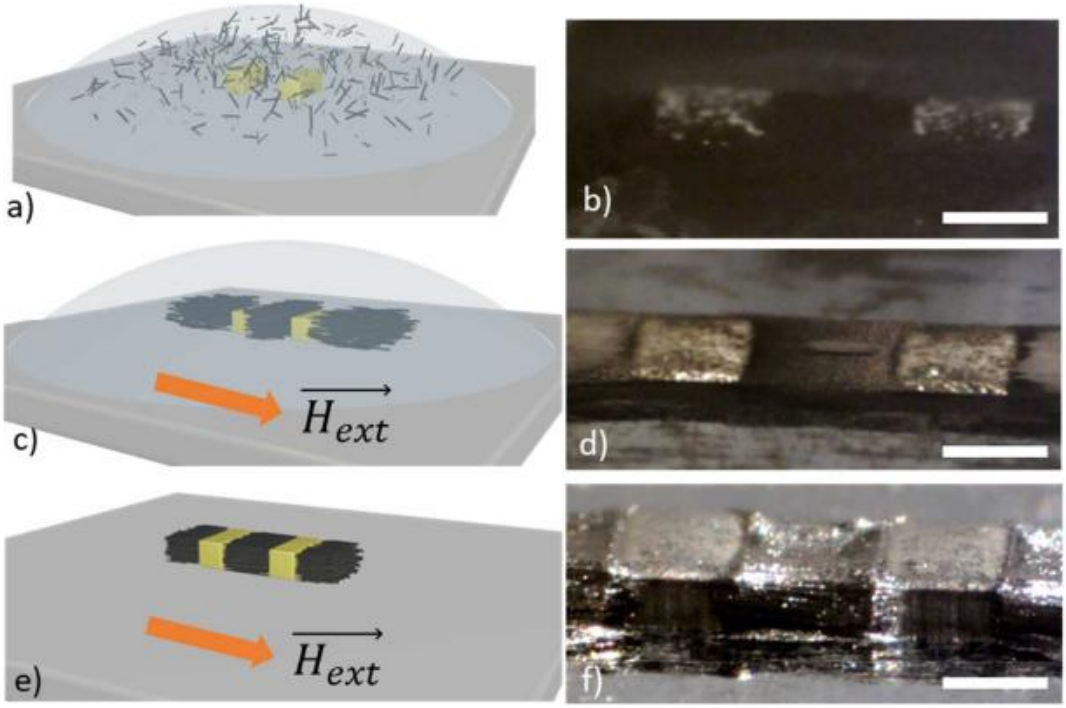

Figure I.28. (a, c, e) Schematic representation of the successive steps in the fabrication of magnetic materials by magnetophoresis and (b, d, f) the corresponding optical images (scale bar = 500 µm). (a, b) Drop-casting of a concentrated Co nanorod suspension onto a substrate patterned with Ni blocks. (c, d) Alignment under an external magnetic field and migration toward the magnetized Ni blocks via magnetophoresis. (e, f) Formation of a dense assembly after complete solvent evaporation [98,99].

Ilona Lecerf then worked, during her PhD at LPCNO and LAAS, on the fabrication of permanent magnet arrays constituted of vertically aligned Co nanorods. While conformal magnets can be obtained between two nickel blocks, the capillary forces encountered during the solvent evaporation yield needle-like assemblies at the surface of a single block [101].

All these previous studies focused on the fabrication and the integration of permanent magnets, using Co nanorods as building blocks. Proof of concept has been obtained for the magnetophoresis-driven assembly of soft magnetic nanoparticles using 15 nm FeC NPs but was not further characterized [98].

4. Conclusion

The preparation of soft magnetic materials for inductors operating in the RF frequency range using a bottom-up approach is an inherently multiscale challenge, spanning everything from nanoparticles and magnetic interactions to the device-level architecture engineering. This chapter has outlined the three fundamental pillars required for progress in this area:

- understanding the electromagnetic criteria that govern the choice of the inductor and magnetic material: permeability, resonance, and loss mechanisms in RF conditions.
- mastering the nanoparticle synthesis routes, particularly the liquid-phase methods, to enable reproducible control over size, composition, and surface chemistry.
- elucidating the forces that direct the magnetic assembly of nanoparticles, where dipolar interactions dictate the emergence of collective organization.

Together, these aspects reveal that optimal inductor performance cannot be addressed by material design alone, but requires a coordinated strategy linking chemistry, physics, and microelectronics. The goal is to obtain material exhibiting soft magnetic behavior with a high saturation magnetization, control their organization in a micromagnet structure, and finally integrate this micromagnet into an inductor with a relevant geometry. This requires the formation of metallic magnetic nanoparticles with monodomain behavior (typically below 20 nm in diameter for FeCo) to prevent multi-domain formation and to minimize eddy currents. The ideal system therefore is macroscopic magnet composed of sub-20 nm metallic magnetic nanoparticles, offering high susceptibility and permeability (typically FeCo alloy) embedded in an insulating matrix, forming a magnetically efficient and electrically resistive metamaterial to prevent short-circuiting of components.

The most promising results have been obtained by drop casting method on planar inductors suspended in a mold, leading to inductors with magnetic material on their two faces. Yet, challenges remain in translating laboratory-scale production into reproducible integration processes, particularly for metallic systems, where oxidation, aggregation and monodispersity must be carefully controlled. For that reason, controlling the organization of the nanoparticles

in a micromagnet structure, and integrate on microcomponent by magnetophoresis is a promising approach to explore.

Overall, the review highlights that nanoparticle-based soft magnetic materials represent a promising route for next-generation RF inductors, provided that advances in synthesis, assembly, and integration can be successfully combined. Bridging these scales is key to unlocking the full potential of magnetic nanomaterials in miniaturized, high-frequency electronic devices. For that, the strategy that we will develop consists in using polyol and organometallic approaches to ensure the synthesis of well-controlled monodisperse metallic nanoparticles, and the magnetophoresis-driven assembly to ensure reproducibility and industrial scalability.

5. References

[1] Coey JMD. Magnetism and magnetic materials. Paperback edition. Cambridge New York Port Melbourne: Cambridge University Press; 2018.

[2] Chang T-H. Ferrite Materials and Applications. In: Han M-G, editor. Electromagn. Mater. Devices, IntechOpen; 2020. https://doi.org/10.5772/intechopen.84623.

[3] Gatel C, Bonilla FJ, Meffre A, Snoeck E, Warot-Fonrose B, Chaudret B, et al. Size-Specific Spin Configurations in Single Iron Nanomagnet: From Flower to Exotic Vortices. Nano Lett 2015;15:6952–7. https://doi.org/10.1021/acs.nanolett.5b02892.

[4] Guo S, Henschel M, Wolf D, Pohl D, Lubk A, Blon T, et al. Size-Specific Magnetic Configurations in Electrodeposited Epitaxial Iron Nanocuboids: From Landau Pattern to Vortex and Single Domain States. Nano Lett 2022;22:4006–12. https://doi.org/10.1021/acs.nanolett.2c00607.

[5] Ma Z, Mohapatra J, Wei K, Liu JP, Sun S. Magnetic Nanoparticles: Synthesis, Anisotropy, and Applications. Chem Rev 2023;123:3904–43. https://doi.org/10.1021/acs.chemrev.1c00860.

[6] Mohapatra J, Liu JP. Rare-Earth-Free Permanent Magnets: The Past and Future. Handb. Magn. Mater., vol. 27, Elsevier; 2018, p. 1–57. https://doi.org/10.1016/bs.hmm.2018.08.001.

[7] Poudyal N, Ping Liu J. Advances in nanostructured permanent magnets research. J Phys Appl Phys 2013;46:043001. https://doi.org/10.1088/0022-3727/46/4/043001.

[8] ON THE THEORY OF THE DISPERSION OF MAGNETIC PERMEABILITY IN FERROMAGNETIC BODIES. Collect. Pap. LD Landau, Elsevier; 1965, p. 101–14. https://doi.org/10.1016/B978-0-08-010586-4.50023-7.

[9] Suemasu T. Rare-earth-free Ferrimagnetic Mn4N Spintronics: IOP Publishing; 2024. https://doi.org/10.1088/978-0-7503-5477-6.

[10] Kittel C. Physical Theory of Ferromagnetic Domains. Rev Mod Phys 1949;21:541–83. https://doi.org/10.1103/revmodphys.21.541.

[11] Kittel C. Theory of the Structure of Ferromagnetic Domains in Films and Small Particles. Phys Rev 1946;70:965–71. https://doi.org/10.1103/physrev.70.965.

[12] Kittel C. On the Theory of Ferromagnetic Resonance Absorption. Phys Rev 1948;73:155–61. https://doi.org/10.1103/PhysRev.73.155.

[13] Walker LR. Magnetostatic Modes in Ferromagnetic Resonance. Phys Rev 1957;105:390–9. https://doi.org/10.1103/PhysRev.105.390.

[14] Walker LR. Resonant Modes of Ferromagnetic Spheroids. J Appl Phys 1958;29:318–23. https://doi.org/10.1063/1.1723117.

[15] White RL, Solt IH. Multiple Ferromagnetic Resonance in Ferrite Spheres. Phys Rev 1956;104:56–62. https://doi.org/10.1103/PhysRev.104.56.

[16] Dillon JF. Magnetostatic Modes in Ferrimagnetic Spheres. Phys Rev 1958;112:59–63. https://doi.org/10.1103/PhysRev.112.59.

[17] Mercereau JE, Feynman RP. Physical Conditions for Ferromagnetic Resonance. Phys Rev 1956;104:63–63. https://doi.org/10.1103/PhysRev.104.63.

[18] Rao JW, Yao B, Wang CY, Zhang C, Yu T, Lu W. Unveiling a Pump-Induced Magnon Mode via Its Strong Interaction with Walker Modes. Phys Rev Lett 2023;130:046705. https://doi.org/10.1103/PhysRevLett.130.046705.

[19] Aharoni A. Exchange resonance modes in a ferromagnetic sphere 2014.

[20] Aharoni A. Angular dependence of nucleation by curling in a prolate spheroid. J Appl Phys 1997;82:1281–7. https://doi.org/10.1063/1.365899.
[21] Viau G, Fiévet-Vincent F, Fiévet F, Toneguzzo P, Ravel F, Acher O. Size dependence of microwave permeability of spherical ferromagnetic particles. J Appl Phys 1997;81:2749–54. https://doi.org/10.1063/1.363979.
[22] Dionne GF. Domain wall resonance effects on high-frequency permeability of ferrites. Dig. INTERMAG 2003 Int. Magn. Conf. Cat No03CH37401, Boston, MA, USA: IEEE; 2003, p. HC-01. https://doi.org/10.1109/INTMAG.2003.1230912.
[23] Daró FR, Migliano ACC, Zanella GP, Hirata AK, De Polli YC, Salvadori MCB. The effect of magnetic domain walls on the complex permeability of bulk Z-type cobalt hexaferrite along both W and Y-phases. Mater Chem Phys 2016;170:12–23. https://doi.org/10.1016/j.matchemphys.2015.12.012.
[24] Dionne GF. Magnetic relaxation and anisotropy effects on high-frequency permeability. IEEE Trans Magn 2003;39:3121–6. https://doi.org/10.1109/TMAG.2003.816026.
[25] Rado GT, Wright RW, Emerson WH. Ferromagnetism at Very High Frequencies. III. Two Mechanisms of Dispersion in a Ferrite. Phys Rev 1950;80:273–80. https://doi.org/10.1103/PhysRev.80.273.
[26] Yamaguchi M, Muroga S, Endo Y, Suzuki M, Inagaki T, Mitsuzuka Y. Ferromagnetic Thin Film Noise Suppressor Integrated to On-Chip Transmission Lines. IEEE Trans Magn 2010;46:2450–3. https://doi.org/10.1109/TMAG.2010.2044763.
[27] Snoek JL. Dispersion and absorption in magnetic ferrites at frequencies above one Mc/s. Physica 1948;14:207–17. https://doi.org/10.1016/0031-8914(48)90038-X.
[28] XIII. On electrical motions in a spherical conductor. Philos Trans R Soc Lond 1883;174:519–49. https://doi.org/10.1098/rstl.1883.0013.
[29] Huo J, Wang L, Yu H. Polymeric nanocomposites for electromagnetic wave absorption. J Mater Sci 2009;44:3917–27. https://doi.org/10.1007/s10853-009-3561-1.
[30] Gradzki PM, Lee FC. Domain wall resonance and its effect on losses in ferrites. PESC 91 Rec. 22nd Annu. IEEE Power Electron. Spec. Conf., Cambridge, MA, USA: IEEE; 1991, p. 627–32. https://doi.org/10.1109/PESC.1991.162741.
[31] Garnero C. Synthèse organométallique de nanoparticules de FeCo pour l'intégration sur inductance. Thèse. Univeristé de Toulouse, 2016.
[32] Dugay J, Tan RP, Meffre A, Blon T, Lacroix L-M, Carrey J, et al. Room-Temperature Tunnel Magnetoresistance in Self-Assembled Chemically Synthesized Metallic Iron Nanoparticles. Nano Lett 2011;11:5128–34. https://doi.org/10.1021/nl203284v.
[33] Dugay J, Tan RP, Ibrahim M, Garcia C, Carrey J, Lacroix L-M, et al. Charge transport and interdot coupling tuned by the tunnel barrier length in assemblies of nanoparticles surrounded by organic ligands. Phys Rev B 2014;89:041406. https://doi.org/10.1103/PhysRevB.89.041406.
[34] Ramprasad R, Zurcher P, Petras M, Miller M, Renaud P. Magnetic properties of metallic ferromagnetic nanoparticle composites. J Appl Phys 2004;96:519–29. https://doi.org/10.1063/1.1759073.
[35] Lagarkov AN, Rozanov KN. High-frequency behavior of magnetic composites. J Magn Magn Mater 2009;321:2082–92. https://doi.org/10.1016/j.jmmm.2008.08.099.
[36] Herzer G. Grain size dependence of coercivity and permeability in nanocrystalline ferromagnets. IEEE Trans Magn 1990;26:1397–402. https://doi.org/10.1109/20.104389.

[37] Bai G, Jin J, Wu C, Yan M. Ultrafine FeCo Nanoparticles Isolated by Ultrathin Dielectric Shells for Microwave Application. ACS Appl Nano Mater 2019;2:3570–6. https://doi.org/10.1021/acsanm.9b00537.
[38] Mohan SS, Del Mar Hershenson M, Boyd SP, Lee TH. Simple accurate expressions for planar spiral inductances. IEEE J Solid-State Circuits 1999;34:1419–24. https://doi.org/10.1109/4.792620.
[39] Roshen WA, Turcotte DE. Planar inductors on magnetic substrates. IEEE Trans Magn 1988;24:3213–6. https://doi.org/10.1109/20.92379.
[40] Roshen WA. Effect of finite thickness of magnetic substrate on planar inductors. IEEE Trans Magn 1990;26:270–5. https://doi.org/10.1109/20.50553.
[41] Wang G, Liu H, Qiu H, Ning K, Yang Y, Li X, et al. MEMS-based fabrication of high-performance inductors with back hollow structure and ferromagnetic film. Microelectron Eng 2017;168:5–9. https://doi.org/10.1016/j.mee.2016.10.005.
[42] Yang C, Koh K, Zhu X, Lin L. On-chip RF inductors with magnetic nano particles medium. 2011 16th Int. Solid-State Sens. Actuators Microsyst. Conf., Beijing, China: IEEE; 2011, p. 2801–4. https://doi.org/10.1109/TRANSDUCERS.2011.5969699.
[43] Zhang J, Yang C, Wang X, Ren T-L, Wang A, Yang Y, et al. INTEGRATED STACKED-SPIRAL RF INDUCTOR WITH NANOPOWDER MAGNETIC CORE. J Circuits Syst Comput 2013;22:1340022. https://doi.org/10.1142/S0218126613400227.
[44] Zhan J, Yang C, Wang X, Fang Q, Shi ZT, Yang Y, et al. Stacked-spiral RF inductors with vertical nanoparticle magnetic core for radio-frequency integrated circuits in CMOS. Sens Actuators Phys 2013;195:231–8. https://doi.org/10.1016/j.sna.2013.02.030.
[45] Zhan J, Cai H-L, Chen X, Wang X, Fang Q, Yang Y, et al. Magnetic-Particle-Composite-Medium-Filled Stacked-Spiral Inductors for Radio-Frequency CMOS Applications. Chin Phys Lett 2013;30:128401. https://doi.org/10.1088/0256-307X/30/12/128401.
[46] Koh K, Park J, Park J, Zhu X, Lin L. Core-shell magnetic nanoparticles for on-chip RF inductors. 2013 IEEE 26th Int. Conf. Micro Electro Mech. Syst. MEMS, Taipei, Taiwan: IEEE; 2013, p. 465–8. https://doi.org/10.1109/MEMSYS.2013.6474279.
[47] Venturin D, Desvaux C, Renaud P, Chaudret B, Parra T. A nanoparticule-based ferromagnetic dielectric Fe/Co composite for RF integrated inductors. 2007 Eur. Microw. Conf., Munich, Germany: IEEE; 2007, p. 5–8. https://doi.org/10.1109/EUMC.2007.4405111.
[48] Desvaux C, Dumestre F, Amiens C, Respaud M, Lecante P, Snoeck E, et al. FeCo nanoparticles from an organometallic approach: synthesis, organisation and physical properties. J Mater Chem 2009;19:3268. https://doi.org/10.1039/b816509b.
[49] Massart R, Cabuil V. Synthèse en milieu alcalin de magnétite colloïdale : contrôle du rendement et de la taille des particules. J Chim Phys 1987;84:967–73. https://doi.org/10.1051/jcp/1987840967.
[50] Lodhia J, Mandarano G, Ferris N, Eu P, Cowell S. Development and use of iron oxide nanoparticles (Part 1): Synthesis of iron oxide nanoparticles for MRI. Biomed Imaging Interv J 2010;6. https://doi.org/10.2349/biij.6.2.e12.
[51] Jolivet JP, Belleville P, Tronc E, Livage J. Influence of Fe(II) on the Formation of the Spinel Iron Oxide in Alkaline Medium. Clays Clay Miner 1992;40:531–9. https://doi.org/10.1346/CCMN.1992.0400506.
[52] Vayssières L, Chanéac C, Tronc E, Jolivet JP. Size Tailoring of Magnetite Particles Formed by Aqueous Precipitation: An Example of Thermodynamic Stability of

Nanometric Oxide Particles. J Colloid Interface Sci 1998;205:205–12. https://doi.org/10.1006/jcis.1998.5614.
[53] Jiang W, Yang HC, Yang SY, Horng HE, Hung JC, Chen YC, et al. Preparation and properties of superparamagnetic nanoparticles with narrow size distribution and biocompatible. J Magn Magn Mater 2004;283:210–4. https://doi.org/10.1016/j.jmmm.2004.05.022.
[54] Babes L, Denizot B, Tanguy G, Le Jeune JJ, Jallet P. Synthesis of Iron Oxide Nanoparticles Used as MRI Contrast Agents: A Parametric Study. J Colloid Interface Sci 1999;212:474–82. https://doi.org/10.1006/jcis.1998.6053.
[55] Jiang W, Yang HC, Yang SY, Horng HE, Hung JC, Chen YC, et al. Preparation and properties of superparamagnetic nanoparticles with narrow size distribution and biocompatible. J Magn Magn Mater 2004;283:210–4. https://doi.org/10.1016/j.jmmm.2004.05.022.
[56] Laurent S, Forge D, Port M, Roch A, Robic C, Vander Elst L, et al. Magnetic Iron Oxide Nanoparticles: Synthesis, Stabilization, Vectorization, Physicochemical Characterizations, and Biological Applications. Chem Rev 2008;108:2064–110. https://doi.org/10.1021/cr068445e.
[57] Pereira C, Pereira AM, Fernandes C, Rocha M, Mendes R, Fernández-García MP, et al. Superparamagnetic MFe_2O_4 (M = Fe, Co, Mn) Nanoparticles: Tuning the Particle Size and Magnetic Properties through a Novel One-Step Coprecipitation Route. Chem Mater 2012;24:1496–504. https://doi.org/10.1021/cm300301c.
[58] Sanz B, Cabreira-Gomes R, Torres TE, Valdés DP, Lima E, De Biasi E, et al. Low-Dimensional Assemblies of Magnetic $MnFe_2O_4$ Nanoparticles and Direct *In Vitro* Measurements of Enhanced Heating Driven by Dipolar Interactions: Implications for Magnetic Hyperthermia. ACS Appl Nano Mater 2020;3:8719–31. https://doi.org/10.1021/acsanm.0c01545.
[59] Andrés Vergés M, Costo R, Roca AG, Marco JF, Goya GF, Serna CJ, et al. Uniform and water stable magnetite nanoparticles with diameters around the monodomain–multidomain limit. J Phys Appl Phys 2008;41:134003. https://doi.org/10.1088/0022-3727/41/13/134003.
[60] Calatayud MP, Soler E, Torres TE, Campos-Gonzalez E, Junquera C, Ibarra MR, et al. Cell damage produced by magnetic fluid hyperthermia on microglial BV2 cells. Sci Rep 2017;7:8627. https://doi.org/10.1038/s41598-017-09059-7.
[61] Sanz B, Calatayud MP, Torres TE, Fanarraga ML, Ibarra MR, Goya GF. Magnetic hyperthermia enhances cell toxicity with respect to exogenous heating. Biomaterials 2017;114:62–70. https://doi.org/10.1016/j.biomaterials.2016.11.008.
[62] Pinna N, Grancharov S, Beato P, Bonville P, Antonietti M, Niederberger M. Magnetite Nanocrystals: Nonaqueous Synthesis, Characterization, and Solubility. Chem Mater 2005;17:3044–9. https://doi.org/10.1021/cm050060+.
[63] Richard S, Eder V, Caputo G, Journé C, Ou P, Bolley J, et al. USPIO size control through microwave nonaqueous sol-gel method for neoangiogenesis T_2 MRI contrast agent. Nanomed 2016:nnm-2016-0177. https://doi.org/10.2217/nnm-2016-0177.
[64] Ma Z, Mohapatra J, Wei K, Liu JP, Sun S. Magnetic Nanoparticles: Synthesis, Anisotropy, and Applications. Chem Rev 2023;123:3904–43. https://doi.org/10.1021/acs.chemrev.1c00860.

[65] Chand K, Vasquez-Guardado ES. Magnetic Nanoparticles: Synthesis and Applications in Life Sciences. ChemistryOpen 2025:2500214. https://doi.org/10.1002/open.202500214.
[66] Zhang S, Jiang G, Filsinger GT, Wu L, Zhu H, Lee J, et al. Halide ion-mediated growth of single crystalline Fe nanoparticles. Nanoscale 2014;6:4852–6. https://doi.org/10.1039/C4NR00193A.
[67] Lacroix L-M, Frey Huls N, Ho D, Sun X, Cheng K, Sun S. Stable Single-Crystalline Body Centered Cubic Fe Nanoparticles. Nano Lett 2011;11:1641–5. https://doi.org/10.1021/nl200110t.
[68] Watt J, Bleier GC, Austin MJ, Ivanov SA, Huber DL. Non-volatile iron carbonyls as versatile precursors for the synthesis of iron-containing nanoparticles. Nanoscale 2017;9:6632–7. https://doi.org/10.1039/C7NR01028A.
[69] Dumestre F, Chaudret B, Amiens C, Renaud P, Fejes P. Superlattices of Iron Nanocubes Synthesized from $Fe[N(SiMe_3)_2]_2$. Science 2004;303:821–3. https://doi.org/10.1126/science.1092641.
[70] Lacroix L-M, Lachaize S, Falqui A, Respaud M, Chaudret B. Iron Nanoparticle Growth in Organic Superstructures. J Am Chem Soc 2009;131:549–57. https://doi.org/10.1021/ja805719c.
[71] Lacroix L, Meffre A, Gatel C, Fazzini P, Lachaize S, Respaud M, et al. Nanoparticle Ripening : A Versatile Approach for the Size and Shape Control of Metallic Iron Nanoparticles. ChemPlusChem 2019;84:302–6. https://doi.org/10.1002/cplu.201800665.
[72] Meffre A, Lachaize S, Gatel C, Respaud M, Chaudret B. Use of long chain amine as a reducing agent for the synthesis of high quality monodisperse iron(0) nanoparticles. J Mater Chem 2011;21:13464. https://doi.org/10.1039/c1jm12127h.
[73] Garnero C, Lepesant M, Garcia-Marcelot C, Shin Y, Meny C, Farger P, et al. Chemical Ordering in Bimetallic FeCo Nanoparticles: From a Direct Chemical Synthesis to Application As Efficient High-Frequency Magnetic Material. Nano Lett 2019;19:1379–86. https://doi.org/10.1021/acs.nanolett.8b05083.
[74] Meffre A, Mehdaoui B, Kelsen V, Fazzini PF, Carrey J, Lachaize S, et al. A Simple Chemical Route toward Monodisperse Iron Carbide Nanoparticles Displaying Tunable Magnetic and Unprecedented Hyperthermia Properties. Nano Lett 2012;12:4722–8. https://doi.org/10.1021/nl302160d.
[75] Bordet A, Lacroix L, Fazzini P, Carrey J, Soulantica K, Chaudret B. Magnetically Induced Continuous CO_2 Hydrogenation Using Composite Iron Carbide Nanoparticles of Exceptionally High Heating Power. Angew Chem Int Ed 2016;55:15894–8. https://doi.org/10.1002/anie.201609477.
[76] Bordet A, Landis RF, Lee Y, Tonga GY, Asensio JM, Li C-H, et al. Water-Dispersible and Biocompatible Iron Carbide Nanoparticles with High Specific Absorption Rate. ACS Nano 2019;13:2870–8. https://doi.org/10.1021/acsnano.8b05671.
[77] Fiévet F, Ammar-Merah S, Brayner R, Chau F, Giraud M, Mammeri F, et al. The polyol process: a unique method for easy access to metal nanoparticles with tailored sizes, shapes and compositions. Chem Soc Rev 2018;47:5187–233. https://doi.org/10.1039/C7CS00777A.
[78] Ammar S, Fiévet F. Polyol Synthesis: A Versatile Wet-Chemistry Route for the Design and Production of Functional Inorganic Nanoparticles. Nanomaterials 2020;10:1217. https://doi.org/10.3390/nano10061217.

[79] Soumare Y, Garcia C, Maurer T, Chaboussant G, Ott F, Fiévet F, et al. Kinetically Controlled Synthesis of Hexagonally Close-Packed Cobalt Nanorods with High Magnetic Coercivity. Adv Funct Mater 2009;19:1971–7. https://doi.org/10.1002/adfm.200800822.
[80] Ener S, Anagnostopoulou E, Dirba I, Lacroix L-M, Ott F, Blon T, et al. Consolidation of cobalt nanorods: A new route for rare-earth free nanostructured permanent magnets. Acta Mater 2018;145:290–7. https://doi.org/10.1016/j.actamat.2017.12.009.
[81] Bousnina MA, Dakhlaoui-Omrani A, Schoenstein F, Soumare Y, Barry AH, Piquemal J-Y, et al. Enhanced Magnetic Behavior of Cobalt Nano-Rods Elaborated by the Polyol Process Assisted with an External Magnetic Field. Nanomaterials 2020;10:334. https://doi.org/10.3390/nano10020334.
[82] Fermigier M, Gast AP. Structure evolution in a paramagnetic latex suspension. J Colloid Interface Sci 1992;154:522–39. https://doi.org/10.1016/0021-9797(92)90165-I.
[83] Spatafora-Salazar A, Lobmeyer DM, Cunha LHP, Joshi K, Biswal SL. Hierarchical assemblies of superparamagnetic colloids in time-varying magnetic fields. Soft Matter 2021;17:1120–55. https://doi.org/10.1039/D0SM01878C.
[84] Li H, Peng X, Chen W. Simulation of the Chain-formation Process in Magnetic Fields. J Intell Mater Syst Struct 2005;16:653–8. https://doi.org/10.1177/1045389X05052598.
[85] Chuan Lim EW, Feng R. Agglomeration of magnetic nanoparticles. J Chem Phys 2012;136:124109. https://doi.org/10.1063/1.3697865.
[86] Wu H, Xu Z, Wang J, Bo X, Tang Z, Jiang S, et al. Chain formation mechanism of magnetic particles in magnetorheological elastomers during pre-structure. J Magn Magn Mater 2021;527:167693. https://doi.org/10.1016/j.jmmm.2020.167693.
[87] Barrett M, Deschner A, Embs JP, Rheinstädter MC. Chain formation in a magnetic fluid under the influence of strong external magnetic fields studied by small angle neutron scattering. Soft Matter 2011;7:6678. https://doi.org/10.1039/c1sm05104k.
[88] Myrovali E, Papadopoulos K, Iglesias I, Spasova M, Farle M, Wiedwald U, et al. Long-Range Ordering Effects in Magnetic Nanoparticles. ACS Appl Mater Interfaces 2021;13:21602–12. https://doi.org/10.1021/acsami.1c01820.
[89] Kantorovich S, Ivanov AO. Formation of chain aggregates in magnetic fluids: an influence of polydispersity. J Magn Magn Mater 2002;252:244–6. https://doi.org/10.1016/S0304-8853(02)00651-0.
[90] Ivanov AO, Kantorovich SS. Chain aggregate structure and magnetic birefringence in polydisperse ferrofluids. Phys Rev E 2004;70:021401. https://doi.org/10.1103/PhysRevE.70.021401.
[91] Lalatonne Y, Richardi J, Pileni MP. Van der Waals versus dipolar forces controlling mesoscopic organizations of magnetic nanocrystals. Nat Mater 2004;3:121–5. https://doi.org/10.1038/nmat1054.
[92] Faraudo J, Andreu JS, Calero C, Camacho J. Predicting the Self-Assembly of Superparamagnetic Colloids under Magnetic Fields. Adv Funct Mater 2016;26:3837–58. https://doi.org/10.1002/adfm.201504839.
[93] Furst EM, Gast AP. Dynamics and lateral interactions of dipolar chains. Phys Rev E 2000;62:6916–25. https://doi.org/10.1103/physreve.62.6916.
[94] Laskar JM, Philip J, Raj B. Experimental evidence for reversible zippering of chains in magnetic nanofluids under external magnetic fields. Phys Rev E 2009;80:041401. https://doi.org/10.1103/PhysRevE.80.041401.

[95] Klokkenburg M, Vonk C, Claesson EM, Meeldijk JD, Erné BH, Philipse AP. Direct Imaging of Zero-Field Dipolar Structures in Colloidal Dispersions of Synthetic Magnetite. J Am Chem Soc 2004;126:16706–7. https://doi.org/10.1021/ja0456252.
[96] Klokkenburg M, Erné BH, Meeldijk JD, Wiedenmann A, Petukhov AV, Dullens RPA, et al. *In Situ*Imaging of Field-Induced Hexagonal Columns in Magnetite Ferrofluids. Phys Rev Lett 2006;97. https://doi.org/10.1103/physrevlett.97.185702.
[97] Klokkenburg M, Erné BH, Wiedenmann A, Petukhov AV, Philipse AP. Dipolar structures in magnetite ferrofluids studied with small-angle neutron scattering with and without applied magnetic field. Phys Rev E 2007;75. https://doi.org/10.1103/physreve.75.051408.
[98] Moritz P, Gonon A, Blon T, Ratel-Ramond N, Mathieu F, Farger P, et al. Magnetophoresis-Assisted Capillary Assembly: A Versatile Approach for Fabricating Tailored 3D Magnetic Supercrystals. ACS Nano 2021;15:5096–108. https://doi.org/10.1021/acsnano.0c10215.
[99] Moritz P, Lecerf I, Gonon A, Maties G, Blon T, Cayez S, et al. Hybrid Ni–Co–Ni Structures Prepared by Magnetophoresis as Efficient Permanent Magnets for Integration into Microelectromechanical Systems. Adv Eng Mater 2022;24:2200733. https://doi.org/10.1002/adem.202200733.
[100] Gonon A. Aimants intégrés submillimétriques pour dispositifs de récupération d'énergie. Thèse. Univeristé de Toulouse, 2023.
[101] Lecerf I. Etude magnétique de micro-aimants pour intégration dans un récupérateur d'énergie MEMS. Thèse. Univeristé de Toulouse, 2024.

Chapter II. Synthesis of magnetic nanoparticles – Building block

Summary of Chapter II

1 Organometallic synthesis 75

1.1 Synthesis of iron (Fe) nanoparticles 76

1.1.a Reminder on the nucleation-growth mechanism of this synthesis 76

1.1.b One step synthesis 77

1.1.c Two step synthesis 83

1.1.d Structural and magnetic characterization 87

1.2 Synthesis of iron-cobalt (FeCo) nanoparticles 88

1.2.a Effect of the ammonium/amine ration 89

1.2.b Effect of the atomic composition ($Fe_{1-x}Co_x$) 91

1.2.c Effect of the atomic composition ($Fe_{1-x}Co_x$) 93

1.3 Synthesis of iron carbide (FeC) nanoparticles 95

1.4 Conclusion on the NPs prepared by the organometallic approach 98

2 Towards the synthesis of larger FeCo particles **99**

3 Cobalt-nickel (CoNi) polyol synthesis **102**

3.1 Size control – Heterogeneous nucleation and growth model 103

3.1.a Experimental results on $Co_{1-x}Ni_x$ particles 103

3.1.b Determination of the size of seeds 105

3.1.c Structural and chemical study of the CoNi particles 106

3.2 Magnetic properties of the CoNi particles 115

3.2.a Effect of the particles size: case study on the $Co_{0.50}Ni_{0.50}$ system 116

3.2.b Effect of the chemical composition: case of study on the 66-68 nm NPs 116

3.3 Conclusion on the CoNi particles prepared by the polyol synthesis 117

4 Conclusion **119**

5 References **120**

The development of advanced planar inductors requires the integration of high-performance micromagnets, which rely on magnetic nanoparticle building blocks carefully engineered to exhibit optimized properties and suitable magnetophoresis assembly. This work focuses on the synthesis and selection of magnetic nanoparticles tailored for such applications, emphasizing the methods which offer precise control over material and magnetic properties.

To this end, several synthesis routes were explored. The organometallic synthesis techniques, well established at LPCNO, were employed to produce a variety of Fe-based magnetic nanoparticles. Though inherently complex and limited to laboratory-scale production, this method offers a precise control over the nanoparticle size, shape, and composition. To reach larger particle size, iron-cobalt (FeCo) particles were synthesized via chemical reduction using hydrazine, a method selected for its relative simplicity to obtain submicronic particles. Finally, the polyol method was investigated for the synthesis of cobalt-nickel (CoNi) nanoparticles due to its known scalability and the fine tunability in terms of size and composition of particles.

Each type of nanoparticle was subsequently characterized using transmission electron microscopy (TEM) or scanning electron microscopy (SEM) to assess their morphology and the size distribution. Structural and static magnetic properties were also measured using X-Ray Diffraction (XRD) and Vibrating Sample Magnetometry (VSM), respectively, to characterize the material and its potential interest as magnetic core integrated onto a planar inductor.

1. Organometallic synthesis

In the context of fabricating micromagnets through nanoparticle assembly by magnetophoresis, we focus on investigating the influence of parameters controlling nanoparticle size and morphology. The objective is to synthesize samples with high monodispersity in both size and shape, with a preference for cubic geometries to maximize packing density within the assemblies. Targeting particle sizes in the range of 10–20 nm ensures that the nanoparticles remain within the ferromagnetic single-domain regime, which is better for maintaining low-loss micromagnet.

Organometallic synthesis represents a finely tuned and highly versatile route for producing magnetic nanoparticles, which has been widely used at LPCNO [1–4]. The synthesis relies on the controlled decomposition of organometallic precursors under dihydrogen (typically 3 bars) and in the presence of carefully selected ligands. These ligands play a key role in stabilizing the precursor used, forming a reservoir, and directing the nanoparticle growth. They offer therefore precise control over nucleation and growth kinetics.

To ensure optimal reaction conditions, the syntheses are carried out in Fisher-Porter (FP) bottles, which can withstand pressures up to 5 bars. Due to the high reactivity of the precursors used in this section, all experiments are performed under an inert atmosphere in a glovebox filled with argon. Mesitylene, a non-polar organic solvent capable of sustaining reaction temperatures up to 150°C is used after being carefully purified and degassed. These steps are mandatory to remove any traces of water and oxygen and thus ensure that the solvent remains inert toward both the precursors and the resulting nanoparticles.

Initial efforts focused on synthesizing iron (Fe) NPs, through a highly versatile synthesis, where tuning the ligand type (aliphatic chain length, and functional group) and concentration allowed a fine adjustment of the particle morphology. Then, building on this foundation, bimetallic iron-cobalt (FeCo) NPs were synthesized to exploit their superior magnetic properties, which make them theoretically the best candidates for high-performance inductor cores. Finally, iron carbide (FeC) nanoparticles were explored for their enhanced resistance to oxidation, a crucial advantage for micromagnet applications where stability in air is required.

1.1 Synthesis of iron (Fe) nanoparticles

This process involves the decomposition of an organometallic precursor $[Fe(N(Si(CH_3)_3)_2)_2]_2$ under dihydrogen in the presence of a pair of long-chain acid/amine ligands. These ligands allow controlling the size and shape of the nanoparticles, as previously reported [5,6].

1.1.a Reminder on the nucleation-growth mechanism of this synthesis

The nucleation–growth mechanism governing this synthesis was originally proposed by Lise-Marie Lacroix during her PhD work, based on combined microscopy, magnetometry and Mössbauer spectroscopy studies [6]. This mechanism is based on the iron precursor and its interaction with various long-chain ligands (such as palmitic acid (PA), hexadecylamine (HDA), or both), ultimately guiding the formation of iron NPs.

Nucleation phase. Before decomposition begins, the reaction medium contains a complex mixture of iron species formed by the reaction of the iron precursor, $[Fe(N(Si(CH_3)_3)_2)_2]_2$ referred hereafter as FeNSi, with the ligands. Two distinct iron-containing species have been identified:

- [Fe]_initiator: iron(II) complex, consisting of relatively reactive iron species, likely present in the form of low-stability clusters or complexes. These species decompose rapidly and are primarily responsible for initiating the nucleation.
- PM Fe^{2+}: A paramagnetic species, structurally analogous to iron(II) carboxylates, fairly stable. This species persists throughout the reaction, forming what is often described as a reservoir of Fe(II) that feeds the growth stage of the particles over time.

Thus, the decomposition kinetics likely follow two parallel pathways. First, the fast decomposition of [Fe]_initiator drives nucleation. Then, the slow decomposition of PM Fe^{2+} sustains the growth of the nuclei. It is the acid initially introduced into the system (ex: PA) which reacts almost quantitatively with the precursor to generate this reservoir of carboxylated iron(II), which then gradually contributes to the particle growth.

Growth Phase and Ligand Self-Organization. Following the brief nucleation event, particle growth occurs in a medium that becomes increasingly heterogeneous. This inhomogeneity stems from the self-organization of the long-chain ligands (acid/amine combinations) into organic superstructures, whose formation depends strongly on the acid-to-amine ratio (Y/X) and the overall ligand concentration. These superstructures play a templating role, influencing both the size and the shape of the final nanoparticles. Two distinct growth environments can be proposed:

- Within the organic superstructures: Anisotropic growth occurs, leading to the formation of cubic nanoparticles, particularly in acid-rich environments. This behavior is associated with the selective stabilization of the {100} facets.
- Outside the superstructures: The growth is more homogeneous and isotropic, often resulting in spherical nanoparticles, particularly in amine-rich media where facet stabilization is weaker or less directional.

1.1.b One step synthesis

In the case of iron nanoparticle synthesis carried out in a single step, the general reaction scheme is described by the following chemical equation:

$$[\mathrm{Fe(N(Si(CH_3)_3)_2)_2]_2} + \mathrm{X\ Amine} + \mathrm{Y\ acide} \xrightarrow[\substack{150°C,\ 3bar\ H_2,\ 48h \\ Mesitylene}]{} \mathrm{Fe(0)\ NPs}$$

50mM of FeNSi is dissolved in mesitylene in the presence of long-chain acid/amine ligands. The reaction solution is then placed under pressure of 3 bars of H_2 and immersed in an oil bath at 150°C for 48h. The effects of several parameters on the particle size and shape are described.

1.1.b.i The choice of the ligand pair

In this study, the ligands employed include amines and carboxylic acids with alkyl chain lengths ranging from 8 to 16 carbon atoms. The selected ligands are the following:

- **C8**: Octylamine (OcAm), Octanoic acid (OcAc)
- **C12**: Dodecylamine (DDA), Lauric acid (LA)
- **C16**: Hexadecylamine (HDA), Palmitic acid (PA), Hexadecylammonium chloride (HDAHCl)

The impact of alkyl chain length was systematically studied under fixed experimental conditions (acid carboxylic function, molar ratio Y/X = 1.8/2, temperature = 150 °C, reaction time = 48 h). The observed average particle size for different chain lengths was measured on TEM images (Figure II.1). The observations are summarized in Table II.1.

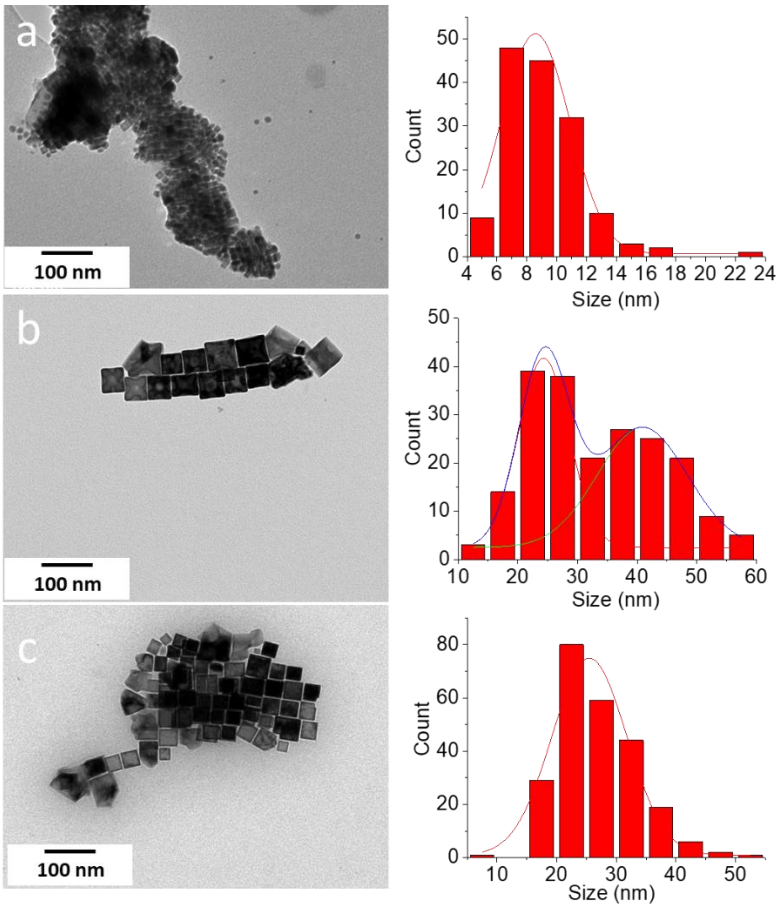

Figure II.1. TEM images with the associated size distribution of Fe nanoparticles obtained in presence of a 1,8/2 ratio of (a) C8 (OcAc/OcAm), (b) C12 (LA/DDA) and (c) C16 (PA/HDA) ligands.

Ligand pair	OcAc/OcAm	LA/DDA	PA/HDA
Size (nm)	8.6±2.3	24.3±4.2 and 40.9±7.5	25.6±6.3
Shape	Cubic	Octopod-cubic	Cubic

Table II.1. Effect of the influence of different ligands on the size and morphology of Fe nanoparticles obtained.

These results confirm that the ligand chain length significantly affects the nanoparticle growth. Notably, an increase from C8 to C16 leads to a considerable increase in size but through a non-linear dependence, suggesting that additional factors play a role.

A closer examination reveals striking differences in particle morphology and dispersion between different ligand pairs. In particular, the C12 system (AL/DDA) produces significantly larger and more polydisperse nanoparticles with an octopod-cubic shape (~24-41 nm), in contrast to the smaller and more monodisperse cubes (~26 nm) formed in the presence of the C16 ligand pair (AP/HDA). This suggests that the C12 system promotes a more pronounced coalescence phenomenon.

Two non-exclusive hypotheses could explain this behavior:

- **Prolonged coalescence**: The C12 ligands may stabilize the reservoir of iron carboxylate species more effectively, delaying the nucleation and allowing particles to grow over an extended time.
- **Reduced nanoparticle stabilization**: C12 ligands might provide less efficient surface passivation especially thus allowing for particle coalescence and uncontrolled growth.

In either case, the results clearly highlight the critical role of alkyl chain length in modulating both the stability of intermediate species and the surface dynamics of the growing nanoparticles.

1.1.b.ii Effect of the acid/amine ratio (Y/X)

The acid-to-amine (Y/X) ratio is a critical parameter influencing both the nucleation and the growth steps. A general and well-documented trend is that increasing the proportion of the acid (Y) relative to the amine (X) promotes particle growth by stabilizing iron carboxylate species. This stabilization indeed reduces the number of nucleation events and therefore promotes larger particles during the growth phase. The effect of the acid/amine ratio was studied with the different ligand systems (C8, C12, C16). While we limit the discussion in the manuscript to the C16 systems, the results for the C8 and C12 ligands can be found in Appendix 1.

The effect of large HDA excess was investigated. Experiments were carried out at varying reaction durations to ensure near-equilibrium states. The reaction conditions and observations from the TEM microscopy (Figure II.2) are summarized in Table II.2.

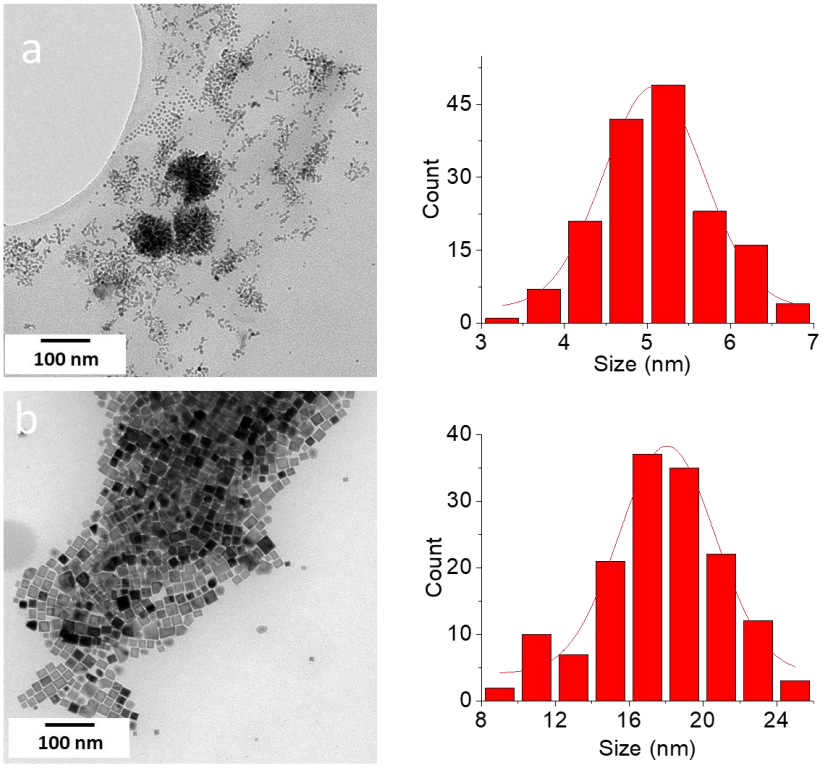

Figure II.2. TEM images with the associated size distribution of Fe NPs prepared in presence of an acid/amine (PA/HDA) ratio of (a) 1.5/20 and (b) 1.5/1.

High amine concentrations seem to reduce the availability of iron carboxylates, slowing down the reaction and limiting the particle growth. Additionally, as reported in the literature, long-chain amines such as HDA can promote particle coalescence under certain conditions [7].

1.1.b.iii Effect of the acid nature: use of ammonium chloride

Replacing carboxylic acid, which leads to the stabilization of Fe(II) reservoir by ammonium chloride salt allows to fasten the reaction kinetics as previously reported by L.-M. Lacroix et A. Meffre [8,9]. Three different conditions with a reaction time of 24h were explored, considering the previous results (Table II.2). When using a 0,9/5 HDAHCl/HDA ratio, small cubes of 8.2 nm were obtained (Figure II.3a). Such a large excess of HDA being detrimental in the perspective of reaching high magnetic volume fraction in the final micromagnets, its quantity was limited to 2 equivalents per Fe atoms. A 1,5/2 HDAHCl/HDA ratio leads to larger cubes of 10.8 nm (Figure II.3b). Since it has been reported that the long chain amine (HDA) could play the role of reducing agent, the synthesis was tested in the absence of molecular hydrogen. Nanocubes of fairly similar sizes (11.0 nm) were obtained with a fairly good reaction yield (70%), confirming that hydrogen-free synthesis could efficiently produce Fe^0 NPs.

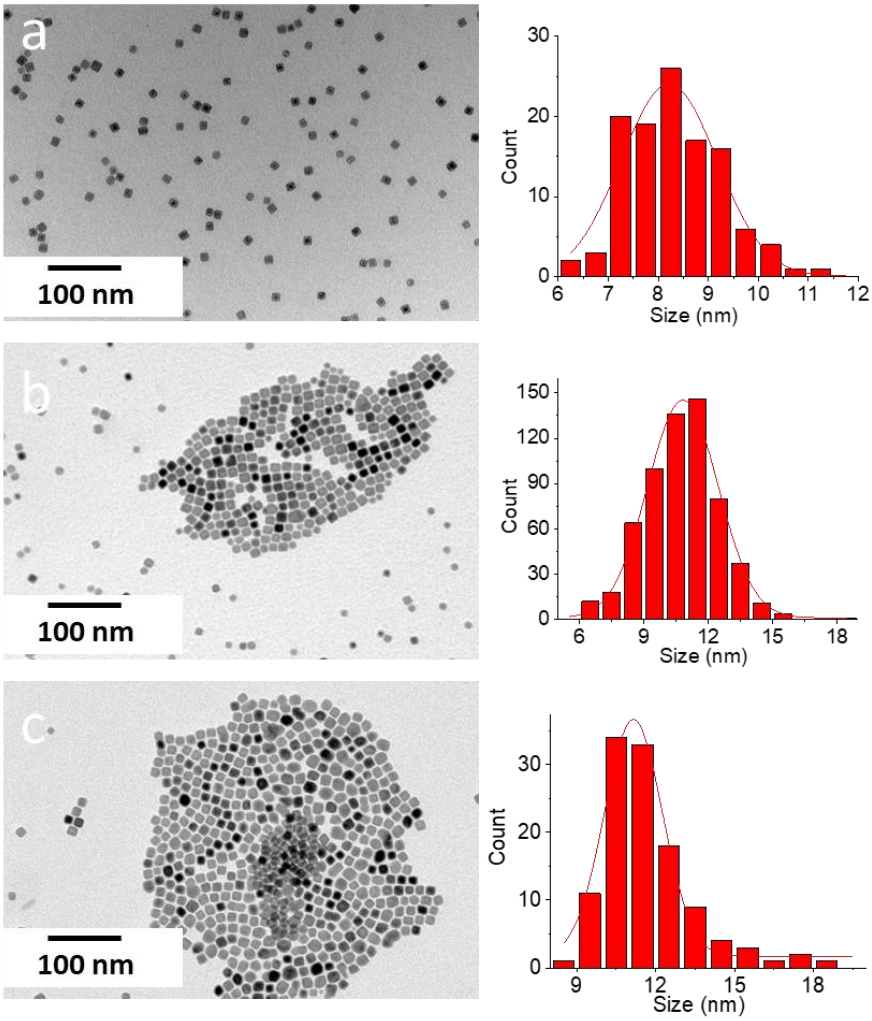

Figure II.3. TEM images with the associated size distribution of Fe NPs prepared with 2 equivalents of HDA and (a) 0.9 or (b) 1.5 equivalent of HDAHCl under H_2 or (c) Ar.

The observations confirm that increasing the proportion of acid leads to bigger particles, but to a lower extent compared to the carboxylic acid counterparts. Indeed, in presence of HDAHCl particle sizes remain in a narrow range of 8 to 11 nm with well-defined cubic morphologies.

	PA/HDA		HDAHCl/HDA		
Ratio Acid/Amine	1.5/20	1.5/1	0.9/5	1.5/2	1.5/2
Reaction atmosphere	H_2	H_2	H_2	H_2	Ar
Reaction time	10 days	48h	24h	24h	24h
Size (nm)	5.0±0.6	18.1±2.6	8.2±1.0	10.8±3.3	11.0±1.1
Shape	Spheroids + coalesced NPs	Cubes	Cubes	Cubes	Cubes with rounded edges

Table II.2. Size and morphology of Fe nanoparticles obtained for C16 ligand with different acid/HDA ratio.

As a conclusion of this study on the direct synthesis of Fe^0 NPs, the NPs obtained in presence of the HDA/HDAHCl ligands are the most promising since they exhibit a well-defined cubic morphology combined with narrow size polydispersity. However, the achievable size range of these particles remains limited, even using different reaction conditions (reaction time, temperature: see Appendix 2). For this reason, the following section explores a ripening approach as a strategy to extend the accessible size range while preserving the size monodispersity and the shape control.

1.1.c Two-Step Synthesis of Fe^0 NPs benefiting from seeds ripening

In this section, a two-step synthesis route separating the nucleation step of small seeds from their growth through a ripening process is explored using the HDAHCl/HDA ligand system [10]. Specifically, the goal was to increase particle size without inducing structural defects such as porosity or morphological irregularities (e.g., octopods), which are often observed in single-step syntheses on larger particles. The reaction occurs as follows:

Step 1 – Seed Formation

$$[\mathrm{Fe(N(Si(CH_3)_3)_2)_2]_2} \xrightarrow[\substack{150°C,\ 3bar\ H_2,\ 24h \\ Mesitylene}]{} \mathrm{Fe(0)\ 1.5nm\ seeds}$$

As previously reported, iron seeds with an average diameter of 1.5 nm (σ = 0.5 nm) were obtained by decomposing the iron dimer $[Fe(N(Si(CH_3)_3)_2)_2]_2$ under H_2 (3 bar) at 150 °C in mesitylene for 24 hours [11]. These seeds are stabilized solely by hexamethyldisilazane (HMDS), a by-product of the reduction reaction, making them highly reactive and easy to destabilize.

Step 2 – Growth step

$$\mathrm{Fe(0)\ seeds} + \mathrm{X\ HDA} + \mathrm{Y\ HDAHCl} \xrightarrow[\substack{150°C,\ 3bar\ H_2,\ 48h \\ Mésitylène}]{} \mathrm{Fe(0)\ NPs}$$

After cooling down, a mixture of HDA and HDAHCl (in varying ratios) was added to the seed solution. The growth process was then carried out under H_2 (3 bar) at 150 °C for up to 4.5 days. During this phase, the reactive seeds evolve into larger particles through a ripening process. Ligand concentrations were expressed as molar equivalents relative to the total amount of iron introduced in Step 1.

1.1.c.i Effect of the ligand Ratio (HDAHCl/HDA)

A series of ripening reactions was conducted using different HDAHCl/HDA ratios. At first, all reactions were allowed to proceed for at least 4 days to ensure that the system approached equilibrium. The reactions conditions are summarized in Table II.3 associated with the microscopy analysis (Figure II.4, 5).

Ratio HDAHCl/HDA	1/2	1.2/2	1.5/2	1.5/2
Time	4.5 days	4 days	4.5 days	48 h
Size (nm)	14.8±3.6	18.2±3.4	21.0±2.9 and 34.1±6.4	17.7±2.1
Shape	Cubes	Cubes	Cubes	Cubes

Table II.3. Size and morphology of Fe nanoparticles obtained after a seed-mediated growth with HDAHCl/HDA ligand pair with different reaction time.

An increase in the HDAHCl/HDA ratio resulted in a consistent increase in particle size, a trend analogous to the one observed in the one-step synthesis. A 1/2 ratio yields 15 nm particles, and an increase of HDAHCl quantity at 1.2/2 ratio led to 17 nm particles. At high acid content (1.5/2), particles larger than 20 nm were obtained but the system becomes more prone to coalescence, as evidenced by the bimodal size distribution, despite the preservation of cubic morphology. Different reaction times can be used to avoid this coalescence.

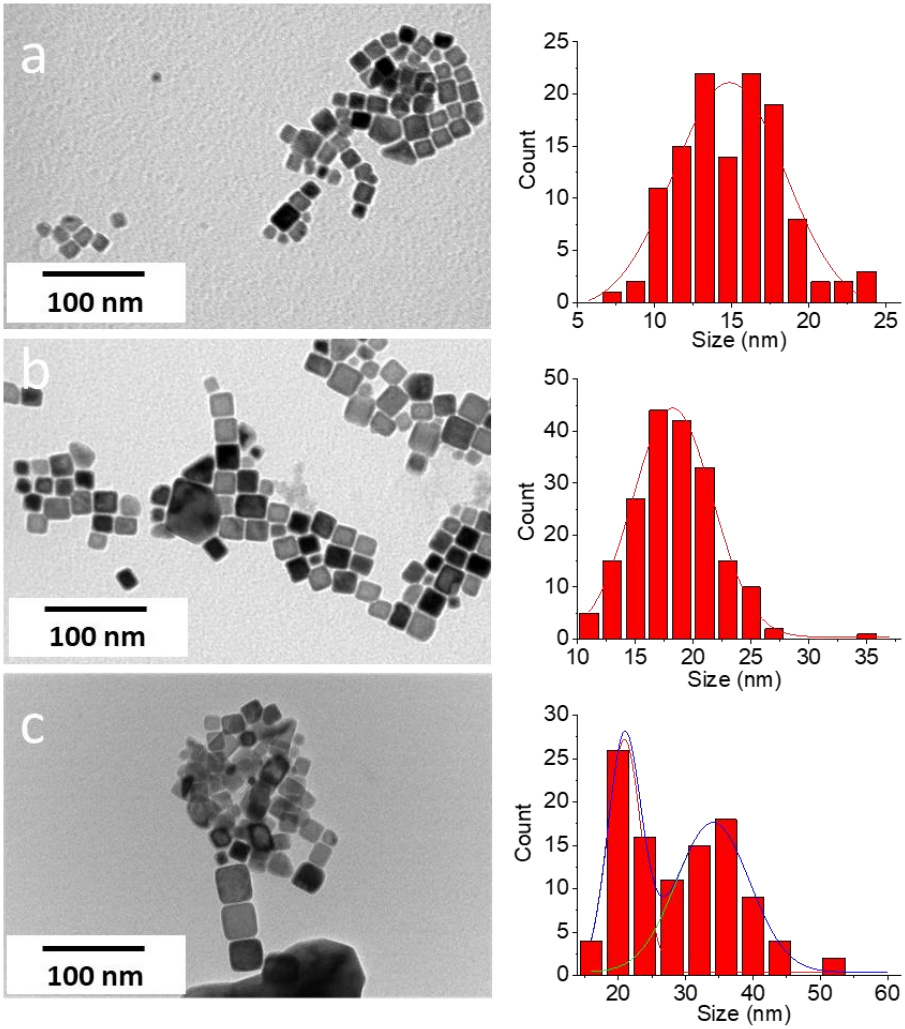

Figure II.4. TEM images with the associated size distribution of Fe NPs obtained using a two-step synthesis using a HDAHCl/HDA ratio of (a) 1/2, (b) 1.2/2 and (c) 1.5/2.

1.1.c.ii Effect of the reaction time

To address the bimodal size distribution, it was necessary to further investigate the growth dynamics. For this purpose, the reaction time was decreased to 2 days while

maintaining a fixed ligand ratio (HDAHCl/HDA = 1.5/2). After 2 days, 17.7 nm nanoparticles exhibiting a narrow size distribution were obtained (Figure II.5). Extended growth times resulted in an increase in the average particle size and a broader size distribution 21–34 nm (Table II.3). The bimodal distribution observed after 4.5 days suggests that not all particles grow uniformly during the ripening step, coalescence probably occurring at longer reaction time.

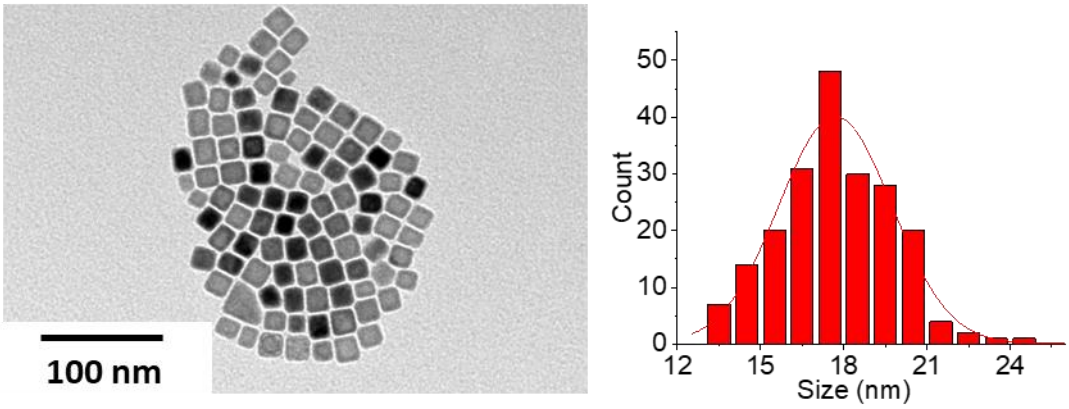

Figure II.5. TEM images with the associated size distribution of Fe NPs obtained in presence of an HDAHCl/HDA ratio of 1,5/2 after a second step reaction of 48h.

1.1.c.iii Conclusion

Overall, as a conclusion for this section, the two-step synthesis approach using preformed iron seeds and controlled growth/ripening in the presence of HDA and HDAHCl enables the formation of larger cubic nanoparticles of 18 nm while maintaining a well-defined cubic morphology. The one-step synthesis yielded significantly smaller nanocubes (10.8 ± 3.3 nm) using the same reaction condition (ligand ratio of 1.5/2; 150 °C, 3 bar H_2, 48 h). This demonstrates that the two-step protocol effectively increases particle size beyond what is achievable through the direct synthesis under the same ligand and temperature conditions. Both ligand ratio and reaction time play crucial roles in tuning the final size and uniformity of the particles. The results highlight the advantages of temporal separation between nucleation and growth to yield monodisperse Fe^0 NPs for micromagnet fabrication.

1.1.d Structural and Magnetic Characterization

The Fe NPs synthesized in this part exhibit the expected properties of metallic iron. Structural analysis by X-ray diffraction (XRD) shows that these nanoparticles crystallize in the body-centered cubic (bcc) Fe^0 phase, which is characteristic of bulk iron. A representative diffractogram is shown in Figure II.6a. Furthermore, vibrating sample magnetometry (VSM) measurements performed at 300 K reveal that the nanoparticles have a saturation magnetization of 209 ± 20 $A \cdot m^2 \cdot kg^{-1}$ (Figure II.6b), which is very close to that of bulk iron (≈ 217 $A \cdot m^2 \cdot kg^{-1}$) [12]. These results confirm both the crystallinity and the metallic character of the synthesized iron nanoparticles.

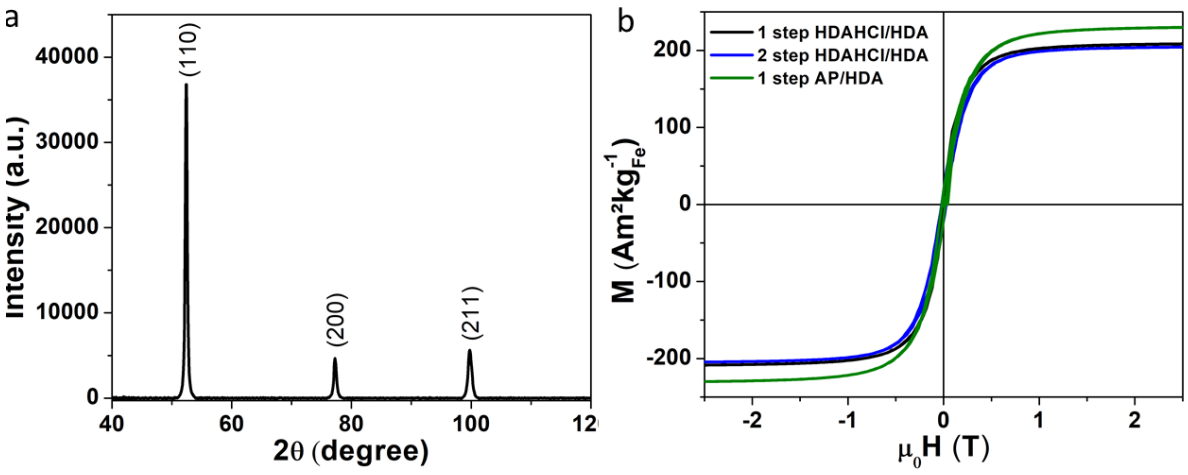

Figure II.6. (a) XRD diffractograms and (b) magnetic hysteresis loops of the different processes of Fe nanoparticles synthesis.

1.2 Synthesis of iron-cobalt (FeCo) nanoparticles

This synthesis of FeCo NPs is directly derived from the iron nanoparticles one. It involves the co-decomposition of organometallic precursors $[Fe(N(Si(CH_3)_3)_2)_2]_2$, and $\{Co(N(Si(CH_3)_3)_2)_2$,THF$\}$ under dihydrogen in the presence of a pair of long-chain acid/amine ligands. These ligands control the size, shape and stabilization of the nanoparticles. Considering the good results obtained with the two-step approach for the synthesis of Fe NPs, preliminary attempts were made for the FeCo NPs (Appendix 3). The results being not satisfactory we followed the one step synthesis approach previously reported by Cyril Garnero, and Julien Marbaix during their phD [13,14]. Two ligand systems have been proven to be effective for producing monodisperse and highly crystalline nanoparticles: palmitic acid/hexadecylamine (PA/HDA) and hexadecylammonium chloride/hexadecylamine (HDAHCl/HDA). We propose to use exclusively the HDAHCl/HDA system in this thesis, as it leads to higher synthesis yields, larger nanoparticles, and higher metal content.

The general reaction scheme is therefore described by the following chemical equation:

$$[Fe(N(Si(CH_3)_3)_2)_2]_2 + [Co(N(Si(CH_3)_3)_2)_2].THF + X\ HDA + Y\ HDAHCl \xrightarrow[Mesitylene]{150°C,\ 3bar\ H_2,\ 24h} FeCo\ NPs$$

The synthesis relies on the co-decomposition of 40 mM of a 1:1 mixture of the organometallic precursors FeNSi and CoNSi, dissolved in mesitylene along with the HDAHCl/HDA. First, the solution is heated at 150 °C for 1 hour in an oil bath to ensure the complete solubilization of HDAHCl. Then, the solution is placed under pressure (3 bars of H_2) and kept at 150°C for 24h.

This protocol leads to the formation of monodisperse and crystalline FeCo nanoparticles. This synthesis is effective but less versatile than the analogous procedure used for Fe^0 nanoparticles. Adjusting the quantity of HDAHCl and HDA can tune the particle characteristics to a limited extent. Significant deviations can lead to polydispersity, coalescence phenomena and formation of larger aggregates. In the following sections, we examine how the acid/amine ratio, and the relative proportion of iron/cobalt precursors can influence the properties of the resulting FeCo nanoparticles.

1.2.a Effect of the ammonium/amine ratio (Y/X)

The ammonium/amine ratio (HDAHCl/HDA) can be used to tune the size and shape of the resulting FeCo nanoparticles. The different experimental conditions are summarized in Table II.4. In presence of a 3/4 ligand ratio (HDAHCl/HDA), the synthesis yields monodisperse FeCo truncated octahedron nanoparticles with a size of 9.7 ± 2.2 nm (Figure II.7a). Increasing the ratio to 3.2/4 results in larger truncated octahedron of 12.5 ± 1.4 nm (Figure II.7c). This trend suggests that a slightly higher proportion of HDAHCl favors particle growth while preserving the same morphology. The reaction is dependent on the ammonium content.

Interestingly, the synthesis can also proceed in the absence of hydrogen, as previously reported by Cyril Garnero. Under an inert atmosphere of Ar, 10.5 ± 2.3 nm nanoparticles exhibiting a different morphology, cubes with rounded edges, called latter “squircle”, were obtained after 48h of reaction in presence of a HDAHCl/HDA ratio of 3/4 (figure 7b). EDX analyses performed by C. Garnero indicate that these particles are much richer in iron (~75% instead of ~50%) [15]. This compositional change may stem from the different reduction kinetics: iron precursors are reduced more rapidly than cobalt precursors in the absence of H_2. As a result, the particles tend to be Fe-rich and thus tend to adopt a cubic shape.

Ratio HDAHCl/HDA	¾	3/4	3.2/4
Atmosphere	H2	Ar	H2
Time	24h	48h	24h
Size (nm)	9.7±2.2	10.5±2.3	12.5±1.4
Shape	Truncated octahedron	Squircle	Truncated octahedron

Table II.4. Size and morphology of FeCo alloy nanoparticles obtained with different conditions.

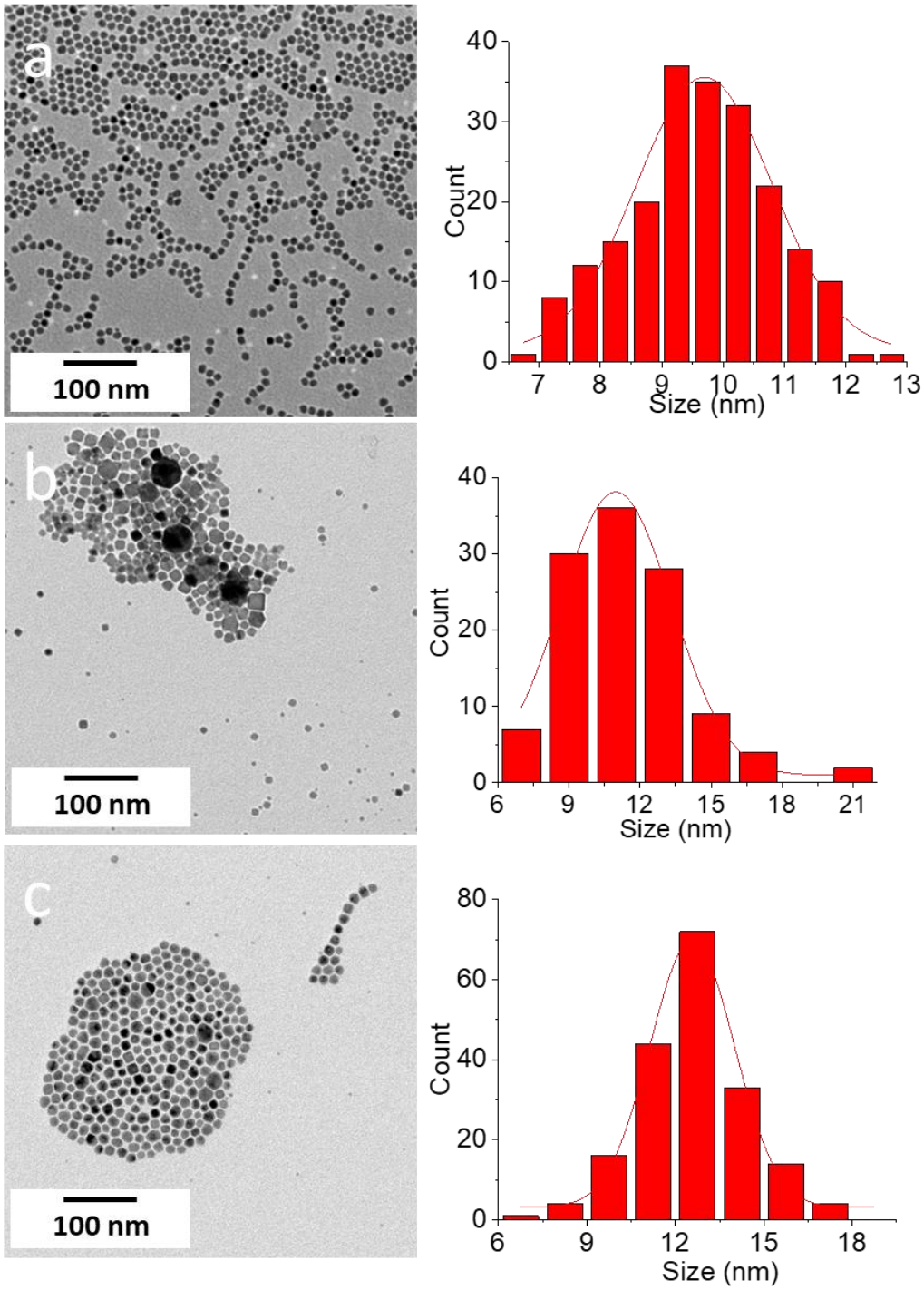

Figure II.7. TEM images with the associated size distribution of (a) FeCo_3/4, (b) FeCo_3/4_Ar, (c) FeCo_3.2/4.

1.2.b Effect of the atomic composition: $Fe_{1-x}Co_x$

To evaluate how the atomic composition affects the size and the morphology of FeCo nanoparticles, we synthesized a series of $Fe_{1-x}Co_x$ alloys by varying the Co content through the fraction of cobalt precursor introduced into the reaction. Specifically, x varied as follows: 0.11, 0.23, 0.30, 0.41, and 0.50. All syntheses were performed under identical reaction conditions to isolate the effect of the metal composition. The total metal precursor concentration was fixed to 40 mM, the metal-to-ligand ratio was maintained to 2 equiv. metals (here Fe and Co) / 7 equiv. ligands, with a ligand ratio: 3 HDAHCl / 4 HDA (Y/X = 3/4). The reaction is done in mesitylene at 150 °C for 24 h with 3 bar H_2. The different samples obtained are summarized in Table II.5.

The general reaction reads as follows:

$$2(1-x)\,\mathrm{FeNSi} + 2x\,\mathrm{CoNSi} + 3\,\mathrm{HDA} + 4\,\mathrm{HDAHCl} \xrightarrow[\substack{150°C,\ 3bar\ H_2,\ 24h \\ Mesitylene}]{} \mathrm{Fe_{1-x}Co_x\ NPs}$$

Due to a lack of time, elementary composition analysis could not be made on our sample. We will refer to the ICP-MS and EELS studies performed by J. Marbaix during his thesis which confirmed that the metal ratios in the final nanoparticles closely match the ratios of metal precursors introduced [14].

At lower Co content (x = 0.11 and 0.23), the particles are large (~17 nm), mostly cubic, but tend to show a bimodal distribution (Figure II.8a, b). Indeed, a minor population of spherical particles (~6 nm) can be seen. As the cobalt content increases (x ≥ 0.30), the average particle size decreases and the NPs are more uniform in size and shape (Figure II.8c, d) but without reaching the best results obtained for x=0.5 and described in the previous section (Figure II.7a).

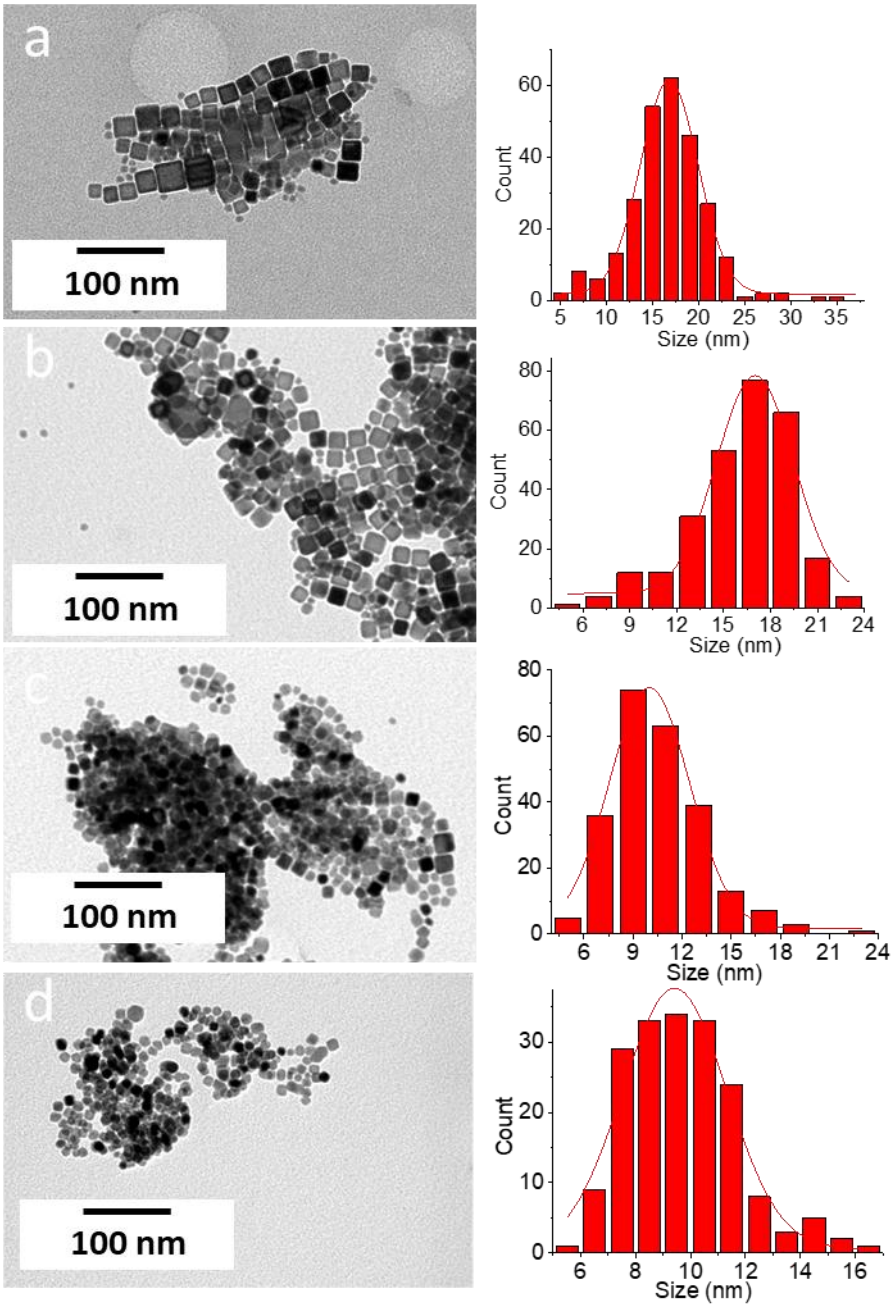

Figure II.8. TEM images with the associated size distribution of (a) $Fe_{0.89}Co_{0.11}$, (b) $Fe_{0.77}Co_{0.23}$, (c) $Fe_{0.70}Co_{0.30}$, (d) $Fe_{0.59}Co_{0.41}$.

Thus, by increasing the Co content, the particle shape shifts from cubes to squircles, and then to truncated octahedra suggesting a strong correlation between the alloy composition and the final nanoparticle morphology. The increase in cobalt content seems to favor more spherical shapes (truncated octahedra and squircles). A similar trend has been described by Karipoth *et al.* for FeCo particle prepared by the polyol synthesis [16]. The authors explained

their results by different growth direction: pure Fe particles grow so as to exposed {100} facets leading to cubic nanoparticles, while cobalt rich samples have a multidirectional growth pattern.

These findings also explain earlier observations (see section 1.2.a) where FeCo nanoparticles synthesized without H_2 appeared with a squircle shape and an estimated composition around $Fe_{0.75}Co_{0.25}$. This matches the trend here, where intermediate compositions (x ≈ 0.30) yield cubic and squircle-shaped particles of ~10 nm, consistent with the hypothesis that morphology is primarily dictated by atomic composition.

Composition ($Fe_{1-x}Co_x$)	x =0	x = 0.11	x = 0.23	x = 0.30	x = 0.41	x = 0.50
Size (nm)	10.8±3.3	16.8±3.1	17.0±2.5	10.0±2.5	9.4±1.9	9.7±2.2
Shape	Cubes	Cubes + spheroids	Cubes + few spheroids	Cubes + squircles	Squircles	Truncated octahedron
Coercive field $\mu_0 H_{c,300K}$(mT)	7	10	9	13	23	11
$M_{s,300K}$ $(A.m^2.g^{-1})$	209	212	223	242	225	221
$M_{s,300K\ bulk}$ $(A.m^2.g^{-1})$ [17]	217	225	230	245	240	232

Table II.5. Summary of the morphological and magnetic properties of the different $Fe_{1-x}Co_x$ NPs. M_s: saturation magnetization.

1.2.c Structural and Magnetic Characterization

The crystalline structure of the $Fe_{1-x}Co_x$ nanoparticles was determined by X-ray diffraction (XRD) illustrated on Figure II.9a. For all the compositions studied, the two main diffraction peaks observed with our Co source, appear at approximately 53° and 78° which correspond, respectively, to the (110) and (200) planes of a body-centered cubic (bcc) structure. Indeed, a progressive and slight shift of the (110) diffraction peak can also be observed, revealing a modification of the lattice parameters with the chemical composition

(Figure II.9b). These results confirm that all the $Fe_{1-x}Co_x$ alloys adopt the bcc solid-solution structure, in agreement with the literature [13,14].

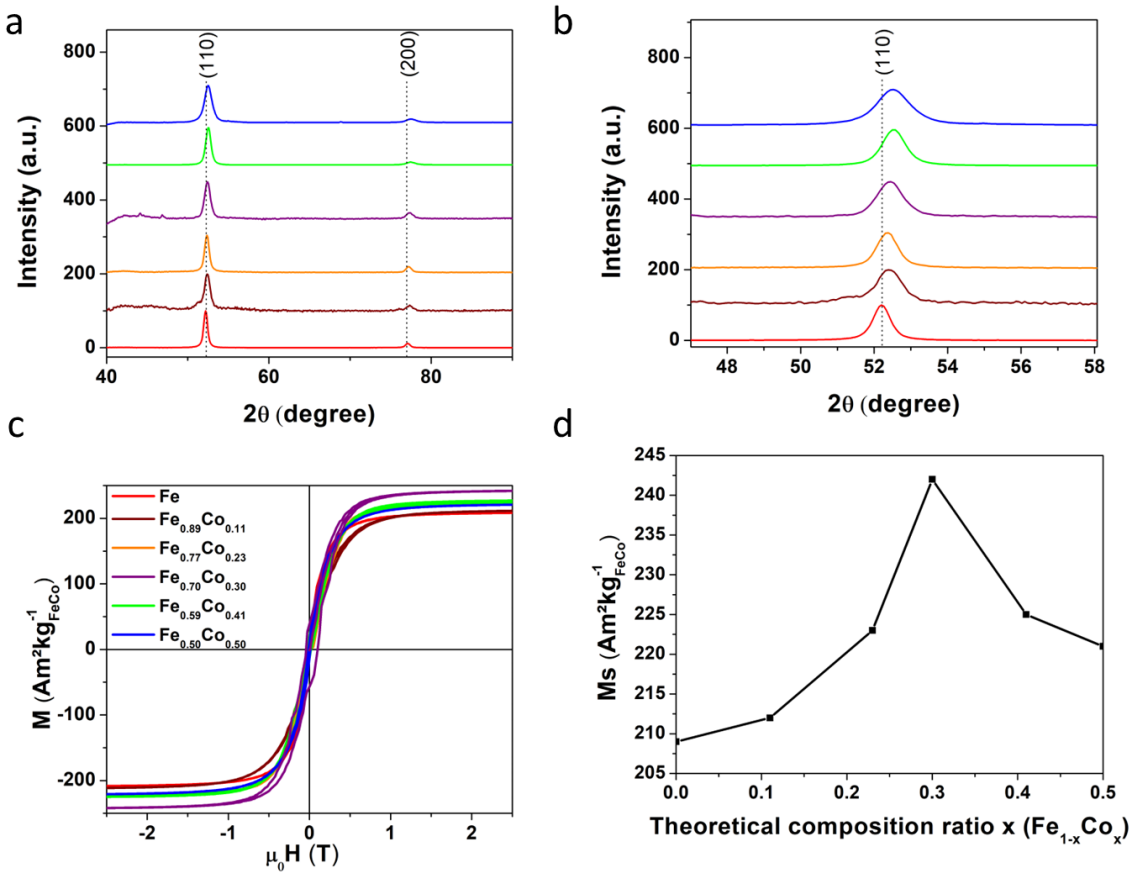

Figure II.9. (a) XRD diffractograms and (b) enlarged view on the (110) diffraction peak of Fe (red), $Fe_{0.89}Co_{0.11}$ (wine), $Fe_{0.77}Co_{0.23}$ (orange), $Fe_{0.70}Co_{0.30}$ (purple), $Fe_{0.59}Co_{0.41}$ (green) and $Fe_{0.50}Co_{0.50}$ (blue). (c) Magnetic hysteresis loops recorded at 300 K on randomly oriented powders of $Fe_{1-x}Co_x$ nanoparticles. (d) Experimental variation of the magnetic saturation as a function of the targeted $Fe_{1-x}Co_x$ composition.

The magnetic behavior of the $Fe_{1-x}Co_x$ nanoparticles was analyzed at 300 K (Figure II.9b). The coercive fields (μ_0Hc) and saturation magnetizations (Ms) measured experimentally are summarized in the Table 5 hereabove and compared with the bulk values [17]. The saturation magnetization increases gradually with cobalt content, reaching a maximum of 242 $A \cdot m^2 \cdot kg^{-1}$ at x = 0.30 ($Fe_{0.30}Co_{0.70}$). Beyond this point, Ms slightly decreases for higher cobalt fractions (x = 0.41 and 0.50), which is consistent with the bulk values reported in the literature [12,14,17].

1.3 Synthesis of iron carbide (FeC) nanoparticles

The synthesis of iron carbide (FeC) nanoparticles aims to improve the oxidation resistance of iron nanoparticles (Fe^{o} NPs) by transforming them into a more stable carbide phase. This method follows the procedures described by Alexis Bordet and Julien Marbaix, involving two key steps: (1) synthesis of monodisperse Fe^{o} nanoparticles with controlled size and shape, and (2) carbidization using a CO/H_2 atmosphere at elevated temperature and pressure [18–20] (Scheme II.1).



Scheme II.1. Schematic view of the carbidization process starting from pre-formed Fe^{0} *NPs. The reaction time allow stabilizing core shell Fe@FeC or homogeneous carbide FeC NPs.*

Fe NPs were synthesized as previously described in section 1.1.2. Nanospheres of 12.6 ± 0.7 nm and nanocubes of 19.5 ± 2.2 nm were obtained using PA/HDA ligands with a ratio of 1.2/1 and 1.5/1. (Figure II.10a-b). In a glovebox, 100 mg of the Fe^{0} NPs were transferred into the same Fischer–Porter vessel used for their synthesis. 20 mL of mesitylene was added, along with a column of 3 Å molecular sieves placed in the upper neck of the vessel (not in contact with the liquid phase). The sieves act to scavenge water released during the reaction and accelerate carbidization. The reactor was pressurized with a 3 bar CO/H_2 (1:1) gas mixture and heated at 150 °C for 48 hours for the synthesis with 13 nm particles and for 5 days with 20 nm particles, in order to achieve complete carbidization. The iron carbide nanoparticles obtained from that process are described in Table II.6.

Notably, the initial shape of the Fe^{0} nanoparticles was preserved during carbidization: the 12.6 nm Fe^{0} nanospheres yielded spherical FeC NPs of a slightly larger size (14.5 ± 1.1 nm)

(Figure II.10a, c). The 19.5 nm Fe^0 nanocubes were converted into 20.0 nm FeC NPs with a fairly similar cubic shape (Figure II.10b, d).

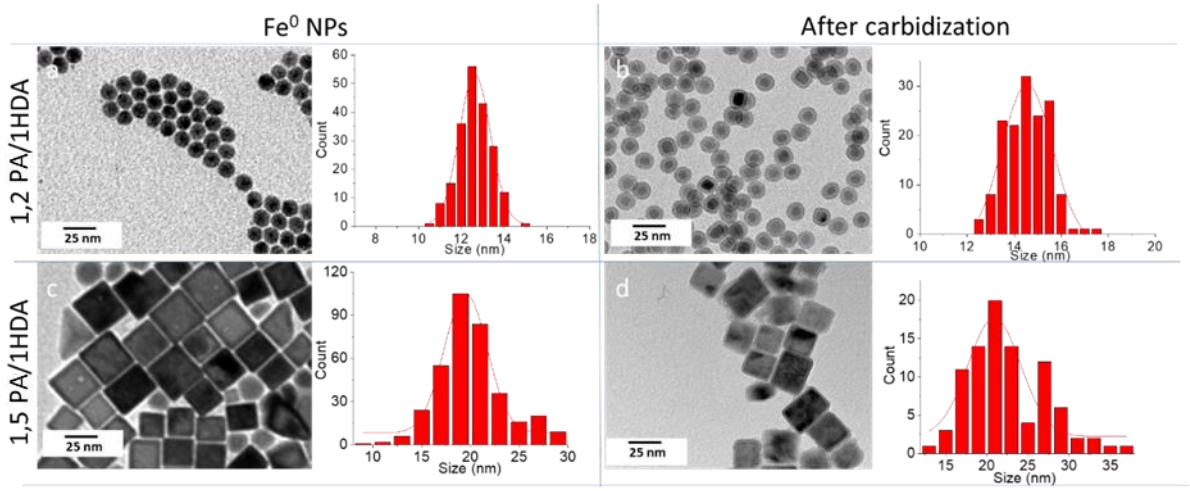

Figure II.10. TEM images with the associated size distribution of the starting Fe^0 NPs of (a) 12 and (c) 19 nm and (b,c) the resulting FeC NPs.

In the framework of the fabrication of dense micromagnets, we focused on the cubic NPs and compared their structural and magnetic properties before and after the carbidization process (Figure II.11 and Table II.6).

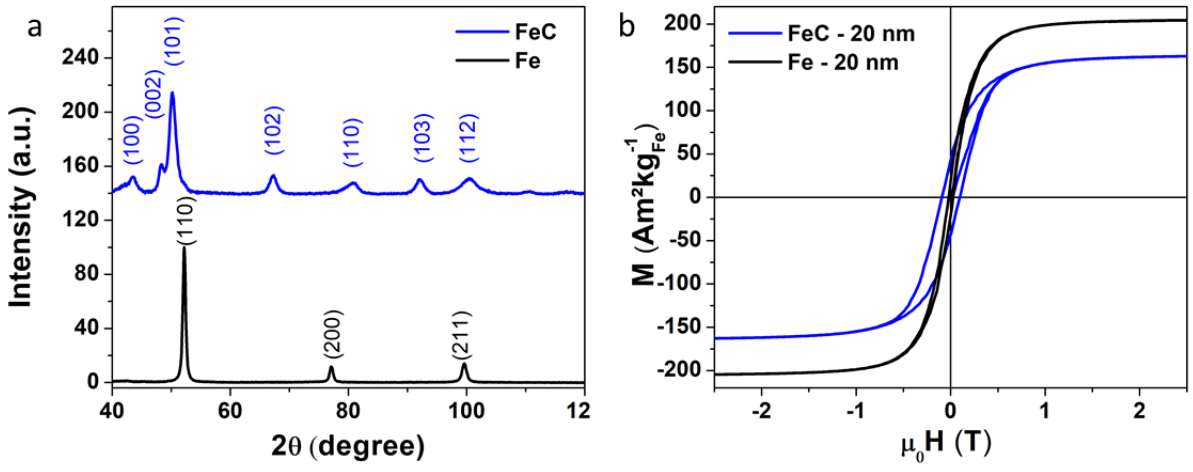

Figure II.11. (a) XRD diffractograms and (b) magnetic hysteresis loops of Fe and FeC after carbidization.

	TEM size (nm)	Crystallite size XRD (nm)	Coercive field $\mu_0 H_{c,300K}$(mT)	$M_{s,300K}(A.m^2.kg_{Fe}^{-1})$
Before carbidization	12.6 ± 0.7	10 ± 2	19	205
	19.5 ± 2.2	17 ± 1	23	205
After carbidization	14.5 ± 1.1	7 ± 2	103 [18]	170 [18]
	20.0 ± 3.1	8 ± 3	95	164

Table II.6. Structural and magnetic evolution of Fe and FeC.

After reaction under CO/H_2 (1:1) at 150 °C, the XRD diffractogram revealed a major structural transformation of the nanoparticles (Figure II.11a). The three characteristic peaks of the bcc Fe^0 phase completely disappeared. They were replaced by seven new peaks that match the pseudo-hexagonal $Fe_{2.2}C$ phase, confirming the successful conversion of Fe^0 into iron carbide (FeC). The crystallite size calculated from XRD (≈ 8 nm) is significantly smaller than the TEM particle size (≈ 20 nm), indicating that the FeC NPs are not single crystals but rather polycrystalline or consist of a crystalline core surrounded by a fairly amorphous shell. Magnetic characterization shows that carbidization leads to the decrease of the saturation magnetization M_s from 205 to 164 $A{\cdot}m^2.kg^{-1}$, and an important increase of the coercive field $\mu_o H_C$ from 23 to 95 mT (Figure II.11b). These trends are consistent with the transformation of metallic iron into a harder magnetic phase. Alexis Bordet reported a similar trend for 15 nm FeC NPs (M_S ≈ 170 $A.m^2.kg_{Fe}^{-1}$ and $\mu_o H_C$ ≈ 103 mT at 300 K) [18].

1.4 Conclusion on the NPs prepared by the organometallic approach

Fe, FeCo and FeC nanoparticles were prepared using the organometallic approach. Adjusting the ligands allows a fine tuning of the nanoparticle mean size. In view of the future fabrication of integrated micromagnets, NPs exhibiting large saturation magnetization and low coercivity are sought. While FeCo alloys clearly demonstrate the largest magnetization, Fe^0 nanocubes could be quantitatively prepared using either the direct decomposition of the FeNSi precursor in presence of fairly large PA/HDA ratio or through the two-step ripening approach in presence of HDAHCl/HDA mixture. The carbidization process which aimed at protecting the particles from oxidation could be satisfactorily performed but induced the hardening of the magnetic properties. An alternative consists in preparing larger metallic NPs and benefit from the native oxide shell which will form to act as a barrier towards further oxidation. Several alternative routes to the organometallic synthesis were reported for the large-scale synthesis of magnetic NPs with submicrometric sizes, we will report hereafter on the co-reduction using hydrazine a strong reducing agent and the polyol method.

2. Towards the synthesis of large FeCo particles

Submicronic FeCo particles were synthesized using a straightforward chemical reduction method involving hydrazine [21]. While this approach does not offer the same level of control in terms of size, structure and composition as the organometallic approach, it was selected for its simplicity, and rapid execution leading to FeCo microparticles.

All reagents used were of analytical grade and employed without further purification. The general synthesis protocol was derived from the ref [1] and reads as follows:

$$[FeSO_4 \cdot 7H_2O] + [CoCl_2 \cdot 6H_2O] + 56\ PEG_400 + 2.8\ C_6H_{12} \xrightarrow[\substack{H_2O,\ NaOH,\ N_2H_4}]{78°C,\ 30min} FeCo\ NPs$$

This synthesis consists of dissolving 0.72 g of iron(II) sulfate heptahydrate ($FeSO_4 \cdot 7H_2O$), 0.64 g of cobalt(II) chloride hexahydrate ($CoCl_2 \cdot 6H_2O$), i.e. $[Fe^{2+}] + [Co^{2+}] = 0.1$ M. The cobalt and iron salts are dissolved in presence of 6.88 g (2.8 M) of polyethylene glycol (PEG, Mw ≈ 400), and 0.8 mL (0.14 M) of cyclohexane in 50 mL of deionized water under an argon atmosphere. PEG and cyclohexane have been reported as playing the role of shaping agents: their concentration controls the morphology and the size of the particles; nanoplates being obtained without them. The mixture is sonicated for few minutes at room temperature to ensure homogeneity. It is then heated to 78 °C, temperature at which the reducing solution containing 26 mL of hydrazine monohydrate (NH_2-$NH_2 \cdot H_2O$, 85%) and 2.47 g of sodium hydroxide dissolved in 4 mL of water was added. The reaction proceeds for 30 minutes at 78 °C. The resulting black precipitate is finely collected by magnetic decantation, washed successively with acetone and ethanol, and dried under vacuum at room temperature.

Due to a lack of reproducibility when repeating the reported procedure, this synthesis route had to be modified in order to obtain particles that were homogeneous in terms of size and shape. Four different experiments were conducted varying the condition of the reducing agent addition.

First, the hydrazine solution was added without stirring. Scanning electron microscopy (SEM) revealed highly polydisperse particles with sizes ranging from 50 to 500 nm (Figure II.12a). This sample is called FeCo-Hydrazine-1. When the stirring was maintained during the addition

of the reducing agent, SEM images showed a narrower size distribution centered around ~100 nm, though large particles/agglomerates up to 500 nm were still observed (Figure II.12b). This sample is called FeCo-Hydrazine-2. In the case when the hydrazine solution was introduced using a dropping funnel to create a directed jet, particles were fairly polydisperse in size, ranging from 100 to 800 nm. This is probably due to a non-constant addition rate of the reducing solution (Figure II.12c). Finally, a dropwise addition of the hydrazine/NaOH solution through the dropping funnel was tested. SEM images revealed particles with an average size of approximately 140 nm, reduced polydispersity, though some large aggregates (~500 nm) were still present (Figure II.12d).

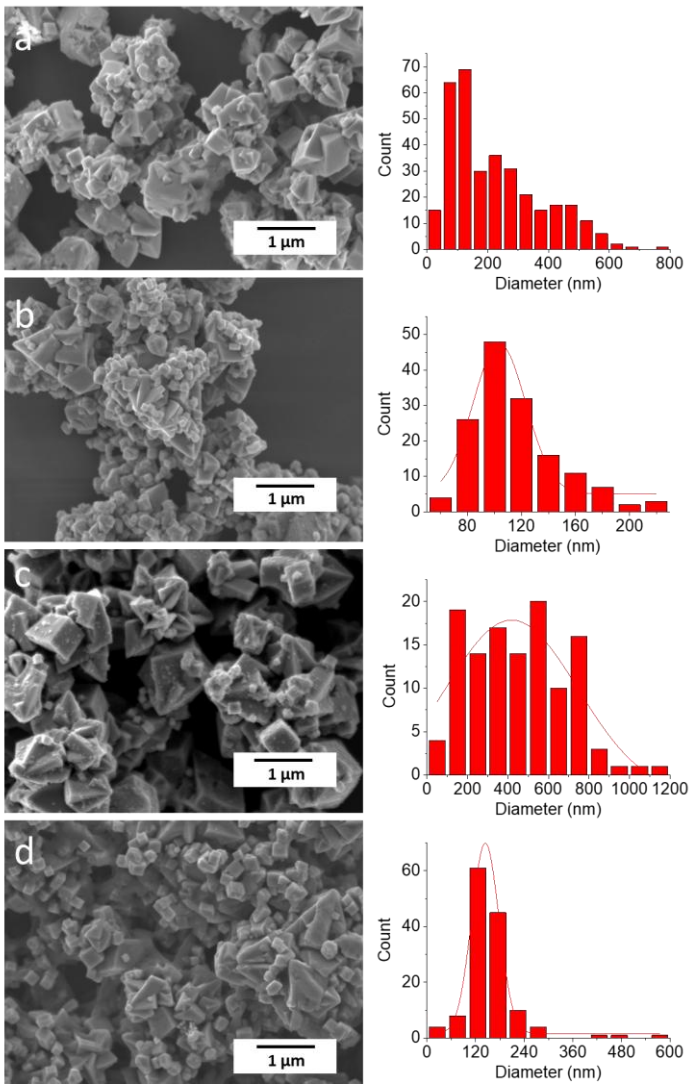

Figure II.12. TEM images with the associated size distribution of FeCo NPs obtained when hydrazine is added (a) without stirring or (b-d) while maintaining an agitation, the addition being performed (b) with a simple needle, or using a dropping funnel (c) fastly or (d) drop by drop.

These results demonstrate the critical influence of the addition rate of hydrazine on particle nucleation and growth. While this method remains relatively crude compared to more sophisticated organometallic routes, it offers a fast and accessible pathway to FeCo particles suitable for preliminary magnetic application and comparative analysis.

The particles obtained by this method are rich in metal, with a content of over 90% according to TGA measurements. X-ray diffraction analysis shows the three main diffraction peaks correspond perfectly to the (110), (200), and (211) peaks of the BCC (body-centered cubic) structure of FeCo (Figure II.13a). The absence of oxide peaks reveals that the particles obtained at the end of the synthesis are almost purely metallic. Magnetization measurements performed at 300 K allows determining the saturation magnetization (Ms), after normalizing by the metallic content of the sample considered (Figure II.13b). For all the NPs obtained, the Ms stays in the range 216 ± 20 $A.m^2.kg_{FeCo}^{-1}$ which is fairly close to the reported values for bulk $Fe_{0.5}Co_{0.5}$ alloy (232 $A.m^2.kg^{-1}$) [12].

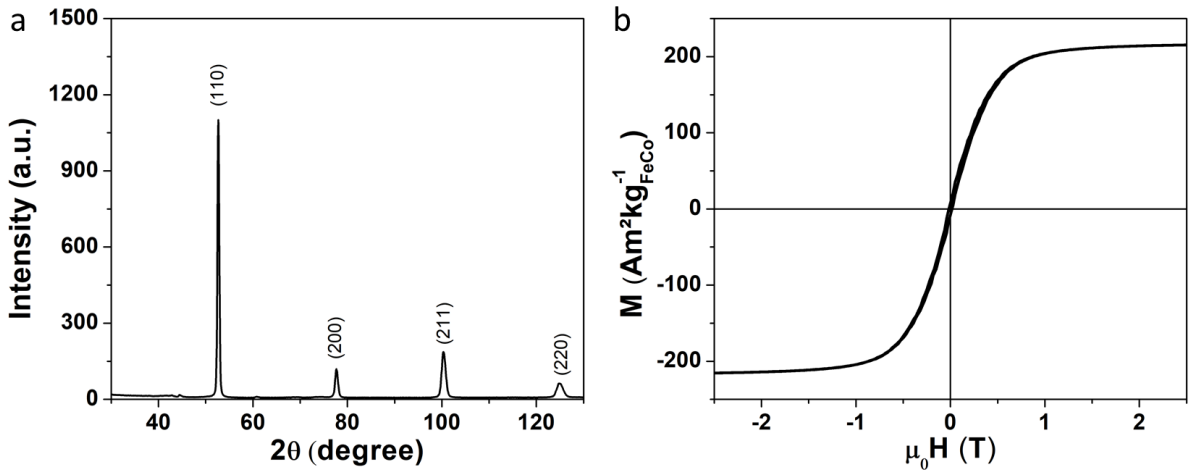

Figure II.13. (a) XRD diffractogram and (b) magnetic hysteresis loops at 300K of the FeCo NPs obtained when the hydrazine is introduced through a needle while maintaining an agitation.

To further improve the control over the particle size and lower the polydispersity, it would be interesting to implement a syringe pump system for the reducing agent addition. This setup would indeed enable precise control over the hydrazine addition rate, which is a critical parameter influencing the nucleation and growth dynamics of the particles. Such a method could potentially bridge the gap between the simplicity of this synthesis and the precision of the organometallic routes while maintaining a large mean particle size.

3. Cobalt-nickel (CoNi) polyol synthesis

The polyol synthesis route offers a versatile and large-scale method for producing magnetic particles, particularly for applications where high quantity of particles are needed, making it attractive for potential future industrial deployment. Submicronic particles are interesting to limit the deterioration of magnetic properties due to oxidation. In this approach, the polyol serves multiple roles: it acts as a high-dielectric constant solvent for dissolving the metallic precursors, as a reducing agent for the metal cations, and stabilizes the resulting particles by coordinating to their surfaces [22]. As introduced in chapter 1 section 2.2.3, the polyol approach was successfully used to produce Pt, Pd, Co, Ni-based particles… However, the reduction of iron is difficult to achieve while maintaining a good size control along with large synthesis yield [23]. Therefore, Fe-based NPs have been discarded for this study. Despite its lower magnetization, CoNi alloys have been chosen: the polyol synthesis allows indeed a fine control over the particle morphology and their chemical composition, opening a promising alternative for micromagnet fabrication, particularly in environments where long-term air stability is essential.

The synthesis of CoNi particles was carried out following the polyol process originally described by Philippe Toneguzzo and Guillaume Viau in the literature [24–28]. In this approach, several samples of $Co_{1-x}Ni_x$ particles with different sizes and compositions were produced by coprecipitation in a basic medium of 1,2-propanediol. Cobalt(II) acetate tetrahydrate and nickel(II) acetate tetrahydrate (total metal concentration [Co] + [Ni] = 0.08 M) are dissolved in 100 mL of 1,2-propanediol containing NaOH (0.2 M, 2,5 eq.). The large excess of sodium hydroxide allows promoting co-precipitation and the reduction of the precursors. Potassium tetrachloroplatinate (K_2PtCl_4), preliminary dispersed in ethyleneglycol, is used as a nucleating agent to control the size and the dispersion of the CoNi particles. The reaction mixture is heated at 185 °C under reflux for 2 hours.

$$Co[CH_3COO]_2, 4H_2O + Ni[CH_3COO]_2, 4H_2O + K_2PtCl_4 \xrightarrow[Propanediol-1,2]{185°C,\ NaOH(0.2M),\ 2h} \text{CoNi particles}$$

3.1 Size control - Heterogeneous nucleation and growth model

The CoNi particle synthesis is based on a heterogeneous nucleation mechanism, initiated by adding a small quantity of potassium tetrachloroplatinate (K_2PtCl_4) as a nucleating agent. Previous studies [29] have shown that the amount of K_2PtCl_4 added directly determines the size of the particles due to a particular nucleation-growth model. This model relies on two main assumptions. First, the size of the platinum nuclei does not depend on the amount of Pt salt introduced. Therefore, increasing the Pt concentration leads to more nuclei but not to yield larger one. Then, the second assumption is that it's a one-to-one growth, which means that each platinum nucleus leads to a single CoNi particle by atomic addition, without later coalescence. Based on those assumptions, the relationship between the CoNi particle diameter (d) and the concentration of platinum [Pt] can be expressed as [28]:

$$d = \left(\frac{6M_{CoNi} * V_{PM} * \rho_{Pt}}{\pi * \rho_{CoNi} * M_{Pt}}\right)^{\frac{1}{3}} * \left(\frac{[Pt]}{[Co+Ni]}\right)^{\frac{-1}{3}} \qquad (\text{II. } 1)$$

Where M is the molecular weight, ρ the density, and V_{PM} the volume of a nucleus of noble metal (see Appendix 4 for more details).

3.1.a Experimental results on $Co_{1-x}Ni_x$ particles

During this thesis several CoNi particles with various compositions and sizes have been synthesized, few examples being shown on Figure II.14a-d. and Figure II.15. A key experimental observation is that for each of the compositions tested, the particle diameter (d) varied linearly with the ratio of the metal concentration $\left(\frac{[PM]}{[Co+Ni]}\right)^{\frac{-1}{3}}$ in agreement with the stepwise growth mechanism. Figure II.15 shows the microscopy images of $Co_{0.50}Ni_{0.50}$ particles of different sizes for the same composition.

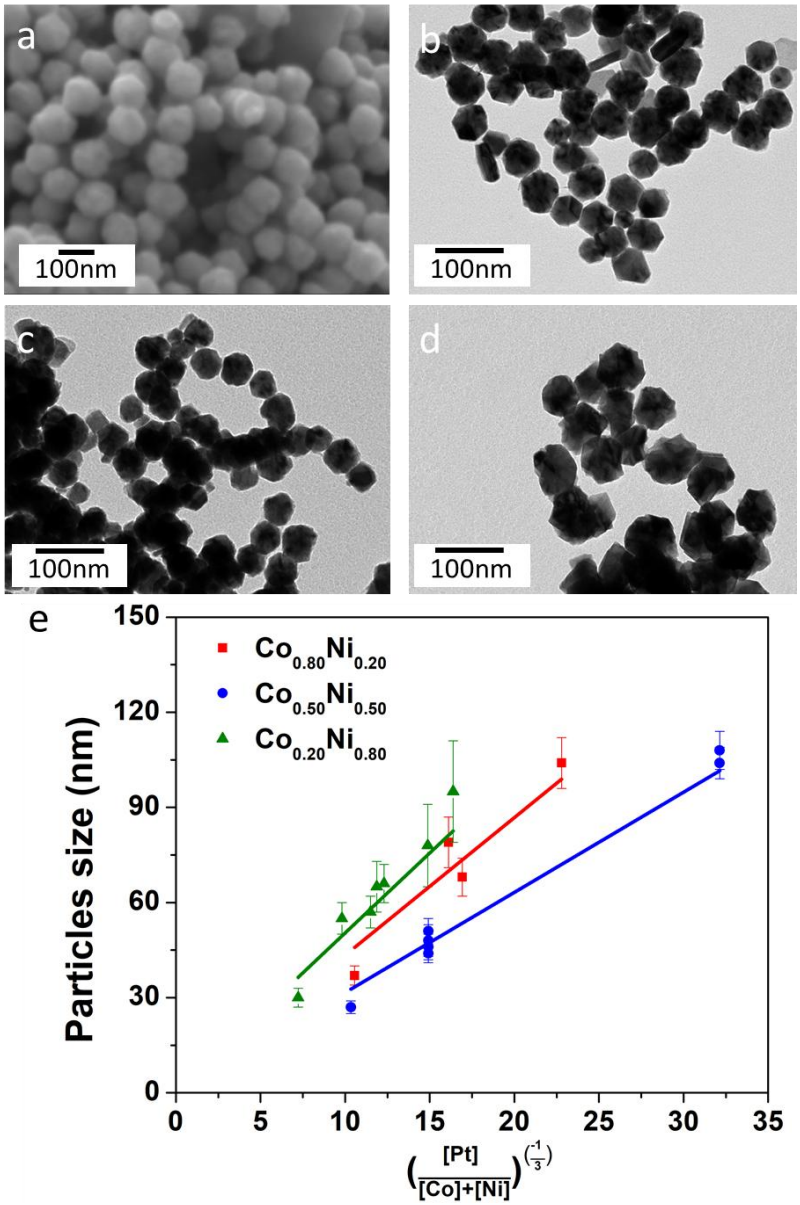

Figure II.14. (a) SEM image of $Co_{0.50}Ni_{0.50}$ (d= 104 ± 9 nm) particles. TEM images of (b) $Co_{0.50}Ni_{0.50}$ particles (d= 49 ± 6 nm), (c) $Co_{0.80}Ni_{0.20}$ (d= 42 ± 5 nm) and (d) $Co_{0.20}Ni_{0.80}$ (d= 57 ± 4 nm). Mean diameter (d) of particles prepared versus $\left(\frac{[PM]}{[Co+Ni]}\right)^{\frac{-1}{3}}$ (lines) for the three different compositions tested. (red: $Co_{0.80}Ni_{0.20}$, blue: $Co_{0.50}Ni_{0.50}$ and green: $Co_{0.20}Ni_{0.80}$)

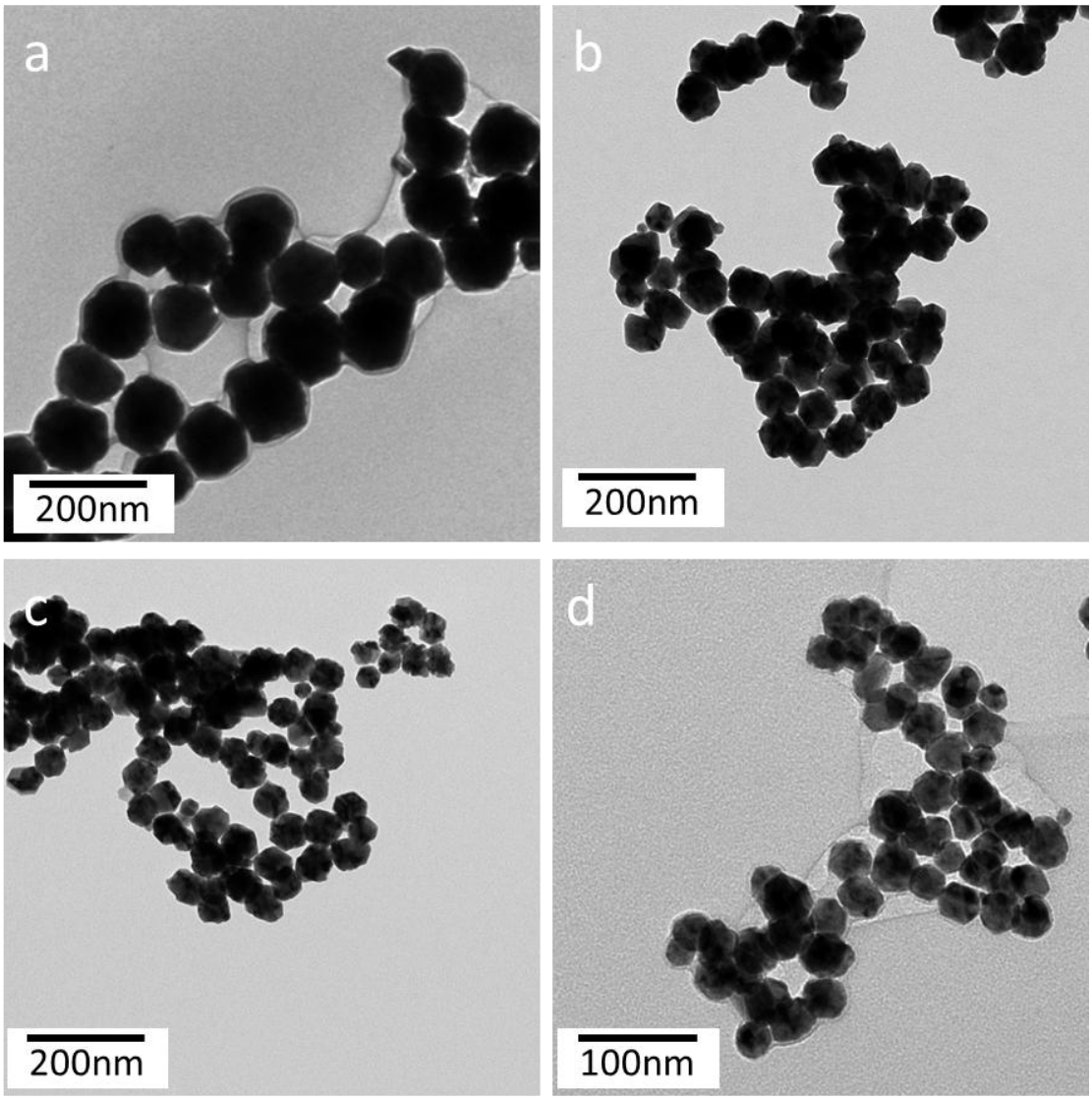

Figure II.15. TEM images of $Co_{0.50}Ni_{0.50}$ particles of different diameters of (a) d= 108 ± 11 nm, (b) d= 68 ± 7 nm (c) 53 ± 6 nm and (d) d= 31 ± 5 nm.

3.1.b Determination of the size of seeds

Considering equation II.1, one can extract the mean volume of the Pt seeds from the slope *a* of the linear fitting:

$$a = \left(\frac{6M_{CoNi} * V_{PM} * \rho_{Pt}}{\pi * \rho_{CoNi} * M_{Pt}}\right)^{\frac{1}{3}} \qquad \text{(II. 2)}$$

$$\text{so } V_{PM} = a^3 \times \frac{\pi \times \rho_{CoNi} \times M_{Pt}}{6M_{CoNi} \times \rho_{Pt}} \qquad \text{(II. 3)}$$

If we suppose that the Pt seeds have a spherical shape, we can then easily deduce their diameters : $$d_{PM} = a \times \left(\frac{\rho_{CoNi} \times M_{Pt}}{M_{CoNi} \times \rho_{Pt}}\right)^{1/3} \quad \text{(II. 4)}$$

The average platinum seed size was estimated for the three different alloy compositions and reported in Table II.7. The seed size measurements using TEM and its comparison with these estimates are addressed in the following.

Composition	Pt seed size estimated	Pt seed size measured
$Co_{0.20}Ni_{0.80}$	5.6 ± 0.6 nm	2.1 ± 0.2 nm
$Co_{0.50}Ni_{0.50}$	3.7 ± 0.6 nm	1.7 ± 0.2 nm
$Co_{0.80}Ni_{0.20}$	4.8 ± 0.6 nm	1.8 ± 0.2 nm

Table II.7. Summary of the Pt seed size estimated from the model 1 Pt seed = 1 CoNi particle and the experimental size measured by electron microscopy studies.

3.1.c Structural and chemical study of the CoNi particles

3.1.c.i X-ray diffraction study of the CoNi particles

As previously reported by P. Tonneguzzo and G. Viau, XRD analysis confirmed that the CoNi particles crystallize predominantly in a face-centered cubic (fcc) phase. The characteristic XRD pattern of $Co_{0.20}Ni_{0.80}$, $Co_{0.50}Ni_{0.50}$ and $Co_{0.80}Ni_{0.20}$ are shown in Figure II.16. For Co-rich compositions, a minor hexagonal close-packed (hcp) phase is sometimes observed (<10% by Rietveld refinement), leading to peak broadening. The crystallite size estimated by XRD remains close to 10 nm, regardless of particle size or composition, indicating that the particles are polycrystalline. A progressive and slight shift of the (311) diffraction peak can also be observed confirming a solid-solution structure similarly to the previous case for FeCo alloy.

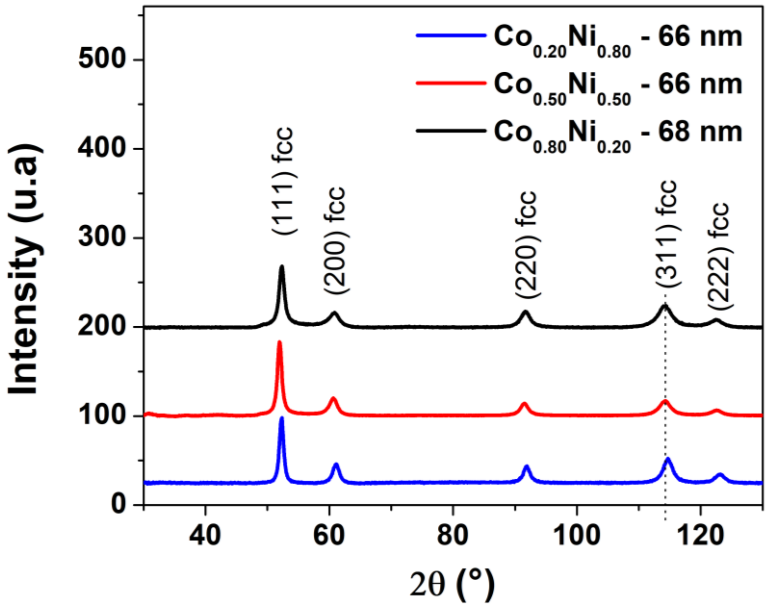

Figure II.16. XRD diffractograms of $Co_{0.20}Ni_{0.80}$, $Co_{0.50}Ni_{0.50}$, and $Co_{0.80}Ni_{0.20}$ around 66-68 nm.

3.1.c.ii Advanced microscopy study of the CoNi particles

While P. Tonegguzzo and G. Viau could not verify the model they proposed due to the resolution limitation of the electron microscopes in the 90's, we now have access to aberrated corrected microscopes which allow characterizing such complex objects. Providing that the CoNi particles were not too large (typically below 60 nm) high-angle annular dark-field (HAADF) and bright-field (BF) images could be acquired by Felipe Quiroga-Suavita at the Centre de microcaractérisation CASTAING using a JEOL ARM 200F microscope operating at 200 kV in scanning TEM mode (STEM).

HR-TEM analyses on the 53 ± 6 nm $Co_{0.50}Ni_{0.50}$ particles

HR-TEM images reported in Figure II.17 show that the NPs were polycrystalline exhibiting a face-centered cubic (fcc) structure in agreement with the XRD analysis (Figure II.17a, b). The corresponding FFT patterns could be indexed as resulting from different zone axes (<011> and <-111>, Figure II.17-c-e). The observation of Moiré fringes in some case supported the polycrystalline nature of the NP (Figure II.17f).

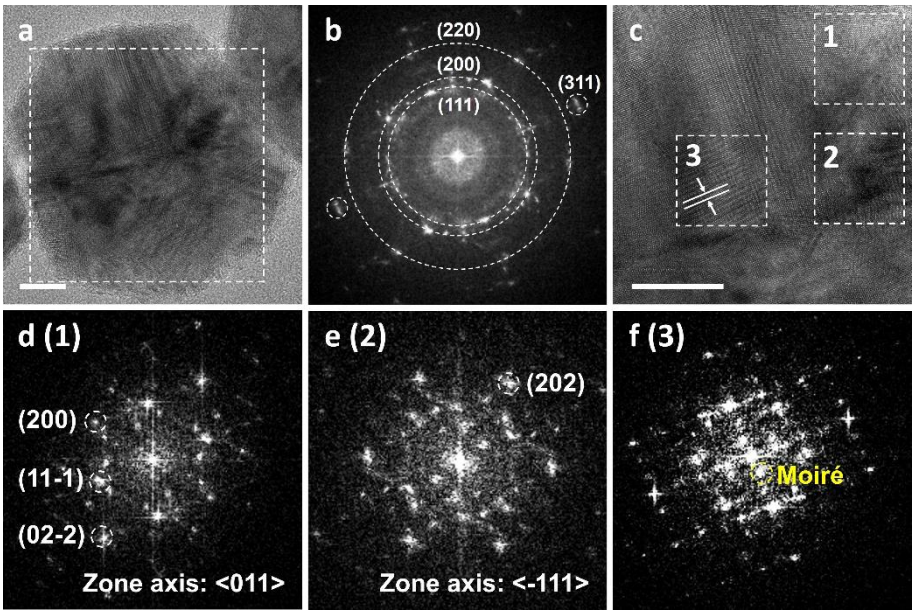

Figure II.17. HR-TEM analysis on 53 ± 6 nm $Co_{50}Ni_{50}$ NPs: (a) Micrograph of a single particle and (b) FFT pattern of the dashed square in (a). (c) Higher magnification micrograph of the same particle and (d,e) FFT patterns of (1,2) ROIs respectively. (f) FFT pattern of ROI (3) showing the presence of Moiré fringes (planes shown in (c), (scale bars = 10 nm).

Chemical study on the $Co_{0.50}Ni_{0.50}$ NPs

Starting with the smallest $Co_{0.50}Ni_{0.50}$ NPs we could prepared (31 ± 5 nm), STEM-HAADF images revealed the presence of brighter regions inside the NPs (Figure II.18d-f). The contrast in STEM-HAADF scales approximately with the square of the atomic number and with the sample thickness and therefore enable a fairly clear visualization of the Pt seeds within the CoNi matrix (Z_{Pt} = 78, Z_{Co} = 27, Z_{Ni} = 28).

Energy-dispersive X-ray spectroscopy (EDS) analysis confirms that these bright regions contain indeed platinum, while no Pt signal is detected elsewhere in the particles (figure II.18g-h).

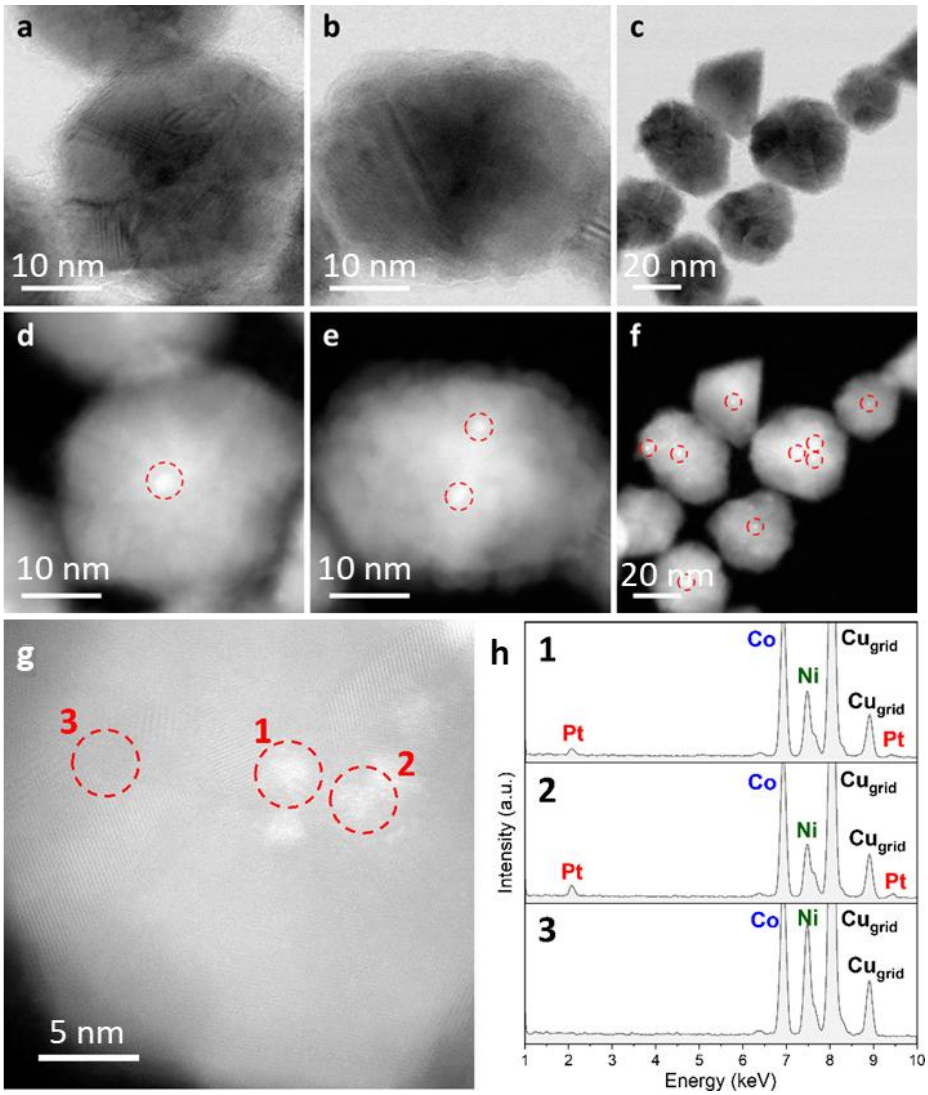

Figure II.18. STEM analyses on 31 ± 5 nm $Co_{0.50}Ni_{0.50}$ NPs: (a-c) BF-STEM and (d-f) HAADF-STEM images. Red dashed circles indicate the location of Pt seed. STEM-EDX analysis in a Pt multi-seeded NP: (g) HAADF-STEM image and (h) EDX spectra of the red dashed in (g).

Measurements across several particles showed that while the majority of the particles contained a single Pt seed (62% of the 80 $Co_{0.50}Ni_{0.50}$ NPs measured), some showed multiple seeds (Figure II.19). The Pt seeds have a mean diameter of 1.7 ± 0.1 nm, which is significantly smaller than the predicted size for this composition (3.5 ± 0.6 nm, Table II.7).

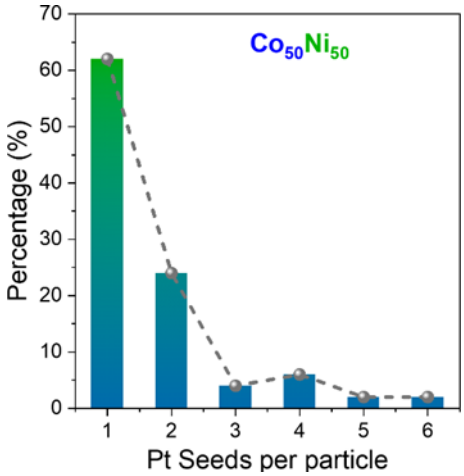

Figure II.19. Pt seed per particle counts on 31 ± 5 nm $Co_{0.50}Ni_{0.50}$ NPs.

EDS mapping and zone analysis revealed that Co and Ni were rather in a core-shell distribution than in a homogenous alloy (Figure II.20). According to the line profile analysis, the NPs exhibit a clear composition gradient: Co being highly predominantly in the core and Ni being more concentrated in the outer regions. (Figure II.20c-e). This study also supports that the Pt seed is located at the center of the particle (Figure II.20f).

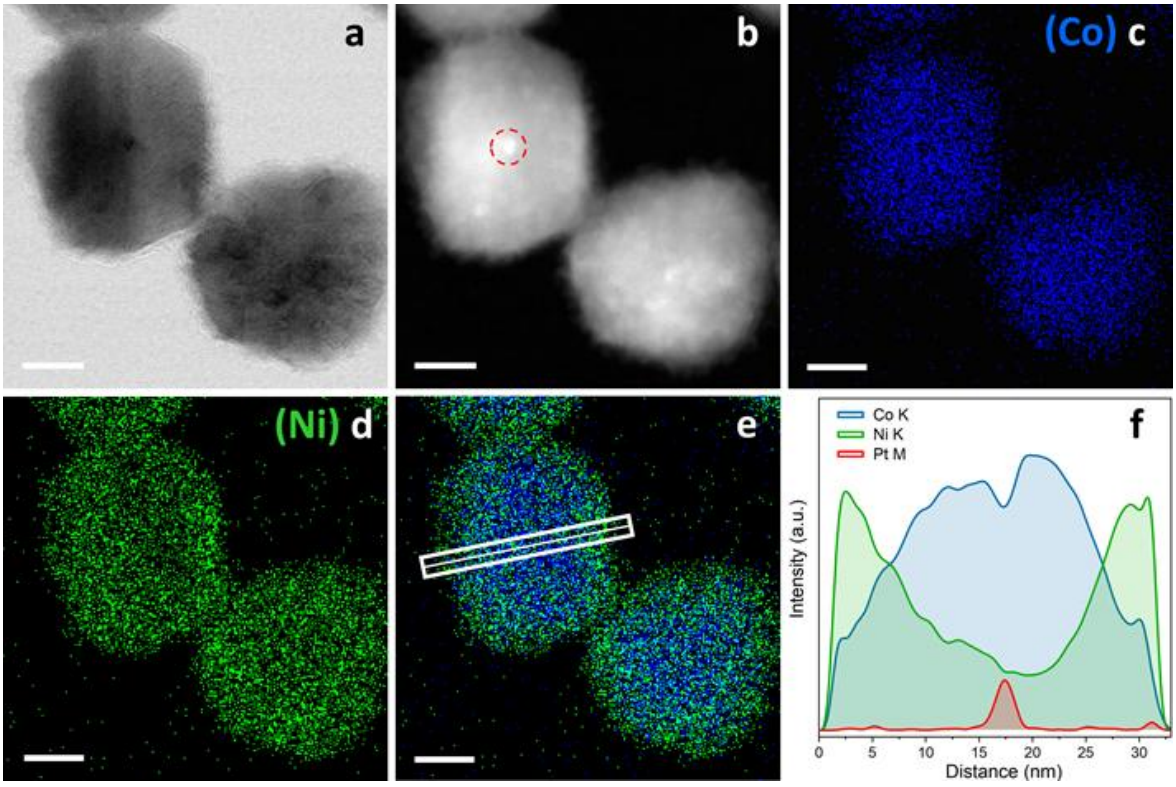

Figure II.20. STEM analyses on 31 ± 5 nm $Co_{0.50}Ni_{0.50}$ NPs: (a) BF-STEM, (b) HAADF-STEM images and STEM-EDX analysis of the sample, (c) Co (blue), (d) Ni (green), (e) overlap of Co and Ni maps (scale bars = 10 nm), and (f) Co-K, Ni-K and Pt-M line profiles along the white box in (e).

For larger $Co_{0.50}Ni_{0.50}$ NPs (53 ± 6 nm), a single Pt seed is observed at the center of each particle, with a similar mean diameter of 1.7 ± 0.2 nm (Figure II.21), confirming what the model proposed about nucleation and growth phenomena. Due to the larger size of the CoNi particles, it was not possible to detect Pt by STEM-EDX.

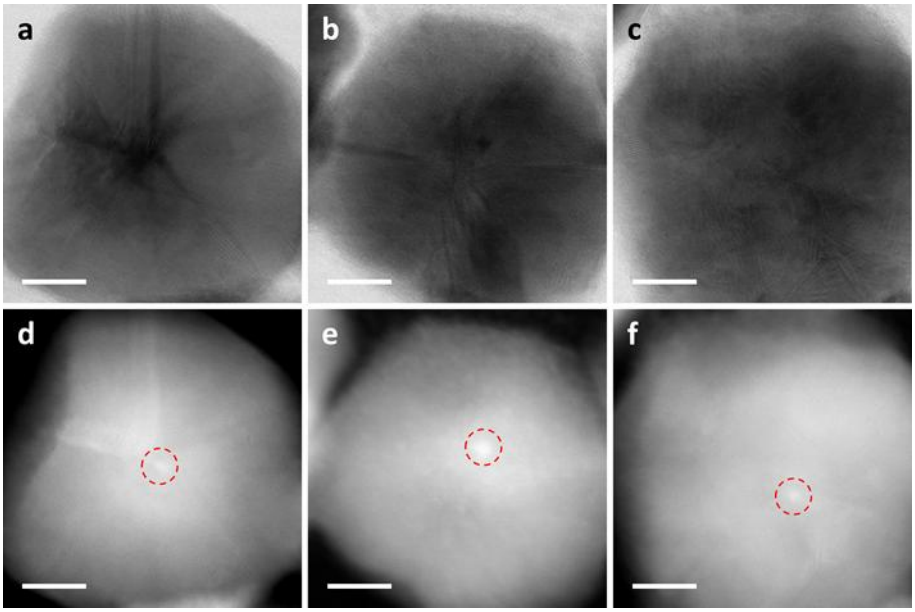

Figure II.21. STEM analyses on 53 ± 6 nm $Co_{0.50}Ni_{0.50}$ NPs: (a-c) BF-STEM and (d-f) HAADF-STEM images (scale bars = 10 nm). Red dashed circles indicate the location of Pt seed.

These observations provide direct experimental evidence supporting the nucleation–growth mechanism proposed. However, the difference with the seed size predicted by the model and the presence of multi seeds for the smaller CoNi NPs requires deeper investigation.

Chemical study on the other CoNi compositions

Complementary $Co_{0.20}Ni_{0.80}$ NPs of 57 ± 4 nm were analyzed. Elemental mappings of these Ni rich NPs displayed a thick Ni shell, Co being concentrated in the core (Figure II.22). Due to the large size of the CoNi core, the Pt seed could not be detected by STEM-EDX but were observed on STEM-HAADF images, revealing single seed at the center of each NP (Figure II.23).

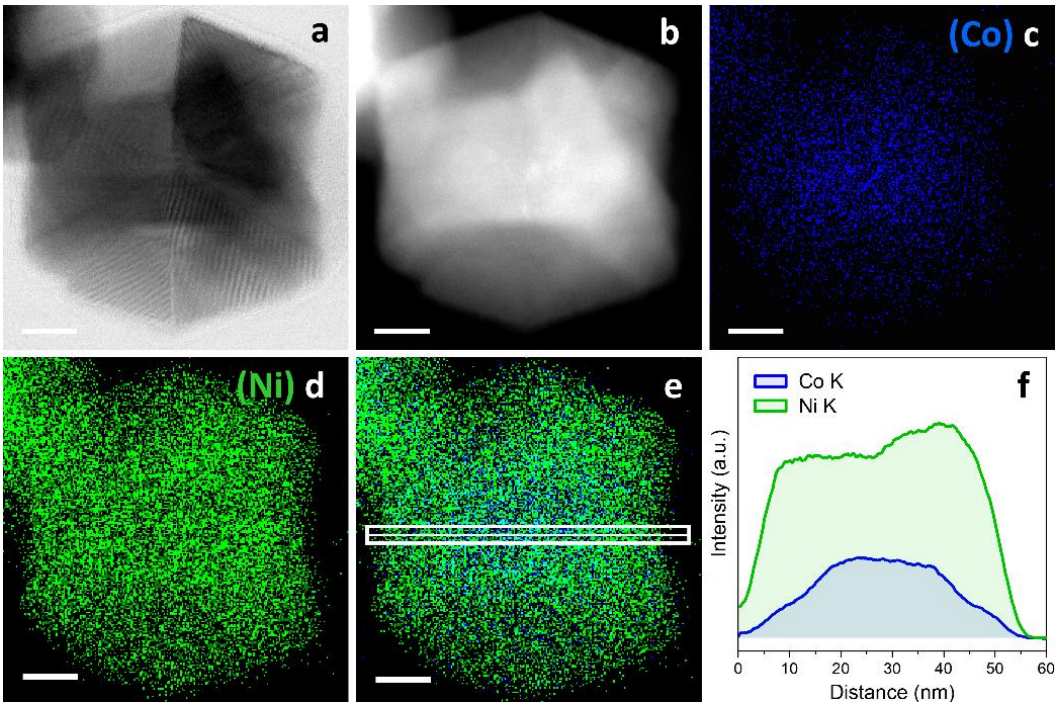

Figure II.22. STEM analyses on 57 ± 4 nm $Co_{0.20}Ni_{0.80}$ NPs: (a) BF-STEM, (b) HAADF-STEM images and STEM-EDX analysis of the sample, (c) Co (blue), (d) Ni (green), (e) overlap of Co and Ni maps (scale bars = 10 nm), and (f) Co-K and Ni-K line profiles along the white box in (e).

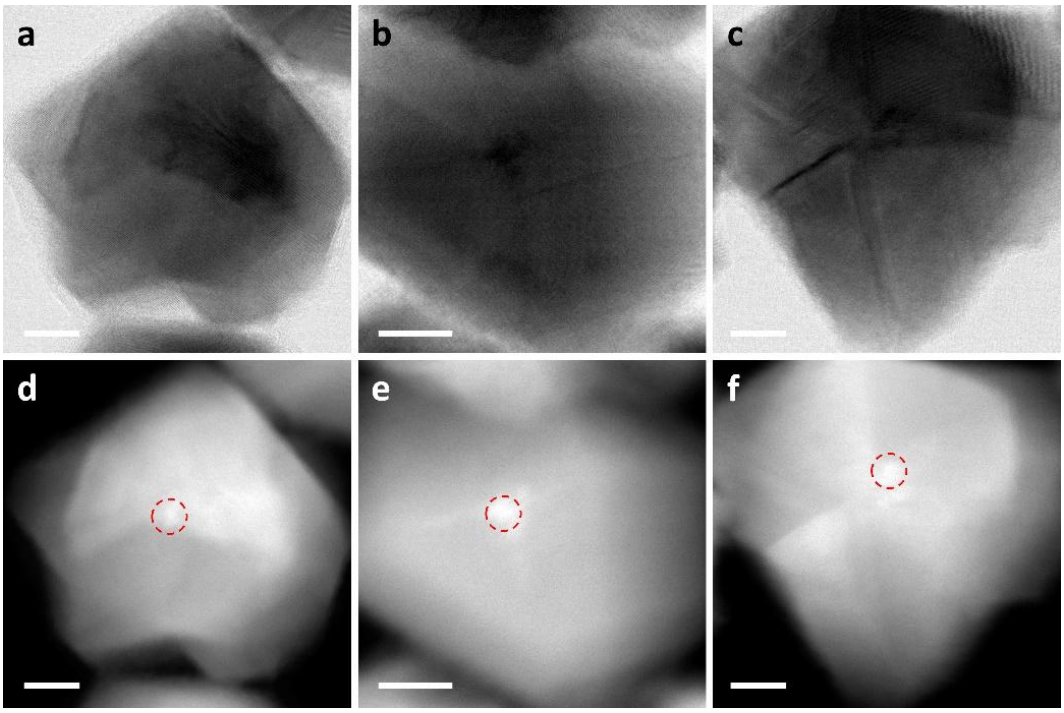

Figure II.23. STEM analyses on 57 ± 4 nm $Co_{0.20}Ni_{0.80}$ NPs: (a-c) BF-STEM and (d-f) HAADF-STEM images (scale bars = 10 nm). Red dashed circles indicate the location of Pt seed.

$Co_{0.80}Ni_{0.20}$ NPs of 42 ± 5 nm were finally investigated (Figure II.24). While most of them presented a single seed, few of them exhibit multi-seeding (Figure II.24e). No major differences were observed between single-seed and multi-seed particles based on microscopy analyses.

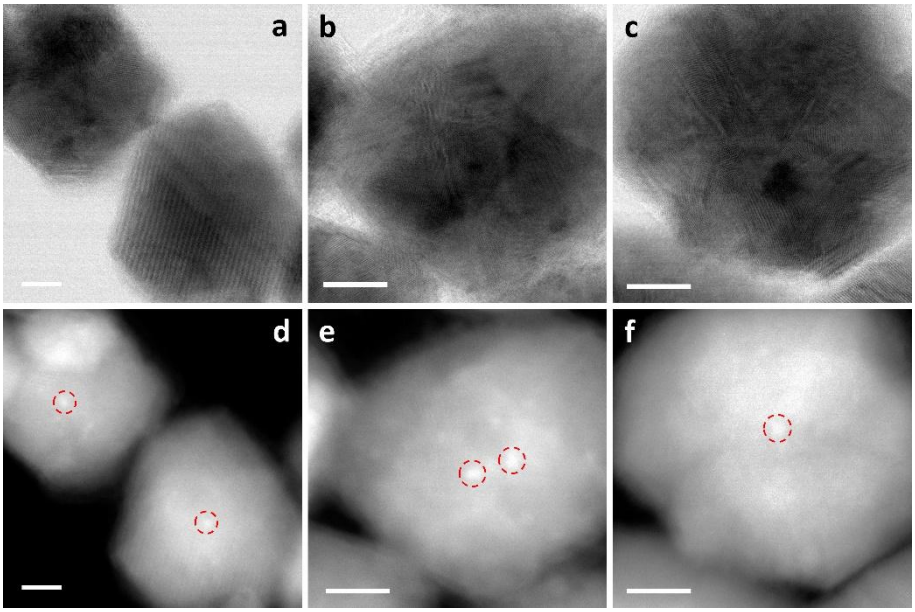

Figure II.24. STEM analyses on 42 ± 5 nm $Co_{0.80}Ni_{0.20}$ *NPs: (a-c) BF-STEM and (d-f) HAADF-STEM images (scale bars = 10 nm). Red dashed circles indicate the location of Pt seed.*

Given that in most cases it was possible to observe the Pt seed thanks to their high contrast in HAADF-STEM, the seed size was measured to compare with the proposed values from the model (5.6 ± 0.6, 3.7 ± 0.6 and 4.8 ± 0.6) nm for $Co_{0.20}Ni_{0.80}$, $Co_{0.50}Ni_{0.50}$, and $Co_{0.80}Ni_{0.20}$ respectively. The experimental sizes of the visible Pt seeds were found to be significantly smaller than the expected ones, being 2.1 ± 0.2, 1.7 ± 0.2 and 1.8 ± 0.2 nm respectively (Table II.7).

3.1.c.iii Conclusion on the chemical analysis of CoNi particles

The advanced microscopy characterization supports the nucleation–growth mechanism proposed by P. Tonneguzzo and G. Viau but also introduces a limit in the description of the first nucleation step, in particular for the smallest particles obtained. A concise mechanism model can be proposed:

1. Nucleation of the platinum seeds: Pt nuclei form early in the reaction; the number of seeds depends on the amount of Pt salt contrarily to their size which is constant (experimental proof obtained on $Co_{0.50}Ni_{0.50}$ NPs),
2. CoNi deposition: the Co precursor reduces first and deposits on the Pt nuclei, leading to a cobalt-rich core, independently of the composition. The Ni precursor reduces slowly forming a Ni -rich shell.

The discrepancy between the predicted Pt size and the one measured experimentally (Table II.7) was studied considering different hypothesis that we will briefly resume here:

- The Pt concentration indeed introduced varies significantly compared to the one wanted. We considered for that the uncertainty linked with the preparation of the K_2PtCl_4 solution and the proper volume pipetting (10%, more details in Appendix 4 part 2). We also considered that the Pt precursor could be partially hydrated (up to 3 H_2O molecules per Pt), leading to a total error of 12% on the Pt concentration. The resulting trend remains linear (Figure II.25) and corresponds to a Pt seed size of 3.5 nm rather than 3.7 nm, still far larger than the experimental one.

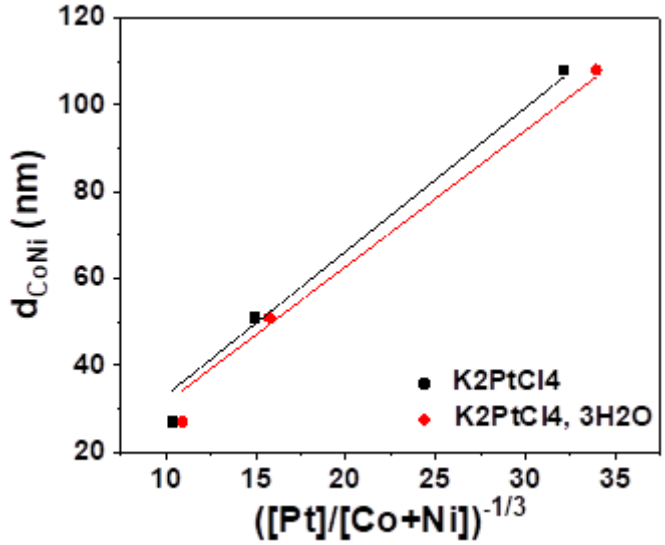

Figure II.25. Evolution of the diameter of the $Co_{0.50}Ni_{0.50}$ NPs as a function of the precursor ratio considering a fresh K2PtCl4 salt (black squares) and a hydrated one (red circles).

- More than a single Pt seed is needed to yield a CoNi NP: The experimental Pt size can only be derived from the linear fitting if 5 Pt seeds are present in each NPs (see Appendix 4). The presence of multi-seeds was indeed observed for the smallest CoNi NPs but not in such an extent.
- All the Pt seeds produced are not active. Only 20% of the seeds are catalyzing the reduction of the Co and Ni precursors and thus the growth of the NPs. This proportion remains constant, independently of the Pt concentration.

Eventhough we cannot conclude unambiguously on the mechanism involved in the growth of the CoNi NPs, this first advanced electron microscopy study gives important information. In-situ studies using X-Ray scattering would be of key interest to fully rationalize the mechanism but could not be performed during this thesis.

3.2 Magnetic properties of the CoNi particles

As previously reported by P. Tonneguzzo and G. Viau, the magnetic properties of the CoNi particles could be finely tuned by playing on the size and on the composition. To assess the

properties of the different particles synthesized in our study, the 300K hysteresis cycle of randomly oriented powders were measured using VSM magnetometry.

3.2.a Effect of the particle size: case study on the $Co_{0.50}Ni_{0.50}$ system

The magnetic measurements are shown in Figure II.26a and Table II.8. The magnetic saturation decreases slightly at smaller size (from 112 $Am^2.kg^{-1}$ at 104 nm down to 98 $Am^2.kg^{-1}$ at 31 nm). This can be due to the passivating oxide shell which forms at the NP surface. This shell has a fairly constant thickness independently of the mean core size and thus affects more significantly the magnetization at smaller size.

The coercive field is also decreasing with the size; this can be explained by the transition between the multi domain configuration, characterized by a weak coercivity, and the single domain configuration known to exhibit larger coercivity providing a size above the superparamagnetic limit (chapter 1, section 1.1).

3.2.b Effect of the chemical composition: case study on the 66-68 nm NPs

Nickel is well known for its low coercive field and its moderate magnetic saturation contrarily to cobalt which is a semi-hard magnet [12]. The effect is illustrated on the Figure II.26b for NPs of 66-68nm of different compositions. When the cobalt content increases from 20 to 80%, the coercive field increases linearly with the cobalt content, from 25 mT to 41 mT, as expected from the magnetocrystalline constant in the bulk material, while the magnetic saturation increases from 71 $Am^2.kg^{-1}$ to 132 $Am^2.kg^{-1}$[30]. The results are summarized in Table II.8.

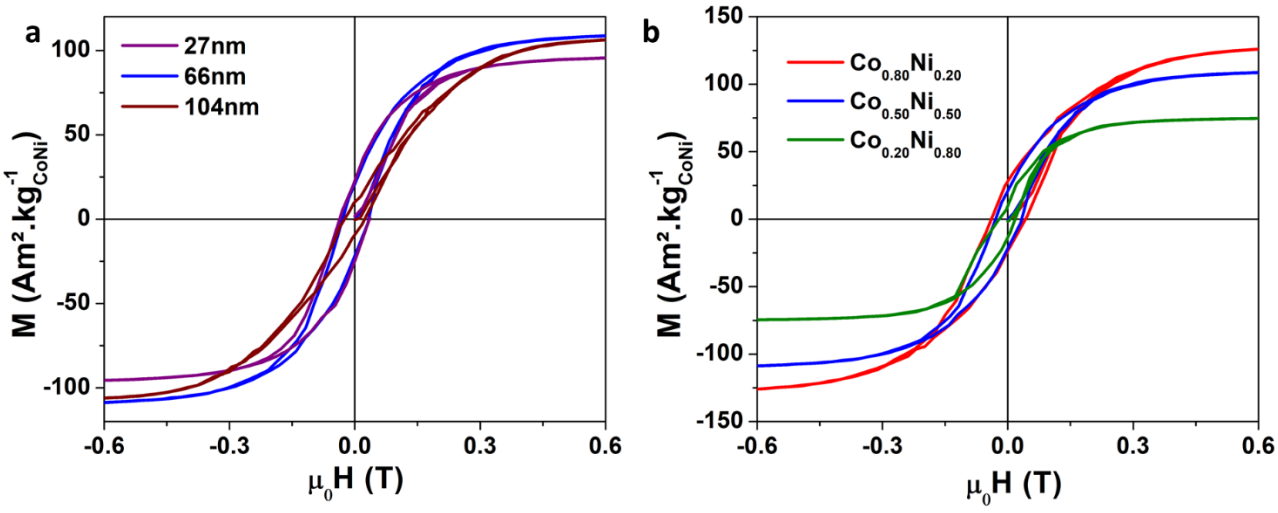

Figure II.26. Magnetic hysteresis recorded at 300K on randomly oriented powders of a) $Co_{0.50}Ni_{0.50}$ particles of 27 (violet), 66 (blue) and 104 nm (brown) and b) 66 to 68 nm NPs of $Co_{0.50}Ni_{0.50}$ (blue), $Co_{0.80}Ni_{0.20}$ (red) and $Co_{0.20}Ni_{0.80}$ (green).

Chemical composition	Size (nm)	Coercive field $\mu_0 H_{c,300K}$(mT)	$M_{s,300K}(A.m^2.kg^{-1})$ Experimental value	$M_{s,300K}(A.m^2.kg^{-1})$ bulk [17]
$Co_{0.50}Ni_{0.50}$	31 ± 5	36	98	112
	66 ± 7	32	112	112
	104 ± 5	24	110	112
$Co_{0.20}Ni_{0.80}$	66 ± 11	25	71	78
$Co_{0.80}Ni_{0.20}$	68 ± 11	41	132	142

Table II.8. Magnetic properties as a function of the particle size and the chemical composition of $Co_{1-x}Ni_x$ particles.

3.3 Conclusion on the CoNi particles prepared by the polyol synthesis

CoNi nanoparticles were synthesized via a polyol process based on a heterogeneous nucleation mechanism, initiated by the addition of a small amount of potassium tetrachloroplatinate (K_2PtCl_4) as a nucleating agent. By adjusting the quantity of the nucleating precursor, the particle size could be finely tuned from approximately 20 nm to over 100 nm.

The resulting nanoparticles exhibited a distinct compositional gradient, with cobalt predominantly concentrated in the core and nickel enriched in the outer regions. The study

further indicates that the platinum seed is located at the center of each particle. For particles larger than 40 nm, nearly all were found to originate from a single seed, while smaller particles were also predominantly single-seeded.

HRTEM measurements revealed that the visible Pt seeds were significantly smaller than those predicted by theoretical models.

By varying both the composition and size of the CoNi nanoparticles, their magnetic properties, specifically coercivity and magnetic saturation can be effectively tuned. This demonstrates precise control over static magnetic behavior through coordinated adjustment of composition and particle size.

4. Conclusion

In summary, this chapter has demonstrated the versatility and complementarity of several chemical routes for the synthesis of magnetic nanoparticles, each offering distinct advantages depending on the targeted material properties and application constraints. The reduction by hydrazine provided a simple and rapid means of producing FeCo particles, with limited control over size distribution.

The organometallic approaches have been highly effective in tailoring the nanoparticle size, shape, and composition, thereby enabling a fine adjustment of their magnetic properties. Through systematic variation of ligand pairs, acid/amine ratios, and reaction parameters, Fe and FeCo nanoparticles with well-defined morphologies were obtained, while the ripening strategies allowed to further extend the size control. Moreover, post-synthetic carbidization of iron nanoparticles successfully yielded FeC phases with enhanced stability against oxidation, thus addressing a key limitation of metallic nanoparticles while under atmosphere.

Finally, the polyol synthesis of CoNi particles highlighted a scalable route to submicronic particles, governed by a heterogeneous nucleation-growth mechanism, and enabling fine-tuning of the static magnetic properties through both composition and particle size.

Altogether, these results establish a comprehensive toolkit of synthesis strategies that can be leveraged to engineer magnetic nanoparticles with optimized characteristics for integration into planar microsystems. The ability to deliberately control the morphology, the composition, and the magnetic response represents the preliminary crucial step for the development of efficient micromagnets made of nanoparticles for advanced inductor core applications. In the next chapter, these nanoparticles are assembled into micromagnets by magnetophoresis. In addition to describing the structural assembly, the objective is also to define its control thanks to understanding the mechanisms governing the micromagnet formation.

5. References

[1] Philippot K, Chaudret B. Organometallic approach to the synthesis and surface reactivity of noble metal nanoparticles. Comptes Rendus Chim 2003;6:1019–34. https://doi.org/10.1016/j.crci.2003.07.010.

[2] Chaudret B. Organometallic approach to nanoparticles synthesis and self-organization. Comptes Rendus Phys 2005;6:117–31. https://doi.org/10.1016/j.crhy.2004.11.008.

[3] Amiens C, Chaudret B, Ciuculescu-Pradines D, Collière V, Fajerwerg K, Fau P, et al. Organometallic approach for the synthesis of nanostructures. New J Chem 2013;37:3374. https://doi.org/10.1039/c3nj00650f.

[4] Estrader M, Soulantica K, Chaudret B. Organometallic Synthesis of Magnetic Metal Nanoparticles. Angew Chem Int Ed 2022;61. https://doi.org/10.1002/anie.202207301.

[5] Margeat O, Dumestre F, Amiens C, Chaudret B, Lecante P, Respaud M. Synthesis of iron nanoparticles: Size effects, shape control and organisation. Prog Solid State Chem 2005;33:71–9. https://doi.org/10.1016/j.progsolidstchem.2005.11.002.

[6] Lacroix L-M, Lachaize S, Falqui A, Respaud M, Chaudret B. Iron Nanoparticle Growth in Organic Superstructures. J Am Chem Soc 2009;131:549–57. https://doi.org/10.1021/ja805719c.

[7] Ramirez E, Eradès L, Philippot K, Lecante P, Chaudret B. Shape Control of Platinum Nanoparticles. Adv Funct Mater 2007;17:2219–28. https://doi.org/10.1002/adfm.200600633.

[8] Meffre A, Lachaize S, Gatel C, Respaud M, Chaudret B. Use of long chain amine as a reducing agent for the synthesis of high quality monodisperse iron(0) nanoparticles. J Mater Chem 2011;21:13464. https://doi.org/10.1039/c1jm12127h.

[9] Lacroix L-M. Nanoparticules de fer de taille contrôlée pour l'hyperthermie : Synthèse par voie organométallique, caractérisations magnétiques et mesures de puissance dissipée. Univeristé de Toulouse, 2008.

[10] Lacroix L, Meffre A, Gatel C, Fazzini P, Lachaize S, Respaud M, et al. Nanoparticle Ripening : A Versatile Approach for the Size and Shape Control of Metallic Iron Nanoparticles. ChemPlusChem 2019;84:302–6. https://doi.org/10.1002/cplu.201800665.

[11] Lacroix L-M, Lachaize S, Falqui A, Blon T, Carrey J, Respaud M, et al. Ultrasmall iron nanoparticles: Effect of size reduction on anisotropy and magnetization. J Appl Phys 2008;103:07D521. https://doi.org/10.1063/1.2837625.

[12] Coey JMD. Magnetism and magnetic materials. Paperback edition. Cambridge New York Port Melbourne: Cambridge University Press; 2018.

[13] Garnero C, Lepesant M, Garcia-Marcelot C, Shin Y, Meny C, Farger P, et al. Chemical Ordering in Bimetallic FeCo Nanoparticles: From a Direct Chemical Synthesis to Application As Efficient High-Frequency Magnetic Material. Nano Lett 2019;19:1379–86. https://doi.org/10.1021/acs.nanolett.8b05083.

[14] Marbaix J, Mille N, Lacroix L-M, Asensio JM, Fazzini P-F, Soulantica K, et al. Tuning the Composition of FeCo Nanoparticle Heating Agents for Magnetically Induced Catalysis. ACS Appl Nano Mater 2020;3:3767–78. https://doi.org/10.1021/acsanm.0c00444.

[15] Garnero C. Synthèse organométallique de nanoparticules de FeCo pour l'intégration sur inductance n.d.

[16] Karipoth P, Thirumurugan A, Justin Joseyphus R. Synthesis and magnetic properties of flower-like FeCo particles through a one pot polyol process. J Colloid Interface Sci 2013;404:49–55. https://doi.org/10.1016/j.jcis.2013.04.041.

[17] Cullity BD, Graham CD. Introduction to magnetic materials. Second edition. Piscataway: IEEE Press; 2009. https://doi.org/10.1002/9780470386323.
[18] Bordet A, Lacroix L, Fazzini P, Carrey J, Soulantica K, Chaudret B. Magnetically Induced Continuous CO_2 Hydrogenation Using Composite Iron Carbide Nanoparticles of Exceptionally High Heating Power. Angew Chem Int Ed 2016;55:15894–8. https://doi.org/10.1002/anie.201609477.
[19] Bordet A, Landis RF, Lee Y, Tonga GY, Asensio JM, Li C-H, et al. Water-Dispersible and Biocompatible Iron Carbide Nanoparticles with High Specific Absorption Rate. ACS Nano 2019;13:2870–8. https://doi.org/10.1021/acsnano.8b05671.
[20] Asensio JM, Marbaix J, Mille N, Lacroix L-M, Soulantica K, Fazzini P-F, et al. To heat or not to heat: a study of the performances of iron carbide nanoparticles in magnetic heating. Nanoscale 2019;11:5402–11. https://doi.org/10.1039/C8NR10235J.
[21] Wei X-W, Zhu G-X, Liu Y-J, Ni Y-H, Song Y, Xu Z. Large-Scale Controlled Synthesis of FeCo Nanocubes and Microcages by Wet Chemistry. Chem Mater 2008;20:6248–53. https://doi.org/10.1021/cm800518x.
[22] Fiévet F, Ammar-Merah S, Brayner R, Chau F, Giraud M, Mammeri F, et al. The polyol process: a unique method for easy access to metal nanoparticles with tailored sizes, shapes and compositions. Chem Soc Rev 2018;47:5187–233. https://doi.org/10.1039/C7CS00777A.
[23] Viau G, Fiévet-Vincent F, Fiévet F. Monodisperse iron-based particles: precipitation in liquid polyols. J Mater Chem 1996;6:1047–53. https://doi.org/10.1039/JM9960601047.
[24] Toneguzzo P. CoNi and FeCoNi fine particles prepared by the polyol process: Physico-chemical characterization and dynamic magnetic properties n.d.
[25] Viau G. Nucleation and growth of bimetallic CoNi and FeNi monodisperse particles prepared in polyols. Solid State Ion 1996;84:259–70. https://doi.org/10.1016/0167-2738(96)00005-7.
[26] Fievet F, Lagier JP, Figlarz M. Monodisperse Métal Powders in Micrometer and Submicrometer Sizes by the Polyol Process n.d.
[27] Viau G, Toneguzzo P, Pierrard A, Acher O, Fiévet-Vincent F, Fiévet F. Heterogeneous nucleation and growth of metal nanoparticles in polyols. Scr Mater 2001;44:2263–7. https://doi.org/10.1016/S1359-6462(01)00752-7.
[28] Toneguzzo P, Viau G, Acher O, Fiévet-Vincent F, Fiévet F. Monodisperse Ferromagnetic Particles for Microwave Applications. Adv Mater 1998;10:1032–5. https://doi.org/10.1002/(SICI)1521-4095(199809)10:13%253C1032::AID-ADMA1032%253E3.0.CO;2-M.
[29] Toneguzzo P, Viau G, Acher O, Fiévet-Vincent F, Fiévet F. Monodisperse Ferromagnetic Particles for Microwave Applications. Adv Mater 1998;10:1032–5. https://doi.org/10.1002/(SICI)1521-4095(199809)10:13%253C1032::AID-ADMA1032%253E3.0.CO;2-M.
[30] Hall RC. Single Crystal Anisotropy and Magnetostriction Constants of Several Ferromagnetic Materials Including Alloys of NiFe, SiFe, AlFe, CoNi, and CoFe. J Appl Phys 1959;30:816–9. https://doi.org/10.1063/1.1735247.

Chapter III. Assembly of nanoparticles into submillimeter magnets

Summary of Chapter III

1 Methods for preparing and analyzing samples 126

1.1 Sample preparation 126

1.1.a Assembly in solution: in-situ studies 127

1.1.b Assembly on support 127

1.1.c Magnetophoresis-driven assembly on microchips 128

1.2 Structural analyses 129

1.2.a Introduction to SAXS 129

1.2.b Analysis of anisotropic 2D SAXS image 132

1.2.c Experimental procedure 133

1.3 Random close pack assemblies of particles 135

1.3.a Assemblies of CoNi particles 135

2 Assemblies of FeCo NPs **138**

3 Ordered assemblies of nanoparticles: the case of nanocubes **140**

3.1 Characterization of the different nanocubes used 140

3.2 Characterization of the micromagnet obtained by magnetophoresis 140

3.3 Characterization of the assemblies in solution 143

3.3.a Assembly formed under 100 mT 143

3.3.b Effect of the magnetic field amplitude 145

3.4 Characterization of thin films 147

3.4.a Assembly of 20nm FeCo nanocubes 147

3.4.b Assembly of 11nm Fe nanocubes 148

4 Mechanism investigation **151**

4.1 Effect of the NP shape on the thin film assembly 151

4.2 Effect of the magnetic field on the thin film assembly 153

4.3 Effect of the polydispersity 155

4.4 Other parameters (concentration, solvent) 156

4.5 Proposed mechanism 159

5 Conclusion **162**

6 References **163**

Following the synthesis of magnetic nanoparticles (NPs), their integration into micro-components such as for radiofrequency (RF) applications requires the formation of dense, controlled and reproducible micromagnets with submillimetric dimensions. Indeed, to interact efficiently with such micro-devices, the magnet must be scaled to match the size of the targeted devices. It should also have controlled and reproducible structural organizations to optimize its physical properties. Therefore, developing and studying the parameters for controlling magnetic assemblies is essential for such applications.

This chapter focuses on the controlled assembly of magnetic nanoparticles into organized structures under magnetic fields, aiming to elucidate the mechanisms governing alignment, aggregation and densification. Several experimental configurations are explored to provide additional information on the influence of the external magnetic field, local field gradients and the nanoparticles used. This study is mostly based on Small Angle X Ray Scattering (SAXS) technique performed on a laboratory instrument located in LGC Toulouse, using a specially developed magnetic cell allowing for in-situ characterization of the alignment in solution; and on the SWING beamline at the SOLEIL synchrotron (Paris, France) using a microbeam configuration (μSAXS) specifically adapted for the micromagnet characterization. The SAXS data interpretation being a bit complex, we will first present the methodology used. Then, several cases studied will be presented and some trends proposed. The treatment and analysis of the entire data step is still on-going due to the large set of data acquired, resulting from the numerous experimental conditions tested, and their fairly recent acquisition. The treatment was made possible thanks to the help of Simon Cayez and Nicolas Ratel-Ramond who developed Python codes to perform all the pretreatment steps, ranging from file type conversion allowing for 2D SAXS image visualization to the integration of 1D profile through the reference subtraction.

1. Methods for preparing and analyzing samples

1.1 Sample preparation

The objective of this study is to fabricate dense, controlled, and reproducible micromagnets with submillimetric dimensions. Magnetophoretic assembly involves three main steps (Figure III.1): (i) drop-casting the nanoparticle (NP) suspension, (ii) aligning the NPs under an external magnetic field to form chains and attract them towards regions of high magnetic field gradients, and (iii) evaporating the solvent and compacting the deposit.

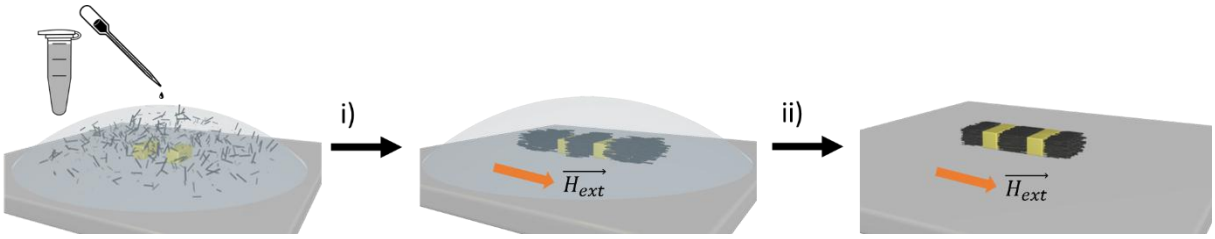

Figure III.1. Schematic view of the different steps of the magnetophoresis-driven assembly of NPs: (i) drop casting the NP suspension, (ii) alignment of the NPs under the external magnetic field resulting in chain formation and attraction toward the area of high magnetic field gradients, (iii) solvent evaporation and compaction of the deposit [1].

To gain a deeper insight into the underlying mechanisms of this process, three complementary assembly strategies under an external magnetic field were employed: (a) in solution, (b) on a solid support, and (c) on microelectronic devices thanks to magnetophoresis. Each configuration provides a distinct perspective on the assembly dynamics. Assembly in solution isolates and highlights the mechanism of nanoparticle alignment during the process. Assembly on a support reproduces this alignment while also incorporating the influence of substrate interactions and compaction during solvent evaporation. Finally, magnetophoretic assembly introduces field-gradient–driven attraction, resulting in highly localized densification between nickel blocks. Together, these approaches establish a comprehensive framework for understanding and optimizing the fabrication of submillimetric micromagnets suitable for integration into RF microdevices.

1.1.a Assembly in solution: in-situ studies

To study with in-situ SAXS the alignment behavior of nanoparticles in solution under homogeneous magnetic fields, assemblies were prepared in borosilicate glass capillaries (1.5 mm diameter). Each capillary is filled with approximately 85 µL of colloidal dispersion at a concentration of ~ 10 g_{NP}/mL and sealed with wax to limit solvent evaporation. This step can be taken in the glove box to prevent the NP oxidation. The filled capillary was then placed in a magnetic cell (Fig III.2) developed by Pierre Roblin, research engineer at LGC and expert in SAXS. This cell enables the amplitude of the applied magnetic field to be controlled by adjusting the gap between two NdFeB permanent magnets (indicated as 2 in Fig. III.2). The magnetic field is oriented perpendicular to the length of the capillary, favoring the formation of magnetic assemblies in solution at the center of the X-ray beam (see Fig. III.2b).

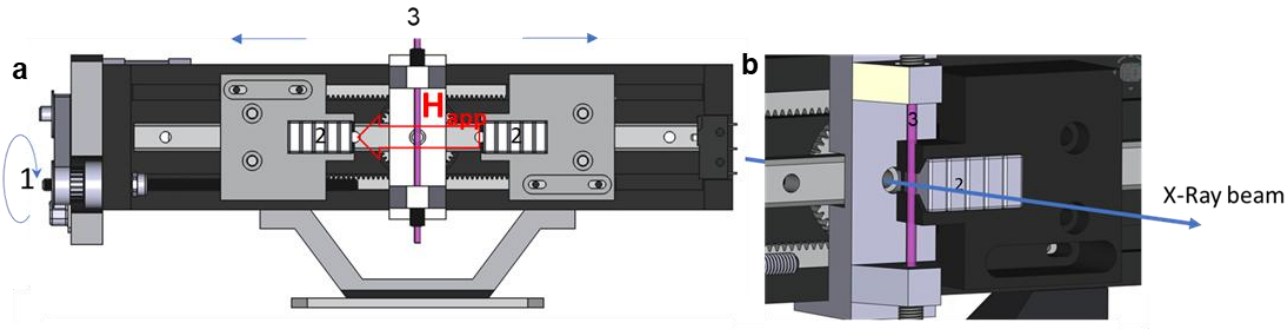

Figure III.2. a) front view of the magnetic cell used with a motor (marked 1) allowing to tune the gap between the 2 arrays of NdFeB magnets (marked 2). The capillary is placed at the center (marked 3). The blue arrows represent the translational motion of the NdFeB magnets, and the red arrows represent the magnetic field applied. b) 3D view of the capillary with the interacting X-Ray beam.

1.1.b Assembly on support (microscope glass slide)

To observe the behavior of the magnetic nanoparticle assembly on support, a second configuration was implemented using microscope glass slides (20 x 20 mm). A colloidal solution of nanoparticles (7 g_{NP}/mL) was dropped-casted (100 µL) onto the glass surface under a static magnetic field varying between 400 mT and 1T, which was generated by an

electromagnet. The sample was then left to dry in the applied field, which promoted the densification of the magnetic structure into thin films on the substrate (Figure III.3a).

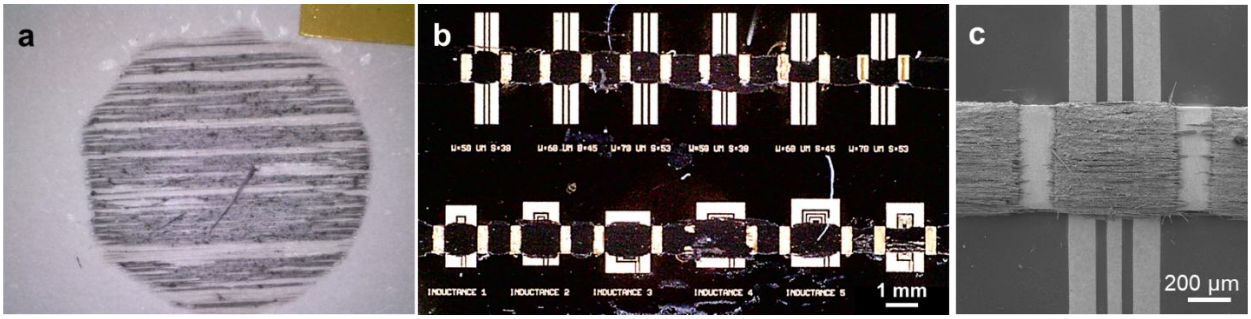

Figure III.3: Optical images of the NP assembly obtained under external magnetic field (a) on glass slide and (b) on RF characterization chip which contain Ni blocks inducing the magnetophoresis-driven assembly. (c) SEM image of a micromagnet assembled onto a CPW.

1.1.c Magnetophoresis-driven assembly on microchips

Micromagnets were obtained using the magnetophoresis-driven assembly on predefined area of a microchip. This technique leverages both an external magnetic field and directed local magnetic field gradients to localize the assembly of nanoparticles towards targeted regions thanks to nickel blocks (Fig. 1 and 3b-c).

Two types of deposition environments were studied.

Magnetophoresis under air at 1T. A chip patterned with nickel blocks was immersed in an ethanol bath positioned at the center of an electromagnet generating a uniform field $\mu_0 H$ in the range 0.5-1.0 T. Two 100µL drops of the colloidal suspension (5 g_{NP}/mL) were deposited under magnetic field on each side of the chip to ensure uniform coverage. The deposition step was repeated twice to ensure complete filling of the inter-block regions. The surface was subsequently rinsed with ethanol and dried at room temperature under the magnetic field for about 10 min to promote densification through capillary forces during solvent evaporation.

Magnetophoresis under controlled/inert atmosphere at 0.4 T. To prevent oxidation, deposition was also performed under argon in a glovebox using toluene as solvent. In this case, NPs were initially deposited in absence of external magnetic field. The field was gradually

applied by adjusting the gap between two permanent NdFeB magnets. To remove the excess of NPs, rinsing steps were performed.

1.2. Structural analyses

1.2.a Introduction to SAXS (Small-angle X-ray scattering**)**

Small-Angle X-ray Scattering (SAXS) is a reciprocal-space technique that provides a non-destructive method of investigating nanostructures in liquids and solids. It is particularly well-suited to studying nanoparticles assemblies, as it provides quantitative information on size, shape, orientation, and spatial correlation at multiple scales, without requiring crystalline order. Indeed, SAXS provides structural features with characteristic sizes between 1 and 100 nm, covering both the dimensions of the primary particles and how they organize into larger aggregates or ordered structures.

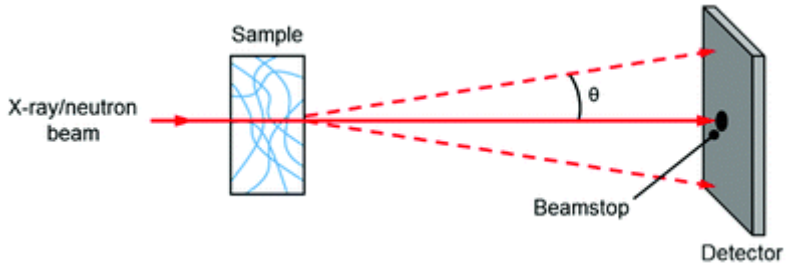

Figure III.4. Basic cartoon schematic of a small angle scattering experiment [2].

In SAXS experiments, a monochromatic X-ray beam with a wavelength λ and an incident wave vector k_i interacts with the sample (Fig. III.4). The elastically scattered radiation is recorded as a function of small scattering angles 2θ on the 2D detector. Elastically scattered signal means that there is no change in wavelength, k_s the wave vector of the scattered beam has the same modulus as k_i. The scattering vector $\vec{q} = \overrightarrow{k_s} - \overrightarrow{k_i}$ is the key analysis parameter, thanks to its relationship with θ the scattering angle, and d the interplanar distance in real space when $\vec{q}$ matches with a reciprocal vector of the probed lattice: <f

$$q = \frac{4\pi}{\lambda}\sin(\theta) = \frac{2\pi}{d} \qquad (III.1)$$

The measured scattering intensity, $I(q)$, can be decomposed into two contributions: the form factor $P(q)$, and the structure factor $S(q)$, which describes the spatial arrangement, interparticle correlations and ordering:

$$I(q) \propto P(q).S(q) \qquad (III.2)$$

The form factor $P(q)$ reflects the electron density distribution within individual particles describing their size, shape and polydispersity. In dilute systems where interparticle interactions are negligible, $S(q) \approx 1$, the scattering is dominated by the form factor $P(q)$. The structure factor $S(q)$ describes spatial arrangement, from liquid-like correlations to crystalline ordering useful to determine average interparticle distances and stacking symmetry. The experimental scattering patterns are typically collected on a two-dimensional detector, allowing both radial averaging and precise angle integration (Figure III.5).

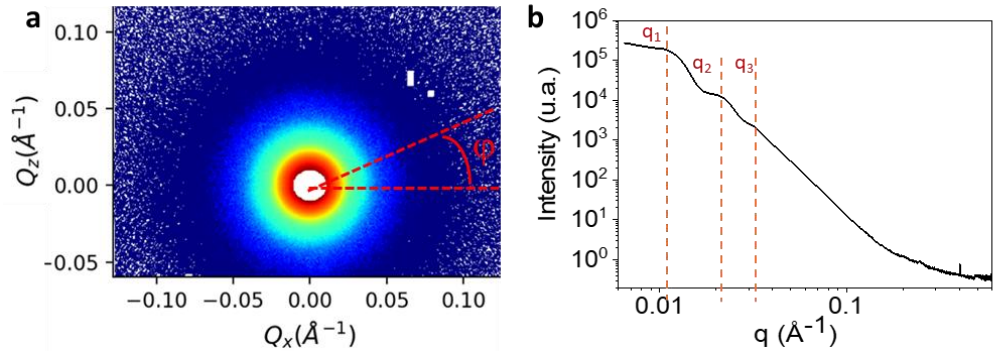

Figure III.5. (a) Typical 2D SAXS pattern of assemblies of CoNi NPs, (b) 1D radial-profile obtained from the integration over the entire azimuthal range φ = 0 – 360°.

A typical SAXS curve can be divided into three mains q-regions, each providing complementary information:

- The Guinier regime at low q, the intensity exhibits a plateau which quantifies the overall size of the scattering object.

- the Fourier region at intermediate$q$, which is directly related to the dimensionality of the object. In this regime, the scattering intensity follows a power-law decay, $I(q) \propto q^{-n}$, where the exponent n depends on the particle geometry. Typically, spherical objects exhibit n = 4,

plate-like (two-dimensional) objects n = 2, and elongated one-dimensional rods n = 1. Thus, the slope of the scattering curve in this regime provides a direct criterion for linking the scattering profile to the Euclidean or fractal dimension of the objects under investigation. Porod regime at high q, is sensitive to the interface between the objects and the surrounding media [3–5]. This behavior is illustrated in Figure III.6a.

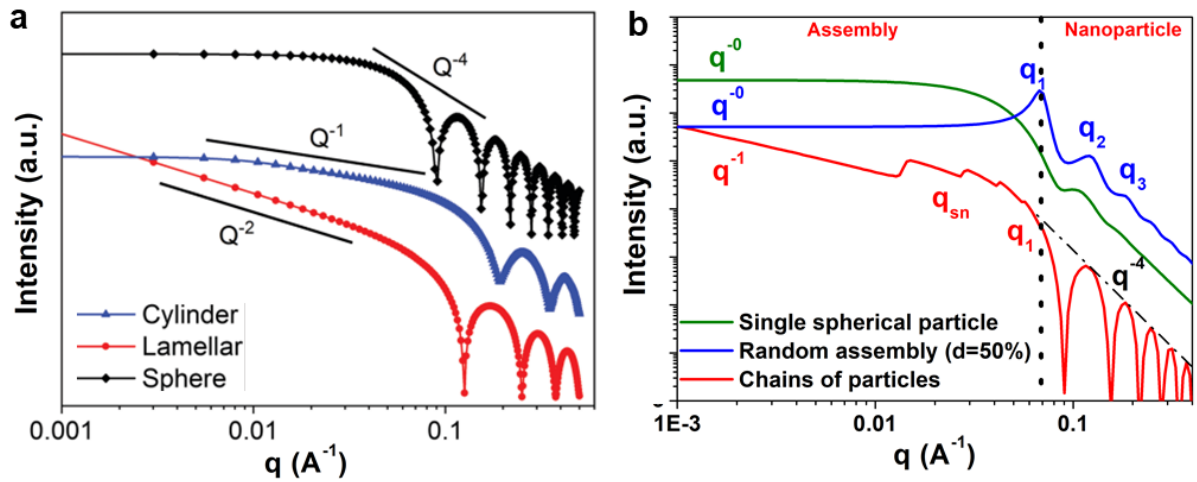

Figure III.6. Scattering patterns simulated using SASVIEW for (a) diluted particles (S(q)=1) of monodisperse spheres (d = 10 nm, black), lamellae (thickness = 5 nm, red) and cylinders (diameter = 4 nm and length = 40 nm, blue) [2] and (b) diluted spheres with a polydisperse size (green) and their assembly as 1D chain of 10 particles (red) or random assembly (blue).

In this study, small-angle X-ray scattering (SAXS) is employed to investigate assemblies of magnetic nanoparticles both in solution (capillaries) and on solid substrates (glass slides and characterization chips). SAXS offers several advantages for this purpose:

1. **Orientation analysis.** Anisotropic scattering patterns reveal preferential particle orientations, as well as chain or fiber alignment.
2. **Multi-scale sensitivity.** SAXS simultaneously provides information on features associated with individual nanoparticles and on their collective organization into chains, bundles, or dense aggregates leading to the appearance of correlation peaks (Figure III.6b and Appendix 5) or even diffraction peaks.

1.2.b Analysis of anisotropic 2D SAXS image

The 1D radial profile obtained after integration on the whole azimuthal angle φ are particularly suited for isotropic patterns. The presence of ordered assemblies eventually leads to anisotropic 2D SAXS signals and the presence of diffraction peaks. In this work we observed typically three different types of patterns exhibiting: isotropic symmetry with continuous rings (Figure III.7a), cubic symmetry (Figure III.7b) or hexagonal symmetry (Figure III.7c).

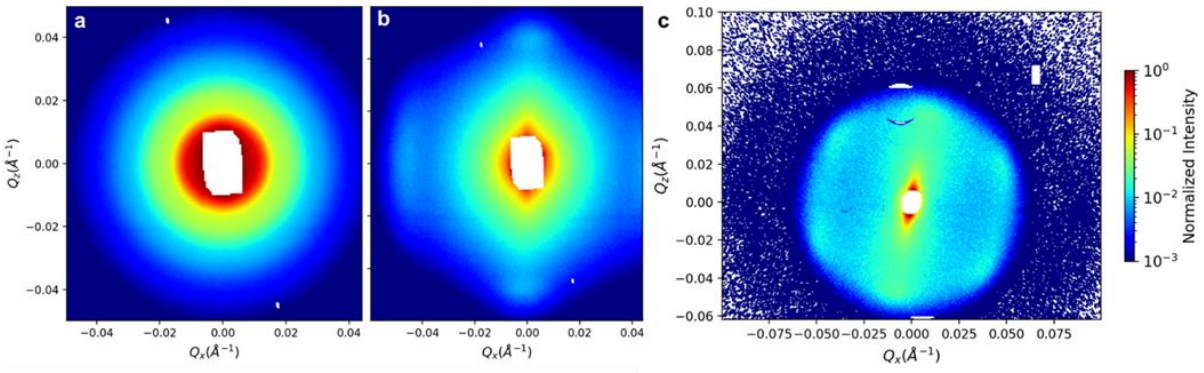

Figure III.7. Characteristic 2D SAXS images of NP assemblies exhibiting (a) isotropic, (b) cubic and (c) hexagonal patterns. White areas correspond to dead areas of the detector and beam stop.

To index these patterns, one needs to consider the different possible crystal orientations which are listed on the intercalary 1 and Appendix 7. The angles between the diffraction peaks and the ratio between the peak positions, experimentally determined from the azimuthal and radial profile, respectively, will be of key importance to determine the most-likely crystal orientation to consider. Finally, the center-to-center interparticle distance retrieved from the indexation will allow to distinguish the different crystal orientation. One can indeed expect an center-to-center interparticle distance $D = d_{TEM} + t_{ligands}$ (Eq. 3), with d_{TEM} the mean size determined by TEM and $t_{ligands}$ the thickness of the ligand shell, which is typically in our case of ~2 nm [6–8].

1.2.c Experimental procedure

Small angle X-ray scattering (SAXS) of the fibers both in solution and on support was performed on a XEUSS 2.0 laboratory instrument from the platform FERMAT and located in LGC Toulouse, equipped with a pixel detector PILATUS 1 M (DECTRIS) and a Cu Kα X-ray source provided by GeniX3D (λ = 1.54 Å). The sample detector distance was fixed to record the SAXS signal in the q range 0.015-1 $Å^{-1}$. The local characterization of the micromagnets deposited on RF components were carried out on the SWING beamline at the SOLEIL synchrotron (Paris, France) using a microbeam configuration (μSAXS). The beam energy was 12 keV, with a q range of 0.015 – 1.15 $Å^{-1}$. Acquisition times were set to 10 ms, and the beam spot size was 21 × 20 $μm^2$ allowing for a high-resolution mapping of the microstructures within the magnets (Figure III.8). This unique technique allows to probe the homogeneity of the assembly through the entire micromagnet.

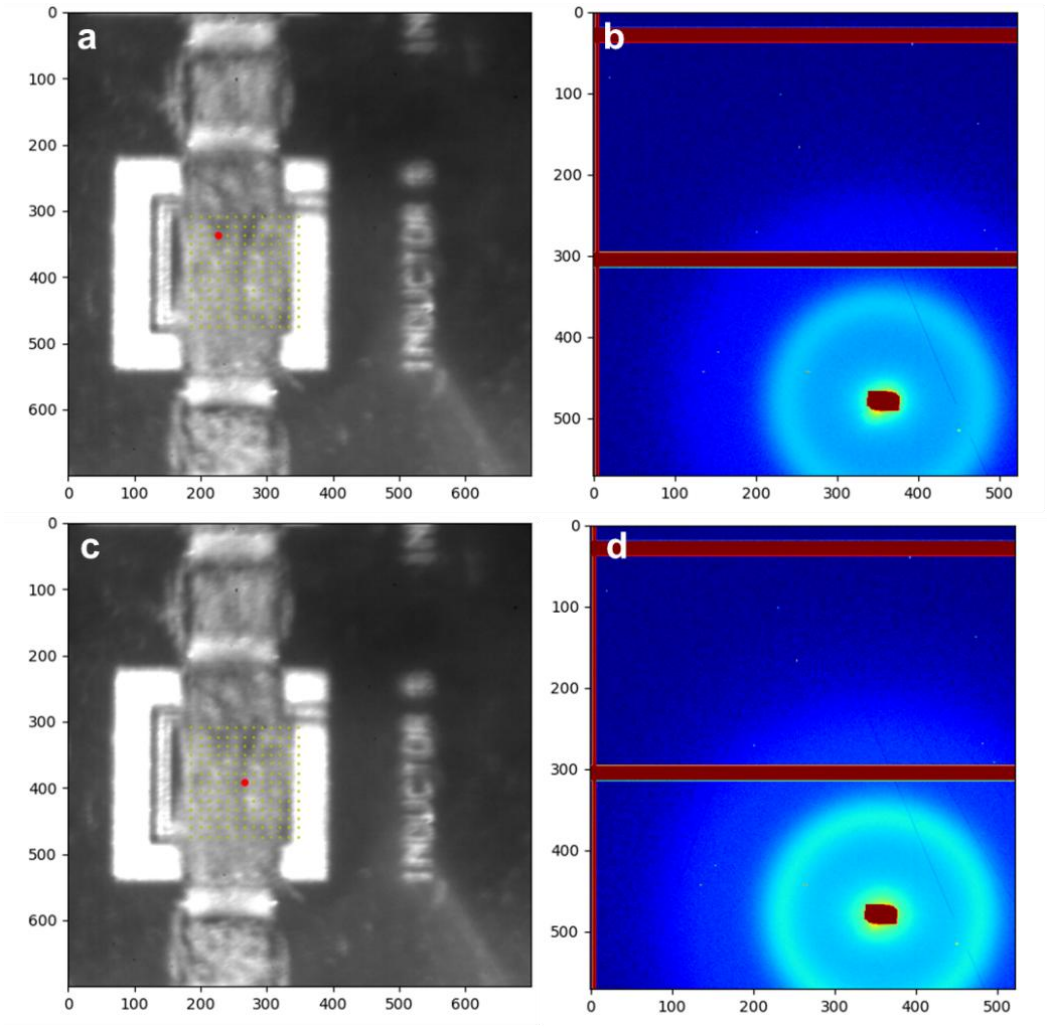

Figure III.8. (a,c) Optical image of a characteristic micromagnet studied by µSAXS at the SWING beamline. The yellow dots visualize the different beam positions (here an array of 13 x 13 positions) and the red spot indicates the current position. (b,d) Corresponding 2D SAXS image, the area in wine corresponds to the dead zone of the detector. The scale is in pixels. A further conversion is needed to plot the 2D image in q scale as presented hereafter in the manuscript and a rotation is applied to set the magnetic field direction applied during the magnetophoresis horizontal.

1.3. Random close pack assemblies of NPs

1.3.a Assemblies of CoNi particles

A first fairly simple case study concerns the magnetic assembly of CoNi NPs, synthesized via the polyol method. Assemblies obtained in liquid-state, using the in-situ magnetic set-up, or dense micromagnets integrated on microelectronic chips by magnetophoresis were studied. The 2D SAXS patterns are presented in Figure III.9. Independently of the experimental condition used, in particular the magnetic field applied and the mean NP size, isotropic patterns were observed, despite the appearance of macroscopic fiber-like structures along the magnetic field direction.

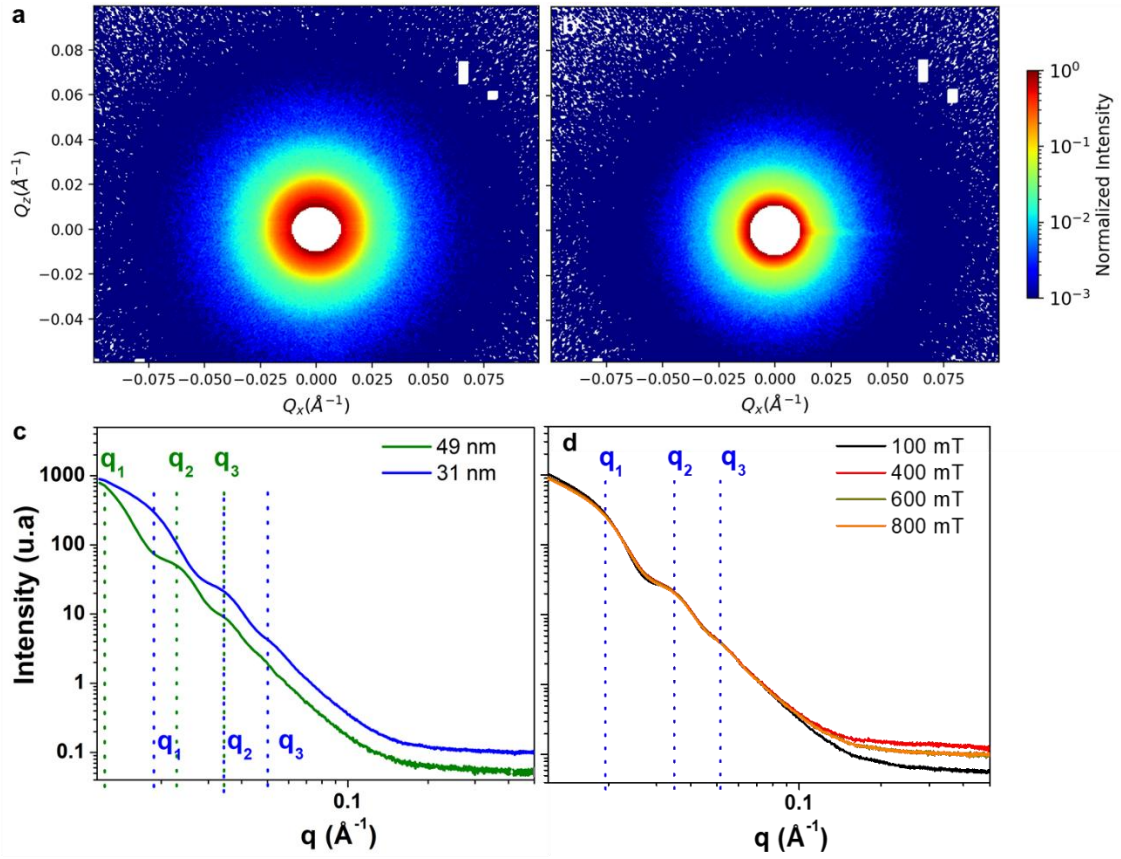

Figure III.9. 2D SAXS pattern observed from the assembly of $Co_{0.5}Ni_{0.5}$ NPs of (a) 31 ± 5 nm and (b) 49 ± 6 nm in liquid-state under an external magnetic field of 800mT and (c) the corresponding isotropic integration. The positions of the three correlation peaks are indicated by dashed lines. (d) 1D SAXS profile for the 31 nm size NP assemblies formed under varying magnetic field.

The 1D SAXS intensity profiles obtained by radial integration of these 2D patterns exhibit three distinct peaks q_1, q_2, q_3. The positions and relative ratios of the q_n peaks are consistent with a random close-packed (RCP) arrangement. The peak positions indeed align with the structure factor predicted by the Percus–Yevick approximation for hard-sphere liquids [9]. In this model, the first peak q_1 corresponds to the interparticle center-to-center distance while the peak ratio $\frac{q_2}{q_1}$ and $\frac{q_3}{q_1}$ is modulated by the packing fraction of the assembly (Figure III.10c). The results for the two sizes of CoNi NPs are summarized in Table III.1. In both cases, the center-to-center distance, determined from the first peak position, is in good agreement with the mean size determined by TEM and a 2nm organic layer. The peak ratio indicates a packing fraction of η ≈50% independently of the experimental condition used.

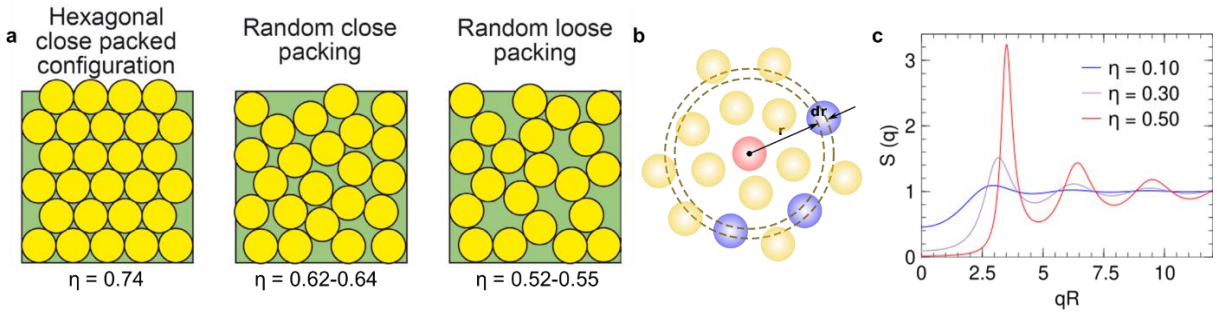

Figure III.10. (a) Schematic view of different hard sphere assemblies ranging from the densest HCP configuration to the random packing [10]*. (b) Schematic view of the radial distribution function calculation, which leads to the (c) static structure factor of the hard-spheres liquid in Percus–Yevick approximation at three different packing fractions η in function of qR with R the hard sphere radius. Illustration taken from Wikimedia Commons.*

d_{TEM} (nm)	$q_1(\text{Å}^{-1})$	D (nm)	$q_2(\text{Å}^{-1})$	$q_3(\text{Å}^{-1})$	$\frac{q_2}{q_1}$	$\frac{q_3}{q_1}$	η
31 ± 5 nm	0.019	33	0.034	0.051	1.79	2.84	0.5
49 ± 6 nm	0.012	52	0.022	0.034	1.83	2.83	0.5
53 ± 6 nm	0.011	55	0.020	0.032	1.83	2.86	0.5

Table III.1. Summary of the peak positions q_i, the derived center-to-center distance D and the packing fraction η.

Micromagnets were prepared using another batch of $Co_{0.5}Ni_{0.5}$ nanoparticles which exhibit a slightly larger mean diameter of (53 ± 6) nm. The magnetophoresis-driven assembly was performed in an electromagnet, under an external field of 1 T. SEM imaging provided direct evidence of the localized NP assembly: NPs were almost entirely confined between the nickel blocks, yielding a dense micromagnet with few cracks (Figure III.11a). At higher magnification, SEM revealed short interparticle distances but no discernible long-range ordering (Figure III.11b). The 2D SAXS patterns were fairly similar to the one observed in liquid-state, with isotropic rings, evidence a random packing (Figure III.11c). The center-to-center distance D and the packing fraction η were derived from the peak position on the 1D radial profile (Figure III.12d). Interestingly, the final drying step of the fabrication process did not lead to a significant increase in the packing fraction, which remains close to 50% as in the liquid-state.

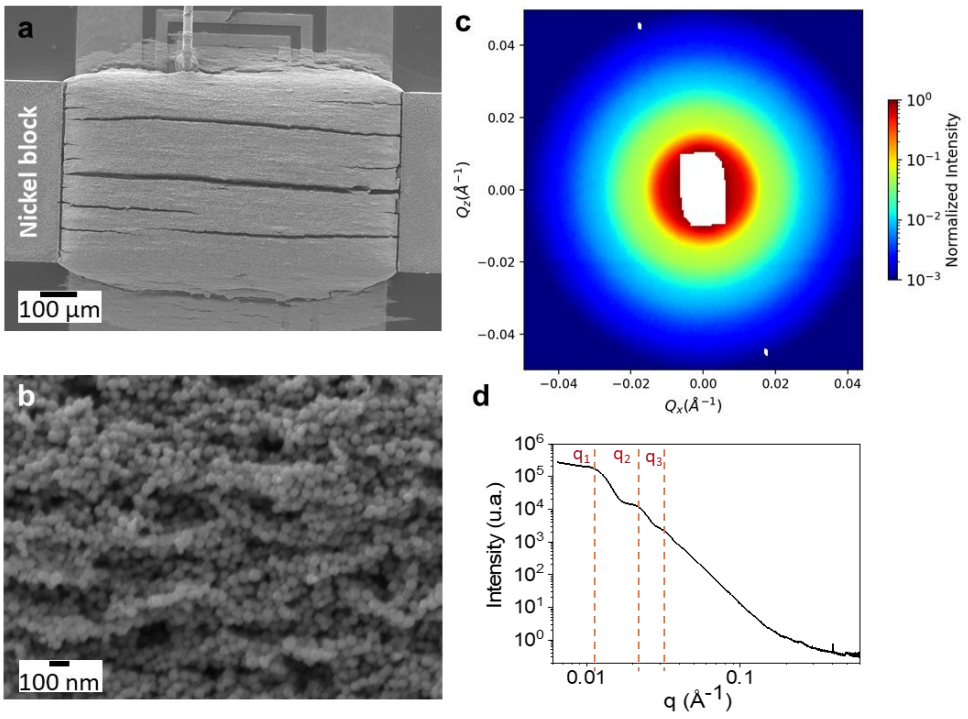

Figure III.11. (a) SEM image showing a micromagnet composed of (53±6) nm $Co_{0.5}Ni_{0.5}$ NPs formed between nickel blocks, with visible wire bonding. (b) High-magnification SEM image revealing dense, random packing of CoNi nanoparticles. (c) 2D SAXS pattern indicating isotropic scattering, consistent with random close-packed (RCP) structure. (d) Radial integration of SAXS signal showing multiple peaks (q_1, q_2, q_3), with distance correlation characteristic of an RCP structure.

2. Assemblies of FeCo NPs

Micromagnets were prepared from similar particles, spheroidal/octahedral FeCo nanoparticles with an average diameter of 9 ± 2 nm (Figure III.12a) by magnetophoresis either in the glove box using toluene as solvent with a 0.4 T external magnetic field or in the electromagnet using ethanol as solvent with a 1 T external magnetic field. In both cases, SEM imaging confirmed the efficient localization of nanoparticles between nickel guiding blocks, yielding dense micromagnets (insets Figure III.12b and c). The assemblies exhibited short interparticle distances but no visible long-range order at 0.4T (Figure III.12b).

Consistently with SEM observations, SAXS measurements revealed isotropic scattering patterns for the assembly performed at 400 mT (Figure III.12e). Such pattern can be interpreted as a random close-packed (RCP) assembly with a center-to-center distance of ~11 nm (q_1 = 0.059 Å^{-1}), and a packing fraction of ~50%. These results are in good agreement with the TEM size and a 2 nm thick ligand shell around the FeCo NPs.

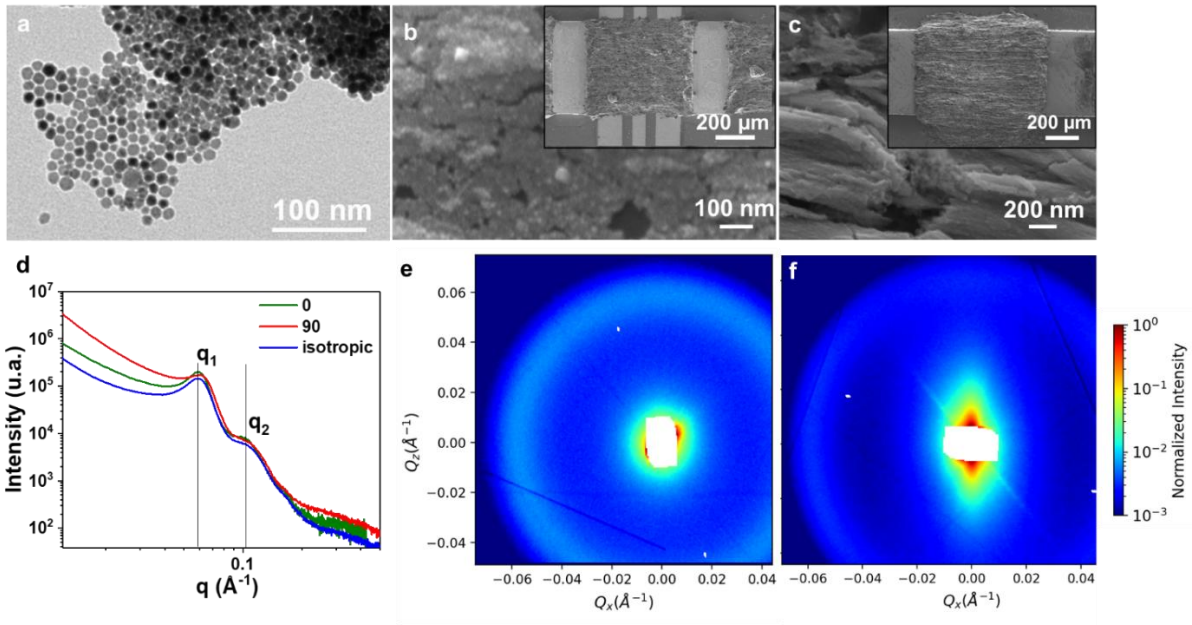

Figure III.12. (a) TEM image of 9 ± 2 nm FeCo NPs. SEM images (b-c) and the corresponding (e-f) 2D µ-SAXS patterns of their assembly obtained by magnetophoresis under (b, e) $\mu_0 H$ = 400 mT (glove box) and (c, f) 1T (electromagnet). Inset: SEM image of the micromagnet. (d) 1D profile obtained after an isotropic integration (blue line) for pattern (e) and on the azimuthal sector $\varphi = 0 \pm 5°$ (green) and $\varphi = 90 \pm 5°$ (red) for pattern f.

When the magnetophoresis is performed at higher field, the assemblies appear as compact, elongated structures in the field direction (Figure III.12c). The 2D SAXS image (Figure III.12d and f) reveals both an isotropic ring at the same q_1 = 0.059 $Å^{-1}$ along with an anisotropic feature along φ = 90°. The 1D profiles extracted from the azimuthal sectors φ = 0 ± 5° and φ = 90 ± 5° are pretty similar at large q vectors and superimpose with the 1D profile of the micromagnet prepared at 400 mT. At short q however, the intensity slopes are slightly different. The intensity decayed indeed as $q^{-2.5}$ along φ = 90°, consistent with disordered and largely isotropic arrangements dominated by particle sphericity. In contrast, along 0° (parallel to the field), the decay followed a $q^{-1.8}$ slope, indicative of lamellar or fiber-like structures aligned with the magnetic field. Assuming that line broadening is dominated by the size of the crystals, the FWHM obtained after baseline subtract and gaussian fitting from the integration of the peak related to q_1 yielded a correlation length defined as $\frac{2\pi}{FWHM}$ ~ 42 nm, implying fibers approximately three particle diameters in width.

These results demonstrate that nanoparticles with rounded geometries can organize into fiber-like assemblies under high magnetic fields as schematized in Figure III.13.

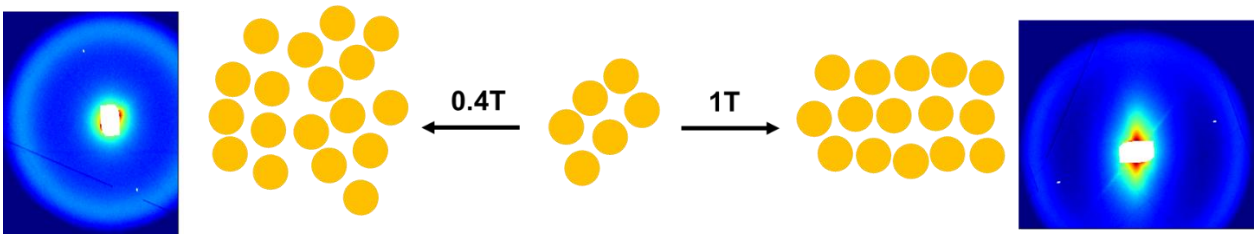

Figure III.13. Schematic view of the proposed magnetically-induced assembly of FeCo NPs.

3. Ordered assemblies of nanoparticles: the case of nanocubes

3.1. Characterization of the different nanocubes used

Due to the time allocated access to the two SAXS set-up (synchrotron Soleil and LGC laboratory) we could not perform the full set of characterization on the very same batch of NPs. Therefore, we have deliberately checked different batches of NPs, exhibiting cubic shapes all synthetized using HDA/HDAHCl as ligand couple, as shown in Figure III.14 and discuss hereafter the characteristic SAXS patterns obtained.

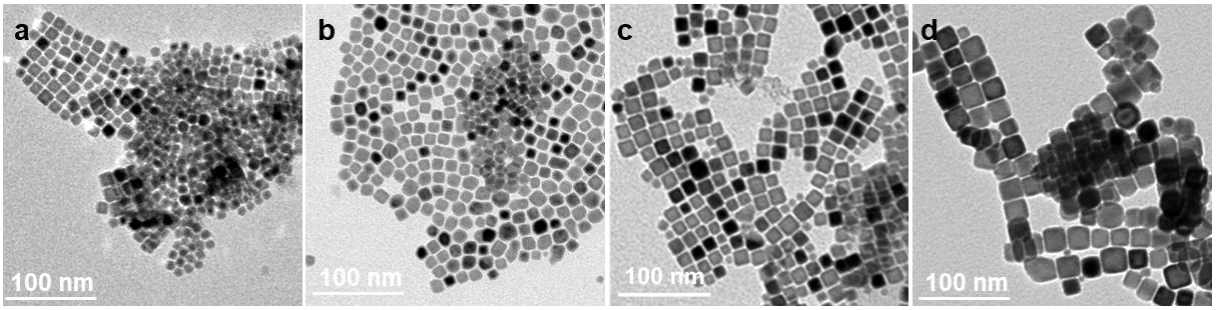

Figure III.14. TEM images of the nanocubes used in the following section. Fe NPs with an average size of (a) 10 ± 2 nm, (b) 11 ± 1 nm and (c) 13 ± 1 nm. (d) $Fe_{0.9}Co_{0.1}$ nanoparticles with an average size of 20 ± 4 nm.

3.2. Characterization of the micromagnet obtained by magnetophoresis

Micromagnets were prepared from cubic Fe nanoparticles with an average diameter of 13 ± 1 nm (Figure III.14c) using the electromagnet under an external field of 1 T. SEM imaging confirmed the efficient localization of nanoparticles between the nickel guiding blocks, yielding dense deposits (Fig. III.15). At higher magnification, the assemblies appeared as compact elongated fibers, composed of individual chains of nanoparticles aligned along the applied magnetic field.

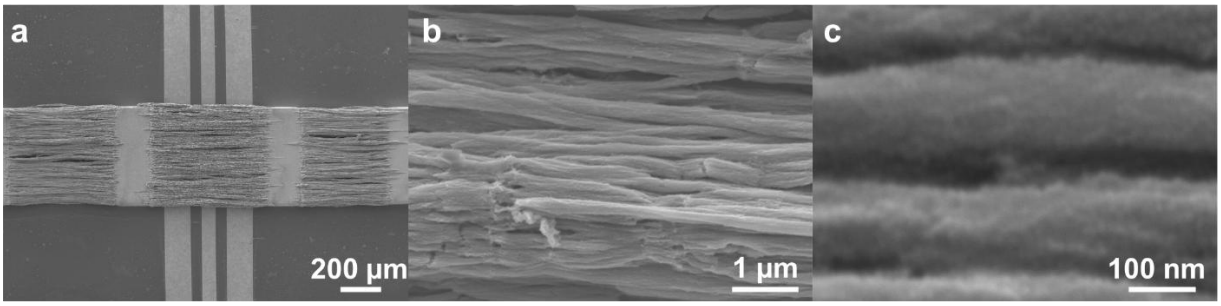

Figure III.15. (a) SEM image of micromagnet made of cubic Fe nanoparticle with an average size of 13 ± 1 nm obtained from magnetophoresis at 1 T. (b, c) Different high magnification SEM images of this micromagnet with fibers and the nanoparticles chains visible inside the fibers.

SAXS measurements (Figure III.16) further corroborated these observations. The 2D scattering patterns exhibit marked anisotropy, reflecting preferential alignment of the particles along the magnetic field direction. The cubic-like symmetry could be due to a cubic assembly of the particles.

The diffraction peaks were retrieved from the integration along the azimuthal sectors (φ = 0°) and (φ = 90°, Figure III.16c). Three peaks can be seen and the peak ratios $\frac{q_n}{q_1}$ followed approximately the sequence 1–2–3, characteristic of a cubic packing along a [001] zone axis. The full width at half maximum (FWHM) of the first peak yielded a correlation length of ~80 nm, *i.e.* approximately five particles large.

Azimuthal profile was plotted for q_1 = 0.040 $Å^{-1}$ evidencing 4 peaks, periodically spaced by $\Delta\varphi \approx 90°$ (Figure III.16d). The difference of peak width confirms a preferential orientation along the magnetic field direction, narrow peaks being observed at φ =90 and -90°.

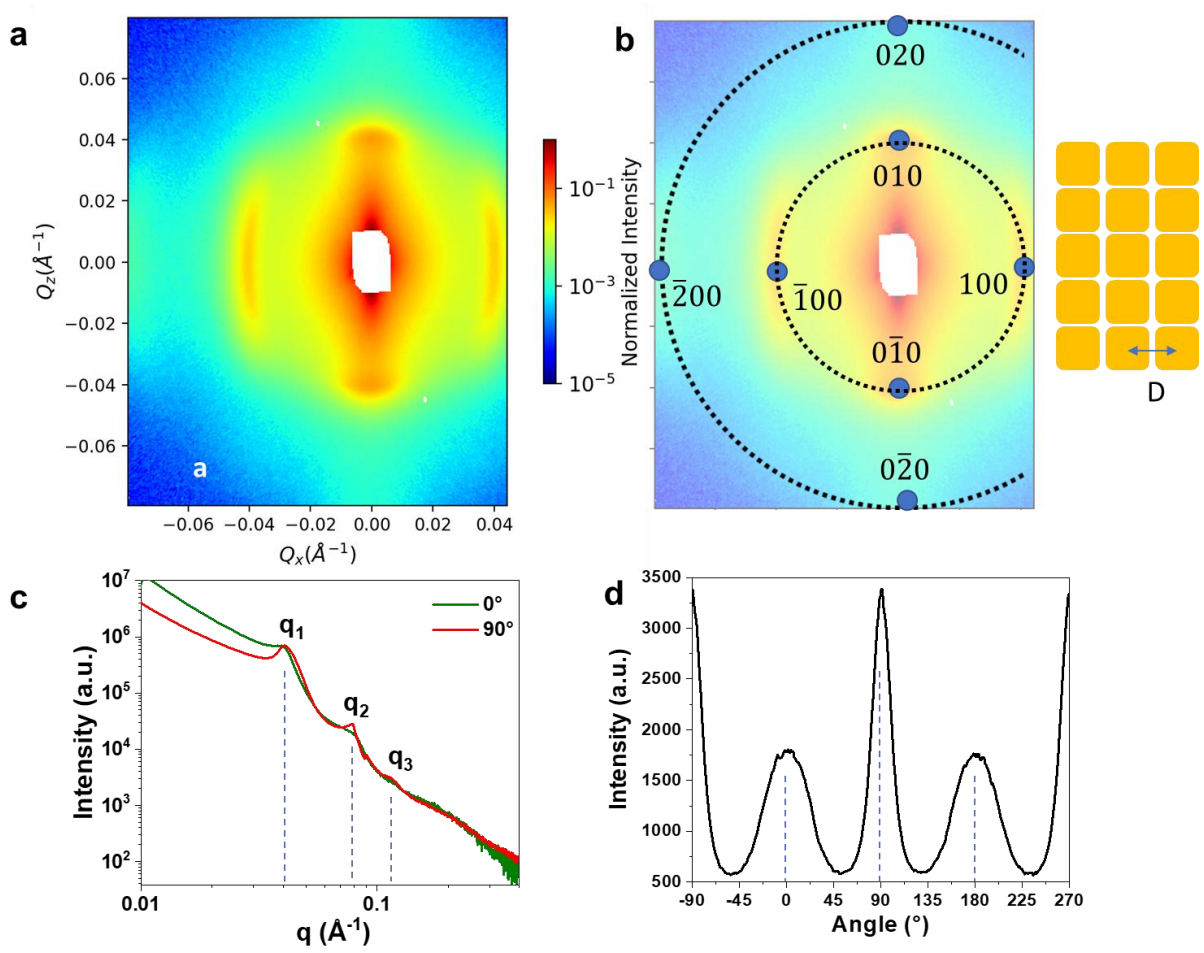

Figure III.16. (a) 2D μ-SAXS pattern of the Fe nanocube assembly limited to q = -0.08 – 0.08 Å^{-1} region for visualization's sake. (b) Indexation of the pattern considering a simple cubic arrangement with a center-to-center spacing D. Dashed lines: q_1 = 0.040 Å^{-1} and q_2 = 0.079 Å^{-1}. (c) 1D profile obtained after integration on the azimuthal sector φ = 0 ± 5° (green) and φ = 90 ± 5° (red). (d) Azimuthal profile determined at q_1.

The indexation of the 2D SAXS pattern was made considering the 3 different cubic organizations viewed along the [001] zone axis (Intercalary 1). The center-to-center distances were retrieved from the peak positions q_1 and q_2 as summarized in Table III.2. If one take into account the mean particle size of 13 ± 1 nm determined by TEM and the ~2nm ligand shell, a center-to-center distance of ~15 nm is expected. The only indexation consistent with this is the simple cubic, the interparticle distance being estimated at 15.7 nm.

	q ($Å^{-1}$)	D_{SC} (nm)	D_{BCC} (nm)	D_{FCC} (nm)	D_{TEM} (nm)
q_1 ($Å^{-1}$)	0.040	15.7 (q_1=q_{100})	19.2 (q_1=q_{110})	22.2 (q_1=q_{200})	13 ± 1
q_2 ($Å^{-1}$)	0.079	15.9 (q_2= q_{200})	19.5 (q_2= q_{220})	22.5 (q_2= q_{400})	

Table III.2. Summary of the different center-to-center distances determined considering different cubic organizations: SC (simple cubic), BCC (body-centered cubic) or FCC (face-centered cubic), observed along the zone axis [001]. Indexations and calculations are proposed considering Intercalary 1.

Fairly similar results were obtained from the magnetophoresis-driven assembly of Fe NPs with an average diameter of 10 ± 2 nm (Appendix 6). Due to a poorer stability of the nanoparticle dispersion prior to the assembly, the pattern exhibits a lower contrast.

3.3. Characterization of the assemblies in solution

This experiment was performed on cubic $Fe_{0.9}Co_{0.1}$ nanoparticles with an average size of 20 ± 4 nm (Figure III.14d) dispersed in toluene at a concentration of 10mg/mL and aligned using the in-situ magnetic cell set-up developed at LGC.

3.3.a Assembly formed under $\mu_0 H$ = 100 mT

When the capillary was subjected to a magnetic field of 100 mT, the 2D SAXS pattern displayed a pronounced anisotropy with hexagonal symmetry (Figure III.17a). This symmetry was confirmed by radial integrations of the scattering intensity, which revealed peaks spaced by $\Delta\varphi \approx 60°$ in azimuth (Figure III.17b). Accordingly, the SAXS intensity was integrated along three specifical azimuthal angles corresponding to this symmetry: φ =0 ± 5° (parallel to the field),

φ =30 ± 5° and φ =90 ± 5° (perpendicular to the field) illustrated by Figure III.17c.

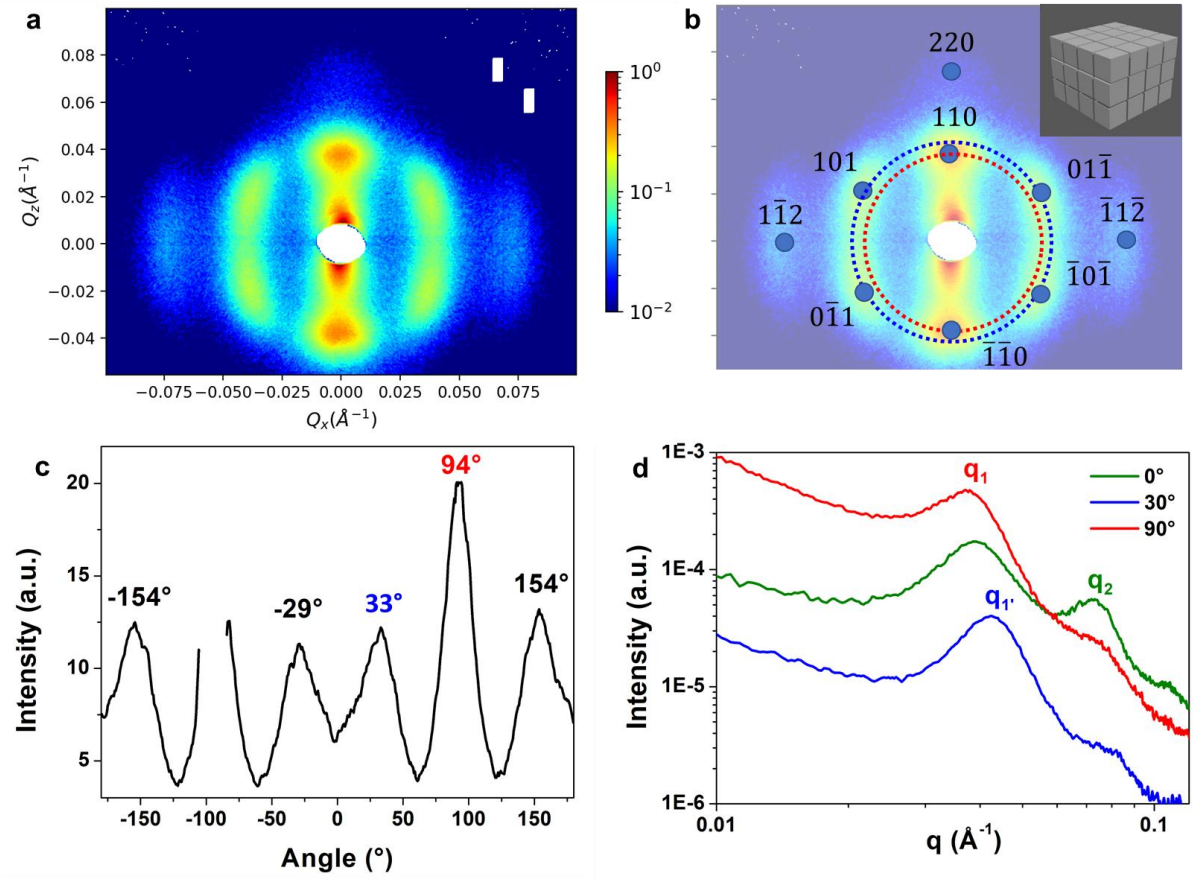

Figure III.17. (a) 2D µ-SAXS pattern of the 20 nm FeCo nanocube assembly limited to q_x = -0.1 – 0.1 $Å^{-1}$ and q_y = -0.05 – 0.1 $Å^{-1}$ region for visualization's sake. (b) Indexation of the pattern considering a simple cubic (SC) arrangement. Dashed lines red: q_1 = 0.038 $Å^{-1}$ and q_1' = 0.042$Å^{-1}$. (c) Azimuthal profile determined at q = 0.040 ± 0.002 $Å^{-1}$ (d) 1D profile obtained after integration on the azimuthal sector φ = 0 ± 5° (green), φ = 30 ± 5° (blue) and φ = 90 ± 5° (red).

As evidenced by the two circles on Figure III.17b, the first diffraction peaks are slightly shifted between φ = 90° (q_1 = 0.038 $Å^{-1}$) and φ = 30° (q_1' = 0.042$Å^{-1}$). M. Klokkenburg *et al.* reported a similar distortion in field-induced columns in magnetite ferrofluids [12]. Following their approach, they considered that these two peaks correspond to the same reflection but distorded due to the field application. They propose therefore considering q'_1 as the reference for the ratio between successive peaks. The ratio $\frac{q_2}{q_{1'}} = 1{,}73$ matched the theoretical value of $\sqrt{3}$, confirming the hexagonal symmetry of the arrangement (Table III.3).

Depending on the projection (i.e. zone axis), a hexagonal pattern can arise from either cubic arrangement (SC, BCC and FCC) viewed along the [111] or a hexagonal crystal HCP observed

along the [0001] direction as summarized in Intercalary 2. The center-to-center distances were calculated considering the different arrangements and the two peaks q_1' and q_2. In this case, given the mean TEM size of 20 nm, the pattern may correspond to the [$\bar{1}$11] projection of a SC lattice. So, interestingly, the assembly is a SC lattice as in the previous cases of the micromagnets but observed along a different zone axis.

	$\frac{q_2}{q_1'}$	D_{SC} (nm)	D_{BCC} (nm)	D_{FCC} (nm)	D_{HCP} (nm)	D_{TEM} (nm)
q_1' = 0.042 Å^{-1}	1,73	21,1 ($q_1'=q_{110}$)	18,3 ($q_1'=q_{110}$)	29,9 ($q_1'=q_{220}$)	17,3 ($q_1'=q_{100}$)	20 ± 4
q_2 = 0.073 Å^{-1}		21,1 ($q_2=q_{211}$)	18,2 ($q_2=q_{211}$)	29,8 ($q_2=q_{422}$)	17,2 ($q_2=q_{110}$)	

Table III.3. Summary of the different center-to-center distances determined considering SC, BCC or FCC crystals viewed along the [111] direction or an HCP crystal observed along the [0001] zone axis. The indexation of q_1' and q_2 and calculations are proposed considering the Intercalary 2.

Assuming that the line broadening is dominated by the finite crystal size, the full width at half maximum (FWHM) of the reflections yields a correlation length of ~53 nm. This corresponds to approximately two to three particle diameters. The nanoparticles are aligned in parallel chains along the field direction, with shorter interparticle distances within each chain than between neighboring chains. This structural model is consistent with previous reports on the assembly of magnetic nanoparticles under applied fields, where dipolar interactions drive the formation of chain-like arrangements that subsequently bundle into small fibers [6,7,11].

3.3.b Effect of the magnetic field amplitude

When the applied magnetic field progressively increased up to 800 mT, the anisotropic 2D SAXS pattern with distorted hexagonal symmetry was preserved (Figure III.18). However, subtle differences emerged. Visual inspection of the capillaries revealed the formation of longer fibers, which, in turn, reduced the number of nanoparticles intersecting the SAXS beam.

This reduction in scattering volume explains the decreased signal intensity and the poorer signal to noise ratio observed at high field strengths.

Analysis of the SAXS signal evolution with increasing magnetic field intensity (Figure III.18) revealed that the appearance of superstructure peaks, observed at low q values, for $\mu_0 H \geq 400$ mT. Once formed, these superstructures persisted even when the field was subsequently reduced back to 100 mT, indicating that their formation is irreversible under the conditions tested. Interestingly, the pattern obtained after the complete evaporation of the solvent looks a bit more disoriented than in the liquid state (Figure III.18f).

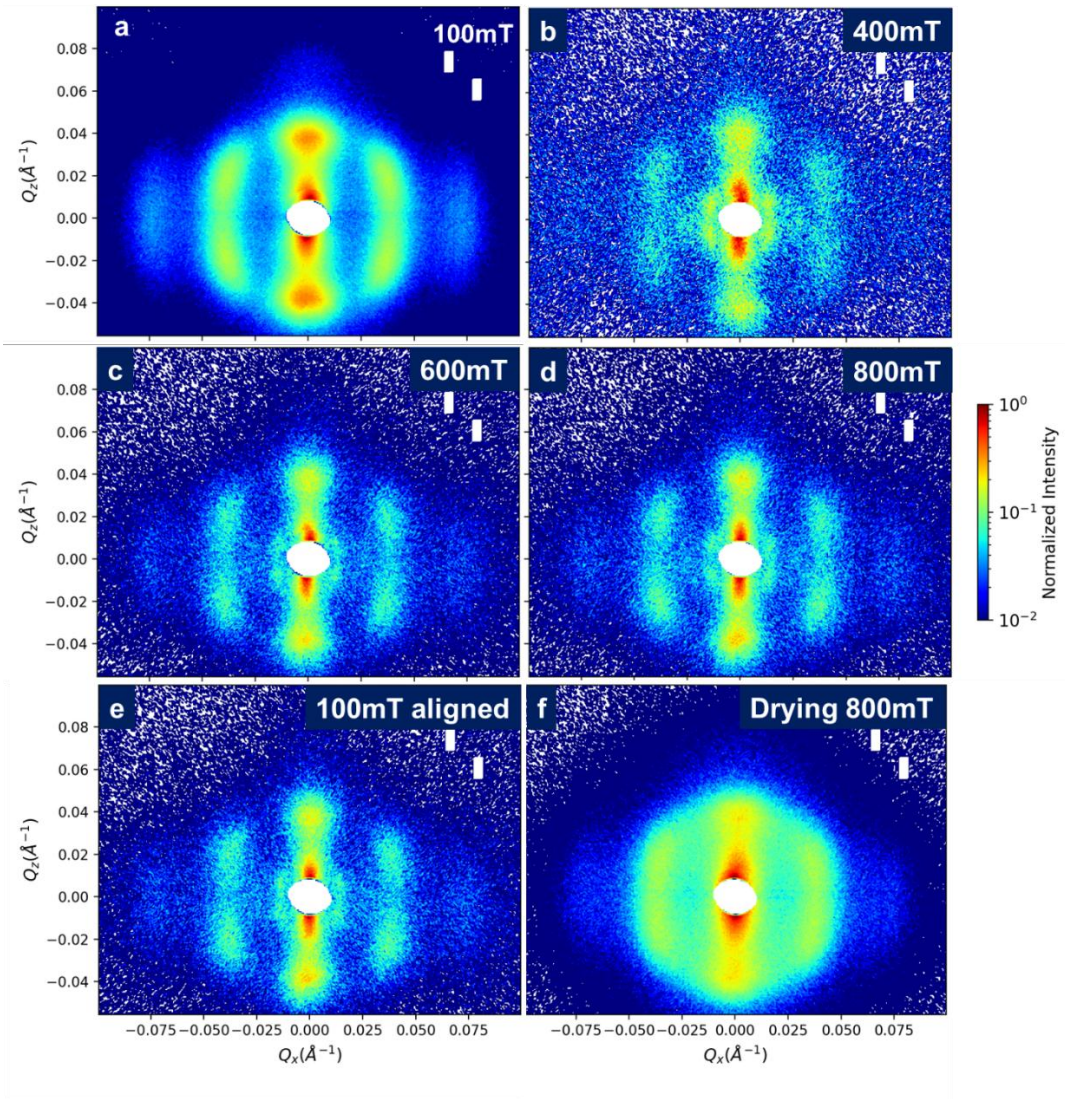

Figure III.18. 2D SAXS pattern of magnetically-induced assembly of a suspension of $Fe_{0.9}Co_{0.1}$ nanoparticles with an average size of 20 ± 4 nm for different external magnetic fields (a) 100 mT, (b) 400 mT, (c) 600 mT, (d) 800 mT, (e) 100 mT after being exposed to 800 mT. (f) Dried assembly obtained after allowing the solvent to be evaporated under an applied field of 800 mT.

3.4. Characterization of thin films

Dried assemblies of nanoparticles, deposited as thin film on glass slide, may differ from the assemblies formed in solution that we described hereabove. The strong capillary forces encountered during the solvent evaporation and the presence of a solid substrate may alter the assembly. 100µL of colloidal dispersion of NPs (7 g_{NP} mL^{-1}) was drop-casted onto a microscope glass slide (20 × 20 mm^2) under a static magnetic field ($\mu_0 H$ = 500 mT to 1 T) generated by an electromagnet. Drying occurred under the applied field, promoting densification of the nanoparticle arrangement while maintaining the alignment.

3.4.a Assembly of 20 nm FeCo nanocubes

The 2D SAXS pattern shown in Figure III.19a is fairly similar to the ones obtained in liquid phase with the same FeCo nanocubes (Figure III.17 and 18). A hexagonal-like symmetry is observed which can be indexed as a simple cubic arrangement viewed along the [111] direction. The pattern is however slightly distorted as revealed by the reduced separation of peaks around 0°/180°, moreover the second reflection corresponding to $(\bar{1}1\bar{2})$ is barely seen.

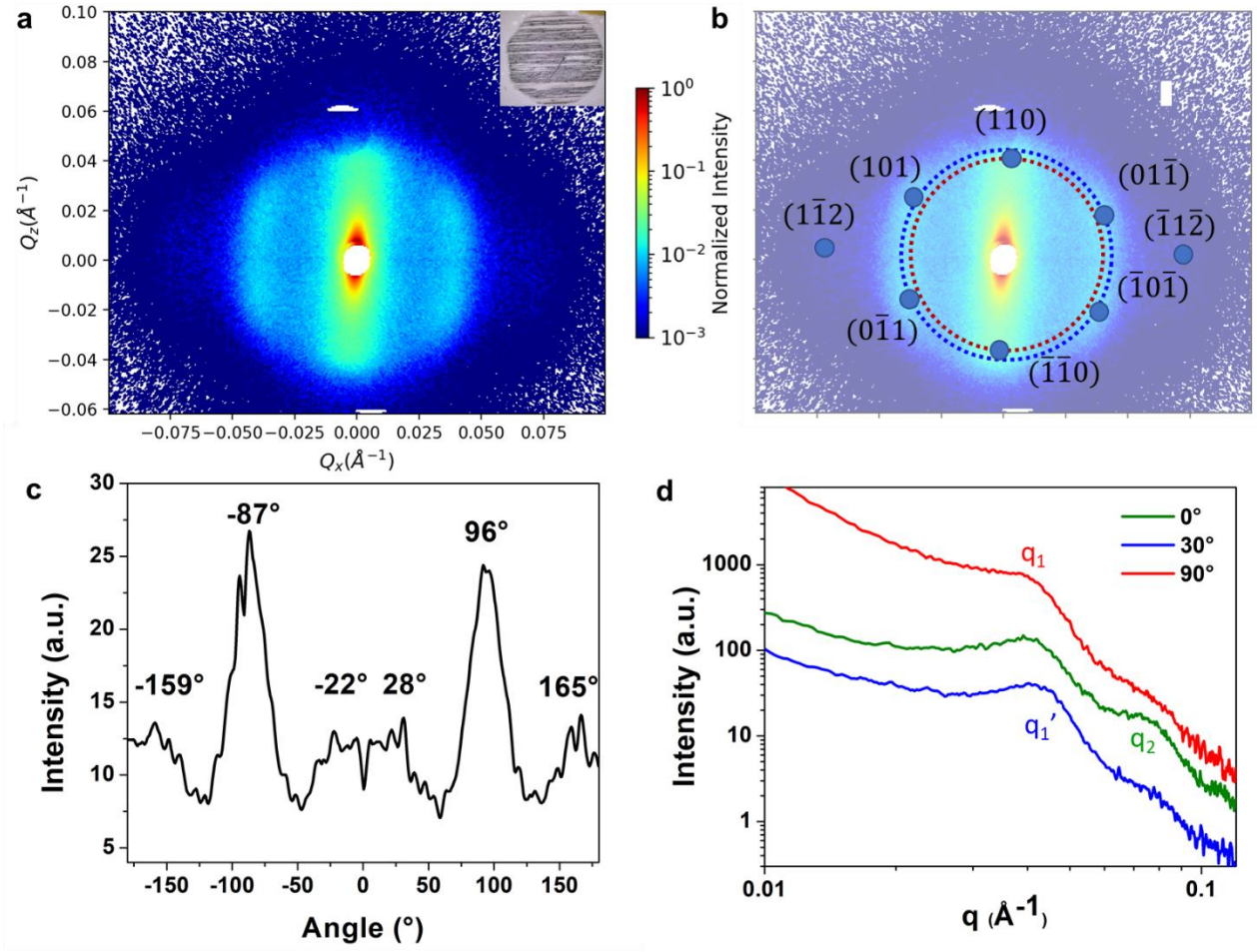

Figure III.19. (a) 2D μ-SAXS pattern of the 20 nm FeCo nanocube assembly limited to q_x = -0.1 – 0.1 Å^{-1} and q_y = -0.05 – 0.1 Å^{-1} region for visualization's sake. Inset: optical image of the deposit on the glass slide. (b) Indexation of the pattern considering a simple cubic arrangement. Dashed lines red: q_1 = 0.038 Å^{-1} and q'_1 = 0.042Å^{-1}. (c) Azimuthal profile determined at q = 0.040 ± 0.002 Å^{-1}. (d) 1D profile obtained after integration on the azimuthal sector φ = 0 ± 5° (green), φ = 30 ± 5° (blue) and φ = 90 ± 5° (red).

3.4.b Assembly of 11 nm Fe nanocubes

To evaluate the effect of particle size while keeping the cubic morphology constant, the same experiment was conducted using smaller Fe nanoparticles (11 ± 1) nm (Figure III.14b).

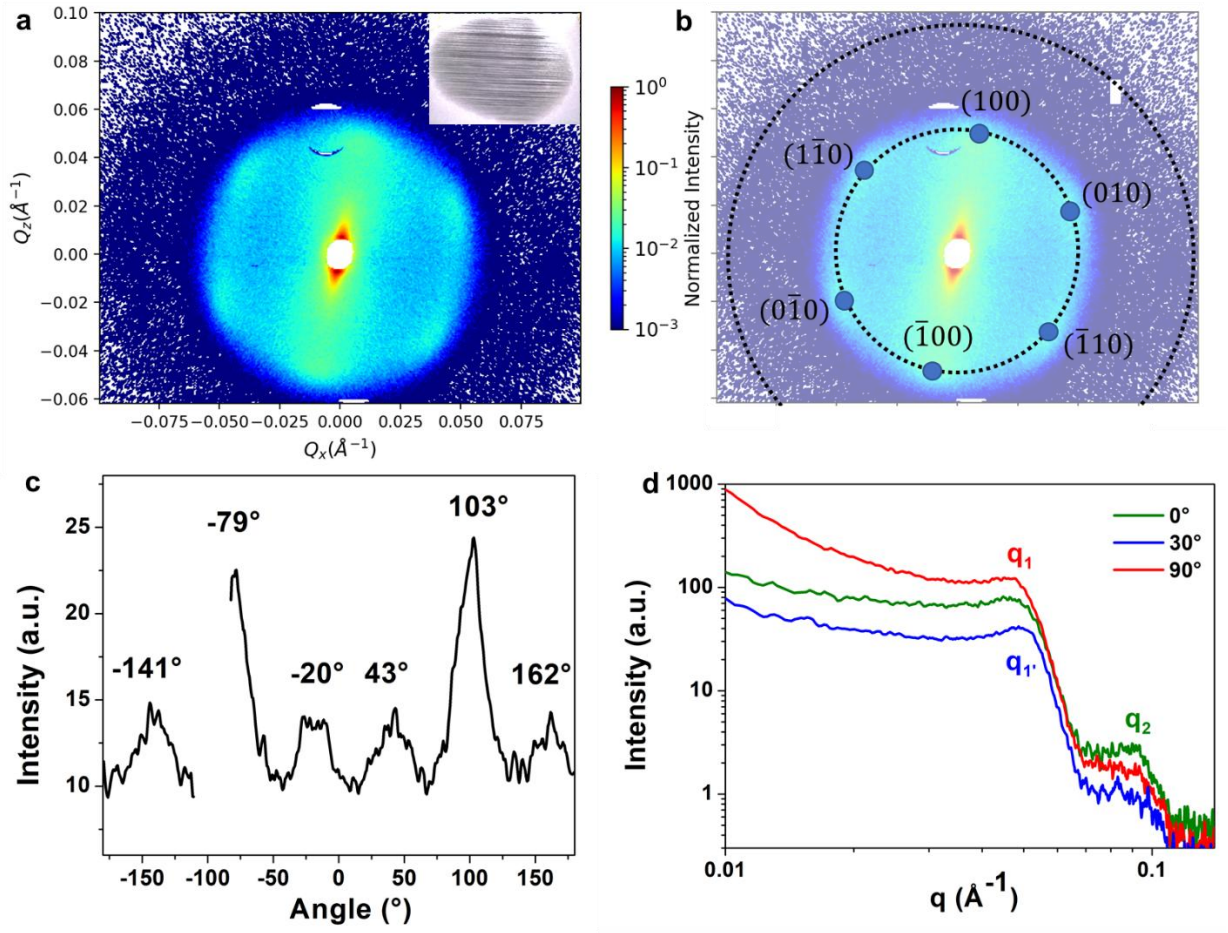

Figure III.20. (a) 2D μ-SAXS pattern of 11 nm Fe nanocube assembly limited to q_x = -0.1 – 0.1 Å^{-1} and q_y = -0.05 – 0.1 Å^{-1} region for visualization's sake. Inset: optical image of the deposit on the glass slide obtained at $\mu_0 H$ = 1T. (b) Indexation of the pattern considering an hcp arrangement. Dashed lines q_1 = 0.051 Å^{-1} and q_2 = 0.089 Å^{-1}. (c) Azimuthal profile determined at q_1. (d) 1D profile obtained after integration on the azimuthal sector φ = 0 ± 5° (green), φ = 30 ± 5° (blue) and φ = 90 ± 5° (red).

The 2D SAXS pattern again displayed pronounced anisotropy with hexagonal-like symmetry (Figure III.20a). Radial integrations revealed six distinct peaks evenly separated by 60° (Figure 20c). SAXS intensities were integrated along three directions: 0° (parallel), 30°, and 90° (perpendicular) illustrated on Figure III.20d. Following the same methodology, the first diffraction peak at 90° was denoted q_1, the peak at 30° as $q_{1'}$, the second peak at 0° as q_2. The ratio $\frac{q_2}{q_{1'}} \approx 1{,}75$ is close to the theoretical $\sqrt{3}$, supporting hexagonal ordering. The center-to-center distances were calculated considering the different arrangements and reported in Table III.4. Considering the mean nanoparticle size determined by TEM, the arrangement can be this time indexed as an HCP viewed along the [0001] zone axis.

	$\frac{q_2}{q_1'}$	D_{SC} (nm)	D_{BCC} (nm)	D_{FCC} (nm)	D_{HCP} (nm)	D_{TEM} (nm)
$q_1' = 0.051$ Å^{-1}	1,75	17.4 ($q_1'=q_{110}$)	15.1 ($q_1'=q_{110}$)	24.6 ($q_1'=q_{220}$)	14.2 ($q_1'=q_{100}$)	11 ± 1
$q_2 = 0.089$ Å^{-1}		17.3 ($q_2=q_{211}$)	15.0 ($q_2=q_{211}$)	24.4 ($q_2=q_{422}$)	14.1 ($q_2=q_{110}$)	

Table III.4. Summary of the different center-to-center distance determined considering a hexagonal projection of SC, BCC or FCC crystals viewed along the [111] direction or an HCP crystal observed along the [0001] zone axis. The indexation of q_1' and q_2 are proposed considering the Intercalary 2.

Overall, the results confirm that cubic nanoparticles on a support under a magnetic field consistently form fiber-like assemblies. Large cubic nanoparticles adopt SC assembly while smaller particles will tend to assemble in HCP.

4. Mechanism investigation

4.1. Effect of the NP shape on the thin film assembly

To assess the impact of particle morphology on assembly behavior, the organization of FeCo NPs of 11 ± 2 nm with a more spherical geometry approximating a squircle-like (a shape intermediate between a square and a circle, Figure III.21c) was investigated and compared with the cubic Fe NPs of 11 nm presented hereabove (Figure III.20).

The 2D SAXS pattern displayed clear anisotropy noticeable by the difference of intensity scattering at low-q values, reflecting preferential particle orientation under the applied magnetic field (Figure III.21a). To analyze this anisotropy, the scattering intensity was integrated over azimuthal sectors corresponding to φ = 0° and 90° (Figure III.21d).

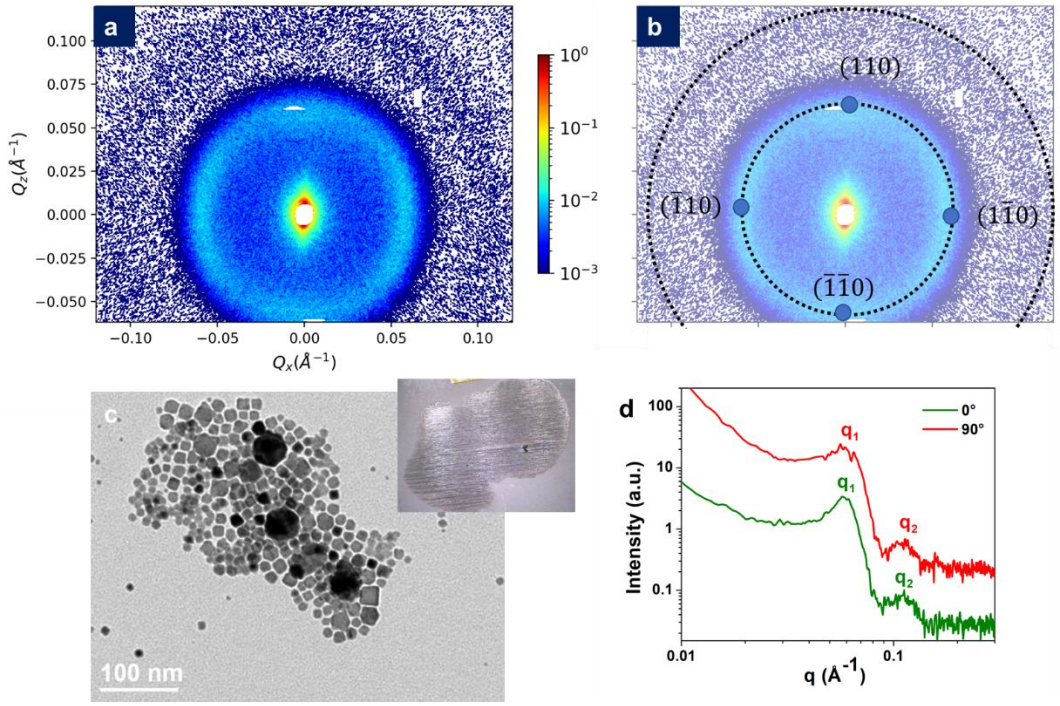

Figure III.21. (a) 2D μ-SAXS pattern of the assembly of 11 nm squircle FeCo NP obtained on glass at $\mu_0 H$ = 1T. (b) Indexation of the pattern considering a bcc[001] arrangement. Dashed lines q_1 = 0.058 Å^{-1} and q_2 = 0.111Å^{-1}. (c) TEM image of the NPs Inset: optical image of the thin film assembly. (d) 1D profile obtained after integration on the azimuthal sectors φ = 0 ± 5° (green), and φ = 90 ± 5° (red).

The first diffraction peak appeared at the same q-value of 0.058 $Å^{-1}$ in both directions and was denoted q_1, while a second-order peak at q_2 was observed at 0.111 $Å^{-1}$, with a ratio $\frac{q_2}{q_1} = 1.92$ very close to the expected value of 2 for a cubic arrangement viewed along the [001] zone axis. The different center-to-center distances were calculated considering the different cubic [001] arrangements and are reported in Table III.5. Considering the TEM size of 11 nm, one can suppose that the NP packing is here bcc[001].

	q ($Å^{-1}$)	D_{SC} (nm)	D_{BCC} (nm)	D_{FCC} (nm)	D_{TEM} (nm)
q_1 ($Å^{-1}$)	0.058	10.8 (q_1=q_{100})	13.2 (q_1=q_{110})	15.3 (q_1=q_{200})	11 ± 1

Table III.5. Summary of the different center-to-center distance determined considering a cubic organization SC, BCC or FCC observed along the zone axis [001]. The indexation of q_1 is proposed considering Intercalary 1.

Slope analysis of the integrated scattering curves further clarified the assembly anisotropy. Along 90° (perpendicular), the intensity decayed as q^{-3}, consistent with a high degree of randomness and the absence of long-range structural orientation. This suggests that in this direction, the arrangement is essentially disordered and isotropic, dominated by the approximately spherical particle shape. In contrast, along 0° (parallel to the applied field), the decay followed $q^{-1.6}$, a value indicative of linear or lamellar-like structures. This confirms that despite the spherical-like morphology, the NPs would preferentially align into fiber-like assemblies parallel to the applied magnetic field. Assuming that line broadening is dominated by the size of the crystals, the FWHM obtained after baseline subtract and gaussian fitting from the integration of the peak related to q_1 yielded a correlation length defined as $\frac{2\pi}{FWHM}$ of ~37 nm, corresponding to fibers approximately three particles wide.

In summary, FeCo nanoparticles with rounded geometries organize into BCC-like arrangements within fiber-like assemblies but with low lateral order contrarily to their cubic counterpart.

4.2 Effect of the magnetic field on the thin film assembly

To evaluate the influence of field strength on nanoparticle organization, the same NPs were assembled and let dry under a reduced magnetic field of 0.4 T. In all cases, the 2D SAXS patterns exhibited lower anisotropy compared to the 1T ones (Figure 22).

Cubic $Fe_{0.9}Co_{0.1}$ nanoparticles (20 ± 4 nm) retained a clear anisotropy at 0.4 T (Figure III.22b). The SAXS intensity integrated along $\varphi = 90°$ (perpendicular) and 0° (parallel) both followed power-law decays consistent with elongated, fiber-like assemblies. Importantly, no significant slope change was detected along 90° or 0°, indicating that the structural alignment remained stable under reduced field strength (Figure III.22c). This result demonstrates that large cubic nanoparticles possess sufficient dipolar force to maintain directional order even at low fields. These SAXS patterns can be indexed as SC[111] as obtained for the same NPs assembled in capillaries (Fig. III.17-18) and on a glass substrate (Fig. III.19).

Cubic Fe nanoparticles (11 ± 1 nm). In contrast, the smaller cubic particles showed a marked reduction in anisotropy but still hexagonal symmetry (Figure III.22e). Slope analysis confirmed a loss of alignment (Figure III.22f): the decay at 90° shifted from $q^{-1.5}$ (at high field) to $q^{-2.0}$, while at 0° it changed from $q^{-1.0}$ to $q^{-1.3}$. These values indicate that the assemblies retained some degree of anisotropy under field, but with weaker lateral correlations and reduced alignment compared to high-field conditions.

FeCo squircle-like nanoparticles (11 ± 1 nm). For the rounded FeCo particles, anisotropy was no longer visible in the 2D SAXS pattern at 0.4 T (Figure III.22h). After integration, the intensity decay at 90° remained close to q^{-3}, consistent with disordered, isotropic arrangements, while along 0° the slope increased from $q^{-1.6}$ to $q^{-2.0}$ (Figure III.22i). This shift suggests that at low field the particles form assemblies closer to lamellar-like structures, but without strong directional order.

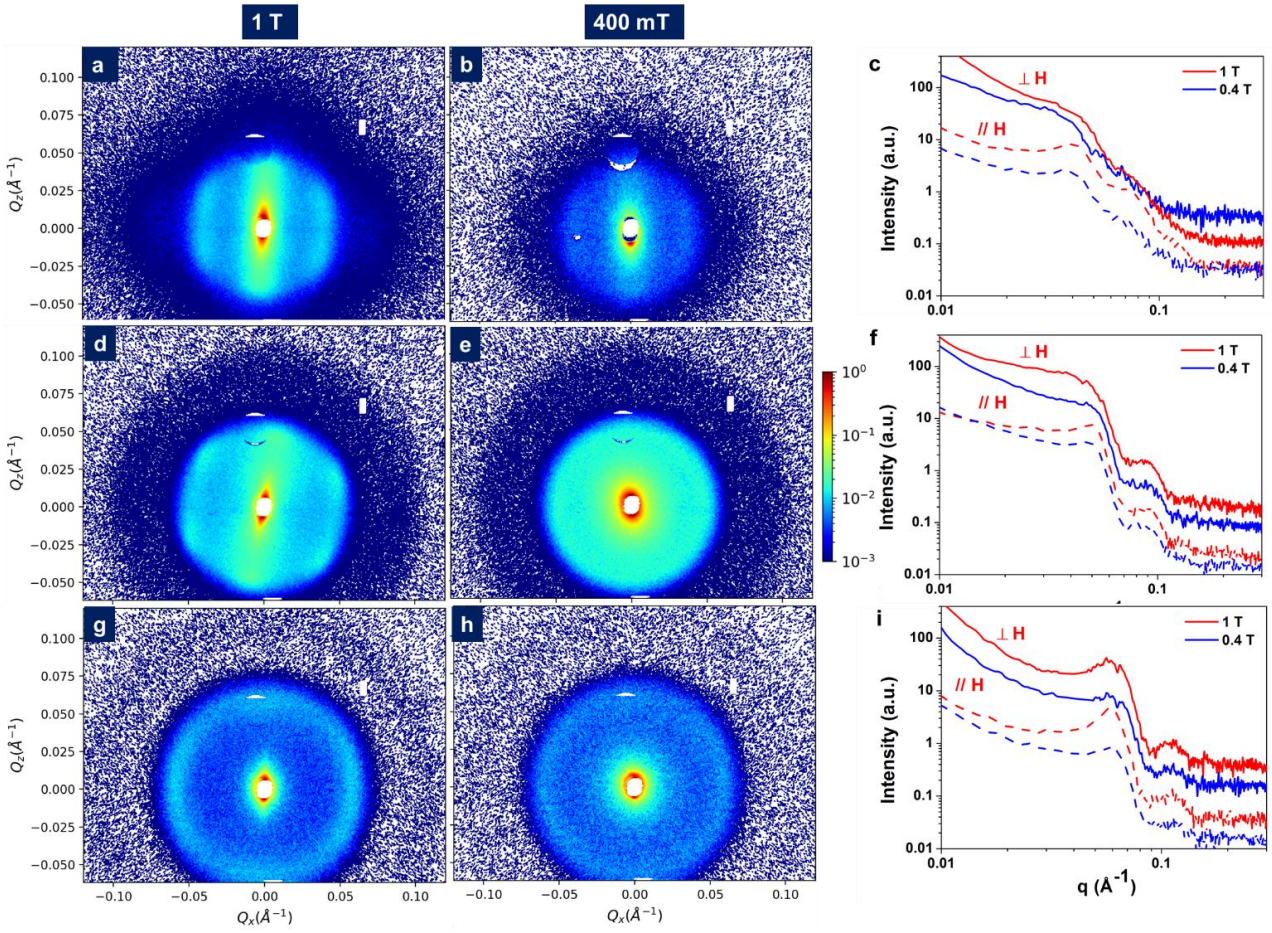

Figure III.22. (a,b;d,e;g,h) 2D SAXS pattern and (c,f,i) 1D profile along azimutal angle 0° (dashed line) and 90°(solid line) of thin film assembly of cubic (a-c) FeCo 20 ± 4 nm and (d-f) Fe 11 ± 1 nm and (g-h) squircle FeCo NPs of 11 ± 1 nm at (a,b) 1 T and (c,d) 0.4 T.

These results in addition highlight the magnetic field intensity effect, it illustrates the combined effect of particle size and morphology on the stability of field-induced assemblies. Larger cubic nanoparticles retain strong anisotropy and fiber-like ordering even at reduced field intensity, whereas smaller cubic nanoparticles lose symmetry and order, and spherical-like nanoparticles become almost isotropic. Thus, both dipolar force (size-dependent) and particle geometry critically determine the threshold field required to sustain anisotropic assembly at low field [12].

4.3 Effect of the polydispersity

To evaluate the role of size and shape dispersion on field-induced assembly, SAXS experiments at 1 T were performed on a more polydisperse sample of cubic Fe nanoparticles with an average size of 15 ± 4 nm (Fig. 23a). The 2D SAXS pattern displayed anisotropy as illustrated by the difference of intensity vertically and horizontally at low-q values, but with less selective angular orientation compared to monodisperse systems (Figure 22a, c, d, f), indicating weaker preferential alignment under the applied magnetic field.

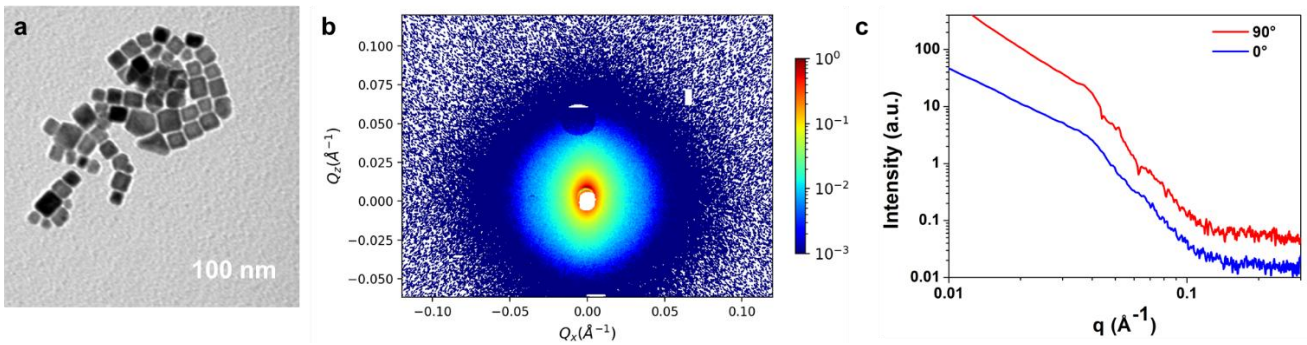

Figure III.23. (a) TEM image, (b) 2D SAXS pattern and (c) the corresponding 1D profile along φ = 0° (blue) and 90°(red) of thin film assembly on glass slide at $\mu_0 H$ = 1T.

To quantify this anisotropy, the scattering intensity was integrated along 0° (parallel to the field) and 90° (perpendicular). In both directions, a slope change appeared at the same q-value, corresponding to the particle size rather than to any specific superlattice reflection. The interparticle distance was estimated at ~17.5 nm, consistent with the nanoparticle diameter plus a ~2–3 nm surfactant shell.

Slope analysis further highlighted the effect of polydispersity. Along 90°, the scattering intensity decayed as $q^{-2.8}$, characteristic of highly disordered, isotropic arrangements with limited long-range order. In contrast, along 0° the decay followed $q^{-2.0}$, indicative of lamellar-like structures aligned with the field. These results suggest that although lamellae can still form along the field direction, the higher degree of polydispersity disrupts long-range hexagonal or cubic ordering and reduces overall anisotropy compared to monodisperse cubic systems. This result is coherent with the literature [13,14].

4.4 Other parameters (concentration, solvent)

The influence of additional experimental parameters, nanoparticle concentration and solvent choice was evaluated in order to assess their role in field-induced organization on glass slide.

Effect of concentration [15,16]. SAXS experiments were first performed with the nanoparticle concentration reduced to half the initial value ($C_0/2$). In all cases, the 2D SAXS patterns exhibited lower anisotropy than at full concentration, indicating that the ability of the magnetic field to induce directional ordering depends not only on field strength and particle properties, but also on particle density in solution (Figure III.24).

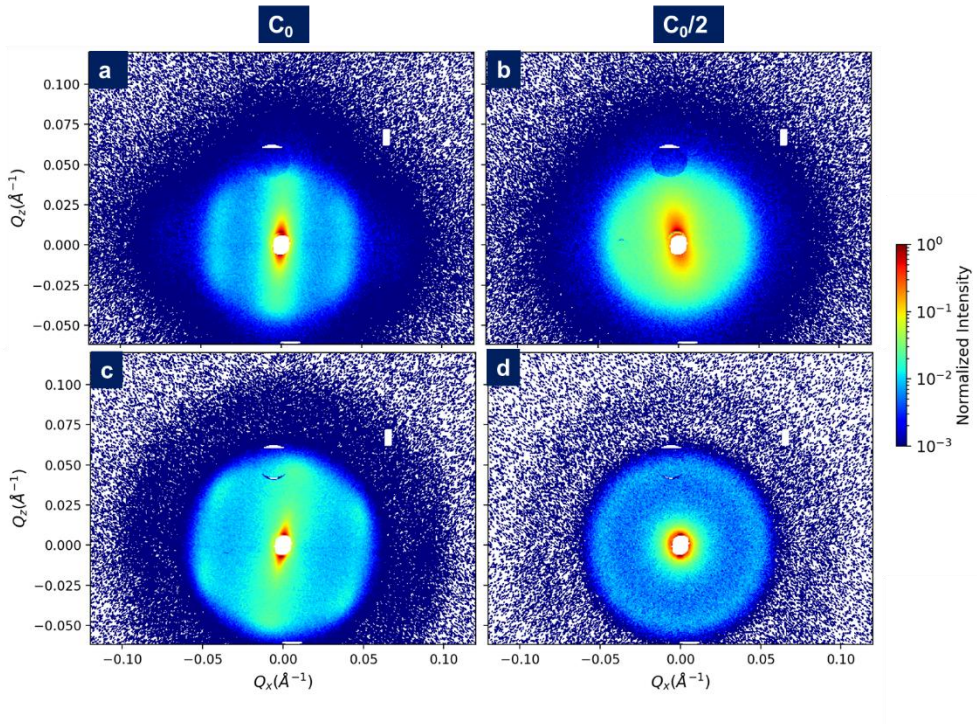

Figure III.24. Comparison of the 2D SAXS pattern obtain from (a-b) $Fe_{0.9}Co_{0.1}$ nanoparticles (20 ± 4 nm) and (c-d) Fe nanoparticles (11 ± 1 nm) assembled on glass slide at 1 T with (a) a concentration (a,c) C_0 and (b,d) $C_0/2$.

Effect of solvent. To assess solvent effects, the same set of nanoparticles was dispersed in ethanol instead of toluene during impregnation. In all cases, anisotropy was further reduced

compared to toluene, highlighting the crucial role of solvent–particle interactions in determining assembly dynamics.

At the macroscopic scale, the morphology of the deposits differed markedly: samples prepared in toluene appeared as networks of thin, interconnected fibers, whereas those obtained in ethanol consisted of dense bundles of thick fibers, with significantly fewer inter-fiber voids and with individual fibers being difficult to distinguish (Appendix 7). This observation consists of ethanol acting as a poor solvent for Fe/FeCo nanoparticles, promoting aggregation and enhancing lateral inter-fiber interactions.

At the nanometer scale, SAXS confirmed these macroscopic differences. As before, only the larger cubic $Fe_{0.9}Co_{0.1}$ nanoparticles (20 ± 4 nm) retained noticeable anisotropy in ethanol though with broader angular dispersion. This anisotropy can be seen by the elongated shape at low q for φ = 90° and through the slope difference on 1D profiles. The power-law decays remained indicative of elongated fiber-like assemblies (Figure III.25c).

By contrast, the smaller cubic Fe nanoparticles (11 ± 1 nm) again showed little to no anisotropy. The SAXS slopes shifted from $q^{-1.5}$ (in toluene) to $q^{-2.0}$ (in ethanol) at 90°, and from $q^{-1.0}$ to $q^{-2.0}$ at 0°, consistent with lamellar-like but isotropic arrangements lacking preferential orientation (Figure III.25f).

Finally, the FeCo squircle-like nanoparticles (11 ± 1 nm) also lost anisotropy in ethanol. Their 2D SAXS patterns appeared isotropic, and slope analysis confirmed the trend: along 90°, the decay remained close to q^{-3}, while along 0° the slope increased from $q^{-1.6}$ to $q^{-2.2}$, suggesting partial lamellar organization without directional alignment (Figure III.25i).

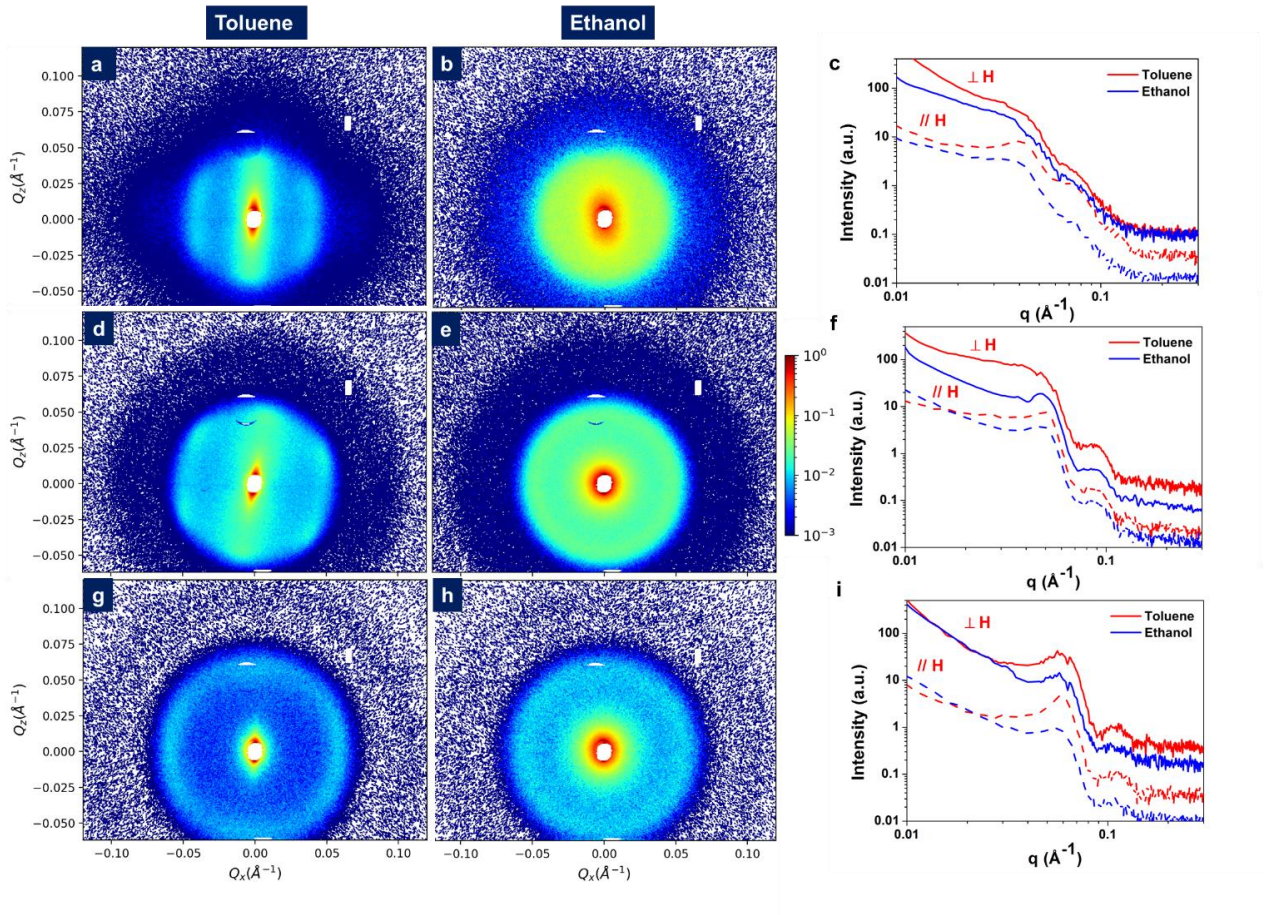

Figure III.25. 2D SAXS pattern of thin film assembly on glass slide of cubic (a-c) $Fe_{0.9}Co_{0.1}$ 20 ± 4 nm and (d-f) Fe 11 ± 1 nm NPs and (g-i) squircle FeCo 11 ± 1 nm NPs after dispersion (a,d,g) in toluene or (b,e,h) in ethanol. Comparison of their SAXS integrations along φ = 0° (dashed line) and 90° (solid line).

To sum up, this systematic investigation of nanoparticle deposition under static magnetic fields has revealed how particle chemistry, size, shape, concentration, and solvent collectively govern the formation of fiber-like assemblies. For CoNi particles synthesized via the polyol route, SAXS analysis demonstrated isotropic random close-packed structures. In contrast, organometallic FeCo nanoparticles, particularly with cubic morphology, exhibited strong field-induced anisotropy and fiber formation, with assemblies adopting distorted hexagonal arrangements. Larger cubic particles maintained structural anisotropy even at reduced fields and lower concentrations, whereas smaller or more rounded particles showed weaker directional order and increasingly isotropic arrangements.

Additional parameters further modulated assembly: high polydispersity disrupted long-range ordering, while solvent choice strongly influenced aggregation dynamics with ethanol being unfavorable for structural order, and anisotropy.

Overall, these results establish that while the applied magnetic field universally drives one-dimensional alignment, the degree of anisotropy, structural organization and long-range order are predominantly dictated by nanoparticle intrinsic properties (size, shape, dispersity) and extrinsic parameters (concentration, solvent, field strength). This understanding provides the basis for rational control of magnetic fiber formation, a crucial step toward the design of dense and reproducible micromagnets.

4.5 Proposed Mechanism

The results obtained in this study highlight the central role of both intrinsic nanoparticle properties (size, morphology, dispersity, and surface chemistry) and external parameters (magnetic field intensity, solvent, and concentration) in governing the structural organization of micromagnets formed by magnetophoresis.

In general, the assembly process can be rationalized as the outcome of competing interactions: *(i)* magnetic dipole–dipole coupling, *(ii)* dipole–field alignment, and *(iii)* steric repulsion mediated by the surfactant shell. The balance among these contributions dictates the head-to-tail chaining of nanoparticles, the lateral association of chains into fibers aligned along the applied field, and the resulting interparticle distances. This competition provides a coherent framework to explain the anisotropic, fiber-like assemblies observed throughout this study.

For cubic nanoparticles, the initial response to the applied magnetic field is the formation of fibers composed of typically three chains parallel to the magnetic field. Within these fibers, nanoparticles may adopt local cubic or hexagonal arrangements depending on the balance of dipolar interactions, spatial confinement, support interaction. Under magnetophoresis, the presence of nickel blocks further concentrates the particles into confined regions, thereby

enhancing lateral interactions. This confinement promotes the bundling of fibers into lamellae, where the overall symmetry often tends toward cubic correlations.

In contrast, spherical nanoparticles exhibit weaker orientational correlations due to their sphericity. These particles preferentially assemble into head-to-tail chains, which then organize into fibers under magnetophoresis with high enough magnetic field. At lower field, isotropic random close-packed (RCP) assemblies are obtained. This result reflects the reduced directional constraint of spherical particles compared to cubic particles.

The role of field intensity can be rationalized by considering the ratio of magnetic dipolar interaction energy to thermal fluctuation energy. At lower fields (0.4 T), thermal disorder competes effectively with dipolar interactions (see Chapter 1), preventing the stable formation of primary chains and resulting in isotropic assemblies mostly random close-packed (RCP) (Figure III.12). This size dependence is particularly evident for cubic particles: larger cubes, owing to their higher magnetic moments ($m \propto V$), are able to maintain anisotropic fiber-like ordering even at moderate fields (0.4–0.5 T), as demonstrated in Section 4.2 (Figure III. 20).

Additional parameters further modulate the assembly pathway. Polydispersity disrupts positional correlations, favoring isotropic packing over ordered structures. Solvent quality influences colloidal stability: poor solvents promote aggregation and lateral interactions, often reducing anisotropy (illustrated by Figure III.25).

Altogether, these findings support a general mechanism in which the interplay of particle shape, size, and magnetic field intensity governs the formation of anisotropic fiber- or lamellae-like micromagnets versus isotropic RCP-type assemblies. The results also emphasize the sensitivity of the assembly process to experimental conditions, underscoring that subtle changes in polydispersity or solvent environment can shift the equilibrium between ordered and disordered structures.

If the density of a micromagnet is to be optimized, priority should be given to a cube assembled in simple cubic with a low amount of ligands. This requires a high external field and sufficiently large particle size.

All the results are resumed in table III.6.

	Spherical NPs	Cubic NPs
Under pure external field		Anisotropic SC
Magnetophoresis 0.4 T	Isotropic RCP	
Magnetophoresis 1 T	Anisotropic fiber	Anisotropic SC fiber

Table III.6. Summarize of the main characteristics for the assembly obtained in that study in function of the shape of the nanoparticles used, and the intrinsic conditions of the assembly.

5. Conclusion

This chapter has demonstrated that the structural organization of micromagnets formed by magnetophoresis arises from a subtle interplay between intrinsic nanoparticle properties and external experimental conditions. Intrinsic parameters such as size, morphology, dispersity, and surface chemistry dictate the primary modes of interaction, while external parameters (including magnetic field intensity, solvent, and concentration) critically modulate the assembly pathway.

Assemblies obtained under homogeneous magnetic fields highlighted the essential role of these parameters in defining the organization of nanoparticles. In particular, cubic and spherical morphologies were shown to form anisotropic fibers, often composed of three parallel chains of particles aligned along the field direction. Under magnetophoresis, the additional spatial confinement imposed by magnetic field gradients enhanced lateral interactions, driving the compaction of these fibers into dense lamellar structures aligned with the applied field.

Magnetic field intensity emerged as a key control parameter. At lower field strengths, particularly for smallest nanoparticles, dipolar interactions were insufficient to overcome thermal fluctuations, preventing chain formation and resulting instead in disordered random close-packed (RCP) assemblies. Conversely, larger cubic particles with stronger dipole moments preserved anisotropy and fiber-like organization even at moderate field intensities.

Overall, these findings support a general mechanism for micromagnet formation: dipole–dipole and dipole–field interactions govern head-to-tail chaining, lateral interaction and ligand-mediated effects regulate interparticle spacing, and magnetophoresis-induced confinement promotes compaction into higher-order lamellar or disordered structures. The balance of these competing factors accounts for the diversity of assemblies observed, ranging from ordered fiber-like lamellae to isotropic close pack micromagnet, and provides guiding principles for the rational design of micromagnets with tunable architectures.

6. References

[1] Moritz P, Gonon A, Blon T, Ratel-Ramond N, Mathieu F, Farger P, et al. Magnetophoresis-Assisted Capillary Assembly: A Versatile Approach for Fabricating Tailored 3D Magnetic Supercrystals. ACS Nano 2021;15:5096–108. https://doi.org/10.1021/acsnano.0c10215.

[2] McDowall D, Adams DJ, Seddon AM. Using small angle scattering to understand low molecular weight gels. Soft Matter 2022;18:1577–90. https://doi.org/10.1039/D1SM01707A.

[3] Anitas EM. Small-Angle Scattering from Fractals: Differentiating between Various Types of Structures. Symmetry 2020;12:65. https://doi.org/10.3390/sym12010065.

[4] Pfeifer P, Ehrburger-Dolle F, Rieker TP, González MT, Hoffman WP, Molina-Sabio M, et al. Nearly Space-Filling Fractal Networks of Carbon Nanopores. Phys Rev Lett 2002;88:115502. https://doi.org/10.1103/PhysRevLett.88.115502.

[5] Rice SA. Small angle scattering of X-rays. A. Guinier and G. Fournet. Translated by C. B. Wilson and with a bibliographical appendix by K. L. Yudowitch. Wiley, New York, 1955. 268 pp. $7.50. J Polym Sci 1956;19:594–594. https://doi.org/10.1002/pol.1956.120199326.

[6] Klokkenburg M, Erné BH, Meeldijk JD, Wiedenmann A, Petukhov AV, Dullens RPA, et al. *In Situ* Imaging of Field-Induced Hexagonal Columns in Magnetite Ferrofluids. Phys Rev Lett 2006;97:185702. https://doi.org/10.1103/PhysRevLett.97.185702.

[7] Klokkenburg M, Erné BH, Wiedenmann A, Petukhov AV, Philipse AP. Dipolar structures in magnetite ferrofluids studied with small-angle neutron scattering with and without applied magnetic field. Phys Rev E 2007;75. https://doi.org/10.1103/physreve.75.051408.

[8] Fiévet F, Ammar-Merah S, Brayner R, Chau F, Giraud M, Mammeri F, et al. The polyol process: a unique method for easy access to metal nanoparticles with tailored sizes, shapes and compositions. Chem Soc Rev 2018;47:5187–233. https://doi.org/10.1039/C7CS00777A.

[9] Percus JK, Yevick GJ. Analysis of Classical Statistical Mechanics by Means of Collective Coordinates. Phys Rev 1958;110:1–13. https://doi.org/10.1103/physrev.110.1.

[10] Schalm O, Anaf W. Laminated altered layers in historical glass: Density variations of silica nanoparticle random packings as explanation for the observed lamellae. J Non-Cryst Solids 2016;442:1–16. https://doi.org/10.1016/j.jnoncrysol.2016.03.019.

[11] Faraudo J, Andreu JS, Calero C, Camacho J. Predicting the Self-Assembly of Superparamagnetic Colloids under Magnetic Fields. Adv Funct Mater 2016;26:3837–58. https://doi.org/10.1002/adfm.201504839.

[12] Barrett M, Deschner A, Embs JP, Rheinstädter MC. Chain formation in a magnetic fluid under the influence of strong external magnetic fields studied by small angle neutron scattering. Soft Matter 2011;7:6678. https://doi.org/10.1039/c1sm05104k.

[13] Kantorovich S, Ivanov AO. Formation of chain aggregates in magnetic fluids: an influence of polydispersity. J Magn Magn Mater 2002;252:244–6. https://doi.org/10.1016/S0304-8853(02)00651-0.

[14] Ivanov AO, Kantorovich SS. Chain aggregate structure and magnetic birefringence in polydisperse ferrofluids. Phys Rev E 2004;70:021401. https://doi.org/10.1103/PhysRevE.70.021401.

[15] Wu H, Xu Z, Wang J, Bo X, Tang Z, Jiang S, et al. Chain formation mechanism of magnetic particles in magnetorheological elastomers during pre-structure. J Magn Magn Mater 2021;527:167693. https://doi.org/10.1016/j.jmmm.2020.167693.
[16] Fermigier M, Gast AP. Structure Evolution in a Paramagnetic Latex Suspension. J Colloid Interface Sci 1992;154:522–39. https://doi.org/10.1016/0021-9797(92)90165-I.

Chapter 4. Dynamic properties and RF applications

Summary of Chapter IV

1 Sample designs, measurements, and characteristic extraction methods 169

1.1 Electrical measurements 169

1.1.a S-parameters measurement 169

1.1.b Inductance measurements 172

1.1.c Determination of the complex permittivity and permeability 173

1.2 RF Electrical characterization chips 176

1.2.a Introduction to SAXS 176

1.2.b Electromagnetic simulation (ADS/HFSS) 182

1.2.c Fabrication process 185

2 FeCo particles obtained from reduction approach **187**

2.1 Reproducibility and measurement uncertainty 187

2.2 Characterization of dynamics properties 189

2.3 Demonstrations on Inductors 190

3 Nanoparticles from organometallic approach **192**

3.1 Oxidation issue 192

3.1.a Fe and $Fe_{0.6}Co_{0.4}$ without epoxy protection 192

3.2 Overcoming the issue of oxidation (epoxy protection, FeC) 194

3.2.a Effect of the NPs size on iron and the role of epoxy 194

3.2.b Composition effect on ≈15 nm particles 197

3.2.c Composition effect on ≈9 nm nanoparticles 199

3.3 Discussion 201

4 CoNi particles from polyol synthesis **204**

4.1 Control of dynamical magnetic and dielectric properties 204

4.1.a Size effect 205

4.1.b Chemical composition effect 207

4.1.c Effect of a static field 208

4.2 Application of the implementation of inductor core 210

4.2.a Inductor core applications without static field 210

4.2.b Inductance tunability with an external bias field 213

5 Conclusion **215**

6 References **217**

The integration of magnetic nanoparticles into radiofrequency applications requires materials that exhibit not only favorable magnetic properties and appropriate dielectric behavior, but also compatibility with soft integration techniques. Furthermore, for electronics engineers, reliable frequency-domain characterization of these materials is essential to ensure their efficient implementation in the design and simulation of electronics devices [1–3]. This chapter addresses the dynamic properties of nanoparticle-based micromagnets and their suitability for RF applications, particularly as magnetic cores for inductors.

The first section of this chapter outlines the design, simulation, and fabrication of dedicated test chips developed for RF characterization. These microfabricated chips incorporate coplanar waveguides (CPWs) enabling extraction of the micromagnet complex permeability and complex permittivity and various inductors used as demonstrators of the effectiveness of the studied micromagnet. Following, the chapter presents the RF performance of micromagnets based on different types of nanoparticles synthesized by distinct chemical approaches. FeCo particles obtained from a reduction approach are used as a reference material, providing criterion for evaluating the impact of more controlled synthetic methods. Nanoparticles produced via an organometallic route are then examined, with particular attention to issues related to oxidation and strategies to mitigate it, such as using epoxy protection or adjusting the intrinsic chemical composition of the NPs using carbidization process. Finally, the dynamic behavior of CoNi particles synthesized by the polyol method are presented with a particular focus on the influence of particle size, chemical composition, and the application of a static magnetic field. All of the materials studied are evaluated both in terms of their intrinsic electromagnetic properties and their contribution when integrated as magnetic cores in inductor demonstrators.

1. Sample designs, measurements, and characteristic extraction methods

1.1 Electrical measurements

1.1.a S-parameters measurement

Electrical characterization was performed using a **vector network analyzer (VNA, Keysight N5247B PNA-X)** with ground-signal-ground (GSG) probes (150 µm pitch). The frequency range spanned from 10 MHz to 40 GHz. These measurements have been performed in LAAS, Toulouse.

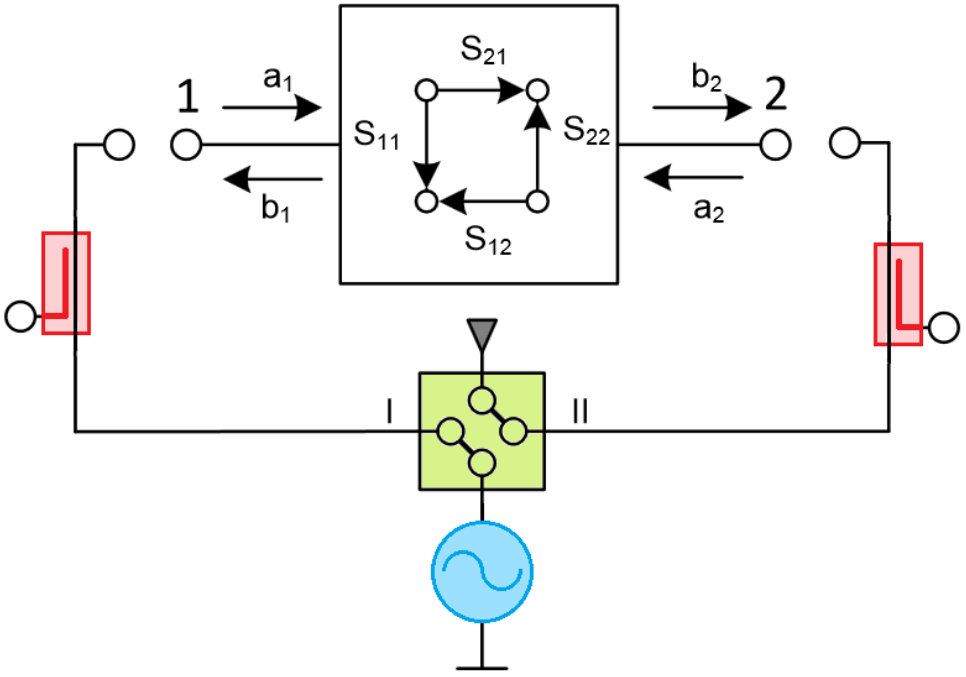

Figure IV.1. Schematic diagram of S-parameter measurement using a VNA with a single RF source [4].

A VNA is used to measure the transmission (S_{21}) and reflection (S_{11}) scattering parameters, commonly referred to as S-parameters [5]. The principle is illustrated by Figure IV.1. It is based on the emission and reception of waves from two different probes. For the characterization of a 2-port network, a typical experiment consists of applying an incident wave a_1 which is applied on the Port 1 of the device under test (DUT), then, the source is commuted at Port 2 the transmitted wave b_2 is measured, and the reflective wave b_1 is measured on the Port 1. The complex relationships between incidents, reflected, and transmitted signals define the scattering matrix (S-matrix) coefficients S_{ij}, which are expressed as:

$$\begin{bmatrix} b_1 \\ b_2 \end{bmatrix} = \begin{bmatrix} S_{11} & S_{12} \\ S_{21} & S_{22} \end{bmatrix} \begin{bmatrix} a_1 \\ b_1 \end{bmatrix} \qquad \text{(IV. 1)}$$

Here, S_{ii} represents the complex reflection coefficient at Port i with $S_{ii} = \left.\frac{b_i}{a_i}\right|_{a_j=0}$, and S_{ij} (for $i \neq j$) is the complex transmission coefficient from Port j to Port i, expressed as $S_{ij} = \left.\frac{b_i}{a_j}\right|_{a_{i=0}}$.

The modelling of a component can further require the admittance matrix (Y-parameters) which connects total voltages and currents at each of the 2 ports:

$$\begin{bmatrix} I_1 \\ I_2 \end{bmatrix} = \begin{bmatrix} Y_{11} & Y_{12} \\ Y_{21} & Y_{22} \end{bmatrix} \begin{bmatrix} V_1 \\ V_2 \end{bmatrix} \qquad \text{(IV. 2)}$$

These Y-parameters can be derived from S-parameters using the following relationships, with Y_0 the reference admittance at each port, assumed to be the same for the two ports [5].

$$Y_{ii} = \frac{(1-S_{ii})(1+S_{jj})+S_{ij}S_{ji}}{(1+S_{ii})(1+S_{jj})-S_{ij}S_{ji}} * Y_0 \qquad \text{(IV. 3)}$$

$$Y_{ij} = \frac{-2S_{ij}}{(1+S_{ii})(1+S_{jj})-S_{ij}S_{ji}} * Y_0 \qquad \text{(IV. 4)}$$

Note that the impedance matrix (Z-parameters), which is the inverse of the Y-parameter matrix can be calculated from S-parameters as well: $Y = Z^{-1}$ (IV. 5)

When working at high frequencies (microwave, radiofrequency), the calibration procedure is critical for the accuracy of measurements. This includes not only the vector network analyzer, but also the effect of interconnections between the VNA and the DUT which cannot be

ignored. Electrical characteristics of a lot of components involved depend on frequency and temperature, and systematic correction is required to ensure meaningful data. For this work, a Short-Open-Load-Through (SOLT) calibration was performed [6], which is based on measurements of a short circuit (S), an open circuit (O), a matched load 50 Ω (L), and a thru 50 Ω line (T). A calibration substrate incorporating all these standard components in a coplanar wave guide configuration (a CPW is a type of electrical planar transmission line which is used to convey microwave-frequency signals), which can be measured under Ground-Signal-Ground (GSG) probes, is used. Comparing measurements and known models of these standards, the VNA internal software can compute and apply appropriate correction to the raw data, using a predefined error model.

Supplementary correction can also be required. This step is called de-embedding, and it consists in shifting the measurement reference planes from the physical probe contact points to the boundaries of the DUT as illustrated on Figure IV.2. For this process, the S-parameters must be rescaled by the inverse of the transmission factor associated with the CPW sections which are just access lines to the tested sample. This factor depends on the propagation constant γ_0 within these accesses. This constant can be determined by measuring the transmission S_{21}^{CPW} of a line without any sample. As the CPW then acts as a homogenous transmission line of total length l_{total}, the corrective factor k can be computed with the following equations.

$$S_{21}^{CPW} = e^{-\gamma_0 l_{total}} \qquad \text{(IV. 6)}$$

$$k^{-1} = (e^{-\gamma_{0(}l_{total}-l_s)})^{-1} = e^{\left[-\frac{l_{total}-l_s}{l_{total}}\ln(S_{21}^{CPW})\right]} \qquad \text{(IV. 7)}$$

Here, $l_s$is the length of the line section which will include the sample under test, delimited by the dimension of the micromagnet in our case, as illustrated on Figure IV.2.

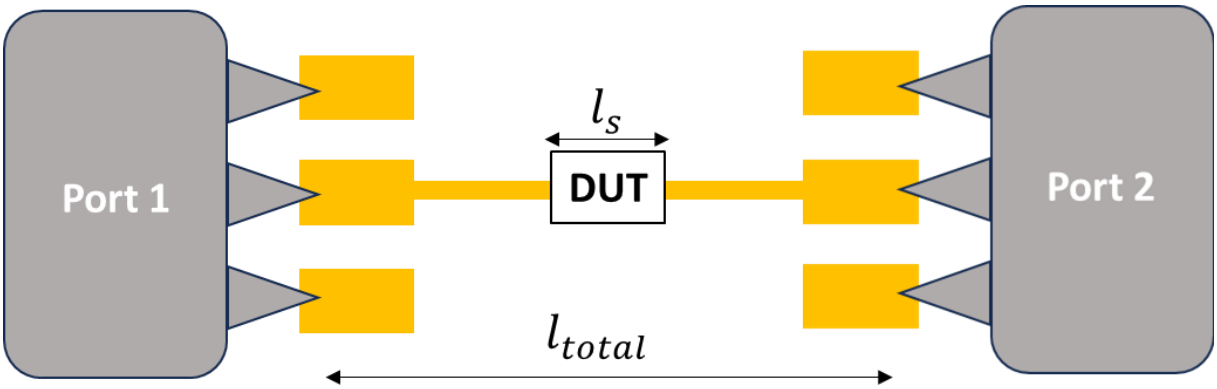

Figure IV.2. Schematic representation of the de-embedding dimensions for a DUT placed between ports 1 and 2. This line has a total length l_{total} (distance between the probes), of which a section of length l_s is the DUT.

So, the direct S-parameters ($S_{ij}^{l_{total}}$) of the total line including the DUT are first measured. Then, after applying the previously described correction, the resulting de-embedded S-parameters (S_{ij}) represent solely the behavior of the CPW segment that contains the DUT. They can be written as:

$$S_{21} = k * S_{21}^{l_{total}} \qquad (\text{IV}.8)$$

$$S_{11} = k * S_{11}^{l_{total}} \qquad (\text{IV}.9)$$

1.1.b Inductance measurements

The demonstrators of the electromagnetic performance of the micromagnets are the inductors integrated on the test chip. The direct measurements of planar inductors before and after magnetic material deposition reveal the effect of the magnetic material, namely the inductance and quality factor values as a function of the microwave frequency. The methodology involves the use of the Y-parameters obtained from the de-embedded S-parameters. The quality factor (Q) and inductance (L) can be extracted as:

$$Q = -\frac{\text{Im}\,(Y_{11})}{\text{Re}\,(Y_{11})} \qquad (\text{IV}.10)$$

$$L = \frac{\text{Im}\,(Y_{11}^{-1})}{\omega} \qquad (\text{IV}.11)$$

Where ω is the angular frequency, and Y_{11} is the input admittance. The quality factor, defined as the ratio of the stored energy to the dissipated one per cycle, is a key figure of merit in resonant and filtering applications, where high Q values indicate superior energy efficiency and frequency selectivity.

Such measurements on inductors have been performed in LAAS, Toulouse, using the same VNA as the CPW measurements described above.

1.1.c Determination of the complex permittivity and permeability

1.1.c.i Transmission/reflection model on CPW

In order to characterize the high-frequency electromagnetic properties of the micromagnet deposited on the CPW, S-parameter measurements up to 30 GHz were conducted on the same CPW before and after deposition. As described before, measurements were conducted using a vector network analyzer (N5247B PNA-X) connected to the devices via Ground-Signal-Ground (GSG) probes. After SOLT calibration and de-embedding, the effective complex permittivity (ε_{eff}) and permeability (μ_{eff}) were extracted using a well-established transmission/reflection model based on S-parameters [7,8]:

$$S_{21} = k * S_{21}^{l_{total}} = \frac{P(1-\Gamma^2)}{1-P^2\Gamma^2} \quad \text{(IV.12)}$$

$$S_{11} = k * S_{11}^{l_{total}} = \frac{\Gamma(1-P^2)}{1-P^2\Gamma^2} \quad \text{(IV.13)}$$

$$\Gamma = \chi \pm \sqrt{\chi^2 - 1} \quad \text{(IV.14)}$$

$$\chi = \frac{S_{11}^2 - S_{21}^2 + 1}{2S_{11}} \quad \text{(IV.15)}$$

$$P = \frac{S_{11} + S_{21} - \Gamma}{1-(S_{11}+S_{21})\Gamma} = |P|e^{j\varphi} \quad \text{(IV.16)}$$

$$\gamma = \frac{1}{L} \cdot \ln\left(\frac{1}{|P|}\right) + j\frac{-\varphi}{L} \quad \text{(IV.17)}$$

$$\gamma_0 = j\frac{\omega}{c} \qquad \text{(IV.18)}$$

$$\varepsilon_{eff} = \left(\frac{\gamma}{\gamma_0}\right) \cdot \left(\frac{1-\Gamma}{1+\Gamma}\right) = \varepsilon'_{eff} - j\varepsilon''_{eff} \qquad \text{(IV.19)}$$

$$\mu_{eff} = \left(\frac{\gamma}{\gamma_0}\right) \cdot \left(\frac{1+\Gamma}{1-\Gamma}\right) = \mu'_{eff} - j\mu''_{eff} \qquad \text{(IV.20)}$$

In these expressions, Γ is the reflection coefficient ($+/-$ sign chosen such that $|\Gamma|<1$), χ relate to transmission coefficient, P is the propagation factor with phase φ, γ is the complex propagation constant in presence of material, and γ_0 is the free-space propagation constant. This model assumes **quasi-TEM wave propagation** and characterizes the electromagnetic behavior of the CPW section placed in a single homogeneous dielectric medium which is composed of the micromagnet and the silicon substrate. It leads to the extraction of the effective characteristics (ε_{eff} and μ_{eff}) of this medium. While they do not represent the intrinsic material constants of the micromagnet alone, these effective properties can provide a comparative evaluation between different materials.

The relative permittivity ε_r and relative permeability μ_r of the micromagnet alone can be further approximated using conformal mapping techniques applied to the CPW geometry [9], assuming a high-resistivity silicon substrate ($\varepsilon_{substrate}$= 11.9 and $\mu_{substrate}$= 1.0):

$$\varepsilon_r = 2\varepsilon_{eff} - \varepsilon_{substrate} \qquad \text{(IV.21)}$$

$$\mu_r = \frac{\mu_{eff}}{2-\mu_{eff}} \qquad \text{(IV.22)}$$

Using this methodology, assuming that the material has a relative permittivity ε_r of at least 1, effective permittivity values exceeding 6.45 are predicted (Eq. IV.21), while effective μ_{eff} permeability values typically range between 1 and 2 for μ_r ranging between 1 and ∞, respectively (Eq. IV.22).

1.1.c.ii FMR measurements from reflection on short-circuited line

In order to evaluate the magnetic response of the deposited micromagnets under dynamic conditions, reflection measurements were also conducted on short-circuited CPW structures when an external static magnetic field is applied. Contrary to the previous introduced measurements on CPW and inductors that have been realized at LAAS, these measurements on short-circuited CPW have been performed in CEMES, Toulouse, with Nicolas Bizière, CR CNRS, on a dedicated set-up. The experimental setup consists of a sample placed inside an electromagnet capable of generating a static magnetic field up to 600 mT. The coplanar waveguide is connected to one port of the VNA (Anritsu MS4642A) via picoprobes and a non-magnetic coaxial cable allowing simultaneous measurements of S_{11} and the application of a controlled magnetic field along the length of the waveguide. The frequency is swept from 10 MHz to 20 GHz. The setup is schematized on Figure IV.3.

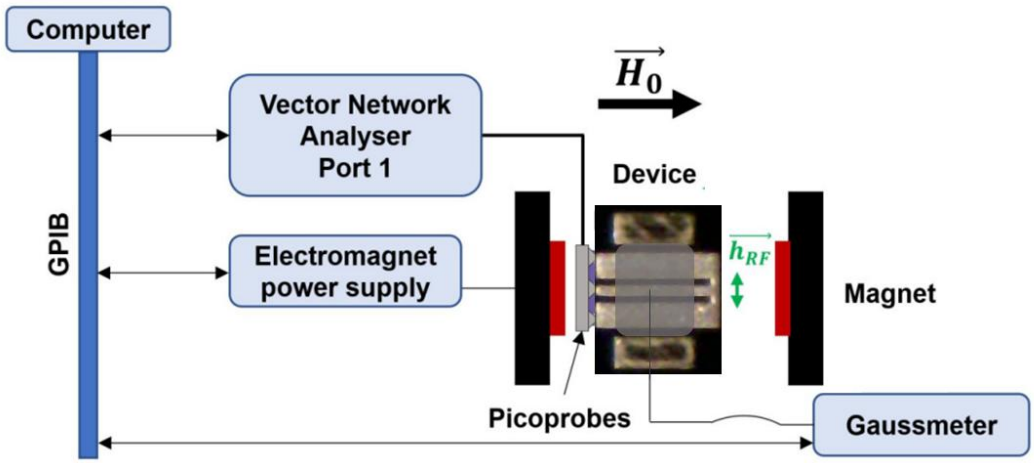

Figure IV.3. Schematic of the VNA-FMR measurement setup using a short-circuited CPW cover with a micromagnet [10].

Given the short length of the short-circuited line, it is modeled as simple RL circuit. This assumption remains valid as long as the material placed on the line does not introduce significant losses, which depend on both the quantity of material and its relative loss factor. Thus, the inductive response of the device was extracted from the variation of the complex input impedance $Z_{11}(H, f)$ as a function of frequency (f) and applied magnetic field (H). Since

the impedance change arises solely from inductive coupling, the corresponding change in inductance $\Delta L_{11}(H,f)$ can be expressed as [11–13]:

$$\Delta L_{11}(H,f) = \frac{Z_{11}(H,f) - Z_{11}^{ref}}{j2\pi f} = \mu_0 \beta l\left(\mu_{eff} - 1\right) \qquad \text{(IV.23)}$$

In this expression, Z_{11}^{ref} represents the reference impedance acquired in the absence of gyromagnetic effect, typically at a magnetic field well beyond resonance. Here, μ_0 is the permeability of free space, β the filling factor, and l the coupling length (= the length of the transmission line where the coupling takes place). This formulation enables to quantify the effect of the magnetic field on the permeability $\mu_{eff}(H,f)$. These experiments are intended to probe the field-dependent ferromagnetic resonance (FMR) in order to assess the dynamic magnetic response. This, in turn, facilitates the interpretation of the real and imaginary parts of the permeability (μ' and μ") obtained from non–short-circuited CPW measurements carried out without an external magnetic field, and thus the frequency-dependent behavior of the inductors.

1.2 RF Electrical characterization chips

1.2.a Description of the chips and micro-components

To evaluate the RF properties of magnetic nanoparticles, two different 1 cm² test chips were designed, chip-1 and chip-2. These chips were fabricated on 400 µm thick high-resistivity silicon substrates (Si/SiO_2, n-type, ρ > 3000 Ω.cm, wafers of 100 mm diameter with (100) direction).

Each Chip-1 (Figure IV.4) contains three pairs of coplanar waveguides (CPWs) and six planar inductors. All structures are fabricated from copper with an approximate thickness of 5 µm. Nickel blocks of 500 µm (length) × 200 µm (width) × 75 µm (thickness) are located on both sides of each of these components to ensure magnetophoresis. The spacing between the nickel blocks and the edge of the component was fixed at 50 µm in order to avoid excessive separation of the blocks, which would diminish the magnetic force acting on the nanoparticles during magnetophoresis. Coplanar waveguide (CPW), and inductor CPW access structures

were designed for avoiding any electrical discontinuities during probing with Ground-Signal-Ground (G-S-G) probes featuring a 150 µm pitch. The CPWs (upper part of Fig. IV.5) have a central strip of width (W), separated by a gap (S) from (W_g) wide ground planes. They exhibit a material-free characteristic impedance (Z_c) of 50 Ω and were designed thanks to ADS and ANSYS-HFSS simulations and optimizations on (W), (S) and (W_g) triplet values. The simulations are described in the next part, in terms of objectives and methodology. S is (38, 45, 53) µm for W values of (50, 60, 70) µm, and W_g (150, 150, and 130) µm respectively. The total CPW length is 2 mm. The notations used are illustrated on Figure IV.4. Each CPW is replicated twice on the cell. This is summarized in Table IV.1.

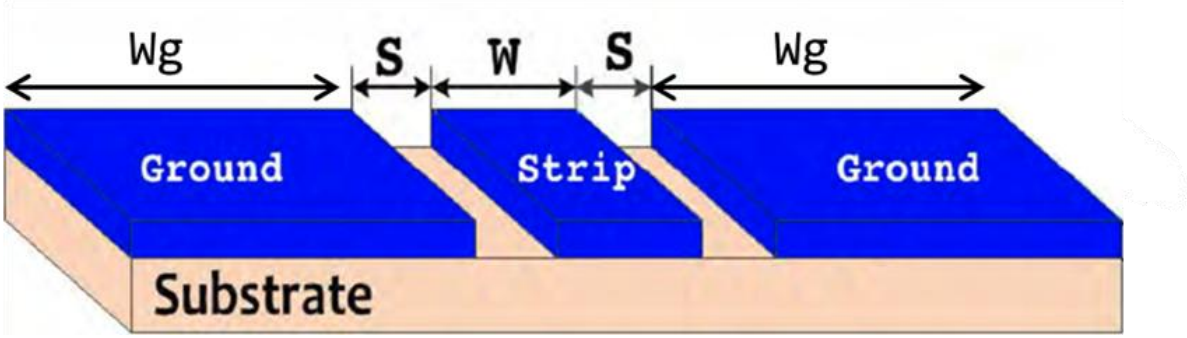

Figure IV.4. Schematic representation of the coplanar line [14].

Six different rectangular inductors (lower part of Figure IV.5) are each surrounded by a 180-µm wide ground ring. The ground ring is used to define the return path; the ring shape is chosen to ensure a homogenous interaction around all the inductor without discontinuities. The different inductors have been designed thanks to simulations and implemented by varying the strip width (W_s), the inter-spiral gap (S_s) and the number of turns in order to present different inductance, Q-factors and working frequencies restricted by the self-resonance frequency f_r. A compilation of these parameters is provided in Table IV.2 for each inductor. With these different variations, these inductors cover a wide range of potential applications.

CPW	W (µm)	S (µm)	W_g (µm)	Z_c (Ω)	Length (mm)
CPW-1 and CPW-4	70	53	130	50	2
CPW-2 and CPW-5	60	45	150	50	2
CPW-3 and CPW-6	50	38	150	50	2

Table IV.1. Geometric parameters of different CPW on chip-1.

Inductors	W_s (µm)	S_S (µm)	Turns	f_r (GHz)	Q-factors	L (nH)
L_1	10	10	1.5	12.0	10	2.0
L_2	30	30	1.5	11.5	16	1.7
L_3	10	10	1.75	6.5	11	4.0
L_4	30	30	1.5	8.0	18	2.5
L_5	30	30	2.5	5.2	19	4.5
L_6	10	10	4.5	3.0	10	13

Table IV.2. Geometric and electrical parameters of inductors on chip-1.

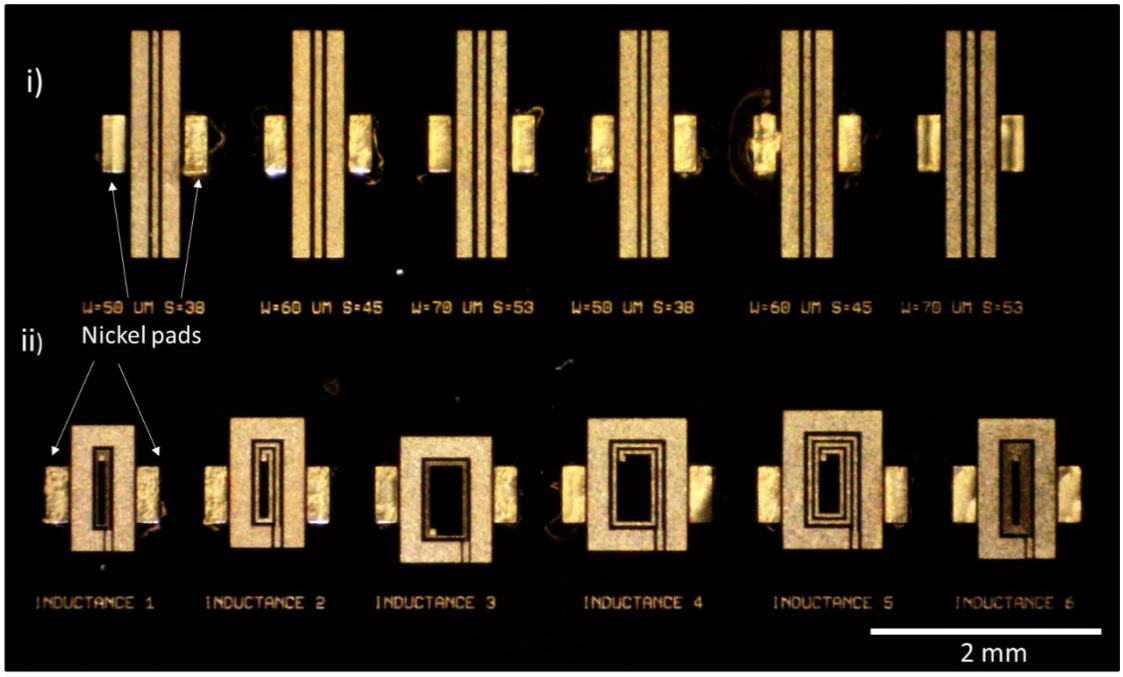

Figure IV.5. Optical photograph of a chip with (i) CPWs, (ii) and inductors with the Ni pads.

The second chip illustrated in figure IV.6 (referred to as chip-2), integrates three CPWs configurations, each corresponding to the one of the three lateral dimension sets (W, S, W_g) previously introduced for chip-1. For each of these three configurations, four short-circuited CPWs were designed, each with a length of 750 µm long to promote a predominantly inductive response. Several sizes were chosen for nickel pad (upper part of Fig. IV.6); the goal is to expose different length of line to the magnetic material. Indeed, the exposed length to the magnetic material plays a crucial role in the measurement: if the length is too short, the influence of the material on the signal may be negligible; conversely, if the length is too long the material may overly attenuate or even completely absorb the RF signal. Also, the optimal length depends on the specific magnetic and dielectric properties of the material under study, so the use of several different pad sizes increases the likelihood of identifying a suitable volume of material for effective RF interaction. Consequently, among the four shorted CPWs in each configuration, three are surrounded by nickel blocks of various sizes: 100 µm × 100 µm, 200 µm × 200 µm, or 200 µm × 500 µm. This new configuration is summarized in Table IV.3.

Chip-2 integrates also nine different inductors, including two inductors with an octagonal shape. This design is expected to enhance the Q-factor compared to rectangular inductors by mitigating edge effects. Their parameters are resumed in Table IV.4 for each inductor.

CPW	W (µm)	S (µm)	W_g (µm)	Length (mm)	Nickel block size (µm)
CPW-1	70	53	130	2	200 × 500
CPW-2	60	45	150	2	200 × 500
CPW-3	50	38	150	2	200 × 500
CPW-1 shorted	70	53	130	0.750	200 × 500; 200 × 200; 100 × 100
CPW-2 shorted	60	45	150	0.750	200 × 500; 200 × 200; 100 × 100
CPW-3 shorted	50	38	150	0.750	200 × 500; 200 × 200; 100 × 100

Table IV.3. Geometric parameters of different CPW on chip-2.

Inductors	Shape	W_s (µm)	S_s (µm)	Turns	f_r (GHz)	Q-factors	L (nH)
L_1	Oct.	20	20	1.5	12.5	13	1.7
L_2	Rect.	40	40	1.5	10.7	11	1.8
L_3	Rect.	20	30	1.5	8.3	8	2.6
L_4	Rect.	50	10	2.5	6.5	7	3.2
L_5	Rect.	20	20	1.5	6.0	6	3.9
L_6	Rect.	15	15	3.5	4.3	4	8.0
L_7	Oct.	15	30	3.5	4.2	4	8.2
L_8	Rect.	20	20	4.25	3.7	4	9.5
L_9	Rect.	30	10	4.5	3.1	3	11.8

Table IV.4. Geometric and electrical parameters of inductors for chip-2.

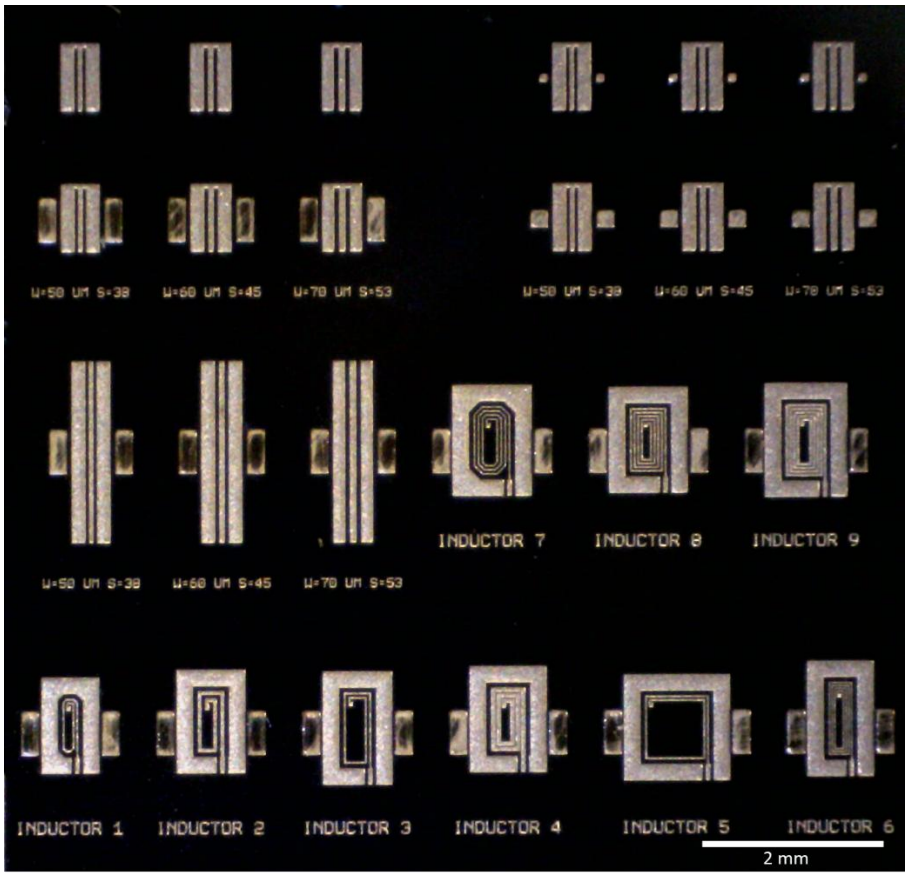

Figure IV.6. Optical photograph of CPWs, and inductors electrodeposited, along with the Ni pads on chip-2.

Since the sample studied (here a deposited micromagnet) only covers a part of the CPW, it is necessary to remove the contribution of the input and output CPW access lines. Therefore, the de-embedding consists in shifting the measurement reference planes from the physical probe contact points to the boundaries of the sample which is the DUT (see section 1.1.a). Figure IV.7 represents the de-embedding dimensions directly on a typical structure used during this study.

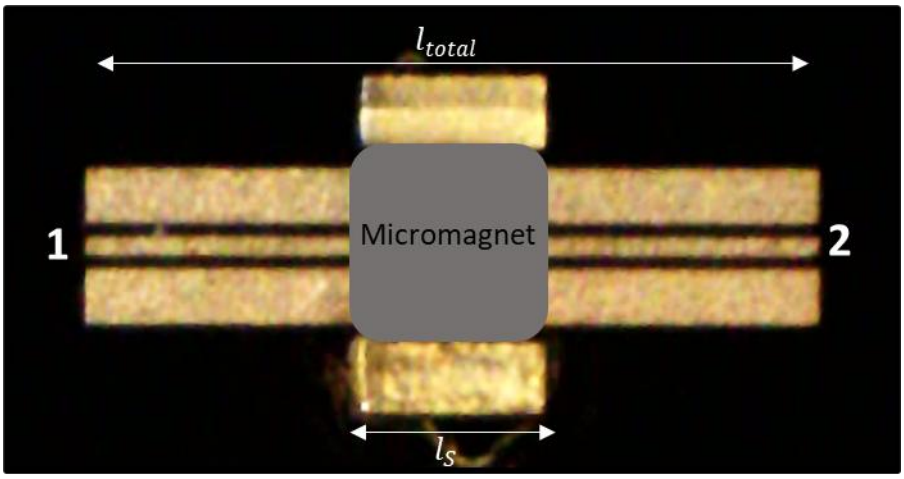

Figure IV.7. Schematic representation of the de-embedding dimensions for a CPW placed between ports 1 and 2. This CPW has a total length l_{total}, of which a section of length l_s is covered by a micromagnet (DUT).

1.2.b Electromagnetic simulation (ADS/HFSS)

This section presents the simulation methodology used to design coplanar waveguides (CPWs) and integrated inductors. Two complementary simulation tools were used: **Keysight Advanced Design System (ADS),** which relies on electrical models, and **ANSYS HFSS**, which is a 3D full-wave simulator that numerically solves Maxwell's equations.

CPW. First, the simulation stage involved the use of ADS LineCalc, a tool based on analytical models developed by G. Ghione [15], to calculate the characteristic impedance of CPW lines. The substrate used was high-resistivity silicon (HR-Si), with a dielectric constant $\varepsilon_{substrate} = 11.9$ and a thickness of 400 µm. The conductive strips were modeled using 5 µm-thick copper with a conductivity of 5.8×10^7 S/m. While maintaining a fixed line length of 2 mm, the signal line width (W) and the gap to ground (S) were varied to achieve a characteristic impedance of 50 Ω. To further optimize the design, HFSS simulations were performed to account for the finite width of the ground planes and to evaluate several key aspects:

- Ensuring not several impacts of the finite width of the ground on the characteristic impedance of the line.

- ensuring that the RF magnetic field is sufficiently confined within the coplanar line and does not interact with the magnetic field from Ni pads and so avoiding parasitic electromagnetic coupling.
- analyzing the intensity and spatial variation of the electromagnetic fields to ensure that most of the wave is confined in a thickness equivalent to the nickel pad thickness.

The CPW structures simulated in HFSS were exciting using wave ports, and simulations were carried out over a frequency range from 0.5 MHz to 10 GHz. W_g was systematically varied and optimized for each CPW geometry selected from ADS.

The three fabricated CPW structures — defined by the dimensions (W= 50 µm, S = 38 µm, W_g = 150 µm), (W =60 µm, S = 45 µm, W_g = 150 µm), and (W = 70 µm, S = 53 µm, W_g = 130 µm) were experimentally tested to validate the simulated characteristic obtained using both ADS and HFSS. The experimental results for these three configurations are presented in Figure IV.8 where the reflection S_{11} are plotted on a normalized Smith chart with a reference impedance of 50 Ω (Figure IV.8). It means that the central point is 50 Ω. Across the measured frequency range, the S_{11} responses confirm that the characteristic impedance Z_c of each CPW closely matches the expected 50 Ω target. Transmission (S_{21}) measurements further confirmed that the losses along the CPW line were negligible (Figure IV.9), an attenuation of about 2 dB is determined, equivalent to 98% of signal transmitted. These results not only validate the accuracy of our simulations but also demonstrate that the fabricated lines exhibit low losses, indicating good impedance matching and high-quality transmission performance.

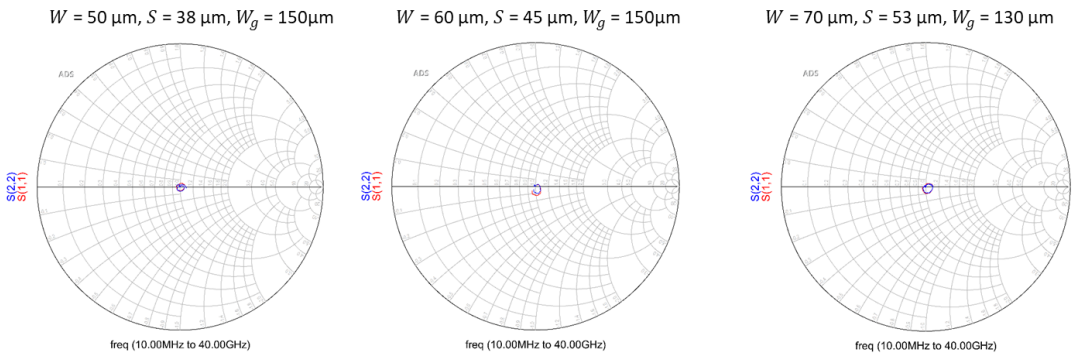

Figure IV.8. Smith chart showing the evolution of the S11 parameter for the three CPW geometries produced.

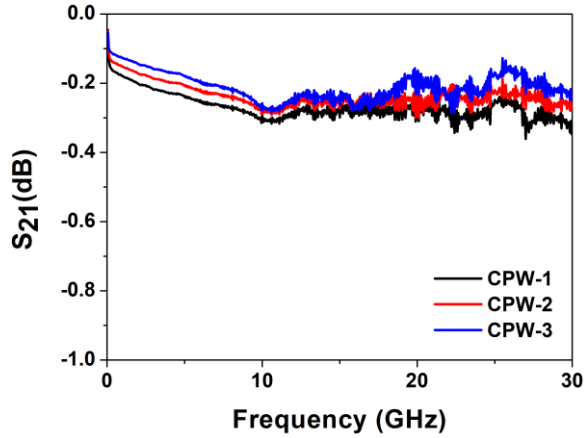

Figure IV.9. Experimental measurements of transmission parameter S21 for the three CPW geometries produced.

Inductor. The objective is to design a series of planar inductor geometries with inductance values ranging from a few to several tens of nanohenries, resonance frequencies reaching up to approximately 10 GHz, and the highest achievable quality factor within the given design constraints. Thus, first, the inductor designs were tested and simulated in ADS over a frequency range from 0 to 10 GHz for determining the inductance and quality factor. The goal is the pre-dimensioning of the inductors. As with the CPWs, ADS does not account for radiation losses or the influence of the ground ring. Therefore, HFSS simulations were necessary to assess inductor behavior in more realistic conditions. HFSS simulations were conducted using wave-port excitations over a 0–10 GHz frequency range. Within the tested range of W_g = 150 ± 50 µm, variations in electrical performance remained moderate. Consequently, a fixed ground ring width of 180 µm was selected. Then the simulated properties has been confirmed by comparison with experimental measurements. The inductance values (L) and quality factors (Q) across the various tested structures were compared on the frequency range below the self-resonant frequency of each inductor. The results, presented in Figure IV.10, indicate that the electromagnetic simulations performed with HFSS provide a more accurate representation of both inductance and Q-factor when compared to those obtained using ADS. This highlights even more the limitations of the analytical model implemented in ADS, particularly its inability to account for the geometric extension of the ground plane. As a result,

the ADS model is useful for quick pre-dimensioning of the structure but not well suited to meet the precision requirements of this project.

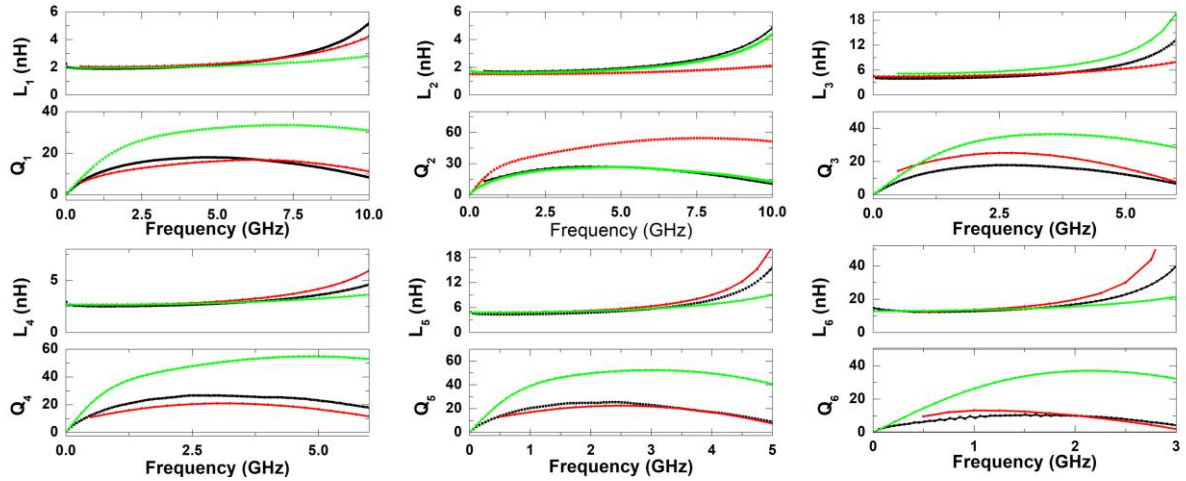

Figure IV.10. Frequency evolution and comparison of the inductance values and quality factors obtained experimentally (black), and through ADS (green) and HFSS (red) simulations, for the following structures: Inductor#1, Inductor#2, Inductor#3, Inductor#4, Inductor#5, and Inductor#6 of chip 1.

1.2.c Fabrication process

The test chips were fabricated on 400 µm thick, high-resistivity silicon wafers (n-type, $\rho > 3000$ Ω.cm, wafers of 100 mm diameter, (100) orientation) using standard microfabrication techniques. After cleaning the wafers (BHF, DI water), a 100 nm Ti/200 nm Cu seed layer was deposited via e-beam evaporation. About 20 µm thick AZ 40XT photoresist mold was patterned by photolithography, followed by electroplating about 5 µm thick Cu layer at 8 A/dm² to define the conductive strips. The mold was then removed using acetone. Next, a 100 µm thick WBR 2100 photoresist mold was laminated and patterned to enable electrodeposition of Ni alignments blocks (500 µm long, 200 µm wide, about 75 µm thick for CPW and inductors, or 500 µm long, 200 µm wide, about 75 µm thick for shorted structured) at 4 A/dm^2. After removing the mold (TechniStrip NF52), the Ti/Cu seed layer was wet-etched, and metal annealing was carried out at 250°C for 20 minutes under nitrogen. A 100 nm-thick Au protective layer was deposited electrolessly on the metal lines and Ni pads. Finally, the

wafer was diced, and individual 1 cm^2 chips were wire-bonded to connect the internal port of the inductors to ground for a simple 1-port characterization.

2. FeCo particles obtained from reduction approach - reference material

With the measurement protocols, device architectures, and extraction models previously described, the following sections concern the characterization of the micromagnet properties. As a preliminary step we examine FeCo microparticles synthesized through a reduction method with hydrazine. This approach is favored for its simplicity, but it offers limited control in particular on size, and size distribution. In that subpart, the dynamical properties of the micromagnet obtained from these particles are presented. These micromagnets particles serve as a benchmark reference.

2.1 Reproducibility and Measurement Uncertainty

To assess the reliability and precision of the parameter extraction methodology for dynamically characterizing micromagnets deposited via magnetophoresis onto CPWs, an evaluation of measurement reproducibility was conducted. Specifically, the effective complex permeability and permittivity values were extracted independently from each of the six CPWs on a test chip (same batch of magnetic particles), allowing for a statistical estimation of the associated uncertainty. This is illustrated in Figure IV.11.

For the real part of the effective permeability (μ'_{eff}), results across the six CPWs remained consistent, with slight variations observed, at 1 GHz, values ranged from 1.52 to 1.70. Based on this, the uncertainty on μ' is estimated at ±0.1, and values will be accordingly reported with one decimal precision. Similarly, the real part of the effective permittivity (ε'_{eff}) varied between 8.7 and 9.7 at 1 GHz, leading to the decision to report ε' values rounded to the nearest unit.

In the following sections, only the data corresponding to the CPW with the median properties (μ/ε) will be reported for each sample, while keeping in mind the estimated confidence interval. The primary sources of uncertainty are attributed not only to limitations of the

electromagnetic extraction model but more significantly to variations in the homogeneity of the nanoparticle deposition by magnetophoresis. One can notice the inferior quality and uniformity of these deposits (Figure IV.13), particularly when compared to those made from more monodisperse nanoparticles synthesized via organometallic or polyol approaches (see in previous chapter), this suggests that the FeCo-hydrazine samples represent a worst-case scenario in terms of error margins.

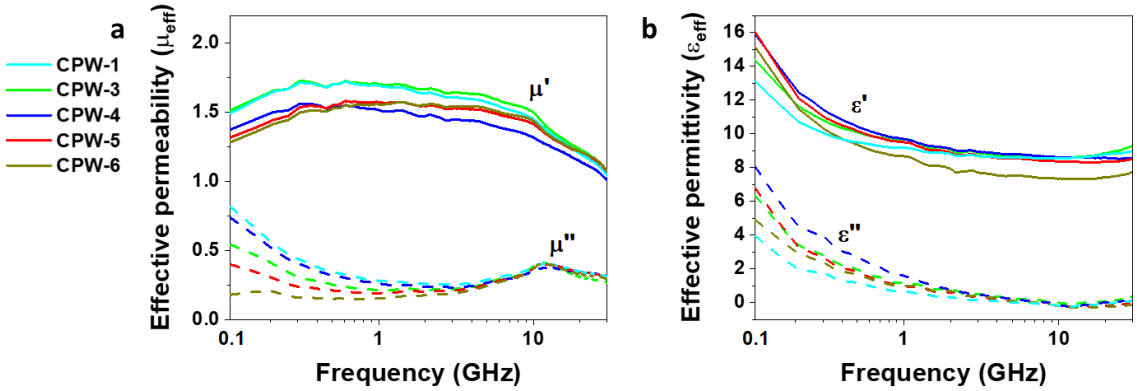

Figure IV.12. a) Effective magnetic permeabilities and b) dielectric permittivities (solid lines: real part; dashed lines: imaginary part) extracted on the different CPW-1, CPW-3, CPW-4, CPW-5, and CPW-6 (chip 1) cover with the same magnetic material FeCo-hydrazine-2.

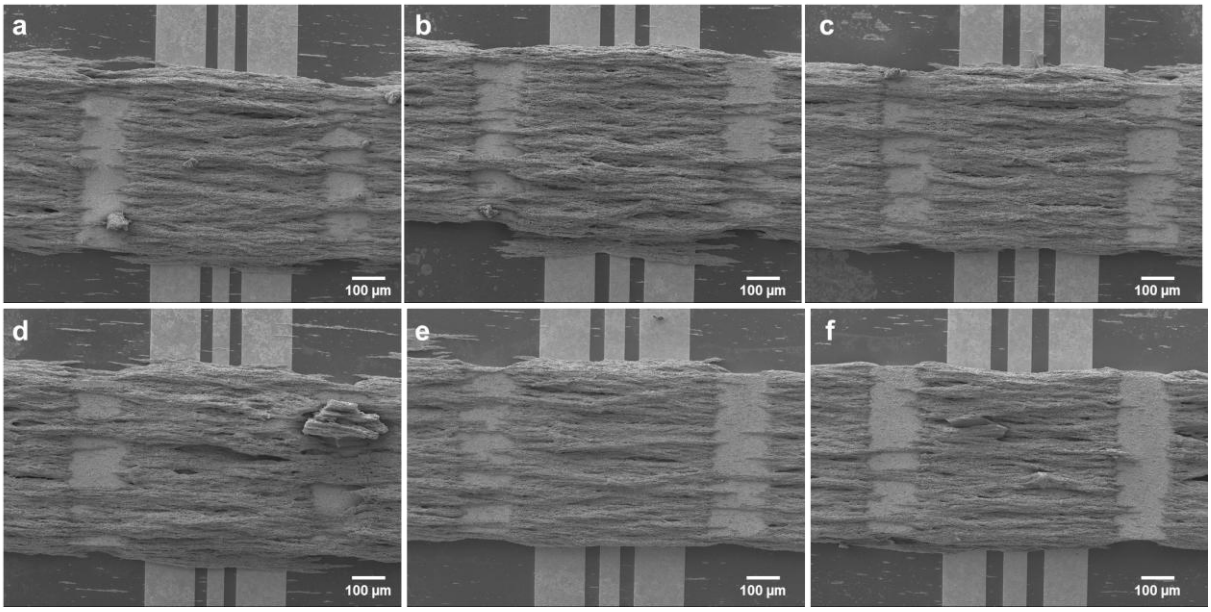

Figure IV.13. Optimal image of FeCo-Hydrazine-2 micromagnet on (a) CPW-1; (b) CPW-2; (c) CPW-3; (d) CPW-4; (e) CPW-5; (f) CPW-6.

2.2 Characterization of Dynamic Properties

The frequency dependence of real and imaginary components of the effective permeability (μ'_{eff}, μ''_{eff}) and permittivity (ε'_{eff}, ε''_{eff}) for FeCo-Hydrazine-1 and FeCo-Hydrazine-2 (see chapter 2) micromagnets are presented in Figure IV.14. Both samples exhibit a dielectric response characterized by quite low electrical losses over a broad frequency range, as indicated by the loss tangent (tan δ = ε″/ε′) remaining below 1. This suggests that the FeCo nanoparticles are effectively electrically insulated, likely due to the presence of an organic surfactant layer (potentially PEG or cyclohexane) and/or surface oxidation upon air exposure [16,17].

At 1 GHz, the real part of the effective permeability (μ'_{eff}) reaches approximately 1.6 for both FeCo-Hydrazine-1 and FeCo-Hydrazine-2, with magnetic losses (μ''_{eff} ≈ 0.25). The real part of the permittivity (ε'_{eff}) is slightly higher for FeCo-Hydrazine-2, though the difference is not significant. Above 7 GHz, the magnetic properties deteriorate, μ'_{eff} begins to decrease towards 1.4, accompanied by a rise in magnetic losses (μ''_{eff} > 0.3). Both samples display a maximum loss peak around 12 GHz, which can be attributed to the ferromagnetic resonance

(FMR) of the micromagnet assemblies. These results indicate that the moderate differences in size and polydispersity between FeCo-Hydrazine-1 and -2 do not result in substantial changes to their dynamic electromagnetic properties.

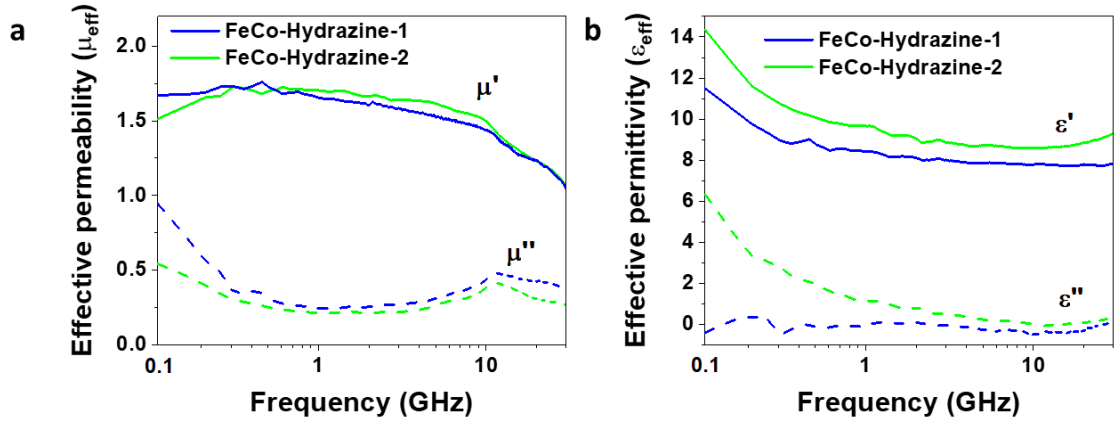

Figure IV.14. a) Effective magnetic permeabilities and b) dielectric permittivities (solid lines: real part; dashed lines: imaginary part) of FeCo-Hydrazine-1 and FeCo-Hydrazine-2.

2.3 Demonstrations on Inductors

The inductors have been measured before and after integration of the micromagnet obtained from FeCo-Hydrazine particles (Figure IV.15). When deposited onto planar inductors, from chip 1, both FeCo-Hydrazine-1 and FeCo-Hydrazine-2 led to measurable improvements in inductance ranging from 20–30%, and 25–35%, respectively. These results are consistent with the effective permeability values determined on CPW. These enhancements remained up to frequencies close to the self-resonance of the inductors (Table IV.2). This confirms that the FMR of the magnet is at high frequency and thus the inductor behavior is not affected.

Two conclusions can be drawn from these results. First, although the differences in permeability between the two FeCo-hydrazine samples appear to be small in absolute terms, they do produce distinguishable effects on inductors. This is validating the sensitivity and reliability of the characterization methodology, including the choice to use the CPW with the median properties (μ/ε). Second, FeCo-based micromagnets synthesized via hydrazine

reduction can achieve an effective permeability of approximately 1.6, leading to inductance enhancements on the order of 30% in integrated inductor demonstrators. This level of improvement can be achieved using a relatively simple and scalable synthesis method, making it a practical reference point for comparison. Consequently, micromagnets exhibiting significantly lower performance should not be considered suitable for practical RF applications. In the following sections, more complex synthesis routes (such as organometallic methods) will be explored, with the expectation that increased synthetic sophistication will translate into higher effective permeability and higher inductance increase.

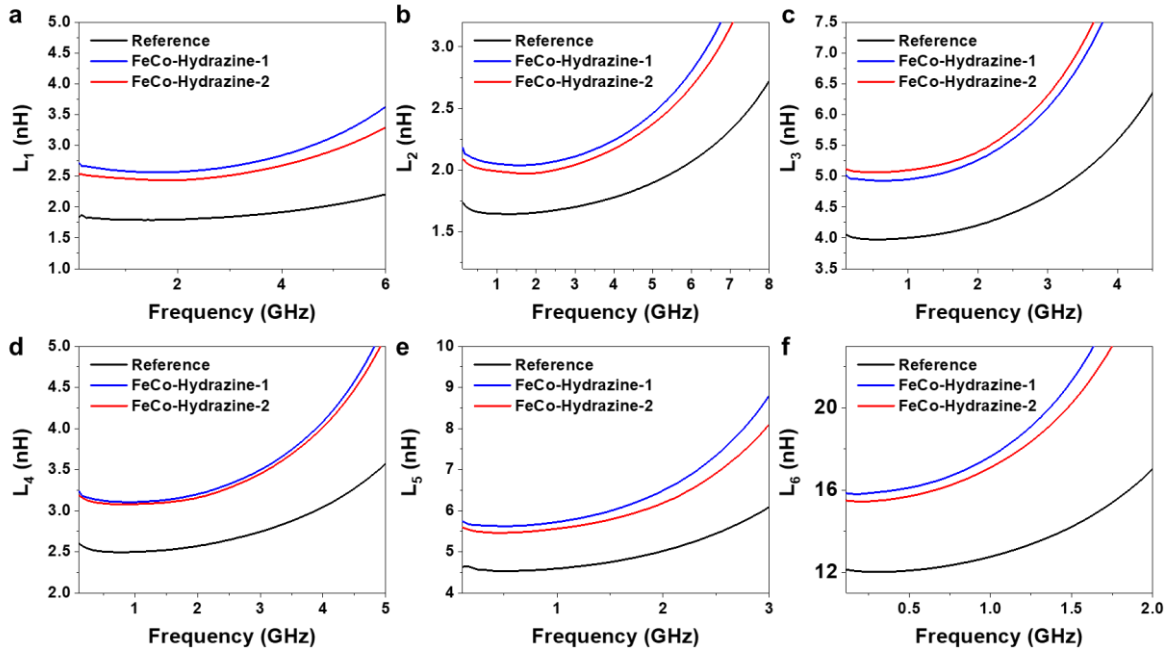

Figure IV.15. Evolution of the inductance value as a function of frequency for inductors a) #1, b) #2, c) #3, d) #4, e) #5, and f) #6 with integrated FeCo-Hydrazine-1 (blue), FeCo-Hydrazine-2 (red) NP-based micromagnets. The intrinsic inductor behavior was indicated as reference (black).

3. Nanoparticles from organometallic approach

In this section, we explore the dynamic properties of micromagnets assembled from nanoparticles synthesized via an organometallic route. This synthesis approach offers better control over the key parameters which are, the chemical composition, the shape and the size ensuring a low polydispersity. Thus, the role of these different individual factors on the high-frequency electromagnetic behavior of the resulting micromagnet will be studied. However, the benefits of this fine control come with a major challenge related to the size constraints. The organometallic route typically yields particles with diameters below 20 nm. At this scale, the high surface-to-volume ratio makes the nanoparticles particularly sensitive to oxidation, especially for zero-valent metals such as Fe or FeCo. Oxidation can strongly degrade magnetic properties, notably reducing saturation magnetization, and real permeability [18–22]. Therefore, it is essential to understand and control oxidation phenomena in order to ensure the viability of these nanomaterials in functional RF devices.

In the following subsections, we address this goal and associated issues in detail. First, we evaluate the RF performance of unprotected Fe and FeCo nanoparticles. Then, we present strategies to overcome the oxidation limitation, such as epoxy protection and carbidization of Fe nanoparticles (FeC) [23–26]. Finally, we analyze how particle size and composition influence the electromagnetic properties of the micromagnets.

3.1 Oxidation issue

3.1.a Fe and $Fe_{0.6}Co_{0.4}$ without epoxy protection

Micromagnets composed of 15 nm iron (Fe) and 10 nm $Fe_{0.59}Co_{0.41}$ single-domain nanoparticles were integrated onto coplanar waveguide (CPW) transmission lines and planar inductors to evaluate their high-frequency electromagnetic performance. In this study, the Fe nanoparticles were deposited under ambient air conditions, which likely led to surface oxidation. The frequency-dependent real and imaginary components of effective permeability

and permittivity are presented in Figure IV.16a and Figure IV.16b, respectively. The micromagnet composed of Fe nanoparticles exhibits a predominantly dielectric behavior with relatively low losses, as indicated by a loss tangent remaining below 1 over most of the frequency range. This suggests that the magnet is electrically insulated. In terms of properties, the effective real permeability (μ'_{eff}) remains around 1.4 for frequencies below 4 GHz, with minimal magnetic losses (μ''_{eff}< 0.3) extending up to 30 GHz. A broad peak is observed around 10 GHz, which is attributed to the ferromagnetic resonance (FMR) of the micromagnet. When integrated into planar inductors, the Fe-based micromagnets resulted in a moderate inductance enhancement of approximately 10% (Figure IV.17a–f), consistent with their modest μ'_{eff} values, this gain persists up to the inductors self-resonance frequencies, consistent with the high frequency FMR. The micromagnet assembled from 10 nm $Fe_{0.59}Co_{0.41}$ nanoparticles exhibit a comparable permeability profile, with similar μ'_{eff} and μ''_{eff} behavior (Figure IV.16). However, its dielectric losses are more pronounced, particularly at low frequencies (f < 0.6 GHz, Figure IV.17), revealing poorer electrical insulation. I suppose that this difference is not intrinsically due to the material but instead related to reproducibility challenges in the nanoparticle washing procedure.

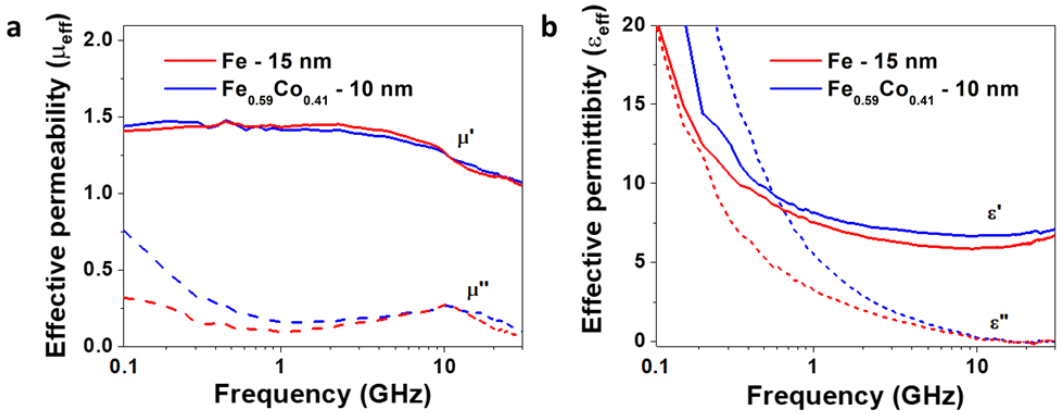

Figure IV.16. a) Effective magnetic permeabilities and b) dielectric permittivities (solid lines: real part; dashed lines: imaginary part) of Fe (red) and $Fe_{0.59}Co_{0.41}$ (blue). Measurements realized on chip 1.

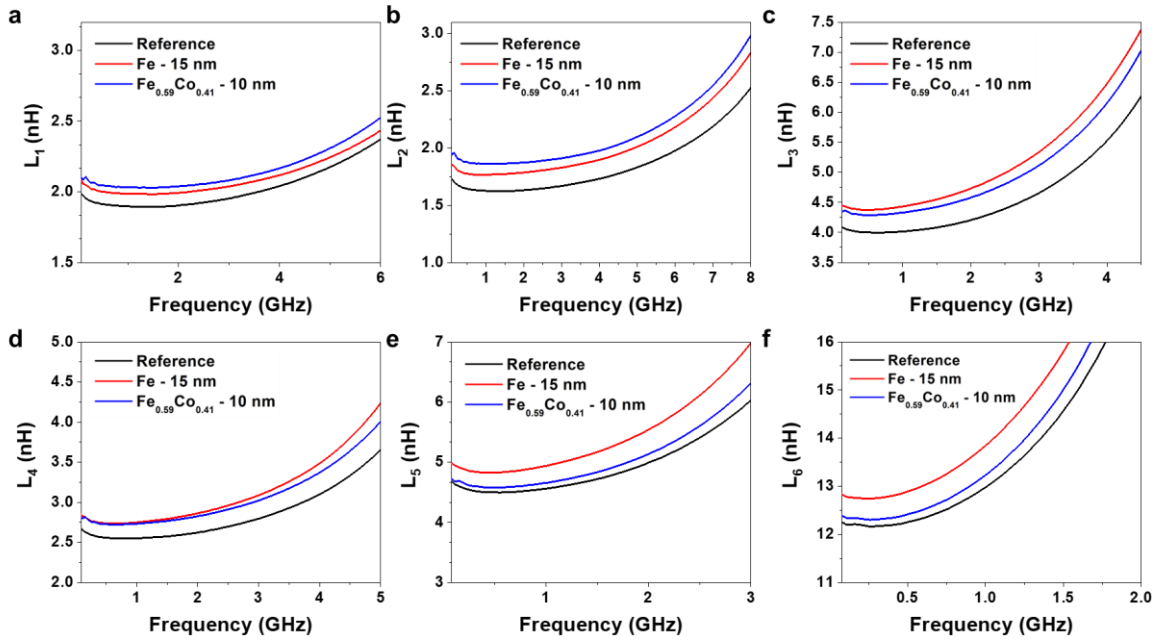

Figure IV.17. Evolution of the inductance value as a function of frequency for inductors a) #1, b) #2, c) #3, d) #4, e) #5, and f) #6 (chip 1) with integrated Fe (red), $Fe_{0.59}Co_{0.41}$ (blue) NP-based micromagnets. The intrinsic inductor behavior was indicated as reference (black).

As a reminder, the hydrazine-based FeCo micromagnets demonstrated an effective permeability of approximately μ'_{eff} = 1.6 and enabled inductance enhancements of up to 30%. In contrast, the micromagnet made of Fe or $Fe_{0.59}Co_{0.41}$ organometallic nanoparticles exhibit lower performances. These micromagnets yield lower permeability values which translate to smaller inductance increases.

3.2 Overcoming the issue of oxidation (epoxy protection, FeC)

3.2.a Effect of the NPs size on iron and the role of epoxy

The influence of nanoparticle (NP) size on magnetic permeability has been investigated in only a few studies [1,2,27–31]. For instance on iron oxide systems, Yun *et al.* [1] reported a significant enhancement in the relative permeability (μ'_r) of maghemite (γ-Fe_2O_3) NPs as the

particle size increased from 8.6 to 17.0 nm. This size-dependent behavior led to an increase in μ_r' from 1 to approximately 9 at 2 MHz, corresponding to an effective permeability (μ_{eff}') increase from 1 to ~1.8.

In the present study, we investigate this size effect for zero-valent iron (Fe) nanoparticles by comparing micromagnets formed from 8 nm and 19 nm Fe NPs. To isolate the intrinsic size effect and to eliminate any oxidative degradation, both nanoparticles were deposited under argon (Ar) atmosphere (0. 4 T) and protected with an epoxy layer.

Magnetic hysteresis measurements at 300 K were performed on the respective NPs powders, randomly dispersed (Figure IV.18c). They reveal that increasing particle size results in a magnetic hardening of the NPs: the coercive field increases from 6.9 mT for the 8 nm particles to 23 mT for the 19 nm particles, reaching a maximum for the 15 nm sample, which exhibits the largest coercive field in the series. Despite the observed increase in coercivity on powders, the measurements realized on the micromagnet reveal that the maximum real part of the effective permeability (μ_{eff}') remains similar for both samples, reaching values around 1.6 (Figure IV.18e). However, the frequency dependence of permeability differs slightly. For the 19 nm particles, the permeability spectrum is shifted toward higher frequencies, suggesting a higher ferromagnetic resonance (FMR) frequency compared to the smaller 8 nm particles. With an FMR frequency related to magnetic anisotropy (see chapter 1, eq. I.6), this is coherent with the larger coercive field measured on 19 nm Fe NPs. When integrated onto planar inductors, these micromagnets yield frequency-dependent increases in inductance (Figure IV. 18f). The 19 nm Fe nanoparticles lead to a 20–40% improvement in inductance, whereas the 8 nm particles provide a more modest increase of 20%. These results confirm that NP size has a measurable, though moderate, impact on performance when used as inductor core materials.

For comparison, the behavior of unprotected 15 nm Fe nanoparticles deposited under ambient air conditions (electromagnet 1 T) without epoxy protection is also shown (Figures IV. 18d–f). This sample exhibits both lower μ_{eff}' values and reduced inductance enhancement, ascribed to reduced magnetic properties due to oxidation. The detrimental effects of oxidation and further underscoring the importance of protective encapsulation for preserving high real permeability at RF frequencies are then confirmed. With epoxy

protection, Fe-based micromagnets exhibit performance comparable to those prepared from FeCo particles synthesized via the hydrazine reduction method. In the following sections, the objective is to further optimize the magnetic and RF properties by tuning the nanoparticle composition.

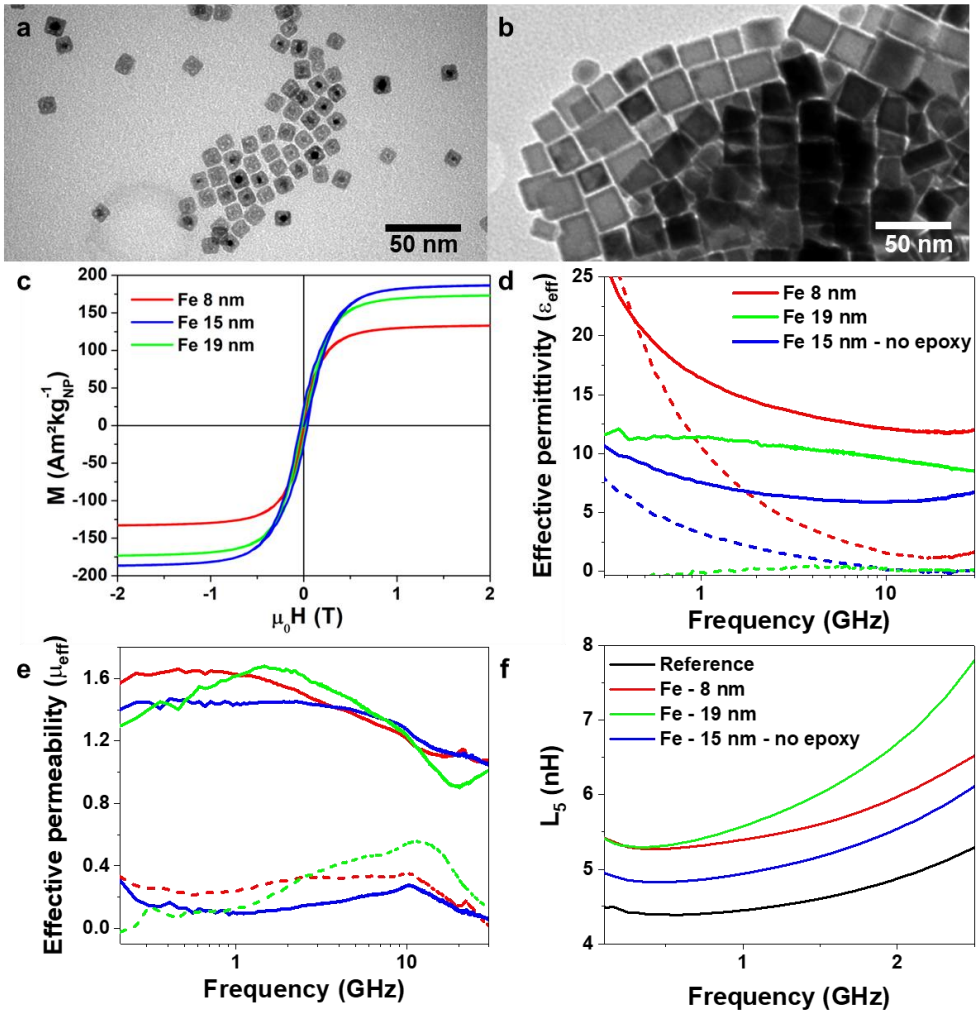

Figure IV.18. a) TEM images of 8 nm Fe, and b) 19 nm Fe nanoparticles and c) magnetic hysteresis loops recorded at 300 K for 8, 15 and 19 nm Fe NPs powders (unexposed to aire). d) Effective dielectric permittivities and e) magnetic permeabilities (solid lines: real part; dashed lines: imaginary part) of CPW. f) Evolution of the inductance value as a function of frequency for inductors #5 (chip 1) decorated with 8 nm Fe (red) or 19 nm Fe (green) NP-based micromagnets deposited under Ar and protected by an epoxy layer. For the sake of comparison, the 15 nm Fe NP based magnet deposited under air is recalled (blue) as long as the intrinsic inductor behavior, i.e., without any deposited magnet, as reference (black).

3.2.b Composition effect on ≈15nm particles

Micromagnets composed of single-domain iron-carbide (FeC), and iron–cobalt ($Fe_{1-x}Co_x$) nanoparticles (NPs) with mean diameters around 15 nm were integrated onto coplanar waveguides (CPWs) and planar inductors to evaluate their high-frequency magnetic properties. FeC and $Fe_{1-x}Co_x$ NPs were deposited under an inert argon atmosphere inside a glovebox. The $Fe_{1-x}Co_x$ NPs were further protected with an epoxy layer post-deposition, whereas the FeC samples were left uncoated, owing to the intrinsic oxidation resistance of iron carbide inferred from previous studies. The micromagnet composed of 15 nm Fe NPs assembled under regular atmosphere conditions without epoxy protection will serve as a comparison.

Micromagnets composed of FeC NPs (14 nm) show low-loss dielectric characteristics but exhibit enhanced magnetic performance (Figure 19c-d): for frequencies below 1.7 GHz, μ'_{eff} reaches values as high as 1.8, leading to stable ~20% inductance gains across all inductors tested. FeC NPs are efficient for moderate enhancement with robust environmental stability. $Fe_{0.89}Co_{0.11}$ NPs (17 nm), protected with epoxy, exhibit a higher permittivity (ε') than pure Fe NPs (previously introduced without protection), while their permeability reaches μ'_{eff} ≈ 1.6 up to 2.0 GHz. Their influence on inductance remains similar to the Fe samples, suggesting that a Co content of ~11% is insufficient to significantly enhance the magnetic response. Optimization of the Fe–Co alloy composition reveals superior performance with $Fe_{0.77}Co_{0.23}$ NPs (17 nm). These epoxy-protected micromagnet demonstrate the highest permeability, achieving μ'_{eff} > 2.0 at ~1 GHz. As a result, inductors incorporating $Fe_{0.77}Co_{0.23}$ micromagnets exhibit substantial inductance improvements, ranging from 40% to 60% up to 4 GHz (Figures 19c–d). Notably, the quality factor (Q) remains unaffected up to approximately 1 GHz (Figure 20), highlighting minimal losses in the low-frequency regime. In presence of the deposited magnet the quality factor drops slightly earlier, mainly due to the inherent magnetic losses, in agreement with the increasing imaginary part of the effective permeability (μ''_{eff}) in Figure 19b. Maximum Q values of 9 and 8 were measured for inductor #1 and #6 with $Fe_{0.77}Co_{0.23}$ micromagnets, respectively.

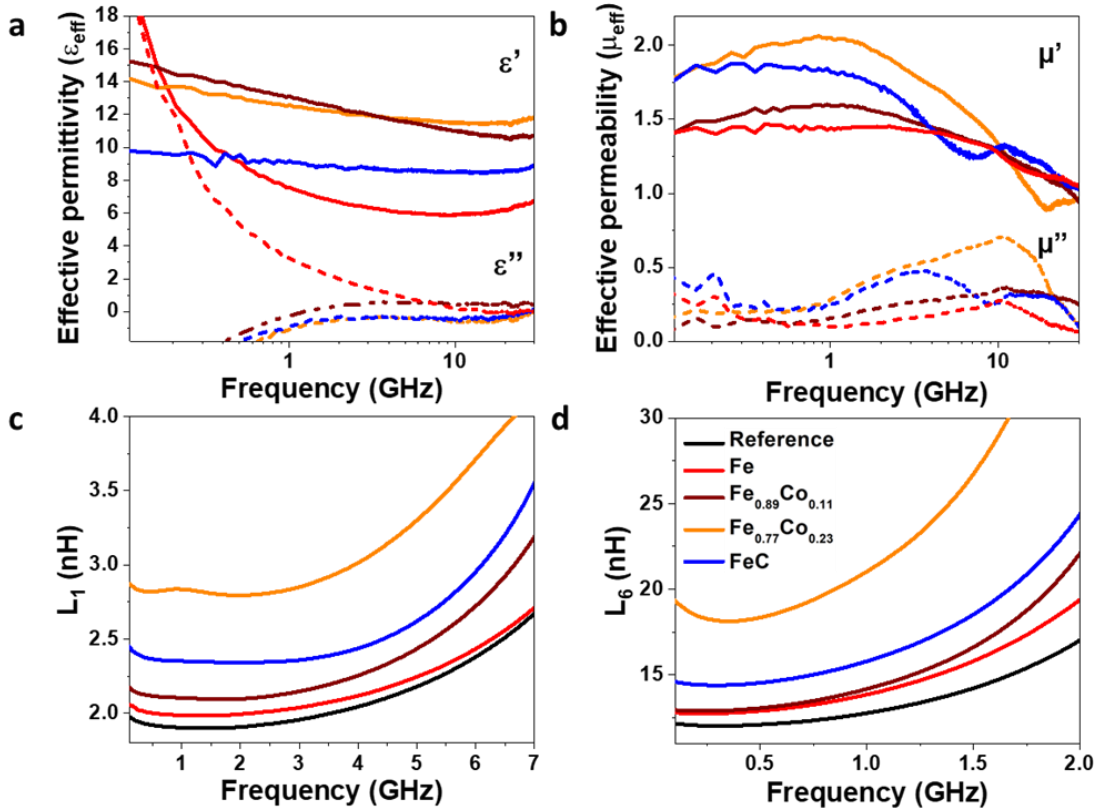

Figure IV.19. a) Effective dielectric permittivities and b) magnetic permeabilities (solid lines: real part; dashed lines: imaginary part) of CPW; evolution of the inductance value as a function of frequency for inductors c) #1 and d) #6 (chip 1) decorated with Fe (red), $Fe_{0.89}Co_{0.11}$ (marron), $Fe_{0.77}Co_{0.23}$ (orange) and FeC (blue) NP-based micromagnets. The intrinsic inductor behavior was indicated as reference (black).

These results underscore the beneficial effect of Co alloying in Fe-based nanoparticles on their dynamic magnetic properties. For particle sizes near 15 nm, a Co content of ~23% significantly enhances permeability. Consequently, it leads to higher inductance increases without compromising the Q factor at low frequencies. The performance achieved with $Fe_{0.77}Co_{0.23}$ micromagnets ranks among the highest reported for nanoparticle-based magnetic materials integrated onto RF components [17,32–36].

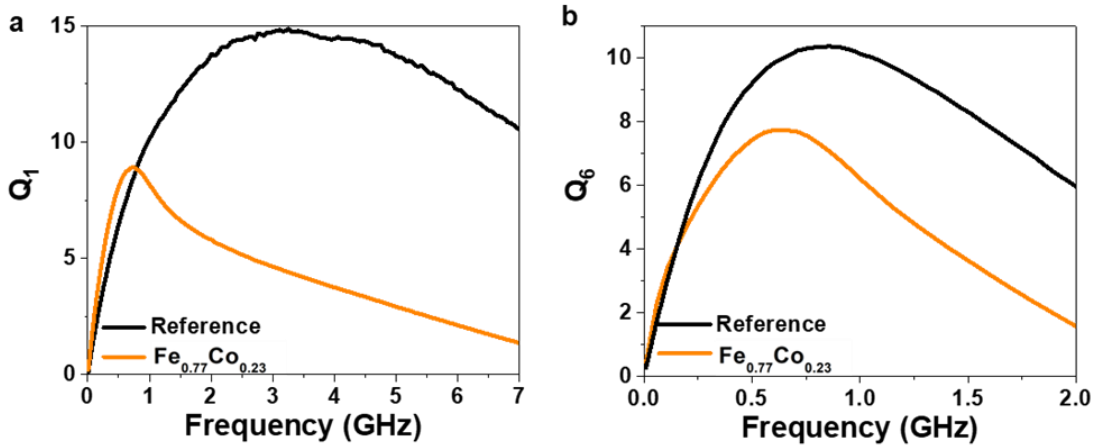

Figure IV.20. Comparisons of the quality factor of (a) inductor #1 and (b) inductor #6 (chip 1) with $Fe_{0.77}Co_{0.23}$ NPs and without materials.

3.2.c Composition effect on ≈9nm nanoparticles

The beneficial influence of Fe-Co alloying on the high-frequency magnetic properties of nanoparticles previously observed for particles around 15 nm in diameter was further investigated for smaller sizes. To this end, micromagnets composed of Fe and $Fe_{0.7}Co_{0.3}$ nanoparticles, with diameters of approximately 8 nm and 10 nm respectively, were synthesized, then integrated onto coplanar waveguides and planar inductors in an inert atmosphere and finally encapsulated in an epoxy matrix to prevent oxidation. A direct comparison between these two micromagnet reveals superior performance for the $Fe_{0.7}Co_{0.3}$ based micromagnet (Figure IV.21). The frequency-dependent effective real permeability (μ'_{eff}) of this sample reaches a maximum exceeding 2.1 near 1.0 GHz, compared to approximately 1.6 for the pure Fe micromagnet at the same frequency (Figure IV.21a). This enhancement in permeability directly translates to improved inductance performance. Inductors associated with the $Fe_{70}Co_{30}$ micromagnet exhibit an increase in inductance ranging from 40% to 60%, comparable to that observed with the 17 nm $Fe_{0.77}Co_{0.23}$ micromagnet (Figure IV.19). However, the 10 nm $Fe_{0.7}Co_{0.3}$ system appears to be well better regarding losses. As evidenced by measurements on inductor #6, the quality factor (Q) remains consistently higher in presence of the micromagnet. Notably, the Q_{max} measured with the $Fe_{0.70}Co_{0.30}$ micromagnet reaches 11, exceeding the Q_{max} of the inductor without micromagnet. Furthermore, the Q-factor of the decorated inductor remains above that of the

reference inductor up to approximately 0.75 GHz, indicating low losses in the operational frequency range. It is important to note that for this material, the maximum quality factor (Q_{max}) exceeds that of the inductor without material only in the case of inductor#6. This is because for this inductor, the quality factor of the reference begins to decline earlier around 0.8 GHz. This frequency approximately coincides with the onset of magnetic losses in the nanoparticle-based micromagnet, thereby this minimizes the relative impact of the added material on the overall Q_{factor}.

The benefit of iron-cobalt alloyed NPs has been confirmed for smaller sizes. It also suggests that optimization of both composition and particle size can lead to micromagnet with enhanced permeability performance and minimal losses, key requirements for radiofrequency applications.

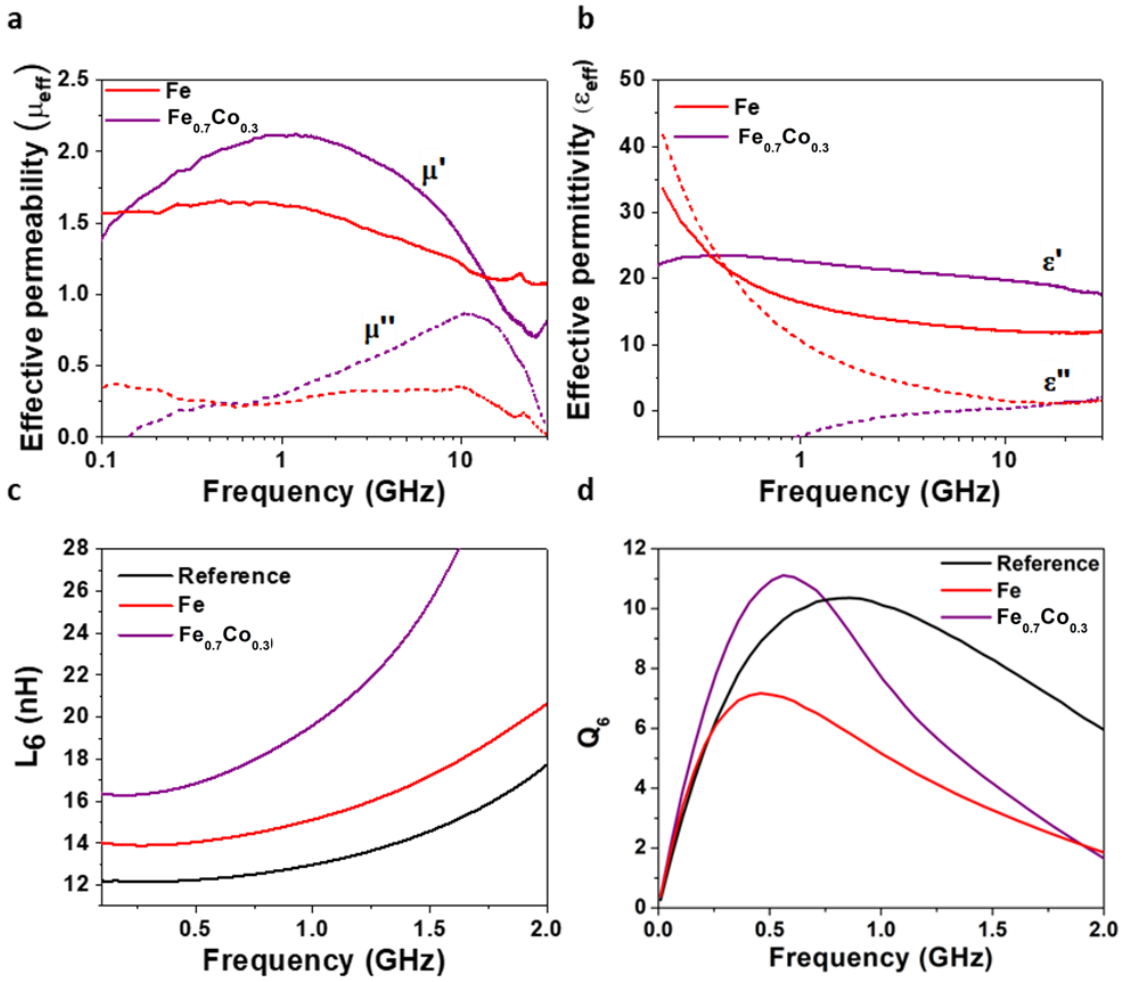

Figure IV.21. a) Effective magnetic permeabilities and b) dielectric permittivities (solid lines: real part; dashed lines: imaginary part) of CPW; c) evolution of the inductance value as a function of frequency for inductors #6 (chip 1) with integrated Fe (red), and $Fe_{0.7}Co_{0.3}$ (purple) NP-based micromagnets. The intrinsic inductor behavior was indicated as reference (black). (d) Comparisons of this inductor with $Fe_{0.7}Co_{0.3}$ NPs and without materials.

3.3 Discussion

The static and dynamic magnetic properties of the nanoparticle-based micromagnets investigated in this study are summarized in Table IV.5. The comparative analysis of Fe, $Fe_{1-x}Co_x$, and FeC systems highlights several critical factors influencing their RF properties, particularly the effects of oxidation, chemical composition and particle size.

First the detrimental impact of oxidation on the magnetic behavior of nanoparticles has been illustrated. When Fe nanoparticles are exposed to air, the formation of surface iron oxides leads to a significant degradation in the real part of the permeability and so the inductance performance. Carbidization, as used in the FeC nanoparticles, offers a route to oxidation resistance without the need of epoxy protection. However, it comes along with a reduction in magnetic performance. The epoxy serves as a highly effective oxidation barrier, preserving the nanoparticles intrinsic magnetic properties over time. However, challenges related to the uniformity and control of the epoxy coating remain, as a significant portion of the devices were lost due to the epoxy flowing over the contact areas and rendering them inaccessible for measurement. These issues could, however, be readily addressed in the future using microfabrication-compatible masking techniques.

The choice of nanoparticle composition significantly affects the RF behavior, $Fe_{1-x}Co_x$ alloyed NPs demonstrating superior permeability in the GHz frequency range compared to pure Fe or FeC compounds. This behavior is attributed to the intrinsic magnetic properties of the materials, particularly their low coercivities and high saturation magnetization, both of which increasing with cobalt content (Table IV.5). Among the compositions tested, $Fe_{0.77}Co_{0.23}$ and $Fe_{0.7}Co_{0.3}$ consistently provided the best performance in terms of permeability and inductor enhancement.

Particle size is another parameter influencing the RF behavior. In this study, smaller Fe nanoparticles (≈8 nm) exhibited permeability peaks at slightly lower frequencies compared to larger Fe particles (≈19 nm). The shift in ferromagnetic resonance (FMR) must be considered for optimal inductor integration.

Taken together, these results establish a clear materials roadmap for the design of high-performance micromagnets for RF applications. The ideal configuration comprises $Fe_{1-x}Co_x$ alloy nanoparticles with diameters approaching the critical domain size, synthesized and deposited under inert conditions and protected with an epoxy layer. This combination enables high permeability in the GHz range, minimal magnetic losses, and robust environmental stability.

Sample	**Magnetophoresis**	**Size (nm)**	**Measured M_s (Am^2/kg)**	**Bulk M_s (Am^2/kg)**	**$\mu_0 H_c$ (mT)**	**μ'_{eff} at 1 GHz**	**μ'_r at 1 GHz (estimated from Appendix 9)**
Fe	air atmosphere	15±4	187	220	38	1.4	2
FeC	air atmosphere	14±1	105	170	33	1.8	3-7
$Fe_{0.89}Co_{11}$	argon atmosphere	17±3	190	225	10	1.6	2-3
$Fe_{0.77}Co_{0.23}$	argon atmosphere	17±2	205	230	9	2.1	> 9
Fe	argon atmosphere	8±1	130	220	7	1.6	2-3
$Fe_{0.7}Co_{0.3}$	argon atmosphere	10±2	210	245	13	2.1	> 9
Fe	argon atmosphere	19±3	174	220	23	1.6	2-3
FeCo via Hydrazine	air atmosphere	~100	216	230	17	1.6	2-3

Table IV.5. Summary of the main characteristics of the NP-based micromagnet samples.

4. CoNi particles from polyol synthesis

This section explores the potential of cobalt–nickel (CoNi) oparticles synthesized via the polyol process for high-frequency magnetic applications. The polyol synthesis route offers several key advantages that make it highly attractive for the scalable production of magnetic materials. In particular, it allows the fabrication of relatively large particles, typically beyond 20 nm, with, ideally, the formation of a passivated oxidized layer preserving a single-domain ferromagnetic core, it could ensure stable magnetic properties without requiring additional protective shell. Although the present system falls within an intermediate regime, particle sizes are closer to the multidomain threshold and to the skin depth potentially increasing the losses. Furthermore, this method enables the synthesis of large quantities of nanopowder (hundreds of milligrams per batch for 100 mL volume batch) while providing precise control over both particle size and chemical composition.

Given this high potential, CoNi particles synthesized by the polyol approach represent an excellent system for investigating the influence of intrinsic material parameters, particle size and composition on dynamic magnetic and dielectric properties in the GHz frequency range. This is an opportunity to confirm the key parameters identified in previous sections. This part of the work aims to decouple and isolate the effects of size and composition unambiguously. Through systematic variation and characterization of CoNi particle-based micromagnets, we aim to assess their potential for integration into planar inductors and evaluate their performance in terms of permeability, inductance increase, and quality factors, both in absence and under an external static magnetic field applied.

4.1 Control of dynamical magnetic and dielectric properties

Micromagnets made of different sizes and composition of CoNi particles have been obtained on coplanar waveguide allowing to decorrelate the effect of composition and size on the permeability and permittivity properties.

4.1.a Size effect

For a fixed $Co_{0.5}Ni_{0.5}$ composition, different sizes were studied 31, 67, and 104 nm. Figure IV.22 illustrates a micromagnet composed of $Co_{0.5}Ni_{0.5}$ particles.

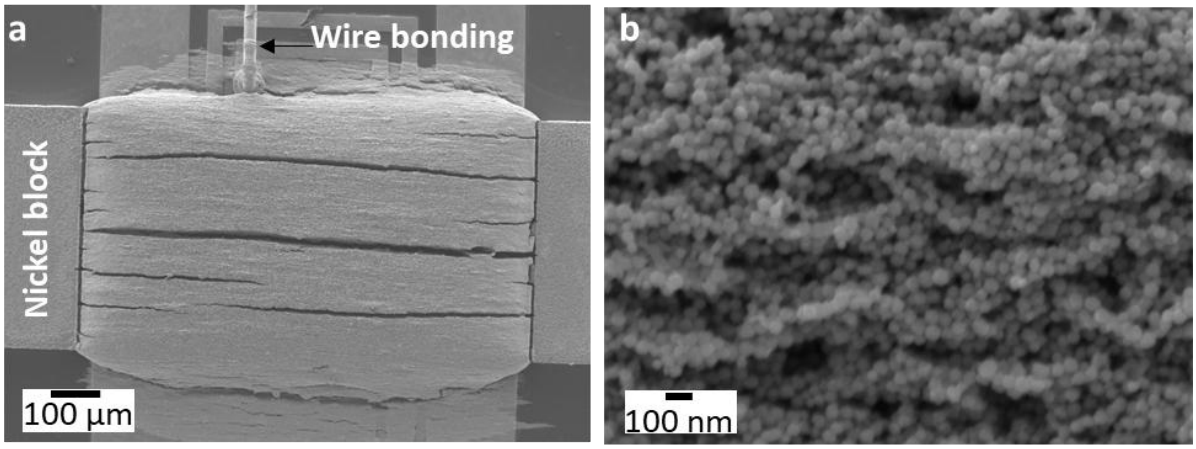

Figure IV.22. (a) SEM image showing a micromagnet composed of (53±6) nm $Co_{0.5}Ni_{0.5}$ nanoparticles formed between nickel blocks with visible wire bonding. (b) High-magnification SEM image revealing the CoNi particles.

The real and imaginary parts of effective dielectric permittivity, and effective permeability of the transmission lines extracted from the measurements are shown on Figure IV.23-24. For the three different sizes the dielectric losses are minimal with permittivity confirming the dielectric nature of the magnetic deposit provided by carboxylate surfactant (or/and oxide layer) surrounding the particles and insulating them electrically. Indeed, a loss tangent $\tan\delta = \varepsilon''/\varepsilon'$ of less than 1 over most of the frequency range indicates a dielectric behavior with acceptable level of losses (Figure IV.24b).

The relative magnetic permeabilities obtained from the transmission lines for the NPs of different sizes are displayed in Figure IV.23 and 24a. It clearly appears a size-dependent behavior, as previously reported [37]. Such a study on similar CoNi particles reported that particles smaller than an experiment critical size (≈ 55 nm) show a single resonance

interpreted as the magnetostatic mode by Kittel (Chapter 1) [38,39], and above that critical size particle start to have a multi-resonance behavior. It can be seen as a curling spin mechanism described by Aharoni (Chapter 1, section 1.2.b) [40]. At larger size (≈ 400 nm), the multi-resonance phenomena is replaced by a large resonance band due to a different magnetic multidomain configuration [37]. Here, the micromagnet based on the smallest particles of 31 nm, and 49 nm display almost exactly the same permeability properties (Figure IV.23). Both samples display a maximum loss peak around 10 GHz, which can be seen as a uniform magnetostatic mode, with no size effect. For larger particles, two resonances are noticeable for 67 nm sample, and three for 104 nm ones. The last resonance at around 10 GHz does not depend on the particle size, therefore it is attributed to the uniform magnetostatic mode. The first peaks depend on the size (a large broad resonance between 1.5-4 GHz for 67 nm, 2 and 5 GHz for 104 nm) and are attributed to non-uniform exchange resonance modes. Consequently, this size range is of great interest, as it allows the magnetic properties of the material to be easily modulated by size. The sample with 67 nm seems to be the more interesting because of its higher real permeability, between 1.7 and 1.9, over a large frequency range, up to 6 GHz. This can be used to obtain constant high increases in inductance over a wide frequency range.

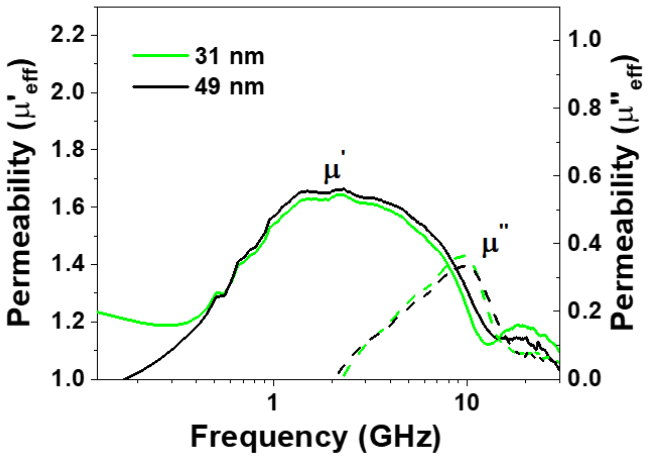

Figure IV.23. Comparison of the effective magnetic permeability of micromagnets made of 31 nm and 49 nm $Co_{0.5}Ni_{0.5}$ particles (chip 1).

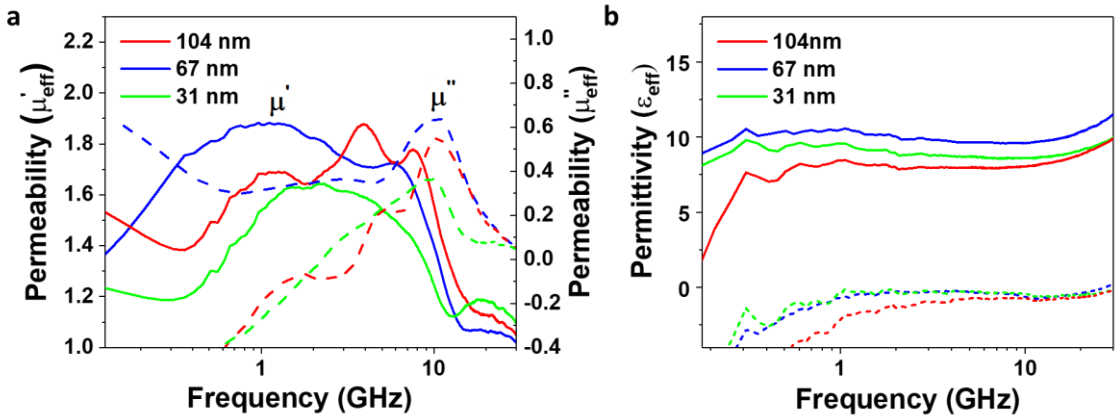

Figure IV.24. Effect of the $Co_{0.5}Ni_{0.5}$ particle size composing the micromagnets on their (a) effective magnetic permeabilities, and on their (b) effective dielectric permittivities (chip 1).

4.1.b Chemical composition effect

To highlight the effect of chemical composition without any ambiguities, for a fixed size of 67 +/- 1 nm, $Co_{0.8}Ni_{0.2}$, $Co_{0.5}Ni_{0.5}$, and $Co_{0.2}Ni_{0.8}$ NPs were studied. Among the different sizes available, this size has been chosen because of its stable high permeability on a large frequency range. The real and imaginary parts of the effective dielectric permittivity, and effective permeability of the transmission lines are shown in Figure IV.25. It is interesting to note that a high nickel content ($Co_{0.2}Ni_{0.8}$ particles) deteriorates the dielectric and insulating properties of the material. While micromagnet composed of $Co_{0.8}Ni_{0.2}$ and $Co_{0.5}Ni_{0.5}$ particles are dielectric with negligible dielectric losses over the entire frequency range studied, for example at 1 GHz, $\varepsilon'_{eff} \approx 9$ and $\varepsilon''_{eff} \approx 0 \pm 1$. (Figure IV.25b).

For a given particle size the permeability depends on the particle composition. The real permeability is higher for nickel rich $Co_{1-x}Ni_x$ particles (Figure IV.25a). Indeed, the magnets prepared from $Co_{0.5}Ni_{0.5}$ and $Co_{0.2}Ni_{0.8}$ NPs have higher permeability than the one obtained with $Co_{0.8}Ni_{0.2}$ NPs. Furthermore, the resonance frequencies are shifted to higher frequencies while the Co content increases. This is the consequence of the high magneto-crystalline anisotropy of cobalt [41,42]. In that case, by fixing the size at 67 nm, the permeability remains on a two-resonance behavior with a well-defined plateau where permeability is constant with frequency, it has been possible to adjust the plateau range by changing the chemical

composition. Here we can conclude that the micro-magnet composed of $Co_{0.5}Ni_{0.5}$ particles is the most interesting for use as an inductor core, since it has the highest permeability over the widest frequency range while maintaining good dielectric properties.

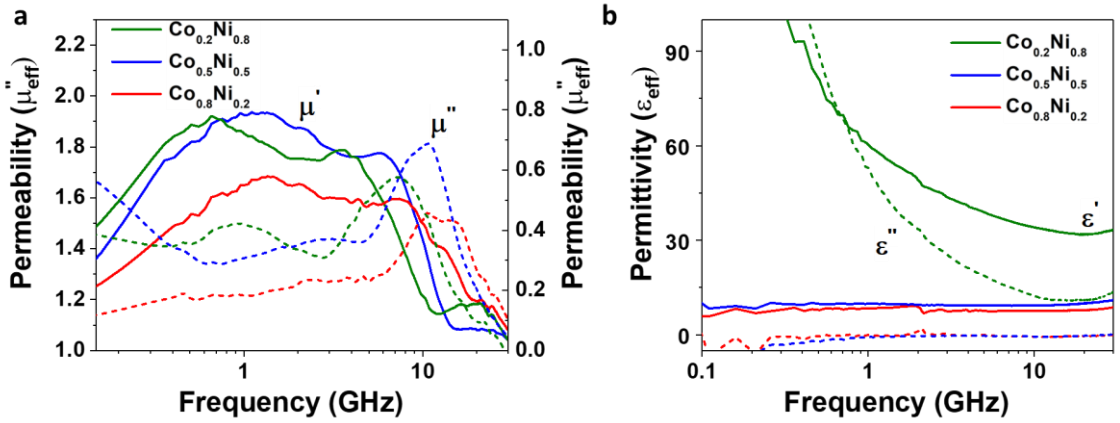

Figure IV.25. Effect of the composition of the $Co_{1-x}Ni_x$ particle (67 nm) composing micromagnets on their (a) effective magnetic permeabilities, and on their (b) effective dielectric permittivities (chip 1).

4.1.c Effect of a static field

The FMR measurements, obtained in reflection configuration on short-circuited coplanar lines (see Section 1.1.c.ii), were conducted by Nicolas Bizière at CEMES (Toulouse). Due to lack of time only two samples $Co_{0.5}Ni_{0.5}$, and $Co_{0.2}Ni_{0.8}$ 67 nm have been measured and chosen to illustrate the *effect of an applied static magnetic field* on dynamical magnetic properties. The objective was to identify the FMR frequency of our micromagnets as a function of the applied field, in order to obtain information about the presumed FMR during previous RF measurements on CPW without applied fields. Indeed, applying a static magnetic field helps to obtain more control and flexibility on the dynamic properties of the micromagnet, with particular focus on the FMR frequency, which is related to the applied magnetic field, in Kittel's well-known formula, which is however only valid in the saturated case (Chapter 1, section 1.2.b). Experimentally, the static magnetic field is applied in the direction of the

coplanar line (as illustrated in Figure IV.3, see section 1.1.c.ii). The impedance parameters (Z_{11}) were acquired, and the corresponding variation in inductance with respect to a reference, ΔL_{11}, was derived using (Eq. IV.23 from section 1.1.c.ii). Figure IV.26 displays the real and imaginary ΔL as a function of the applied magnetic field for the purely inductive line. These variations are directly related to the magnetic permeability components, such that $\Delta L' \propto \mu'$, $\Delta L'' \propto \mu''$. The values shown are relative, and presented in arbitrary units (a.u.), as de-embedding and normalization procedures were not applied to correct parameters such as the filling factor and coupling length. At low applied magnetic fields, a multiresonance behavior is observed in the real part of the magnetic permeability. For $Co_{0.5}Ni_{0.5}$, a broad peak appears between 0.8 and 3 GHz, while a more distinct resonance emerges at around 6 GHz. Similarly, for $Co_{0.2}Ni_{0.8}$, a broad peak is found between 0.5 and 2 GHz, followed by a sharper resonance near 4 GHz. In the imaginary part of the permeability, this behavior manifests as a shoulder at intermediate frequencies (2-3 GHz for $Co_{0.5}Ni_{0.5}$, and 1-2 GHz for $Co_{0.2}Ni_{0.8}$) and well-defined resonance at higher frequencies (around 10 GHz for $Co_{0.5}Ni_{0.5}$ and 6 GHz for $Co_{0.2}Ni_{0.8}$).

As the applied magnetic field increases, the multiresonant behavior gradually diminishes. The lower-frequency shoulder progressively disappears, and under sufficiently strong fields to saturate the sample (approximately 400 mT, as determined from VSM static measurements), only the band corresponding to the fundamental magnetostatic FMR mode described by the Kittel model remains. For instance, at magnetic fields equal to or higher than 300 mT, only a single resonance mode seems to be observed in Figure 26.

This evolution is accompanied by a shift of the resonance frequency (μ'') toward higher frequencies, as qualitatively predicted by Kittel's description of ferromagnetic resonance (FMR). However, a quantitative validation of the model could not be established due to the limited number of data points obtained in the saturated state.

For both micromagnet made of 67 nm $Co_{0.5}Ni_{0.5}$ (Figure 26a) and $Co_{0.2}Ni_{0.8}$ (Figure 26b) particles, the first peak or shoulder associated with the initial resonance completely vanishes above 200 mT. This observation confirms that the resonance observed without an applied static magnetic field (see Section 4.1.a) at higher frequencies (around 10 GHz) correspond to the magnetostatic mode governed by the Kittel model.

Those curves demonstrate the interest of an external magnetic field biasing the micromagnet for modulating the properties of an inductance. In practice it can be a local magnetic field applied by a small permanent magnet close to the micromagnet. For both micromagnet made of 67 nm $Co_{0.5}Ni_{0.5}$ and $Co_{0.2}Ni_{0.8}$ particles, the application of a bias lead to a gradual decrease of real magnetic permeability (μ') at low frequencies (< 1 GHz). Nevertheless, the bias extends the usable frequency range by lowering magnetic losses and pushing the resonance to higher frequencies (μ'').

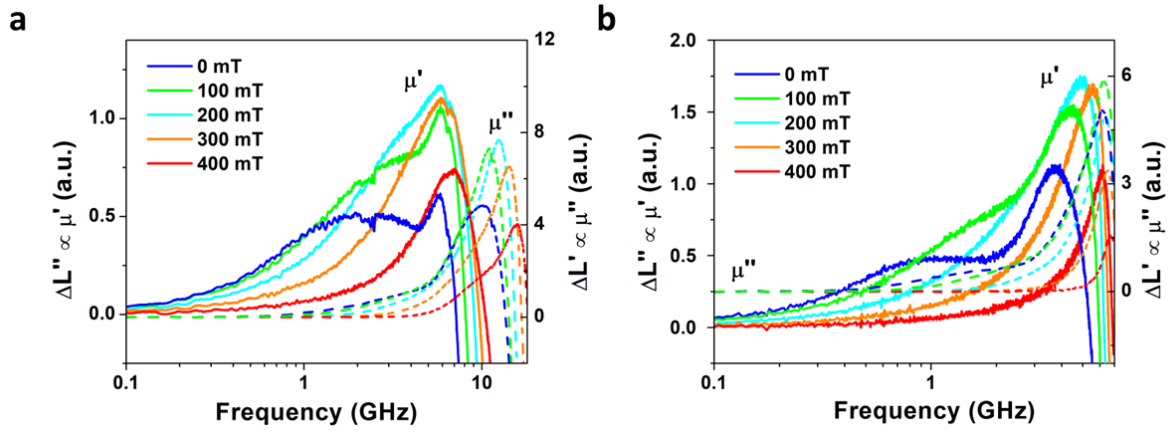

Figure IV.26. Effect of a static applied magnetic field on the magnetic permeabilities which is proportional to the inductance ΔL for micromagnet (a) composed of $Co_{0.5}Ni_{0.5}$ *particles and (b) composed of* $Co_{0.2}Ni_{0.8}$ *particles of 67 nm (on chip 2).*

4.2 Application of the implementation of inductor core

4.2.a Inductor core applications without static field

Following the investigation of sub-millimeter CoNi magnetic particle assemblies and the control of their dynamic magnetic and dielectric properties through size, chemical composition, and static magnetic field effects, this section demonstrates the interest to integrate such materials as inductor cores. To assess the impact of material parameters, we studied the influence of particle size, composition, and magnetic field bias on the performance of inductors cover with CoNi particles. Without any applied magnetic field, the micromagnet

formed from 67 nm $Co_{0.5}Ni_{0.5}$ particles exhibit an effective permeability between 1.7 and 1.9 up to 6 GHz, indicating promising stable performance across a wide frequency range.

Covered with 67 nm $Co_{0.5}Ni_{0.5}$ micromagnet, Inductor#2, inductor3#, inductor#5, and inductor#6, show 50–80% increase in inductance compared to reference without magnetic material (Fig IV.27-a, b), inductor#1 exhibit only 20% of increase. This enhancement is observed up to 2 GHz for L5 and 4.5 GHz for L2, without significant degradation of the quality factor up to 0.8 GHz (Fig IV.27-c, d). A Q_{max} of 15 and 19 are measured on covered inductor #2, inductor #5, respectively. Variations of the Q-factor versus frequency are consistent with the results of the magnet characterization via CPW. At low frequencies, the $Q - factor$ is limited only by resistive losses in the metal strip, and Q values are fairly the same for both inductors with and without magnet. As the frequency increases, the losses in the dielectric increase until they become predominant and result in the decrease of the $Q - factor$ at high frequencies. So, this decrease is higher when the magnet is implemented, mainly because magnetic losses, as evidenced by the increasing imaginary part of the effective permeability (μ''_{eff}) in Fig IV.25-a. For inductor#3, and inductor#6, which reach their Q_{max} at earlier frequency before 1.5 GHz when magnetic losses still acceptable, their Q_{max} is even higher with magnetic material than without.

These performances equal or even exceed the best results reported in the literature for planar inductors decorated with magnetic thin films or nanoparticle deposit, highlighting the potential of this approach and this material for high-frequency inductor applications [17,32–36,43].

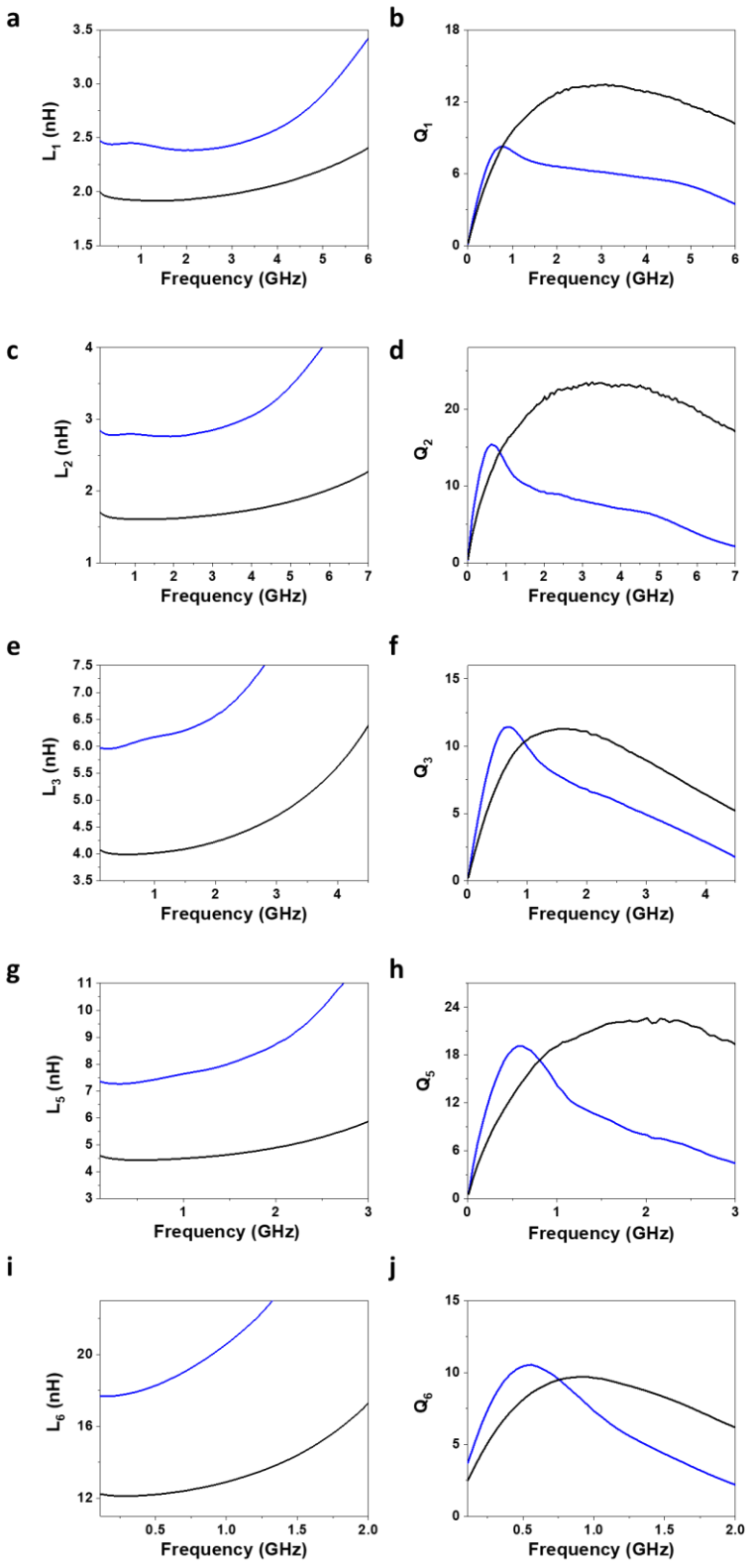

Figure IV.27. Evolution of the inductance and quality factor as a function of frequency for inductors a-b) #1, c-d) #2, e-f) #3, g-h) #5, and i-j) #6 with integrated 67 nm $Co_{0.5}Ni_{0.5}$ *particle-based micromagnets. The intrinsic inductor behavior was indicated as reference (black) (Chip 1).*

4.2.b Inductance tunability with an external bias field

These measurements have been realized by Nicolas Bizière in CEMES Toulouse. The influence of an externally applied static magnetic field on the RF performance of micromagnets composed of 67 nm $Co_{0.5}Ni_{0.5}$ nanoparticles was investigated using inductor #9 on chip-2 (Figure IV.28). At frequencies below 1 GHz, the inductance of the device decreases progressively with increasing static magnetic field intensity in accordance with the previous permeabilities measures. Particularly, this field bias is favorable for increasing the quality factor of the inductor, indeed increasing the static magnetic field applied push further the onset of the magnetic losses. Consequently, this behavior is consistent with the expected effect of field bias measured in the previous section on permeability. These results confirm that static magnetic fields can modulate the electromagnetic response of $Co_{0.5}Ni_{0.5}$ micromagnets on inductor, offering potential for tunable inductance in RF applications. The choice of inductance value and quality factor of the inductor can thus be left to the user and even modified during use. To the best of our knowledge, this represents one of the first proofs of concept of a tunable inductor. It is conceivable to design inductors with an inductance that can vary by up to 60% of their value with only small (and gradually) variation of their quality factor.

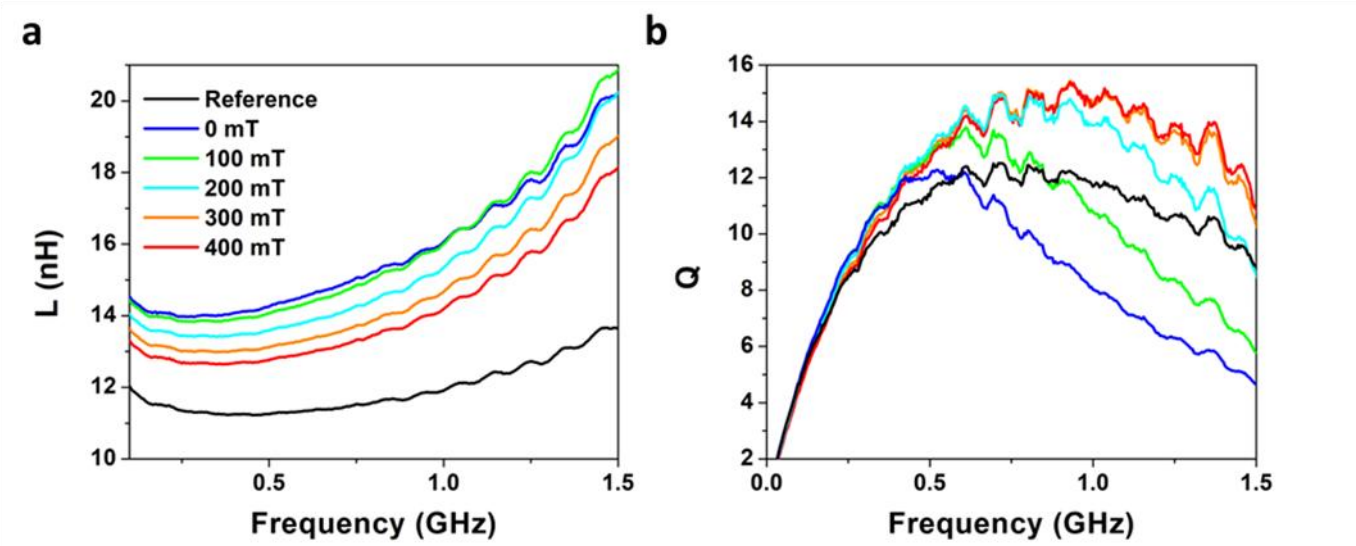

Figure IV.28. Evolution of the (a) inductance and (b) quality factor as a function of frequency for inductor #9 with integrated 67 nm $Co_{0.5}Ni_{0.5}$ particle-based micromagnets under different external static magnetic field applied (Chip 2).

5. Conclusion

This chapter has demonstrated the potential of nanoparticle-based micromagnets as functional materials for high-frequency applications, particularly as magnetic cores in planar inductors integrated onto silicon-based RF chips. The complex permittivity and permeability of various nanoparticle micromagnet assemblies were systematically extracted from the characterization of CPW on which these assemblies have been integrated. Their potentialities have been experimentally confirmed when used on RF planar inductors.

FeCo nanoparticles prepared by the hydrazine reduction method were employed as a benchmark material owing to the simplicity and scalability of this synthesis route. The resulting micromagnets achieved an effective permeability of about 1.6 and an inductance enhancement of up to 30%, demonstrating the feasibility of integrating such materials into RF devices.

Organometallic synthesis routes, although constrained by particle size (<20 nm), enabled low polydispersity, precise control over particle shape, size and composition. This control allowed for detailed studies of how these parameters influence dynamic magnetic behavior. Importantly, the role of surface oxidation was found to be critical, as unprotected Fe and $Fe_{1-x}Co_x$ particles exhibited diminished RF performance. Protection with epoxy significantly improved both permeability and inductive response. The impact of the nanoparticle size and composition was evaluated. The ideal configuration comprises $Fe_{1-x}Co_x$ alloy nanoparticles with diameters approaching the critical domain size, synthesized and deposited under inert conditions and protected with an epoxy layer. This combination enables high permeability in the GHz range, minimal magnetic losses, and robust environmental stability.

On $Fe_{1-x}Co_x$ and $Co_{1-x}Ni_x$ systems, the specific impact of the size and the composition on the magnetic permeability have been described. In both cases, optimal size and composition were proposed for generic applications, resulting in an increase in inductance up to 60%. An external magnetic field has also been applied to reveal the tunability achievable with $Co_{0.5}Ni_{0.5}$ micromagnets. Micromagnet on inductor, offering potential for tunable inductor over a wide range of inductance values for versatile RF application.

Overall, this chapter establishes that by assembling magnetic particles with tailored physical and chemical properties into micromagnet, it is possible to optimize their dynamic magnetic response for GHz-frequency applications. These results not only validate the integration of nanostructured magnetic materials into RF planar inductors but also highlight promising avenues for integration of this micromagnet on more complex micro-components such as filters.

Further increases in inductance beyond the values obtained here will likely require the use of three-dimensional inductor architectures, as planar designs are approaching their theoretical limit (Chapter 1 demonstrated that inductance can at most be doubled). Other potential improvements include minimizing losses and shifting the ferromagnetic resonance to higher frequencies, which could be achieved through further research into nanoparticle size and exploration of different alloy compositions, such as CoFeB.

6. References

[1] Yun H, Liu X, Paik T, Palanisamy D, Kim J, Vogel WD, et al. Size- and Composition-Dependent Radio Frequency Magnetic Permeability of Iron Oxide Nanocrystals. ACS Nano 2014;8:12323–37. https://doi.org/10.1021/nn504711g.

[2] Jadav M, Bhatnagar SP. Particle Size Controlled Magnetic Loss in Magnetite Nanoparticles in RF-Microwave Region. IEEE Trans Magn 2020;56:1–8. https://doi.org/10.1109/tmag.2020.2990769.

[3] Hasegawa D, Yang H, Ogawa T, Takahashi M. Challenge of ultra high frequency limit of permeability for magnetic nanoparticle assembly with organic polymer—Application of superparamagnetism. J Magn Magn Mater 2009;321:746–9. https://doi.org/10.1016/j.jmmm.2008.11.041.

[4] Potéreau M. Contribution à la caractérisation de composants sub-terahertz. Thèse. Université de Bordeaux, 2015.

[5] Pozar DM. Microwave engineering. 4th ed. Hoboken, NJ: Wiley; 2012.

[6] Kruppa W, Sodomsky KF. An Explicit Solution for the Scattering Parameters of a Linear Two-Port Measured with an Imperfect Test Set (Correspondence). IEEE Trans Microw Theory Tech 1971;19:122–3. https://doi.org/10.1109/TMTT.1971.1127466.

[7] Ghodgaonkar DK, Varadan VV, Varadan VK. Free-space measurement of complex permittivity and complex permeability of magnetic materials at microwave frequencies. IEEE Trans Instrum Meas 1990;39:387–94. https://doi.org/10.1109/19.52520.

[8] Weir WB. Automatic measurement of complex dielectric constant and permeability at microwave frequencies. Proc IEEE 1974;62:33–6. https://doi.org/10.1109/PROC.1974.9382.

[9] Bronckers LA, Smolders AB. Broadband Material Characterization Method Using a CPW With a Novel Calibration Technique. IEEE Antennas Wirel Propag Lett 2016;15:1763–6. https://doi.org/10.1109/LAWP.2016.2535115.

[10] Mantion S. Étude de cristaux magnoniques reconfigurables à base d'alliages d'Heusler Co2MnSi. Univeristé de Toulouse, 2023.

[11] Vlaminck V, Bailleul M. Spin-wave transduction at the submicrometer scale: Experiment and modeling. Phys Rev B 2010.

[12] Fallarino L, Madami M, Duerr G, Grundler D, Gubbiotti G, Tacchi S, et al. Propagation of Spin Waves Excited in a Permalloy Film by a Finite-Ground Coplanar Waveguide: A Combined Phase-Sensitive Micro-Focused Brillouin Light Scattering and Micromagnetic Study. IEEE Trans Magn 2013;49:1033–6. https://doi.org/10.1109/tmag.2012.2229385.

[13] Collet M, Gladii O, Evelt M, Bessonov V, Soumah L, Bortolotti P, et al. Spin-wave propagation in ultra-thin YIG based waveguides. Appl Phys Lett 2017;110. https://doi.org/10.1063/1.4976708.

[14] Chaimool S, Akkaraekthali P. CPW-Fed Antennas for WiFi and WiMAX. In: Hincapie R, editor. Adv. Transm. Tech. WiMAX, InTech; 2012. https://doi.org/10.5772/28456.

[15] Ghione G, Naldi C. Analytical formulas for coplanar lines in hybrid and monolithic MICs. Electron Lett 1984;20:179–81. https://doi.org/10.1049/el:19840120.

[16] Desvaux C, Dumestre F, Amiens C, Respaud M, Lecante P, Snoeck E, et al. FeCo nanoparticles from an organometallic approach: synthesis, organisation and physical properties. J Mater Chem 2009;19:3268. https://doi.org/10.1039/b816509b.

[17] Venturin D, Desvaux C, Renaud P, Chaudret B, Parra T. A nanoparticule-based ferromagnetic dielectric Fe/Co composite for RF integrated inductors. 2007 Eur. Microw.

Conf., Munich, Germany: IEEE; 2007, p. 5–8. https://doi.org/10.1109/EUMC.2007.4405111.
[18] Chon GB, Kodama D, Shinoda K, Suzuki S, Jeyadevan B. Alloy Compositional Gradation in Surface Layer and Oxidation Resistance on Chemical Synthesized FeCo Nanoparticles. Mater Sci Forum 2009;631–632:507–12. https://doi.org/10.4028/www.scientific.net/MSF.631-632.507.
[19] Millan A, Urtizberea A, Silva NJO, Palacio F, Amaral VS, Snoeck E, et al. Surface effects in maghemite nanoparticles. J Magn Magn Mater 2007;312:L5–9. https://doi.org/10.1016/j.jmmm.2006.09.011.
[20] Famiani S, LaGrow AP, Besenhard MO, Maenosono S, Thanh NTK. Synthesis of Fine-Tuning Highly Magnetic Fe@Fe_x O_y Nanoparticles through Continuous Injection and a Study of Magnetic Hyperthermia. Chem Mater 2018;30:8897–904. https://doi.org/10.1021/acs.chemmater.8b04056.
[21] Richard S, Eder V, Caputo G, Journé C, Ou P, Bolley J, et al. USPIO size control through microwave nonaqueous sol-gel method for neoangiogenesis T_2 MRI contrast agent. Nanomed 2016:nnm-2016-0177. https://doi.org/10.2217/nnm-2016-0177.
[22] Lacroix L-M, Frey Huls N, Ho D, Sun X, Cheng K, Sun S. Stable Single-Crystalline Body Centered Cubic Fe Nanoparticles. Nano Lett 2011;11:1641–5. https://doi.org/10.1021/nl200110t.
[23] Garnero C, Lepesant M, Garcia-Marcelot C, Shin Y, Meny C, Farger P, et al. Chemical Ordering in Bimetallic FeCo Nanoparticles: From a Direct Chemical Synthesis to Application As Efficient High-Frequency Magnetic Material. Nano Lett 2019;19:1379–86. https://doi.org/10.1021/acs.nanolett.8b05083.
[24] Bordet A, Lacroix L, Fazzini P, Carrey J, Soulantica K, Chaudret B. Magnetically Induced Continuous CO_2 Hydrogenation Using Composite Iron Carbide Nanoparticles of Exceptionally High Heating Power. Angew Chem Int Ed 2016;55:15894–8. https://doi.org/10.1002/anie.201609477.
[25] Bordet A, Landis RF, Lee Y, Tonga GY, Asensio JM, Li C-H, et al. Water-Dispersible and Biocompatible Iron Carbide Nanoparticles with High Specific Absorption Rate. ACS Nano 2019;13:2870–8. https://doi.org/10.1021/acsnano.8b05671.
[26] Meffre A, Mehdaoui B, Kelsen V, Fazzini PF, Carrey J, Lachaize S, et al. A Simple Chemical Route toward Monodisperse Iron Carbide Nanoparticles Displaying Tunable Magnetic and Unprecedented Hyperthermia Properties. Nano Lett 2012;12:4722–8. https://doi.org/10.1021/nl302160d.
[27] Viau G, Fiévet-Vincent F, Fiévet F, Toneguzzo P, Ravel F, Acher O. Size dependence of microwave permeability of spherical ferromagnetic particles. J Appl Phys 1997;81:2749–54. https://doi.org/10.1063/1.363979.
[28] Elmahaishi MF, Azis RS, Ismail I, Matori KA, Muhammad FD. Influence of particle size on the magnetic and microwave absorption properties of magnetite via mechano-mechanical methods for micro-nano-spheres. Nano-Struct Nano-Objects 2024;39:101207. https://doi.org/10.1016/j.nanoso.2024.101207.
[29] Wu LZ, Ding J, Jiang HB, Chen LF, Ong CK. Particle size influence to the microwave properties of iron based magnetic particulate composites. J Magn Magn Mater 2005;285:233–9. https://doi.org/10.1016/j.jmmm.2004.07.045.
[30] Fang P-H, Li H-C, Hsu S-J, Ruan J, Cheng H-L, Chou W-Y. Impact of nanoparticle dimensions on size-induced magnetic transitions in Fe3O4–PBTTT-C14 hybrid films. J Phys Chem Solids 2026;208:113108. https://doi.org/10.1016/j.jpcs.2025.113108.

[31] Herzer G. Grain size dependence of coercivity and permeability in nanocrystalline ferromagnets. IEEE Trans Magn 1990;26:1397–402. https://doi.org/10.1109/20.104389.
[32] Zhan J, Cai H-L, Chen X, Wang X, Fang Q, Yang Y, et al. Magnetic-Particle-Composite-Medium-Filled Stacked-Spiral Inductors for Radio-Frequency CMOS Applications. Chin Phys Lett 2013;30:128401. https://doi.org/10.1088/0256-307X/30/12/128401.
[33] Koh K, Park J, Park J, Zhu X, Lin L. Core-shell magnetic nanoparticles for on-chip RF inductors. 2013 IEEE 26th Int. Conf. Micro Electro Mech. Syst. MEMS, Taipei, Taiwan: IEEE; 2013, p. 465–8. https://doi.org/10.1109/MEMSYS.2013.6474279.
[34] Cai H-L, Zhan J, Yang C, Chen X, Yang Y, Chi B-Y, et al. Application of Ferrite Nanomaterial in RF On-Chip Inductors. J Nanomater 2013;2013:832401. https://doi.org/10.1155/2013/832401.
[35] Kuo Y-M, Duh J-G. Application of nanocrystalline FeHfN soft magnetic films to power inductors. J Magn Magn Mater 2012;324:1084–7. https://doi.org/10.1016/j.jmmm.2011.10.029.
[36] Ni Z, Zhan J, Fang Q, Wang X, Shi Z, Yang Y, et al. Design and Analysis of Vertical Nanoparticles-Magnetic-Cored Inductors for RF ICs. IEEE Trans Electron Devices 2013;60:1427–35. https://doi.org/10.1109/TED.2013.2245418.
[37] Toneguzzo P, Viau G, Acher O, Fiévet-Vincent F, Fiévet F. Monodisperse Ferromagnetic Particles for Microwave Applications. Adv Mater 1998;10:1032–5. https://doi.org/10.1002/(SICI)1521-4095(199809)10:13%253C1032::AID-ADMA1032%253E3.0.CO;2-M.
[38] Kittel C. Theory of the Structure of Ferromagnetic Domains in Films and Small Particles. Phys Rev 1946;70:965–71. https://doi.org/10.1103/physrev.70.965.
[39] Kittel C. Physical Theory of Ferromagnetic Domains. Rev Mod Phys 1949;21:541–83. https://doi.org/10.1103/revmodphys.21.541.
[40] Aharoni A. Exchange resonance modes in a ferromagnetic sphere 2014.
[41] Coey JMD. Magnetism and magnetic materials. Paperback edition. Cambridge New York Port Melbourne: Cambridge University Press; 2018.
[42] Hall RC. Single Crystal Anisotropy and Magnetostriction Constants of Several Ferromagnetic Materials Including Alloys of NiFe, SiFe, AlFe, CoNi, and CoFe. J Appl Phys 1959;30:816–9. https://doi.org/10.1063/1.1735247.
[43] Wang G, Liu H, Qiu H, Ning K, Yang Y, Li X, et al. MEMS-based fabrication of high-performance inductors with back hollow structure and ferromagnetic film. Microelectron Eng 2017;168:5–9. https://doi.org/10.1016/j.mee.2016.10.005.

General conclusion and perspectives.

In this work, we have explored the synthesis, characterization, and potential applications of magnetic nanoparticles as building blocks for their assembly into micromagnets used as cores of planar inductors. The major interests of inductor core are to reduce both the size and the energy losses of these RF microelectronic inductive devices. This study demonstrated that a careful control over the size, shape, composition, etc… is not only essential to tailor the structure of micromagnet but also to finely optimize their magnetic properties. Among the synthesis strategies investigated, methods providing precise control over particle size, shape, and uniformity perfectly meeting the requirements of the applications are introduced.

First of all, the physical parameters controlling the several processes of this project, from the magnetic properties and the magnetic-directed assembly of nanoparticles to the electromagnetic effect of the magnetic core, have been presented. Concise resources have been provided to understand and interpretate the experiment in this multidisciplinary field of research from the synthesis of NPs to the integration of micromagnets on inductors, performing all the necessary characterizations for each step.

An essential prerequisite for this study is the supply in large quantity of monodisperse nanoparticles of well controlled size and shape. For that reason, a comprehensive toolkit has been given for the synthesis of magnetic nanoparticles with high permeability (Fe, FeCo, CoNi) through organometallic or polyol pathway. By systematic variation of ligand pairs, acid/amine ratios, and other reaction parameters, organometallic approaches proved highly effective in tailoring nanoparticles size, shape and composition for Fe and FeCo alloy with a size between 7 nm and 20 nm. The quantity of nanoparticles produced by this approach keep limited to tens of milligrams. Moreover, post-synthetic carbidization of iron nanoparticles successfully yielded FeC phases with enhanced stability against oxidation, thus addressing a key limitation of metallic nanoparticles while under atmosphere. The polyol synthesis of CoNi nanoparticles highlighted a scalable route to submicronic particles, governed by a heterogeneous nucleation-growth mechanism, and enabling fine-tuning of static magnetic properties through

both composition and particle size in a range between 25 and 200 nm. With this approach, several hundred milligrams of particles can be produced in a single batch.

Then, a general mechanism for the formation of magnetically induced assembly of nanoparticles has been described. Thanks to a SAXS study combining the study of assembly in-situ (in solutions), and ex-situ (deposit on microscopy glass side, and deposit by magnetophoresis), it was possible to understand that the structural organization arises from an interplay between intrinsic parameters (size, morphology, permeability, surface chemistry, etc...) and external parameters (magnetic field intensity, concentration, etc...). For the particles obtained by polyol process, only RCP assembly have been obtained. For organometallic particles, two major patterns are observed, first under low field (0.4 T) particles tend to assemble into an isotropic RCP structure, at high field (1 T) particles tend to form anisotropic structure, as instance cubic particles assemble in SC fibers. Wide polydispersity in size/shape unfavored the formation of anisotropic and ordered structures. In order to increase the metallic density, which is essential for achieving high magnetic permeability, one promising approach involves using cubic magnetic nanoparticles in a magnetophoresis process under 1 T magnetic field. The method enables the formation of micromagnets composed of fibrous structures in which the cubic nanoparticles are organized in a simple cubic (SC) arrangement.

To continue, the dynamical dielectric and magnetic properties of different micromagnet have been determined. Thus, the effect of the composition and size of the nanoparticles composing the micromagnet, and the effect of an external field on the dynamic properties of the micromagnet have been described. Which means that it is possible to optimize and tune the dynamic magnetic response of micromagnet within GHz frequency applications. The micromagnets produced have resulted in inductance increase of up to 70% up to over 1 GHz, while in some specific cases (the inductor with the lowest resonances frequencies) the quality factor was not degraded and even increased. Planar inductors have been coated on their upper side only, and the increases already obtained are close to the maximum theoretically reachable value with that configuration. The best results have been obtained with micromagnet made of $Fe_{1-x}Co_x$ nanoparticles synthesized with an organometallic method with a diameter approaching the critical domain size, a high magnetic saturation, and protected with an epoxy layer to prevent the oxidation. This combination enables high permeability in the GHz range, minimal magnetic losses, and robust

environmental stability. Larger particles obtained with polyol process $Co_{1-x}Ni_x$ (>25 nm) allow us to obtain similar results without the need of epoxy protection. Furthermore, we demonstrated that the dynamic properties of these micromagnets can be controlled by applying an external magnetic field, thus resulting in agile inductors with a tunable inductance value.

In conclusion, this study lays the groundwork for the realization of highly integrated planar inductors by advancing the synthesis and engineering of magnetic nanoparticles. While significant progress has been made, ongoing optimization and innovation are still possible to fully exploit the potential of micromagnet synthesized from nanoparticles. This work lays a solid basis for further developments, bridging the gap between nanoscale materials design and practical device implementation at higher scale. The previous results not only validate the integration of nanostructured magnetic materials into RF planar inductors but also highlight promising directions for incorporating such micromagnets into more complex microcomponents, such as filters. Moreover, the encapsulation of radiating components, such as inductors, based on magnetic field confinement, could further enhance integration density by allowing these components to be positioned closer together without inducing parasitic coupling. For having better individual inductors associated with micromagnet two pathways for improvements are possible. First, for higher inductance increase, it will be necessary to switch to more complex configurations, based on sandwich deposit or 3D inductors. Secondly, for operation at higher frequencies with minimal losses, it will be necessary to shift the FMR to higher frequencies, which could involve further research into the size of NPs, and chemical composition of different alloys such as FeCoB.

Another potential application, which was not explored in this work, involves the use of anisotropic nanoparticles as building blocks to fabricate micromagnets exhibiting anisotropic magnetic properties. A component integrating such a magnet could display nonreciprocal behavior, meaning that its response would depend on the propagation direction of the electromagnetic wave. This functionality is particularly valuable for the development of advanced RF components such as isolators (a two-port device that transmits RF signal in one direction only), or circulators (a passive, non-reciprocal three- or four-port device that only allows the transmission of an RF signal from one port to the immediately following port, without any reverse transmission to the preceding port), where material with direction-

dependent transmission (due to direction-dependent permeability) is required. Furthermore, we demonstrated that applying an external magnetic field of variable magnitude enables the control of the micromagnet's characteristics. This property could be exploited to design agile, reconfigurable components with dynamically tunable responses.

Appendix 1. Fe^0 NPs: Effect of the acid/amine ratio for different ligand systems.

AL/DDA. As discussed in chapter 2, section 1.1.b.i, the C12 ligand pair composed of lauric acid (AL) and dodecylamine (DDA) exhibits a distinct behavior compared to C16, likely driven by a coalescence-based growth mechanism. To investigate this, the DDA proportion was systematically decreased to explore whether increasing the acid content would further promote particle growth and reduce polydispersity. Without any amine present (AL/DDA = 2.0/0), the system lacks sufficient stabilization, leading to uncontrolled coalescence and a highly polydisperse particle population (size range: 20–140 nm) as illustrated by the figure A1a. However, even a small amount of amine (AL/DDA = 1.8/0.1) dramatically improves particle stabilization, resulting in more uniform cubes (~40 nm), although still with a relatively high standard deviation (figure A1b). Increasing the amine content to AL/DDA = 1.8/0.5 further enlarges the particles (~49 nm) while maintaining similar polydispersity (figure A1c). At the higher amine concentration (1.8/2), the size distribution becomes bimodal (24.3 ± 4.2 and 40.9 ± 7.5 nm), and the particles adopt an octopod–cubic morphology, suggesting a shift in the growth mechanism (figure A1d). These observations are summarized in table A1.

Ratio AL/DDA	2.0/0	1.8/0.1	1.8/0.5	1.8/2
Size (nm)	Polydisperse 20-140	38.0±13.2	48.7±13.3	24.3±4.2 and 40.9±7.5
Shape	Cubes	Cubes with porosities	Cubes with porosities	Octopod-cubic (bimodal)

Table A1. Size and morphology of Fe nanoparticles obtained for C12 ligand with different AL/DDA ratio.

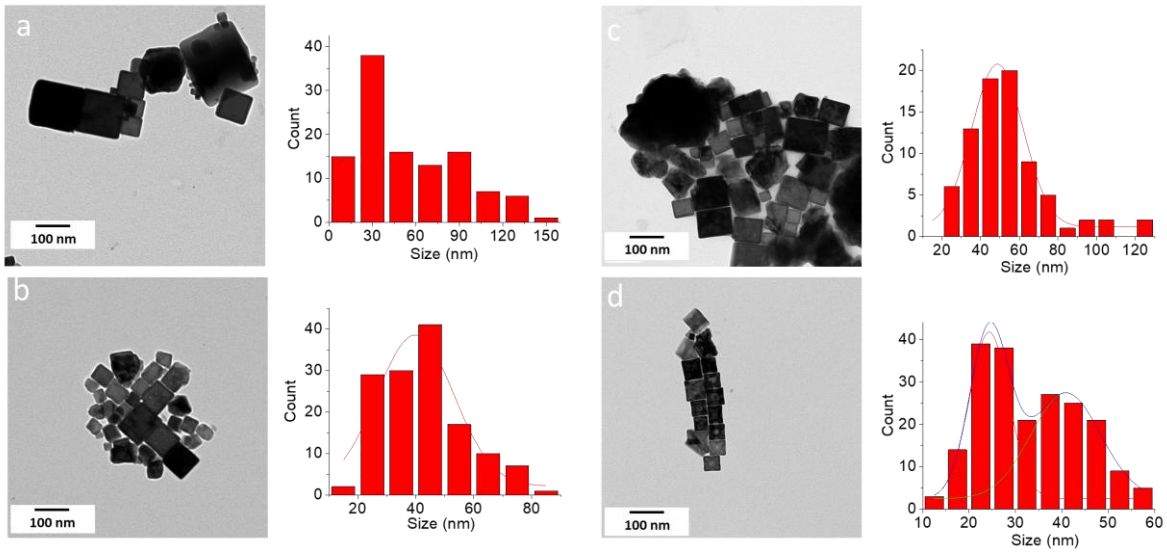

Figure A1. TEM images with the associated size distribution of Fe NPs prepared with a LA/DDA ratio of (a) 2.0/0, (b) 1.8/0.1, (c) 1.8/0.5 and (d) 1.8/2.

These results suggest that DDA plays a dual role moderating coalescence and stabilizing nanoparticle surfaces. A small amount is sufficient to suppress uncontrolled aggregation, while too much may disrupt directional growth processes.

OcAc/OcAm. This C8 system presented an unexpected trend. Experiments were conducted at a slightly lower temperature (135 °C) and increasing the acid proportion from OcAc/OcAm = 1.5/2 to 1.8/2 decreased the average particle size significantly as illustrated by microscopy (figure A2) and resumed in table A2.

Ratio OcAc/OcAm	1.5/2	1.8/2
Size (nm)	22.5±6.0	8.3±4.7
Shape	Cubes and spheres	Cubes

Table A2. Size and morphology of Fe nanoparticles obtained for C8 ligand with different OcAc/OcAm ratio.

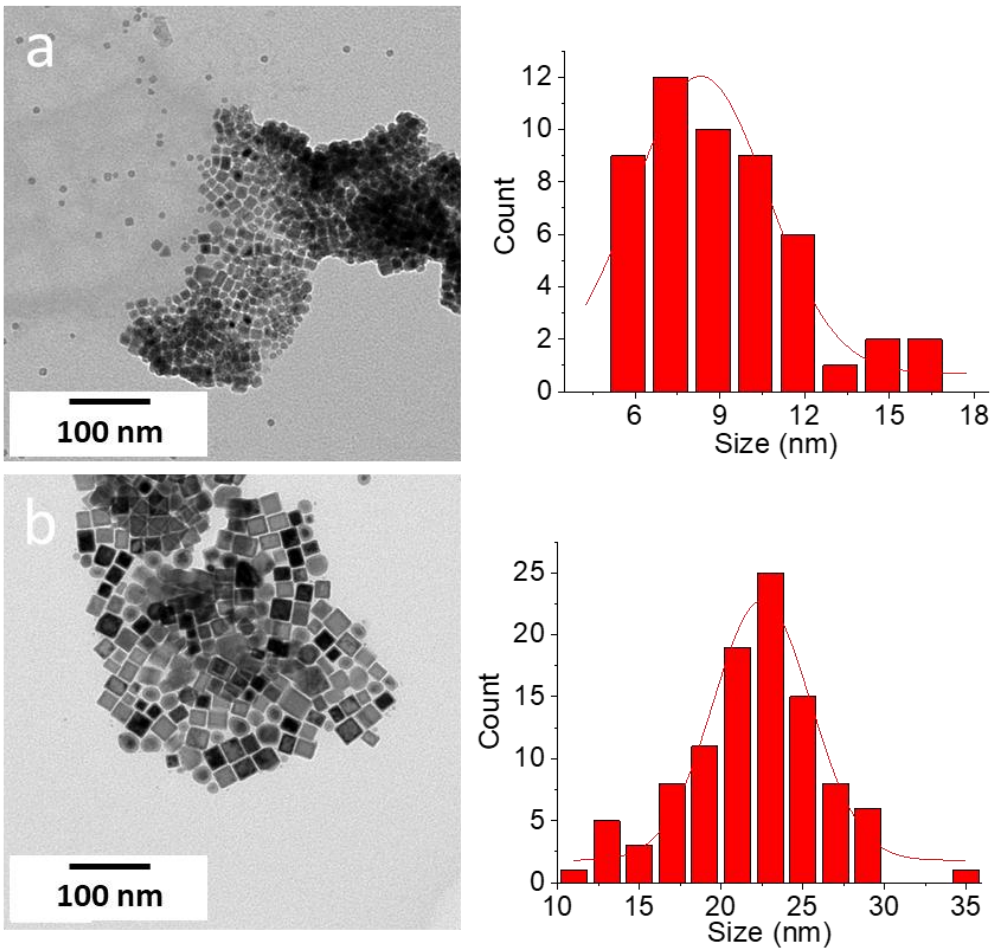

Figure A2. TEM images with the associated size distribution of Fe NPs prepared with a OcAc/OcAm ratio of (a) 1.5/2 and (b) 1.8/2.

This inverse trend compared to the C12 and C16 ligands remains difficult to explain. One hypothesis is that increasing the acid concentration alters the structure or geometry of the organic superstructures in solutions. This shift could influence their templating role, potentially promoting the formation of smaller cubic particles in superstructures over a more mixed population (including spheres) at lower acid content.

The Y/X ratio exerts a multifaceted influence on iron nanoparticle synthesis. While the general trend is that higher acid content promotes particle growth by stabilizing Fe(II) species, deviations from this rule particularly in the C8 system highlight the complex interplay between ligand structure, micelle formation, reaction kinetics etc... These observations reinforce the need for deeper investigation into how ligand ratios influence the supramolecular organization of precursors and intermediates in solutions.

Appendix 2. Effect of the reaction temperature on the formation of Fe(0) NPs.

The influence of reaction temperature on nanoparticle formation was studied. As the reaction kinetics drastically decrease with the temperature, the reaction time was adapted to reach a comparable reaction state.

A well-established trend in the literature is that lower reaction temperatures tend to yield larger nanoparticles. This effect is attributed to the greater stability of the iron reservoir at lower temperatures, which results in a slower release of reactive iron species into the medium. The delayed release, in turn, prolongs the coalescence phase of particle growth. This extended coalescence period leads not only to larger particle sizes but also to increased the polydispersity and the formation of structural features such as porosity.
The different experiments associated with the observation from the TEM images (Figure A3) are resumed in table A3.

	AP/HAD		OcAc/OcAm	
Temperature	135°C	150°C	135°C	150°C
Size (nm)	27.0±1.9 and 36.0±3.9	25.6±6.3	8.3±4.7	8.6±2.3
Shape	Cubes with porosities	Cubes	Cubes	Cubes

Table A3. Size and morphology of Fe nanoparticles obtained for C8 and C16 ligands with a ratio of 1,8/2 when reacting at different temperatures.

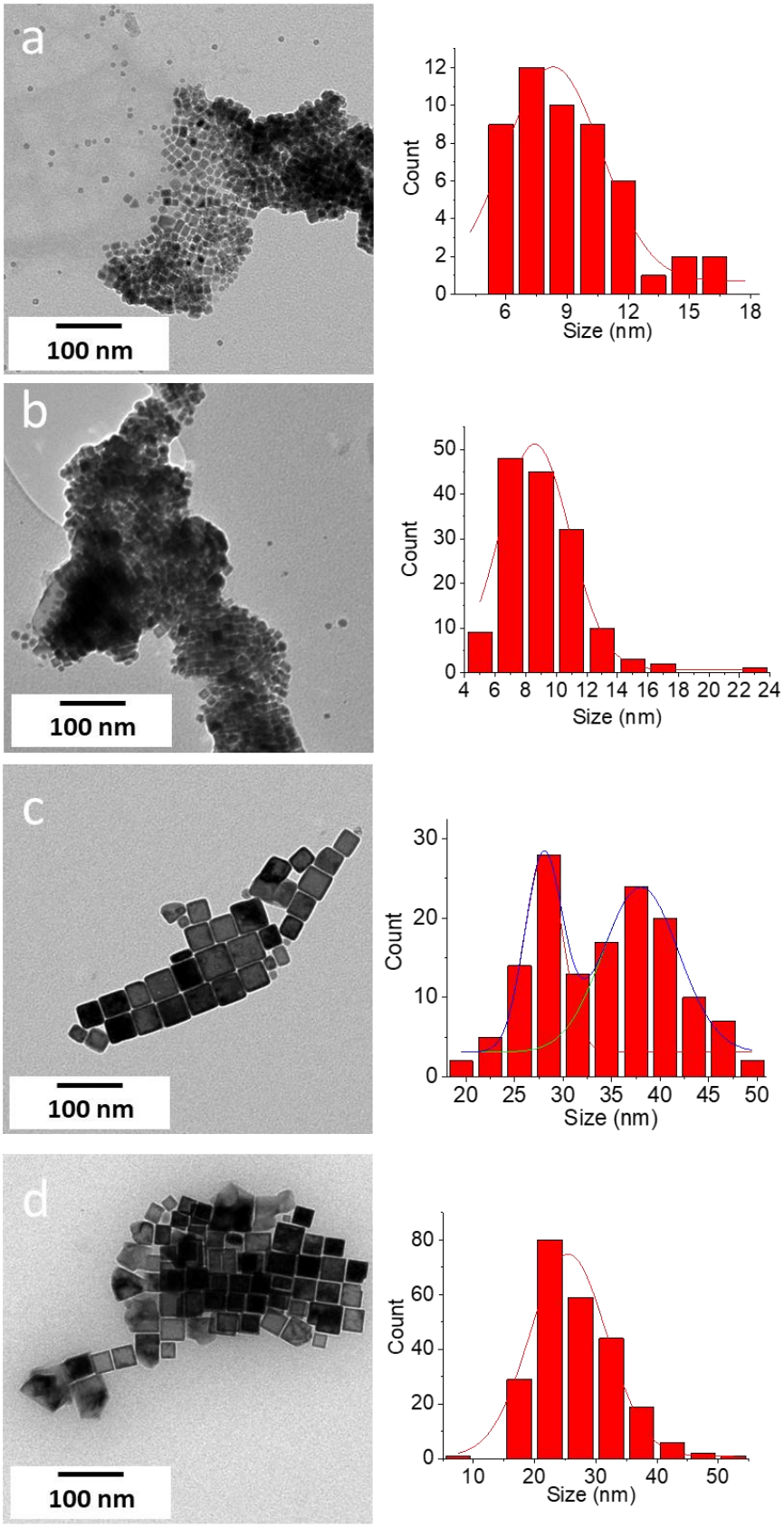

Figure A3. TEM images with the associated size distribution of Fe NPs obtained in presence of a 1.8/2 ratio of (a-b) C16 ligands and (c-d) C8 ligands at (a,c) 135°C and (b,d) 150°C

The behavior described in the literature is clearly illustrated in the **C16 ligand system (AP/HDA)**. When the reaction temperature is decreased from 150 °C to 135 °C under otherwise identical conditions (Y/X = 1.8/2), particles become slightly larger and display features indicative of coalescence, such as porosity and bimodal size distributions.

In contrast, the **C8 ligand system (OcAc/OcAm)** does not follow this trend, highlighting its distinct behavior. Here, increasing the temperature from 135 °C to 150 °C has no effect on particle size, which remains around 8–9 nm. In both cases, the particles morphologies are very similar. This deviation suggests that the C8 system follows a different growth regime, likely driven by different dynamics of ligand–metal interactions or a distinct organization of the organic superstructures acting as growth templates. In particular, the short alkyl chains may not form the same supramolecular structures as the longer C16 chains and may limit coalescence even at lower temperatures.

While the general relationship between lower temperature and increased particle size holds for systems like AP/HDA, the C8-based 1.8/2 OcAc/OcAm system behaves anomalously. This highlights once again the unique and less predictable behavior of these systems, emphasizing the need for further investigation into how chain length and supramolecular structuring influence growth mechanisms at different temperatures.

Appendix 3. Synthesis of FeCo NPs using a two-step approach

In an effort to obtain larger iron-cobalt nanoparticles, a two-step seed-mediated synthesis approach was tested. This strategy separates the nucleation (seed formation) and growth (ripening) stages, inspired by the previously described methodology for iron nanoparticles. However, in that case the results showed limited improvement compared to the one-pot synthesis, with final particle sizes remaining within a similar range.

Step 1 – Seed Formation

Iron-cobalt seeds were generated by thermally decomposing a mixture of iron and cobalt precursors in the absence of stabilizing ligands:

$$[\mathrm{Fe(N(Si(CH_3)_3)_2)_2]_2} + [\mathrm{Co(N(Si(CH_3)_3)_2)_2}].\,\mathrm{THF} \xrightarrow[\substack{150°C,\ 3bar\ H_2,\\ seed\ germination\ time\ (t_g)\\ Mésitylène}]{} \mathrm{FeCo\ seeds}$$

The reaction was carried out in mesitylene at 150 °C under 3 bar of H_2 for various seed germination times (t_g). In the absence of added ligands, the only stabilizing species present were hexamethyldisilazane (HMDS) by-products formed during the decomposition process. As a result, the seeds generated are highly reactive, poorly stabilized, and prone to coalescence or further growth upon the introduction of ligands.

Step 2 – Growth step

After seed formation and subsequent cooling, a defined quantity of long-chain acid/amine ligands (HDAHCl and HDA) was introduced to the reaction mixture:

$$\mathrm{FeCo\ seeds} + \mathrm{X\ HDA} + \mathrm{Y\ HDAHCl} \xrightarrow[\substack{150°C,\ 3bar\ H_2,\ 72h\\ Mésitylène}]{} \mathrm{Fe(0)\ NPs}$$

The growth phase was conducted at 150 °C under 3 bar of H_2 for 72 hours. During this stage, the reactive seeds underwent further growth into larger particles. Ligand concentrations were expressed in molar equivalents relative to the total amount of iron organometallic precursor content introduced in Step 1. The experiments are summarized in table A4.

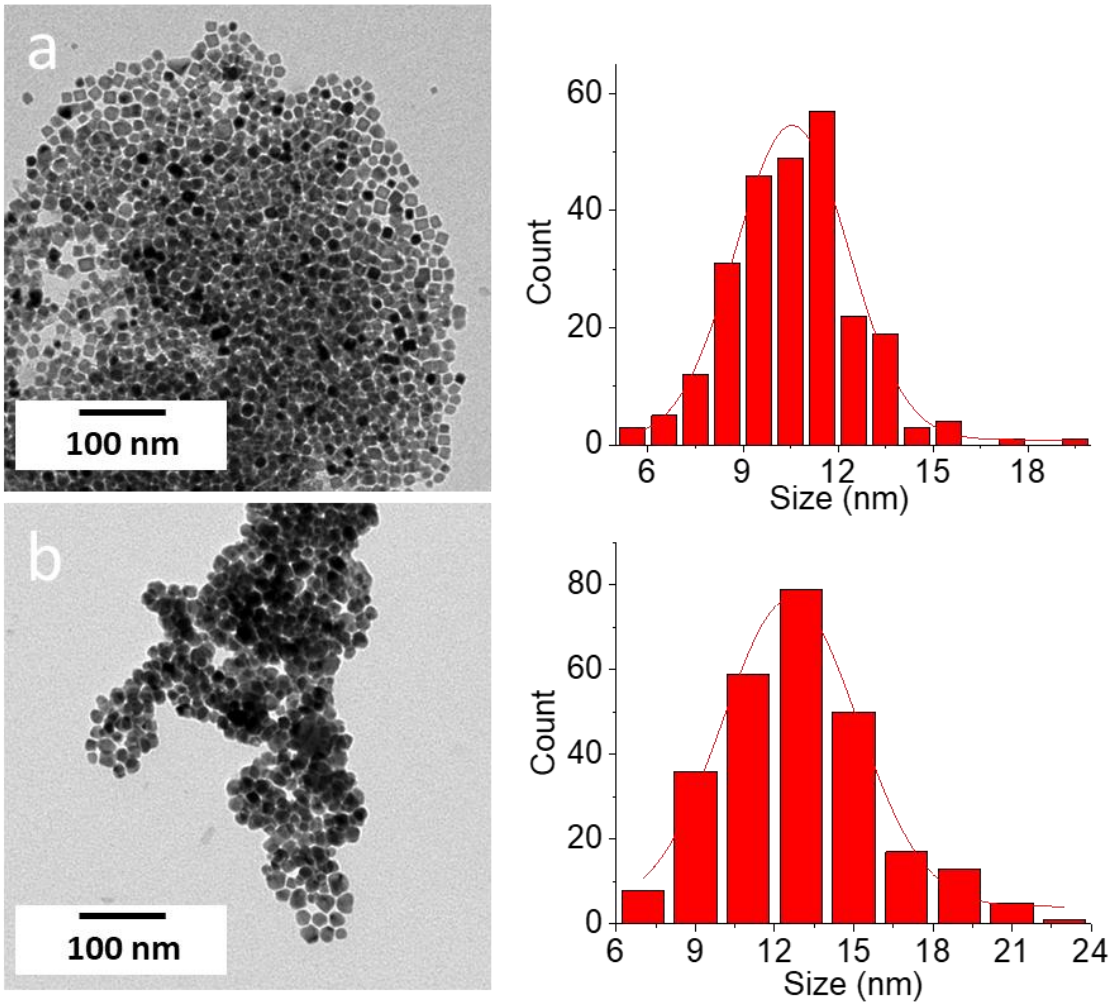

Figure A4. TEM images with the associated size distribution of FeCo NPs obtained in presence of a HDAHCl/HDA ratio of (a) 3/4 and (b) 4/4.

Ratio HDAHCl/HDA	¾	4/4
Germination time t_g	1.5 h	16 h
Size (nm)	10.6±1.8	12.6±2.6
Shape	Squircles and cubes	Truncated octahedron

Table A4. Size and morphology of FeCo nanoparticles obtained after seed-mediated growth.

Combining a short seed time (1.5 h) with a ligand ratio 3 HDAHCl / 4 HDA yielded ~10.6 nm particles, with a mixture of squircles and cubes (Figure A4a). Whereas a longer seed time (16 h) with a ratio of 4/4, larger particles (12.6 nm) with a more defined truncated octahedron

shape were observed (Figure A4b). In that case, the final particle sizes and morphologies were comparable to those obtained in one-pot syntheses using optimized ligand ratios (3.2/4 yielding 12.5 ± 1.4 nm truncated octahedra in 24 h).

This two-step method did not lead to a significant enhancement in particle size or shape control compared to the one-step synthesis. Therefore, it was not pursued further in this study. Moreover, no compositional analyses (e.g., ICP-MS or EDX) were conducted on these samples, leaving the Fe/Co ratios unverified. Since the shape of the particles obtained is not identical, it is possible that their composition varied depending on the synthesis conditions.

Appendix 4. Calculation of CoNi nanoparticle size under the assumption of one nucleus per nanoparticle.

- A single Pt seed per CoNi nanoparticle ⇒ the number of seeds equals the number of particles.

- The seed size is independent of the [CoNi] concentration conditions.

Total available Pt volume = $\frac{[Pt]\times M_{Pt}}{\rho_{Pt}} = V_{Pt.total} = V_{germe\ Pt} \times N_{germes\ Pt}$ => It is assumed that all the Pt has been reduced and has formed nuclei of uniform size.

The number of Pt nuclei can thus be deduced.

$$N_{germes\ Pt} = \frac{[Pt] \times M_{Pt}}{\rho_{Pt}} \times \frac{1}{V_{germe\ Pt}}$$

Hence, the number of Pt nuclei equals the number of CoNi nanoparticles (assumption 1: one nucleus per nanoparticle).

$$N_{NP\ CoNi} = \frac{[Pt] \times M_{Pt}}{\rho_{Pt}} \times \frac{1}{V_{germe\ Pt}}$$

However, the number of CoNi nanoparticles depends on the amount of CoNi available and on the nanoparticle size, following the same reasoning as for Pt.

$$N_{NP\ CoNi} = \frac{[CoNi] \times M_{CoNi}}{\rho_{CoNi}} \times \frac{1}{V_{NP\ CoNi}}$$

So $\frac{[CoNi]\times M_{CoNi}}{\rho_{CoNi}} \times \frac{1}{V_{NP\ CoNi}} = \frac{[Pt]\times M_{Pt}}{\rho_{Pt}} \times \frac{1}{V_{germe\ Pt}}$

Then $V_{NP\ CoNi} = \frac{[CoNi]\times M_{CoNi}}{\rho_{CoNi}} \times \frac{\rho_{Pt}}{[Pt]\times M_{Pt}} \times V_{germe\ Pt}$

And $V_{NP\ CoNi} = \frac{\pi}{6} d_{CoNi}^3$ et $V_{germe\ Pt} = \frac{\pi}{6} d_{germe\ Pt}^3$

So $d_{CoNi}^3 = \frac{[Co+Ni]}{[Pt]} \times \frac{\rho_{Pt}}{\rho_{CoNi}} \times \frac{M_{CoNi}}{M_{Pt}} \times d_{Pt}^3$

Then $\boxed{d_{CoNi} = \left(\frac{[Pt]}{[Co+Ni]}\right)^{-1/3} \times \left(\frac{\rho_{Pt}}{\rho_{CoNi}} \times \frac{M_{CoNi}}{M_{Pt}}\right)^{1/3} \times d_{Pt}}$

With $\rho_{Pt} = 21{,}4\ g.cm^{-3}$, $M_{Pt} = 195\ g.mol^{-1}$

And $\rho_{Co} = \rho_{Ni} = 8{,}9\ g.cm^{-3}$, $M_{Co} \sim M_{Ni} = 58{,}8\ g.mol^{-1}$,

Finally, $\boxed{d_{CoNi} = \left(\frac{[Pt]}{[Co+Ni]}\right)^{-1/3} \times 0{,}898 \times d_{Pt}}$

If we assume that there are two Pt nuclei per CoNi nanoparticle.

$N_{NP\ CoNi} = \frac{1}{2} \times \frac{[Pt] \times M_{Pt}}{\rho_{Pt}} \times \frac{1}{V_{germe\ Pt}}$

So $\boxed{d_{CoNi} = \left(\frac{[Pt]}{[Co+Ni]}\right)^{-1/3} \times \left(2\frac{\rho_{Pt}}{\rho_{CoNi}} \times \frac{M_{CoNi}}{M_{Pt}}\right)^{1/3} \times d_{Pt}}$

Finally, $\boxed{d_{CoNi} = \left(\frac{[Pt]}{[Co+Ni]}\right)^{-1/3} \times 1{,}13 \times d_{Pt}}$

And so on…

This would result in a change only in the slope when plotting d_{CoNi} in function of $\left(\frac{[Pt]}{[Co+Ni]}\right)^{-1/3}$

The linearity clearly indicates that the number of nuclei within the nanoparticles remains constant; however, there is an uncertainty in the deduced size of the nuclei.

Indeed $d_{Pt} = \frac{slope}{\left(n\frac{\rho_{Pt}}{\rho_{CoNi}} \times \frac{M_{CoNi}}{M_{Pt}}\right)^{1/3}} = \frac{slope}{k}$ with n representing the number of Pt nuclei in each CoNi nanoparticle

N	1	2	3	4	5	6
Factor k	0.898	1.13	1.29	1.42	1.54	1.63

Table A5.

Appendix 4 part 2. Introduction of Pt solution in the CoNi synthesis

$$[Pt] = \frac{m_{K_2PtCl_4}}{M_{K_2PtCl_4}} \times \frac{1}{V}$$

Then

$$[Pt]_{stock\ solution} = \frac{10 \times 10^{-3}}{415} \times \frac{1}{10 \times 10^{-3}} = (2{,}4\ \pm 0{,}2\ ) \times 10^{-3} mol/L$$

The amount of Pt introduced is adjusted according to the desired final size of the CoNi nanoparticles. Typically, the quantities of Pt added range between $1{,}8\ \times 10^{-6} mol$ and $2{,}1\ \times 10^{-5} mol$, this corresponds to volumes of the stock solution ranging from 0.75 to 8.8 mL (in the latter case, stock solutions with four times higher concentration were prepared).

If the Pt precursor is hydrated (for instance, due to aging and its hygroscopic nature), and we assume it contains three water molecules, its molar mass becomes 469 g/mol instead of 415 g/mol.

So, for 10 mg of K_2PtCl_4:

$$[Pt]_{stock\ solution} = \frac{10 \times 10^{-3}}{469} \times \frac{1}{10 \times 10^{-3}} = (2{,}1\ \pm 0{,}2\ ) \times 10^{-3} mol/L$$

This leads to an error of approximately 12% in the actual Pt concentration. Consequently, the data points are shifted to the right on the curve of d_{CoNi} in function of $[K_2PtCl_4]$.

Appendix 5. Simulation of SAXS pattern using SASVIEW

The diffusion pattern of two different assemblies of 10 nm NP with a 15% size polydispersity were simulated. A random assembly with a 50% density is reported in blue. The structure factor was modeled using the Percus–Yevick approximation, i.e. a hard sphere approach (blue curve figure A6). This leads to the appearance of distinct peaks, here labeled as q_1, q_2, and q_3. The position of the first peak (q_1) corresponds to the mean interparticle distance, while the ratios q_2/q_1, and q_3/q_1, provide information on the local packing density. For example, at 50% volume fraction, $q_2/q_1 \approx 1.81$.

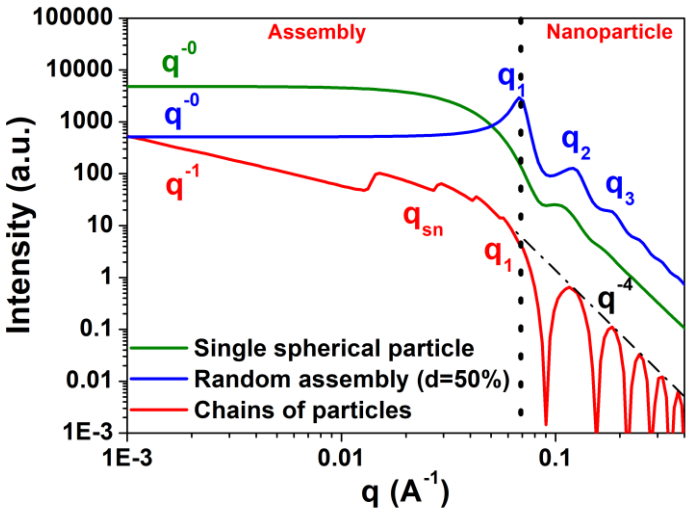

Figure A6. Scattering patterns simulated using SASVIEW for diluted spheres with a polydisperse size (green) and their assembly as 1D chain of 10 particles (red) or random assembly (blue).

A chain like assembly of the 10 NPs was simulated using the "linear pearl model" and is shown in red. The scattered intensity exhibits a series of peaks corresponding to the interparticle distance along the chain (noted q_{sn}). The scattering curve also shows a distinct change in slope: a q^{-4} slope at high q, reflecting the three-dimensional nature of the individual spheres and a q^{-1} slope at low q which reflects the one-dimensional linear arrangement of the chain.

Appendix 6. Magnetophoresis assembly of Fe nanocubes

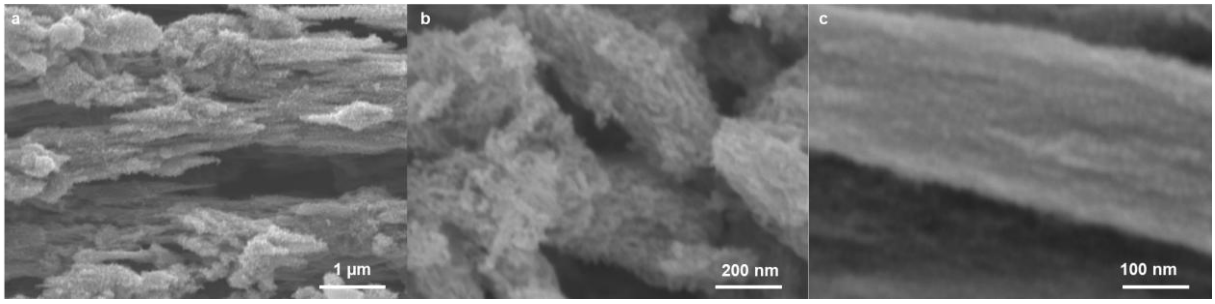

Figure A7. SEM image of micromagnet made of cubic Fe nanoparticle with an average size of 10 ± 2 nm obtained from magnetophoresis 1 T without appropriate dispersion. (b) Focus on disordered clusters and (c) focus on the fibers.

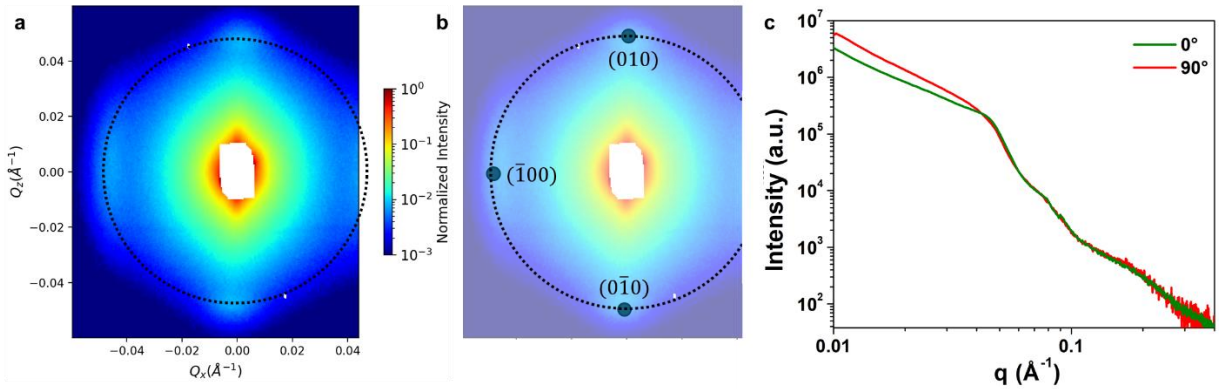

Figure A8. (a) 2D µ-SAXS pattern of the Fe nanocube assembly limited to q = -0.06 – 0.06 Å^{-1} region for visualization's sake. (b) Indexation of the pattern considering a simple cubic arrangement. Dashed lines : q_1 = 0.045 Å^{-1} (c) 1D profile obtained after integration on the azimuthal sector φ = 0 ± 5° (green) and φ = 90 ± 5° (red).

	q (Å^{-1})	D_{CP} (nm)	D_{BCC} (nm)	D_{FCC} (nm)	D_{TEM} (nm)
q_1 (Å^{-1})	0.045	14.0 (q_1=q_{100})	17.1 (q_1=q_{110})	19.7 (q_1=q_{200})	10 ± 2

Table A6. Summary of the different center-to-center distance determined considering a cubic organization CP, BCC or FCC observed along the zone axis [001]. The indexation of q_1 is proposed considering the Intercalary 1.

Appendix 7. Photograph of thin film

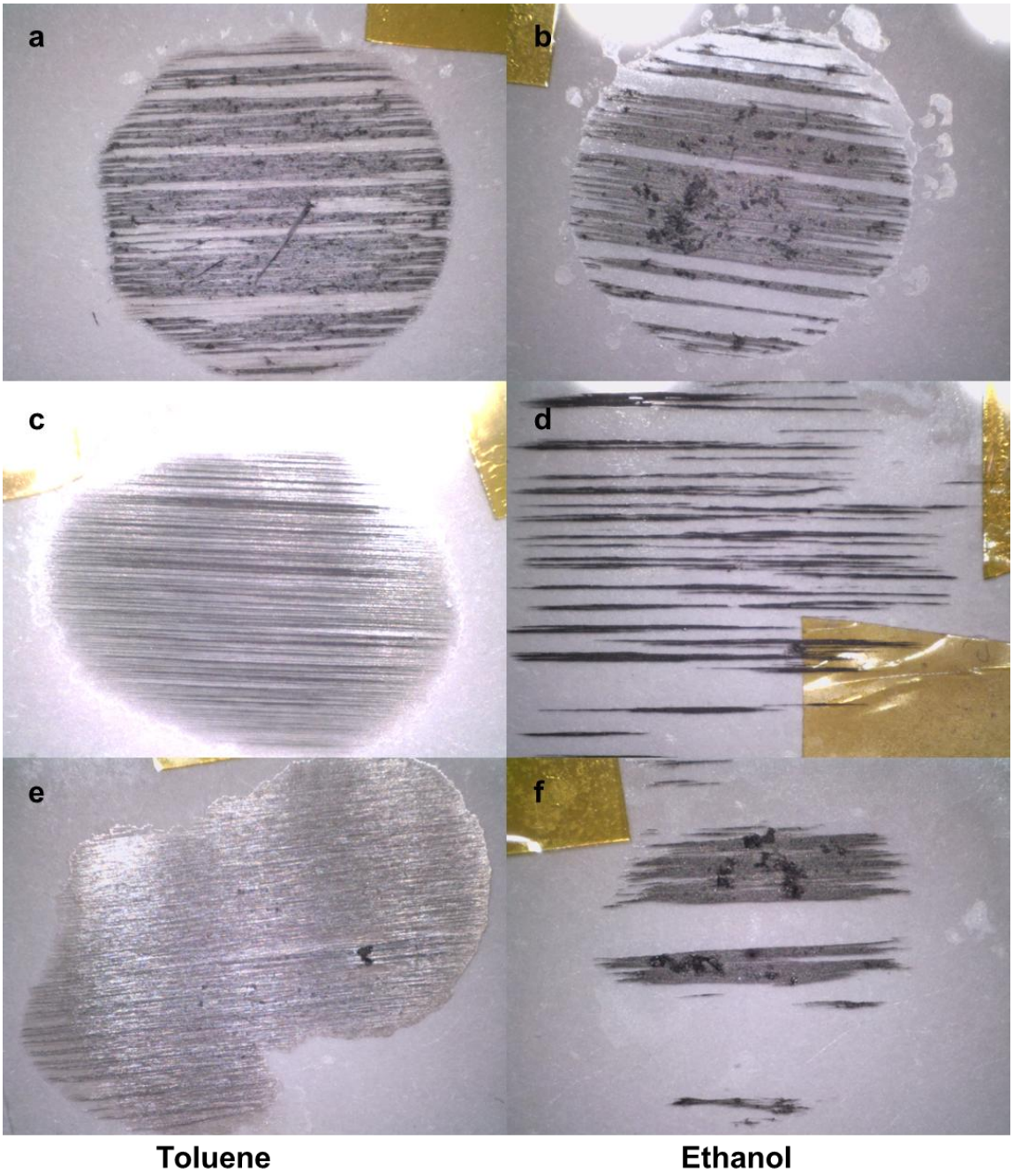

Figure 19. Comparison of optical image of the assembly obtained on the glass substrate with (a) $Fe_{0.9}Co_{0.1}$ 20 ± 4 nm in toluene and (b) in ethanol. (c) The assembly obtained from Fe 11 ± 1 nm in toluene and (d) in ethanol. (e) The assembly obtained from FeCo 11 ± 1 nm in toluene and (f) in ethanol.

Appendix 8. Standard indexation

Standard indexed diffraction pattern exhibiting a cubic symmetry

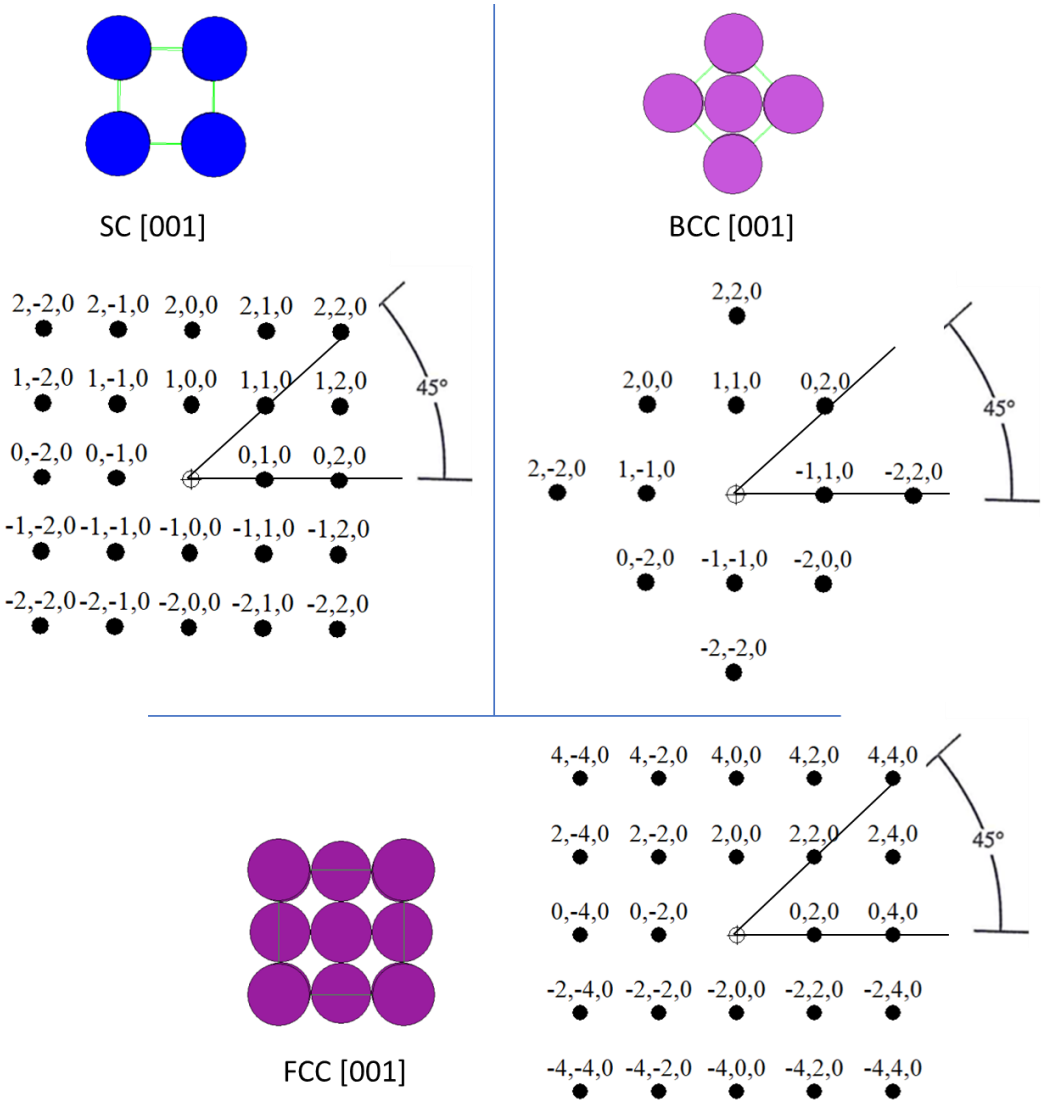

Crystal	Zone Axis	1st spot	2nd spot	D center to center particle distance	$\frac{q_2}{q_1}$
Cubic	[001]	$d_{100} = a$	$d_{110} = \frac{a}{\sqrt{2}}$	$D_{CP} = a = \frac{2\pi}{q_{100}}$	$\frac{q_{110}}{q_{100}} = \sqrt{2}$
BCC	[001]	$d_{110} = \frac{a}{\sqrt{2}}$	$d_{200} = \frac{a}{2}$	$D_{bcc} = \frac{a\sqrt{3}}{2} = \frac{\pi\sqrt{6}}{q_{110}}$	$\frac{q_{200}}{q_{110}} = \sqrt{2}$
FCC	[001]	$d_{200} = \frac{a}{2}$	$d_{220} = \frac{a}{2\sqrt{2}}$	$D_{fcc} = \frac{a\sqrt{2}}{2} = \frac{2\pi\sqrt{2}}{q_{200}}$	$\frac{q_{220}}{q_{200}} = \sqrt{2}$

Standard indexed diffraction pattern exhibiting an hexagonal symmetry

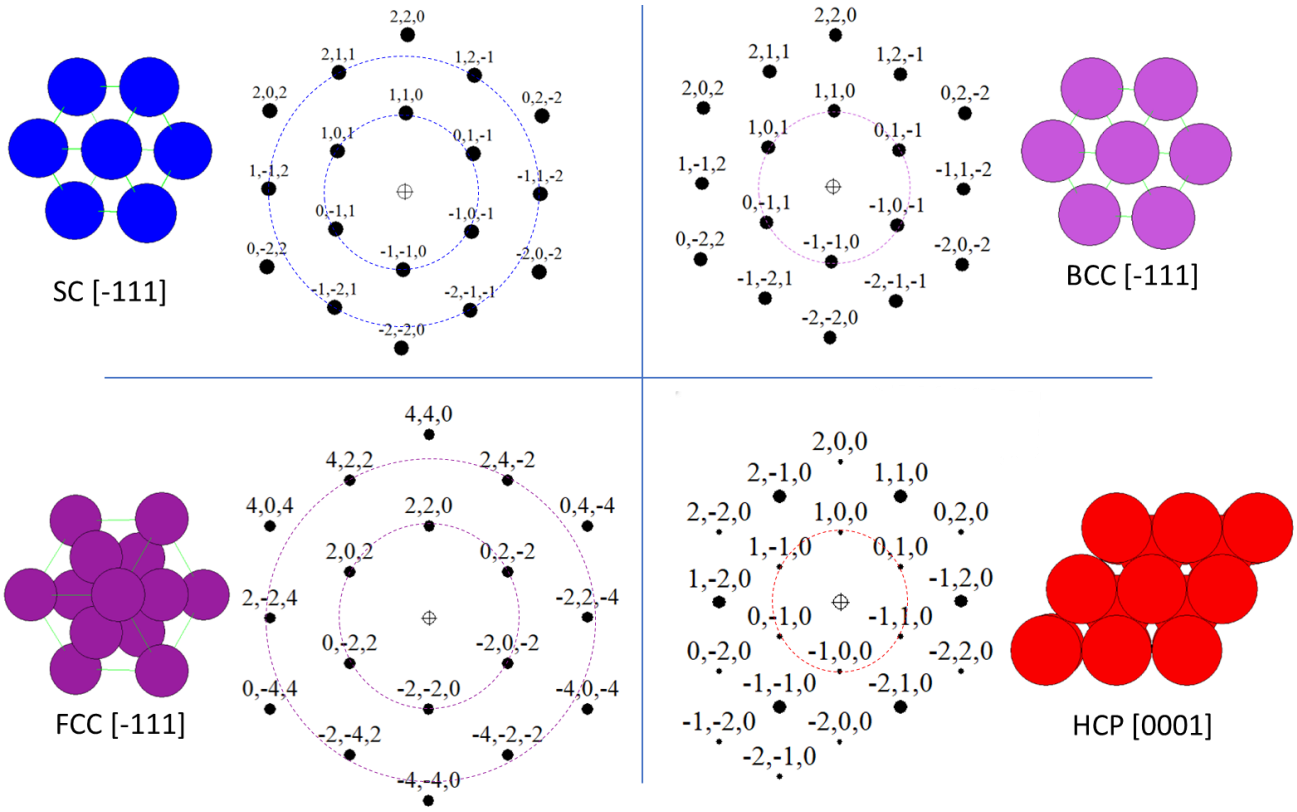

Crystal	Zone Axis	1st spot	2nd spot	D center to center particle distance	$\frac{q_2}{q_1}$
Cubic	[111]	$d_{110} = \frac{a}{\sqrt{2}}$	$d_{211} = \frac{a}{\sqrt{6}}$	$D_{CP} = a = \frac{2\pi\sqrt{2}}{q_{110}}$	$\frac{q_{211}}{q_{110}} = \sqrt{3}$
BCC	[111]	$d_{110} = \frac{a}{\sqrt{2}}$	$d_{211} = \frac{a}{\sqrt{6}}$	$D_{bcc} = \frac{a\sqrt{3}}{2} = \frac{\pi\sqrt{6}}{q_{110}}$	$\frac{q_{211}}{q_{110}} = \sqrt{3}$
FCC	[111]	$d_{220} = \frac{a}{2\sqrt{2}}$	$d_{224} = \frac{a}{2\sqrt{6}}$	$D_{fcc} = \frac{a\sqrt{2}}{2} = \frac{4\pi}{q_{220}}$	$\frac{q_{224}}{q_{220}} = \sqrt{3}$
HCP	[0001]	$d_{100} = \frac{a\sqrt{3}}{2}$	$d_{110} = \frac{a}{2}$	$D_{hcp} = a = \frac{4\pi}{\sqrt{3}q_{100}}$	$\frac{q_{110}}{q_{100}} = \sqrt{3}$

Appendix 9. HFSS simulation of CPW with magnetic material

To gain a better understanding of the correspondence between actual and relative values, particularly in extreme cases, HFSS simulations were performed (Figure A.9).

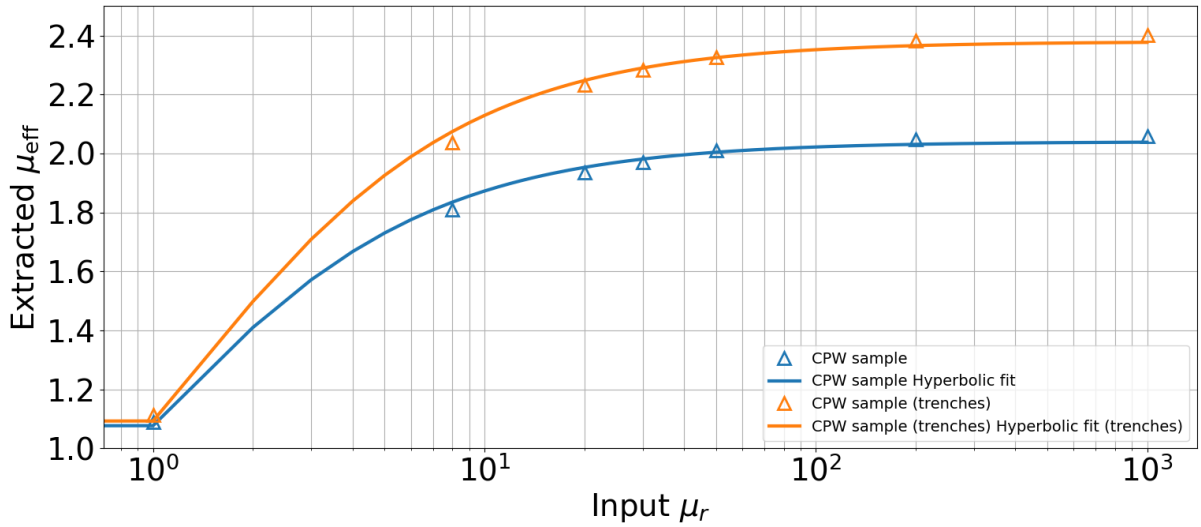

Figure A.9. Correspondence between the effective relative permeability μ'_{eff} extracted from a CPW simulated on HFSS with the defined μ'_r relative permeability of the magnet on this magnet. Two extreme cases are shown, in blue the trenches are empty, and in orange these trenches are full of magnetic material.

RÉPUBLIQUE FRANÇAISE
Liberté
Égalité
Fraternité

Université de Toulouse

Titre : Intégration localisée de matériaux magnétiques doux à partir de nanoparticules pour des applications RF

Mots clés : Microaimant, Magnétophorèse, Nanoparticules magnétiques, Radiofrequence, permeabilité, nanomagnétisme

Résumé : Les cœurs magnétiques à haute perméabilité sont souvent utilisés dans les composants électroniques afin de concentrer les lignes de champ électromagnétique, dans le but d'améliorer leurs performances en radiofréquence ou de réduire la taille des dispositifs tout en maintenant leurs performances. Cette étude présente une nouvelle approche ascendante (bottom-up) pour l'intégration localisée de matériaux diélectriques magnétiques sur des inductances planaires. Les nanoparticules magnétiques sont d'abord synthétisées par une méthode chimique en phase liquide, puis assemblées en micro-aimants submillimétriques sur des inductances et des guides d'ondes coplanaires par un procédé de magnétophorèse réalisé à pression atmosphérique et à température ambiante. Cette approche permet un dépôt conforme tout en limitant les pertes de matériau. Les permittivités et perméabilités des matériaux à base de particules de Fe, FeC, FeCo et CoNi ont été extraites jusqu'à 30 GHz. L'optimisation des propriétés magnétiques des aimants, à travers la taille et la composition chimique des nanoparticules, permet d'augmenter de 40 à 60 % les valeurs nominales d'inductance (2 et 13 nH) jusqu'à 3 GHz. Ces résultats ouvrent de nouvelles perspectives pour la conception de microcomposants électroniques radiofréquences.

Title: Localized Integration of Soft Magnetic Materials Derived from Nanoparticles for RF Device Applications

Key words: micromagnet, Magnetophoresis, magnetic nanoparticles, radiofrequency, permeability, nanomagnetism

Abstract: High permeability magnetic cores are often used in electronic components to concentrate electromagnetic field lines in order to enhance their radiofrequency properties or to reduce the device size while maintaining their performances. This study presents a new bottom-up approach for integrating localized magnetic dielectric materials onto planar inductors. Magnetic nanoparticles are first synthesized by a liquid-phase chemical approach and then assembled into submillimeter magnets onto inductors and coplanar waveguides by a magnetophoresis-directed process, performed at atmospheric pressure and room temperature. This approach allows a conformal deposition while limiting material losses. Permittivity and permeability of Fe, FeC, FeCo and CoNi particles based-materials are extracted up to 30 GHz. Optimizing the magnetic properties of the magnets through the size and chemical composition of the nanoparticles allow increasing of 40 to 60% the nominal inductance values of 2 and 13 nH up to 3 GHz. These results open new perspectives for the design of radio-frequency electronic micro-components.